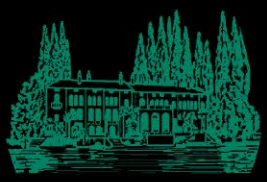

PROCEEDINGS
INTERNATIONAL SCHOOL OF PHYSICS «ENRICO FERMI»

COURSE 202

Mechanics of Earthquake Faulting

edited by A. Bizzarri, S. Das and A. Petri

2 - 7 July 2018

Villa Monastero
Varenna, Lake Como

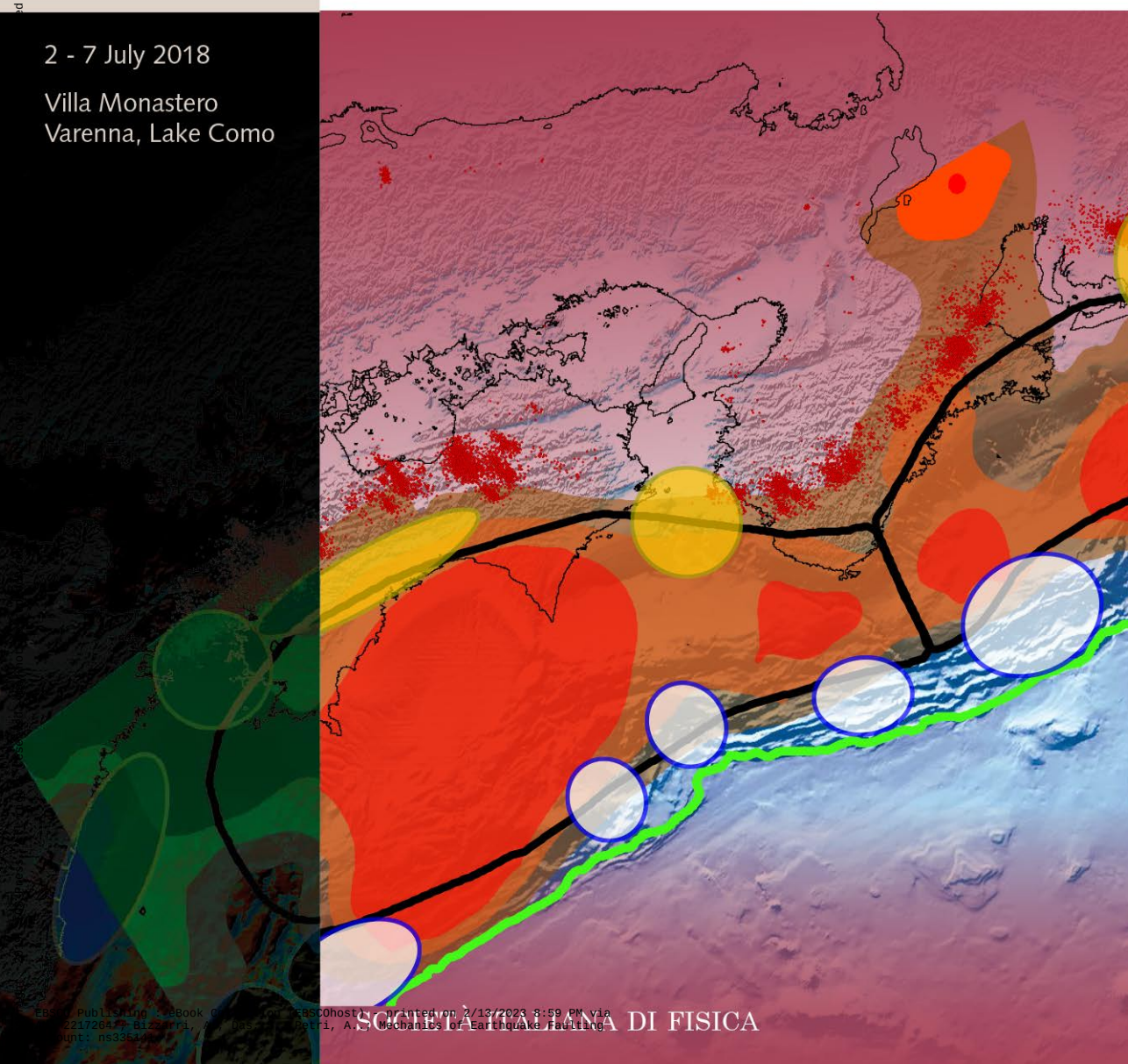

SOCIETÀ ITALIANA DI FISICA

SOCIETÀ ITALIANA DI FISICA

RENDICONTI

DELLA

SCUOLA INTERNAZIONALE DI FISICA

"ENRICO FERMI"

CCII Corso

a cura di A. Bizzarri, S. Das e A. Petri

Direttori del Corso

VARENNA SUL LAGO DI COMO

VILLA MONASTERO

2 – 7 Luglio 2018

Meccanica delle faglie sismogenetiche

2019

SOCIETÀ ITALIANA DI FISICA
BOLOGNA-ITALY

ITALIAN PHYSICAL SOCIETY

PROCEEDINGS

OF THE

INTERNATIONAL SCHOOL OF PHYSICS

"ENRICO FERMI"

Course 202

edited by A. Bizzarri, S. Das and A. Petri

Directors of the Course

VARENNA ON LAKE COMO

VILLA MONASTERO

2 – 7 July 2018

Mechanics of Earthquake Faulting

2019

IOS Press

AMSTERDAM - WASHINGTON DC

ISSN 0074-784X (print)
ISSN 1879-8195 (online)

ISBN 978-1-61499-978-2 (print) (IOS Press)
ISBN 978-1-61499-979-9 (online) (IOS Press)
ISBN 978-88-7438-118-0 (SIF)

jointly published and distributed by:

IOS PRESS
Nieuwe Hemweg 6B
1013 BG Amsterdam
The Netherlands
fax: +31 20 687 0019
info@iospress.nl

SOCIETÀ ITALIANA DI FISICA
Via Saragozza 12
40123 Bologna
Italy
fax: +39 051 581340
order@sif.it

For book sales in the USA and Canada
IOS Press, Inc.
6751 Tepper Drive
Clifton, VA 20124
USA
Tel.: +1 703 830 6300
Fax: +1 703 830 2300
sales@iospress.com

Supported by

Camera di Commercio di Lecco

Istituto Nazionale di Fisica Nucleare (INFN)

Museo Storico della Fisica e Centro Studi e Ricerche “Enrico Fermi”

Univerlecco

Istituto Nazionale di Ricerca Metrologica (INRiM)

Università di Roma Tor Vergata

Gran Sasso Science Institute (GSSI)

Istituto Nazionale di Geofisica e Vulcanologia (INGV)

Produced by the SIF Editorial Staff

Production Editor: Marcella Missiroli

Cover: see Aitaro Kato, *The evolution of fault slip rate prior to earthquake: The role of slow- and fast-slip modes*, p. 53

Graphic elaboration by Simona Oleandri

Printed in Italy by nuova MONOGRAF snc - Bologna

CONTENTS

A. Bizzarri, S. Das and A. Petri – Preface . . . . . p. XIII

Course group shot . . . . . » XVI

Andrea Bizzarri – The mechanics of supershear earthquake ruptures . . . » 1

1. Introduction . . . . . » 1
2. Physical problem . . . . . » 5
3. Numerical solutions . . . . . » 8
4. Frequency content . . . . . » 9
5. The penetration of the forbidden zone . . . . . » 12
6. The shear-Mach and the Rayleigh-Mach cones . . . . . » 14
7. The two transition styles: the direct transition and the mother-daughter mechanism . . . . . » 21
8. Different ground motions . . . . . » 25
9. Concluding remarks . . . . . » 28

Shamita Das – Unusual large earthquakes on oceanic transform faults . . . . » 33

1. Introduction . . . . . » 34
2. Pre-existing zones of weakness on the ocean floor . . . . . » 34
3. Re-activation of old transform faults: earthquakes with conjugate faulting in oceanic environments . . . . . » 38
   - 3·1. The 1989 great Macquarie Ridge earthquake reactivated a dormant conjugate fault . . . . . » 38
   - 3·2. The 1987–1992 and the January 23, 2018 Gulf of Alaska earthquake sequences . . . . . » 40
   - 3·3. The M_w7.8 18 June 2000 Wharton Basin earthquake: simultaneous rupture of conjugate faults in an oceanic setting . . . . . » 42
   - 3·4. The January 11 and 12, 2012 twin Sumatra earthquake ($M_w 8.6, 8.2$) » 43
4. A great earthquake on a fossil fracture zone: the 2004 Tasman Sea earthquake » 44
   - 4·1. Slip below the Moho during earthquakes . . . . . » 49

5. A great earthquake with the main fault plane normal to regional transform faults: the 1998 M_w8.1 Antarctic plate earthquake . . . . . » 49
6. Conclusions . . . . . » 51

Aitaro Kato – The evolution of fault slip rate prior to earthquake: The role of slow- and fast-slip modes . . . . . » 53

1. Wide spectrum of slip rate from fast- to slow-slip . . . . . » 54
   1˙1. Various types of slow earthquakes . . . . . » 55
   1˙2. Complexity of slow earthquakes . . . . . » 58
   1˙3. The early acceleration phase of slow-slip event . . . . . » 61
2. Episodic unlocking of fault prior to large earthquake . . . . . » 62
   2˙1. Foreshock sequence of the 2011 M_{w} 9.0 Tohoku-Oki, Japan earthquake » 63
   2˙2. Foreshock sequence of the 2014 M_{w} 8.2 Iquique, Chile earthquake . . » 66
   2˙3. Triggering of the 2014 M_{w} 7.3 Papanoa, Mexico earthquake by a slow-slip event . . . . . » 69
   2˙4. Foreshock sequence of the 2016 M_{w} 7.0 Kumamoto, Japan earthquake » 70
3. Discussion . . . . . » 72
4. Conclusions . . . . . » 74

Chris Marone – The spectrum of fault slip modes from elastodynamic rupture to slow earthquakes . . . . . » 81

1. Introduction . . . . . » 82
2. Mechanics of slow slip . . . . . » 82
   2˙1. Friction laws for slow slip . . . . . » 83
   2˙2. Laboratory observations of the full spectrum of slip modes from fast to slow . . . . . » 83
   2˙3. Mechanics of laboratory slow earthquakes . . . . . » 86
3. Earthquake scaling laws for dynamic rupture and slow slip . . . . . » 87
4. Conclusions . . . . . » 89

W. L. Ellsworth – From foreshocks to mainshocks: mechanisms and implications for earthquake nucleation and rupture propagation . . . . . » 95

1. Introduction . . . . . » 95
2. Foreshocks and mainshocks . . . . . » 97
   2˙1. 1934 and 1966 Parkfield, California, USA . . . . . » 98
   2˙2. 1992 Joshua Tree, California, USA . . . . . » 98
   2˙3. 1999 Izmit, Turkey . . . . . » 100
   2˙4. 1999 Hector Mine, California, USA . . . . . » 102
3. Mainshock initial rupture process . . . . . » 102
   3˙1. 1989 Loma Prieta, California, USA . . . . . » 103
   3˙2. 2004 Parkfield, California, USA . . . . . » 105
4. Near source observations at SAFOD . . . . . » 105
5. Discussion . . . . . » 109
6. Conclusions . . . . . » 110

ALBERTO PETRI – Experimental statistics and stochastic modeling of stick-slip dynamics in a sheared granular fault . . . . . » 113

1. Motivations . . . . . » 113
   1·1. Crackling noise . . . . . » 114
   1·2. The point of view of the statistical physics . . . . . » 115
   1·3. Critical phenomena . . . . . » 116
   1·4. Universality . . . . . » 117
2. Sheared granular matter in laboratory experiments . . . . . » 119
   2·1. The laboratory set up . . . . . » 119
   2·2. Distribution of dynamical quantities . . . . . » 120
3. A stochastic model for the slider motion . . . . . » 123
   3·1. The friction force . . . . . » 123
   3·2. Results from the model . . . . . » 126
4. Criticality and its possible breakdown . . . . . » 126
   4·1. Where does criticality come from? . . . . . » 126
   4·2. The ABBM model . . . . . » 127
   4·3. Breakdown of criticality . . . . . » 128
5. Summary and perspectives . . . . . » 130

YUN-TAI CHEN, YONG ZHANG and LI-SHENG XU – Inversion of earthquake rupture process: Theory and applications . . . . . » 133

1. Introduction . . . . . » 134
2. Theory and methods . . . . . » 135
   2·1. Seismic inversion . . . . . » 135
      2·1.1. Inversion with fixed rake . . . . . » 136
      2·1.2. Inversion with rake variation . . . . . » 140
      2·1.3. Limitations and constraints . . . . . » 141
      2·1.4. Equations for the three kinds of inversions . . . . . » 142
      2·1.5. An example: The 2009 M_w6.3 L'Aquila, Italy, earthquake . . . » 143
   2·2. Joint inversion of seismic and geodetic data . . . . . » 146
3. Applications . . . . . » 151
   3·1. The M_w7.8 Kunlun Mountain Pass earthquake of 14 November 2001 » 151
      3·1.1. Tectonic settings . . . . . » 151
      3·1.2. Aftershocks . . . . . » 151
      3·1.3. Focal mechanism . . . . . » 151
      3·1.4. Distribution of static slip . . . . . » 154
      3·1.5. Source rupture process . . . . . » 155
      3·1.6. Surface ruptures . . . . . » 157
   3·2. The M_w7.9 Wenchuan, Sichuan, earthquake of 12 May 2008 . . . . . » 157
      3·2.1. Tectonic setting . . . . . » 157
      3·2.2. Focal mechanism and aftershocks . . . . . » 159
      3·2.3. Distribution of static slip . . . . . » 160
      3·2.4. Source rupture process . . . . . » 163
   3·3. The M_w6.9 Yushu, Qinghai, earthquake of 14 April 2010 . . . . . » 165
      3·3.1. Tectonic setting . . . . . » 165
      3·3.2. Focal mechanism . . . . . » 167

3˙3.3. Distribution of static slip . . . . . » 167
3˙3.4. Source rupture process . . . . . » 167
3˙4. Applications to the earthquake emergency response . . . . . » 168
4. Summary . . . . . » 172

Michel Bouchon, David Marsan, Hayrullah Karabulut, Mustafa Aktar, Virginie Durand and Jean Schmittbuhl – Do plates begin to slip before some large earthquakes? . . . . . » 177

1. Introduction . . . . . » 178
2. Izmit earthquake . . . . . » 178
3. Interplate and intraplate earthquakes . . . . . » 182

R. Madariaga – Dynamics and spectral properties of subduction earthquakes . . . . . » 189

1. Introduction . . . . . » 190
2. Observations . . . . . » 191
3. Theory . . . . . » 195
3˙1. Near field from a point source in an infinite medium . . . . . » 195
3˙2. A simplified model . . . . . » 196
4. The 1 April 2014 Iquique earthquake . . . . . » 198
5. The 24 April 2017 Valparaiso earthquake . . . . . » 201
5˙1. Observations of the Valparaiso earthquake . . . . . » 202
6. Discussion . . . . . » 205
7. Conclusions . . . . . » 207

F. Mulargia – Earthquake occurrence, recurrence, and hazard . . . . . » 211

1. Introduction . . . . . » 211
2. Earthquake phenomenology: the state of the art . . . . . » 213
3. Earthquakes according to PSHA . . . . . » 217
Assumption 0. A probabilistic model of earthquake occurrence can be derived . . . . . » 217
Assumption 1. Seismicity is known . . . . . » 218
Assumption 2. Seismicity is time independent . . . . . » 218
Assumption 3. Tectonic strain is released by large earthquakes . . . . . » 219
Assumption 4. Strain energy is released by Characteristic Earthquakes . . . » 219
Assumption 5. The impossible assumption: Characteristic Earthquakes occurring at random . . . . . » 221
Assumption 6. Exceedance probability and Return Time . . . . . » 221
Assumption 7. The sum of ignorance leads to knowledge: the cognitive democracy of logic trees . . . . . » 222
4. Discussion . . . . . » 223
5. Conclusions . . . . . » 224

List of participants . . . . . » 227

The electronic version of volumes from 124 to 201 is available online at the IOS Press web site

http://ebooks.iospress.nl/bookseries/proceedings-of-the-international-school-of-physics-enrico-fermi

Figures with colour source files will appear in colour in the online version.

SIF Members are granted free access to these volumes at
https://members.sif.it

For a complete list of published courses see
https://en.sif.it/books/series/proceedings_fermi

This page intentionally left blank

Preface

Modern investigations of the subject of mechanics of earthquake faulting and its resulting consequences can be said to have begun with the seminal papers in 1964 and 1966 by B. V. Kostrov. We are therefore very pleased to introduce this volume to commemorate the $\sim$ 55th anniversary of the start of our subject. In 2017, the Società Italiana di Fisica (SIF) invited us to organize a school on the *Mechanics of Earthquake Faulting* under the umbrella of the International School of Physics "Enrico Fermi", with support of the Istituto Nazionale di Geofisica e Vulcanologia (INGV). Course 202 was held at the Villa Monastero, Varenna, Lake Como, Italy, from July 2 to July 7, 2018, and was attended by speakers and participants from the four of the five inhabited continents of the world.

One of the most important goals of the school was to present the state of the art of the physics of earthquakes. It is obvious that it is not possible to perform laboratory experiments at the same spatio-temporal scale and with the same boundary conditions as real faults. Therefore, a multi-disciplinary scientific approach which combines laboratory inferences and mathematical models, together with analysis of recorded data from earthquakes, is essential to making progress in our understanding of this very destructive phenomenon. With the very rapid technological advances in computational power, technical facilities for laboratory experiments and high-quality broad-band data from seismological networks, the future of this subject looks very optimistic. We therefore welcome the opportunity to present the proceedings of the lectures presented at the school by some of the most distinguished scholars of this topic today.

The school was arranged into twelve main lectures, which cover widely the most challenging aspects of the mechanics of faulting. These were offered by the three directors (A. Bizzarri (INGV, Bologna), S. Das (University of Oxford) and A. Petri (CNR, Roma)) and by nine scientists of outstanding international fame (R. J. Archuleta (U.C. Santa Barbara), M. Bouchon (Université Grenoble Alpes), Y.-T. Chen (China Earthquake Administration, Beijing), W. L. Ellsworth (Stanford University), A. Kato (University of

Tokyo), R. Madariaga (ENS, Paris), C. J. Marone (PennState University), F. Mulargia (Università di Bologna), and A. Schubnel (ENS, Paris). We also organized four short talks given by respected scientists from Israel and France (I. Lior and A. Ziv (Tel-Aviv University), B. Gardonio and H. S. Bhat (ENS, Paris)). A 21-poster session was included to offer advanced doctoral students and junior researchers the possibility to present and discuss their work with these distinguished scientists, as well as with each other. Overall, 50 students, young researchers and observers attended the school, coming from 15 Countries and of 18 different nations.

Bizzarri presented a comprehensive view of earthquakes that propagate spontaneously with rupture speed greater than the shear wave speed characterizing the medium in which the fault is embedded. He discussed the main differences, from theoretical and numerical points of view, existing between sub- and supershear theoretical earthquakes, by considering both the on-fault and the off-fault solutions, and their practical implications.

In her lectures, Das posed the fundamental basis of the inverse problem of earthquake rupture mechanics and then applied them to great subduction zone earthquakes as well as to large earthquakes on transform faults. The former included a detailed study of the rupture speed of the 2001 M_w 7.8 Tibet earthquake, which not only surpassed shear wave speeds, but almost reached the compressional wave speed of the medium. The latter elucidated that the occurrence of large and great earthquakes taking place in oceans implies that the oceanic crust is crumbling by fracture along pre-existing nearly normal conjugate faults, even in regions where the transform fault is no longer active.

In his lecture entitled "The evolution of fault slip rate prior to earthquake: The role of slow- and fast-slip modes", Kato discussed the complexity of the nucleation stage of seismic ruptures. He showed that recent seismic and geodetic studies of foreshock sequences suggest that partial unlocking of the fault took place episodically through interplay between fast- and slow-slip modes before large earthquakes. He also stressed the importance of assessing the degree of criticality within fault segments adjacent to already ruptured portions.

The world of laboratory experiments was highlighted by Marone, who summarized results from laboratory experiments showing repetitive slow slip, described different friction laws for slow earthquakes and finally discussed the implications of the earthquake scaling laws.

Ellsworth thoroughly scrutinized the differences between the two hypotheses proposed to describe earthquake nucleation, namely, the preslip and the cascade models and highlighted how they take opposing views on the role of aseismic deformation in the nucleation process, as well as the prospects for prediction.

Petri focused on the dynamics of a laboratory spring-plate system, sliding upon a granular bed. Although distant from a seismic fault, this system presents all the hallmarks of critical systems, which are shared by several different physical phenomena including earthquakes. The idea that the dynamics of such systems spring from the presence of a (non-equilibrium) critical transition leads to seek their common features and stimulates to identify the essential mechanisms from which similar statistical properties emerge.

Chen shared with us his experience of the inversion of complex kinematic earthquake rupture processes, by summarizing the most prominent studies made in the past two decades in the analysis of the teleseismic and geodetic data for retrieval of the earthquake rupture process. Such information, released soon after the occurrence of destructive earthquakes, is now routinely being used by local authorities in the task of earthquake emergency response for such catastrophes.

Bouchon illustrated the behaviour of 65 large earthquakes and showed that most of those occurring along the plate interfaces are preceded by foreshocks, while intraplate earthquakes are less prone to foreshocks. He concluded that this difference supports the idea that slow slip of the plate interface precedes many large interplate earthquakes.

Near-field seismic radiation and dynamic inversion of large subduction (or mega-thrust) earthquakes was the subject of Madariaga's lectures. It focused on two great Chilean earthquakes and showed that at low frequencies the ground spectra differ quite significantly from the usual Aki-Brune spectrum used in studies of the far-field spectral properties of earthquakes.

Finally, Mulargia gave a stimulating view of the problem of earthquake occurrence, recurrence and hazard. In particular, he suggested that the Probabilistic Seismic Hazard Assessment (PSHA) —which plays a fundamental role in the defence strategy from earthquake damage of most countries— ignores the physics of the earthquake faulting system and, as a result, PSHA estimates are essentially void of scientific significance and merely speculative.

The stunning location of Villa Monastero with its exceptional historical and cultural heritage, its superb gardens, as well as the charming and breathtaking atmosphere of the Como Lake, with its Manzoniana melancholy, provided a very pleasant backdrop for numerous informal discussions between the entire group of participants, and contributed to the extraordinary success of the school. The topics covered during the school gave a very clear picture of the actual state of the art of the physics of earthquake ruptures and, at the same time, provided a list of open issues and questions that are still under debate, thus providing young researchers with new scientific challenges for the years to come.

Finally, we wish to put on records our thanks to the SIF President, Prof. L. Cifarelli, for promoting this school, the only one to follow earlier schools on similar subjects in 1979 and 1982 —both of them co-directed by Prof. E. Boschi, who passed away while we were writing this preface— and to Dr. T. Pepe (INGV, Rome) for supporting the whole initiative and for his enthusiasm. We also want to acknowledge Dr. S. Topazio (INGV, Rome) for her preliminary help in the very early stages of the organization of the school, our Secretary, Dr. A. M. Loguercio (CNR, Rome) for her precious work, and the whole staff of the SIF (with a special emphasis to B. Alzani) for their invaluable and continuous support in the organization and management of the school.

A. BIZZARRI, S. DAS and A. PETRI

Italian Physical Society

INTERNATIONAL SCHOOL OF PHYSICS «E. FERMI»

COURSE 202

2 - 7 July 2018

VILLA MONASTERO − VARENNA, LAKE COMO

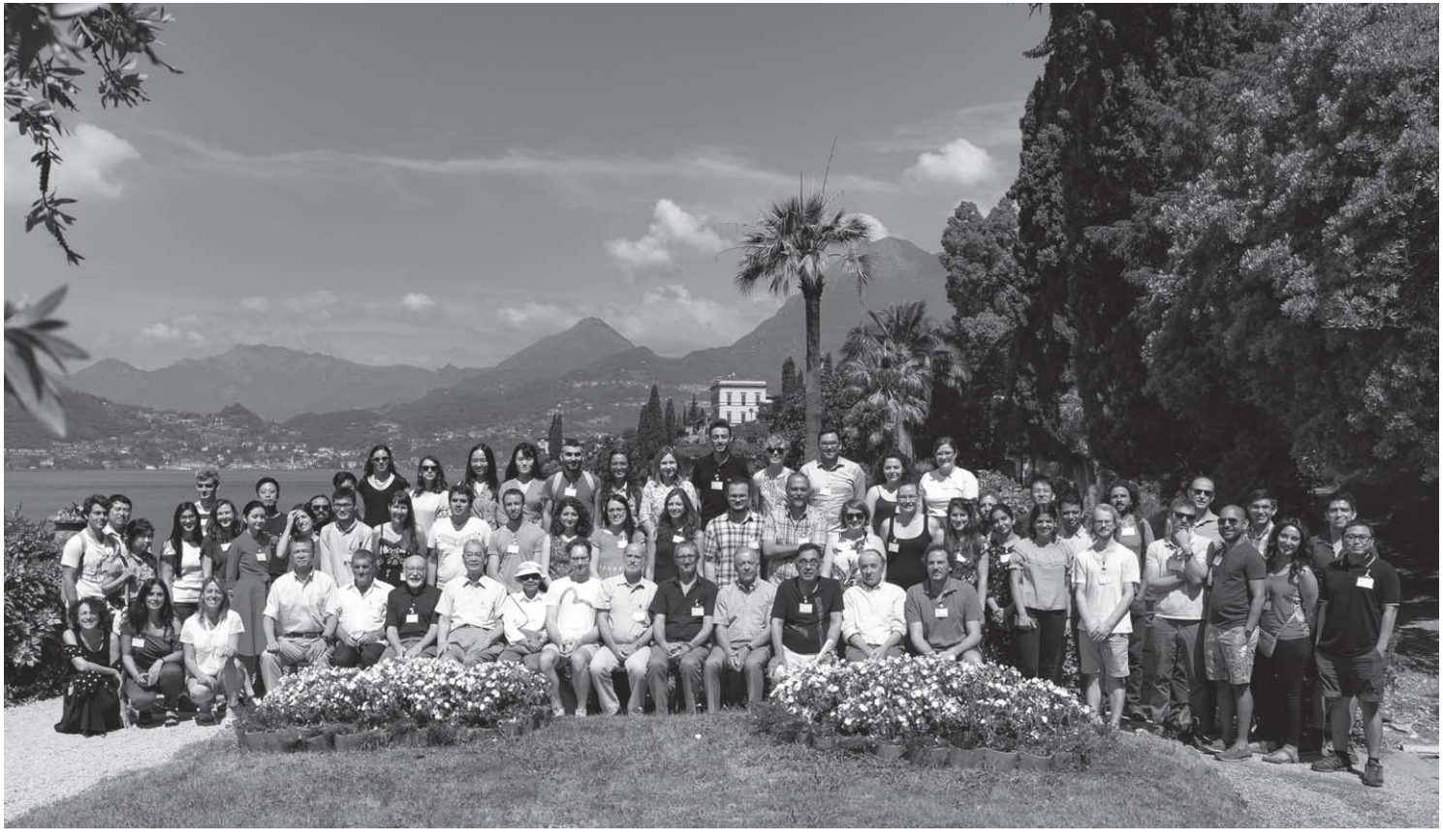

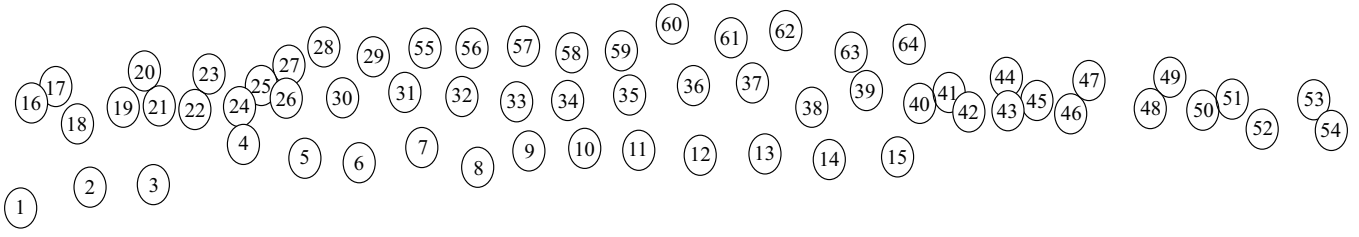

1) Barbara Alzani
2) Anna Maria Loguercio
3) Ramona Brigatti
4) Aitaro Kato
5) Francesco Mulargia
6) William L. Ellsworth
7) Yun-tai Chen
8) Shamita Das
9) Andrea Bizzarri
10) Alberto Petri
11) Chris J. Marone
12) Ralph J. Archuleta
13) Raul Madariaga
14) Michel Bouchon
15) Alexandre Schubnel
16) Corentin Noël
17) Luyi Shen
18) Shanna Chu
19) Lauren Abrahams
20) Barnaby Fryer
21) Paula Burgi
22) Anna Skorkina
23) Takamasa Kanaya
24) Camilla Cattania
25) Jorge Jara
26) Houyun Yu
27) Marty Samson
28) Lou Marill
29) Arefeh Moarefvand
30) Marion Thomas
31) Hugo Samuel Sanchez Reyes
32) Itzhak Lior
33) Paola Forlenza
34) Elvira Battimelli
35) Verena Simon
36) Jan Premus
37) Toni Kraft
38) Christine Ruhl
39) Blandine Gardonio
40) Francesca Pelusi
41) Guilhem Mollon
42) Sivasubramonain Jayalakshmi
43) Deepa Mele Veedu
44) Kurama Okubo
45) Rishabh Dutta
46) Clay Wood
47) Luigi Vadacca
48) Alon Ziv
49) Gilles Hillel Wust-Bloch
50) Harsha Suresh Bhat
51) José Nicolas Castro Perdomo
52) Figen Eskikōy
53) Carlos Villafuerte
54) Taufiqurrahman Taufiqurrahman
55) Jinhui Cheng
56) Xiang Chen
57) Piero Brondi
58) Maddalena Michele
59) Alina Besedina
60) Jérôme Aubry
61) Camilla Penney
62) Sebastian Anger
63) Camilla Rossi
64) Leah Salditch

This page intentionally left blank

Proceedings of the International School of Physics "Enrico Fermi"
Course 202 "Mechanics of Earthquake Faulting", edited by A. Bizzarri, S. Das and A. Petri
(IOS, Amsterdam; SIF, Bologna) 2019
DOI 10.3254/978-1-61499-979-9-1

The mechanics of supershear earthquake ruptures

Andrea Bizzarri(*)

Istituto Nazionale di Geofisica e Vulcanologia, Sezione di Bologna
Via Donato Creti 12, 40128, Bologna, Italy

Summary. — In this paper we will review the fundamental aspects of the supershear earthquake ruptures, *i.e.*, events which propagate with speeds greater than the shear wave speed of the medium surrounding the fault. The rupture starts from an imposed hypocenter and then it spreads spontaneously (*i.e.*, without imposed rupture speed) over the entire fault plane. The latter is characterized by a rheology described by the linear slip-weakening model, which analytically prescribe the evolution of the fault frictional as a function of the cumulated fault slip. The problem is solved numerically, by using two different finite-difference schemes, because it is not possible, even in homogeneous conditions, to solve the elastodynamic problem in an analytical, closed form. We will discuss the main differences exsisting between sub- and supershear synthetic earthquakes, by considering both the on-fault and the off-fault solutions. The results presented here summarizes the most prominent and recent researches in this field, as well as the seismological implications.

1. – Introduction

It is well known that quantitative seismology is a juvenile discipline and therefore the available data are obvioulsy limited. At the same time, it is also well known that it is impossibile to reproduce the physical phenomenon under study (*i.e.*, the rupture

(*) E-mail: andrea.bizzarri@ingv.it

propagation occurring during an earthquake) at the same scale of the real process (the spatial scale is km long) and in the same conditions (in terms of slip velocity and confining stress) of a real-world seismic event.

Theoretical and numerical models are therefore a powerful tool to create realistic scenarios and to construct synthetic catalogs of plausible events to be analyzed and compared against the observed (or inferred) data coming from instrumental networks.

The temporal focus of the present paper is the so-called coseismic phase, lasting from seconds to minutes, during which the stress is released on the fault and re-distributed in the surrounding medium. Within this temporal scale several competing (and potentially concurrent) physical and chemical mechanisms take place (see [1] and references cited therein for a thorough review) and seismic waves are excited. This stage starts in a dynamic fashion after the long preparatory phase (the nucleation stage) and ends with the healing and stopping phases, leading to a new equilibrium state of the seimogenic region, thus preluding an interseismic, re-strengthening phase, which in turn ultimately culminates in a new slip instability (or a new, sometime triggered, earthquake event).

One of the results of the dynamic modeling of earthquakes is the rupture speed, *i.e.*, the velocity at which the rupture (more exactly the rupture front, which separates the region where the fault surface is still at rest from the portion(s) where the stress is releasing) advances. In the class of the so-called spontaneous models this physical observable is not prescribed (*i.e.* not imposed *a priori*, like in the non-spontaneous models), but indeed it is itself a part of the solution of the problem. The rupture speed, v_r thereinafter, is usually compared with the value of the shear wave speed v_S (an intrinsic parameter which characterizes the medium surrounding the seismic fault system) so that two regimes of rupture propagation have been defined (with self-explaining meaning): the subshear regime and the supershear regime.

Indeed, the problem supershear earthquakes has received the increasing interest of theoretical and numerical studies, laboratory experiments and observations of (or inferences from) real-world events. Frist of all, we mention that, using analytical models of non-spontaneous, purely in-plane (mode II) crack, [2-5] and [6] demonstrated that rupture can stably propagate at supershear rupture velocity. On the other hand, numerical simulations showed that spontaneous ruptures governed by a linear slip-weakening friction law ([7-10] in the 2D, purely in-plane case and [11-14] in the 3D one; see fig. 1a), as well as spontaneous ruptures obeying to rate- and state-governing laws ([15] in the 2D case and [13] in the 3D one; see fig. 1b), exhibit, for carefully chosen values of governing parameters, a jump from sub- to supershear rupture velocities. (For the classification of dimensionality and geometries of the problem readers can refer to sect. 2.1 of [1]). Moreover, laboratory experiments by [16] and by [17] showed that supershear stick-slip motion occurred after a stable sliding. Indeed, the prominent experimental result [18,19] is that shear cracks from either projectile impact loading or shear loading with exploding-wire-nucleation can propagate at intersonic speed in homalite (see fig. 2).

In spite of this profusion of analytical, numerical and laboratory evidence it is well known that the observations of crustal earthquakes have revealed that most ruptures tend to propagate with an average velocity that is about 80% of the shear wave ve-

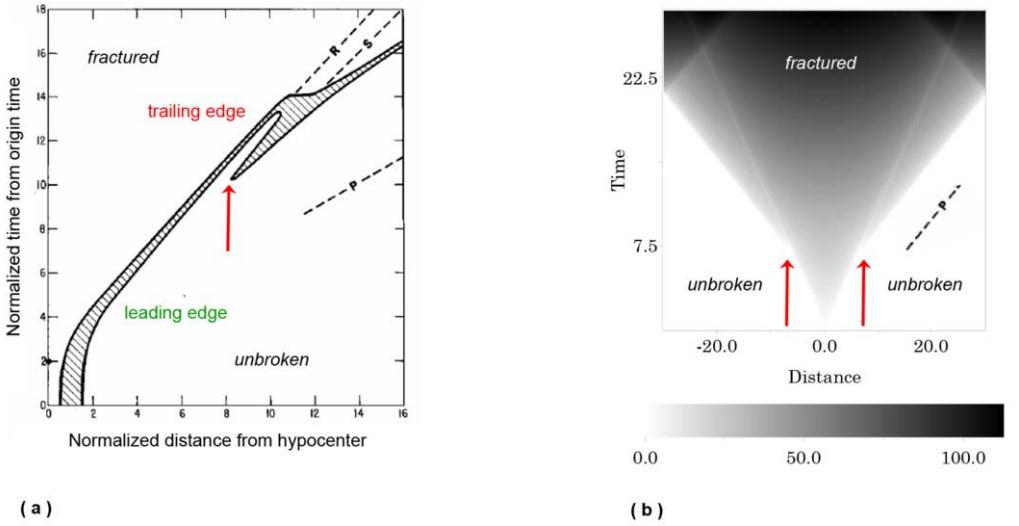

Fig. 1. – Numerical results demonstrating the presence of supershear ruptures. The occurrence of the supershear transition is emphasized by vertical red arrows. (a) 2D model with linear slip-weakening governing model (eq. (3)) and homogeneous conditions. The plot show the behaviour of the fault slip pertaining to a bilateral rupture which nucleates at the origin (for sake of simplicity, only one half of the fault is reported). Modified from [23] with permission of John Wiley and Sons. (b) 2D model obeying to Dieterich-Ruina law (eq. (6)) and bilaterally spreading and again starting from the origin. Scales and color bar are in arbitrary units. Modified from [67]. In both panels the fault slip is reported; in panel (a) only the cohesive zone (*i.e.*, the region in which the stress release is accomplished) is reported; see also fig. 13d for a comparison and sect. **7** for a further discussion.

locity (*e.g.*, [20]). However, there are a few earthquake ruptures which appear to have propagated with a velocity greater than the shear wave velocity; they are listed in table I.

The state-of-the-art knowledge indicates that supershear earthquakes possess some peculiar features:

i) [21] and [22] noted that in classical fracture mechanical models crack tip singularities emit diminished high-frequency motion when traveling at supershear speeds, which might nullify the Mach cone enhancement of high frequencies. This has been theoretically discussed also by [23], basing on the mode II, non-spontaneous, self-similar analytical solution of [2], and further demonstrated for spontaneous 3D rupture governed by different constitutive models by [24], for both homogeneous and heterogeneous conditions.

ii) They emit a Mach cone having enhanced high frequencies [22, 25, 26] and they can radiate a locally planar or conical wave front having less geometric spreading than that radiated from subshear rupture [22].

iii) Supershear earthquakes also emit Rayleigh Mach waves, most evident in the fault-normal and vertical components of particle velocity on the free surface, which interfere and lead to complex velocity and stress fields. Rayleigh Mach fronts do not attenuate with distance from the fault trace [27].

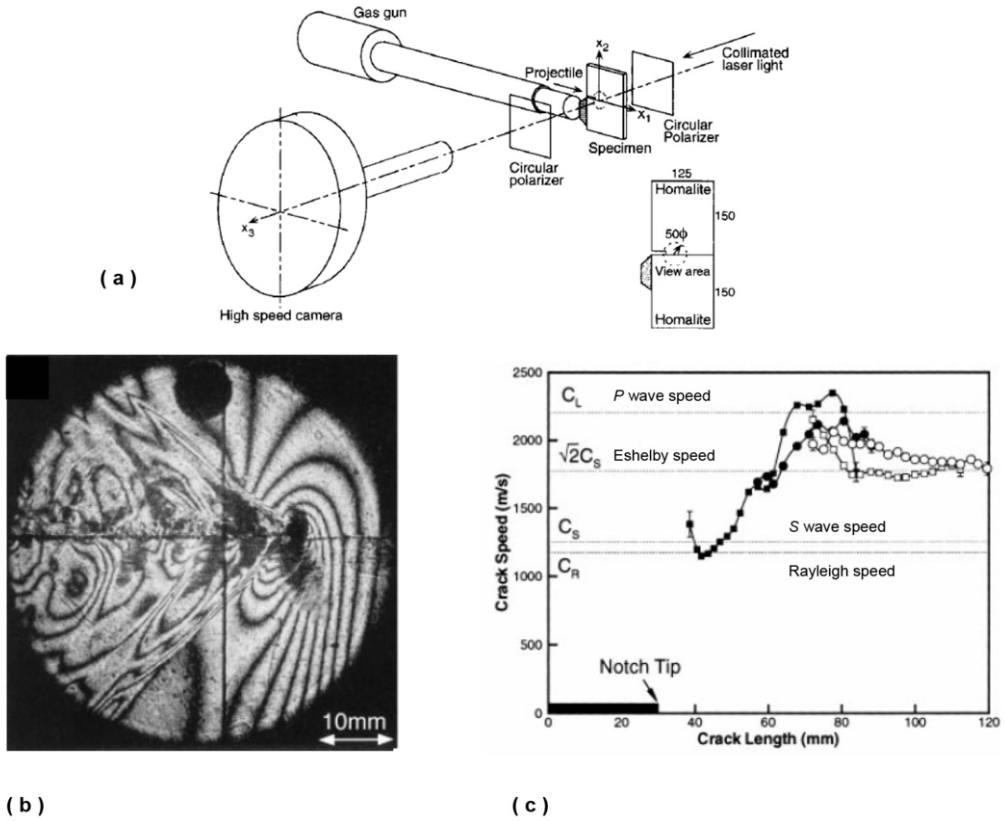

Fig. 2. – (a) The dynamic photoelasticity setup employed in laboratory experiments by Rosakis and coworkers [18]. A Homalite-100 specimen 4 mm thick is subjected to an impact by a steel projectile (having length 75 mm and diameter 50 mm) fired from a high-speed gas gun. The steel projectile impacts a steel piece (at 25 m/s), and the compressive longitudinal wave loads the notch tip in a predominantly shear mode. The dynamic stress field generated by the loading was recorded using photoelasticity in conjunction with high-speed photography and the resulting isochromatic fringe pattern was recorded by a high-speed camera (up to 2 million frames per second). (b) Enlarged view of the isochromatic fringe pattern around a steady-state mode II intersonic crack. (c) Resulting crack speed obtained from the crack length history (squares) and from shock wave angles (circles) for a field of view around the notch tip (solid symbols) and for a field of view ahead of the notch (open symbols). The so-called forbidden zone is marked in pink (for Homalite-100, $v_P = 2200$ m/s and $v_S = 1255$ m/s). Reproduced from [18] with permission from The American Association for the Advancement of Science.

iv) The high-frequency content of a Mach pulse overwhelms that arising from stress heterogeneity; although the heterogeneities can reduce the peaks in ground velocity and can also diminish the coherence of the Mach fronts, ground motions at stations experiencing Mach pulses should be richer in high frequencies compared to stations without Mach pulses [26].

TABLE I. – *List of directly observed* (•) *or inferred* (°) *supershear earthquakes.*

Year	Magnitude	Location	Reference
1906°	7.9	San Andreas Fault, San Francisco, CA, USA	[70]
1979°	6.5	Imperial Fault, Imperial Valley, CA, USA	[71]
1999•	7.4	North Anatolian Fault, Kocaeli (Izmit), Turkey	[72]
1999•	7.2	North Anatolian Fault, Düzce, Turkey	[72]
2001•	8.1	Kokoxili (Kunlun), Tibet	[73]
2002•	7.9	Denali Fault, Alaska	[21]
2010•	6.9	Yushu Fault, Qinghai, China	[74]
2012•	8.6	Indian Ocean	[75]
2013°	7.5	Queen Charlotte Fault, Alaska	[76]

v) Contrarily to subshear ruptures, for which the high-particle velocities are concentrated near the fault trace, supershear ruptures produce ground motions which extend widely in the direction perpendicular to the fault trace, with a predominance of the fault-parallel component of the particle velocity [28].

vi) Supershear earthquake tend to enhance the variation of the rake [13, 29]; this can have consequencies in the formulation of analytical expression of the slip-dependent governing models, as discussed in [30].

vii) Depending on the style of the transition from sub- to supershear regime the ground motions resulting from the earthquake propagation are different [31].

In the following sections we will review in more detail and discuss the above-mentioned features.

2. – Physical problem

We solve the elastodynamic problem for fault, neglecting body forces, *i.e.*, we solve the II law of dynamics for continuum media, which reads

$$\rho \ddot{u}_i = \sigma_{ij,j}, \tag{1}$$

where ρ is the cubic mass density, σ_{ij} is the stress tensor and the Einstein's index summation is assumed. For the sake of simplicity we consider a planar fault, perpendicular to the x_2 Cartesian axis. In the 2D case the rupture propagates along the x_1 axis and the solutions only depends on the spatial coordinate x_1 (pure mode-II geometry) and on time t. In this case the fault slip $\mathbf{u}$ is written in the form $\mathbf{u} = (u_1(x_1, t), 0, 0)$. In the

3D case we consider a vertical, strike slip fault mechanism, so that the fault slip reads: $\mathbf{u} = (u_1(x_1, x_3, t), 0, u_3(x_1, x_3, t))$. Note that in this latter case we have the dependence on both the two on-fault spatial coordinates and that the two shear modes of propagation (mode II and mode III) are coupled together. Rake rotation is allowed and thus the slip azimuth (namely the ratio u_3/u_1) can change both in space and in time during the spontaneous propagation of the rupture. On the contrary, material interpenetration and fault opening is not allowed (this is why $u_2 = 0$ and thus mode I is not permitted in the model).

The medium surrounding the fault is perfectly elastic, homogeneous and initially at rest; it moves only in response to waves excited by the (stress re-distribution caused by the) earthquake source.

The shear components of the stress tensor are linked to the fault governing model, which complements eq. (1); in full of generality this law can be written as follows:

$$\tau = \mu(w_1 O_1, \dots, w_N O_N; p_1, \dots p_M) {\sigma_n}^{\text{eff}}, \tag{2}$$

in which $\{O_i\}_{i=1,\dots,N}$ are the physical observables (or dynamic variables), $\{w_i\}_{i=1,\dots,N}$ are the weights expressing the relative importance of each single chemical or physical process taking place during the seismic event described by $\{O_i\}_{i=1,\dots,N}$ and $\{p_i\}_{i=1,\dots,M}$ are the constitutive parameters. In eq. (2) τ is the modulus of the shear traction, μ stands for the dimensionless friction coefficient and ${\sigma_n}^{\text{eff}}$ is the effective normal stress, which in turn is expressed as the difference between the stress of tectonic origin σ_n (σ_{33} for our fault geometry) and the pore fluid pressure p_{fluid}.

In this paper we will consider the slip-weakening (SW thereinafter) constitutive model, which is the prime example of the class of the cohesive force fault governing equation. It has been originally introduced by [32] basing on the theory of Barenblatt [33,34] on mode I ruptures on metals and subsequently extended to shear modes of propagation. In this formulation the slip begins on the fault only when the traction reaches, for some reason, the upper yield stress $\tau_u = \mu_u {\sigma_n}^{\text{eff}}$. Then it decreases as a function of the developed slip u only. The simplest case, which has been massively employed in numerical models of dynamic ruptures ([7,11,23] among many others in subsequent years) due to its inherent simplicity from a computational point of view, is represented by the linear SW law, which reads

$$\tau = \begin{cases} \left[\mu_u - (\mu_u - \mu_f)\dfrac{u}{d_0}\right] {\sigma_n}^{\text{eff}}, & u < d_0, \\ \mu_f {\sigma_n}^{\text{eff}}, & u \geq d_0, \end{cases} \tag{3}$$

where d_0 —sometimes indicated by D_c by experimentalists— is the characteristic (often and improperly called critical) length of the model and $\tau_f = \mu_f {\sigma_n}^{\text{eff}}$ is the residual, or kinetic, level of friction attained after the stress release. The presence of a characteristic length makes it possible to apply this model at a laboratory scale (where $d_0 \sim$ some μms) as well as at a real-world scale (where $d_0 \sim$ few cms). The nucleation mechanisms, which

cause the transition from an initial stress state τ_0 up to τ_u is not inherently modeled, so that some artificial procedures are needed to initiate a rupture, as compendiously discussed in [35].

In eq. (3) the slip u simply is $u_1(x_1, t)$ in the 2D case, but it can be regarded either as the actual modulus of the slip vector,

$$u^{(mod)}(x_1, x_3, t) \equiv \|\mathbf{u}(x_1, x_3, t)\|, \tag{4}$$

or as the slip cumulated along its path

$$u^{(path)}(x_1, x_3, t) \equiv \int_0^t \|\mathbf{v}(x_1, x_3, t')\| \mathrm{d}t'. \tag{5}$$

in the 3D case. The differences between these two (theoretically different) formulations occur only when a relevant rake rotation takes place [30], *i.e.*, when the slip velocity vector significantly changes (in time and in space) during the rupture propagation. The constitutive model (3) is essentially theoretical (or mathematical) in this origin and it is intentionally simple; in homogeneous conditions it predicts a constant stress drop (accomplished over the breakdown time T_b, which in turn is controlled by d_0; see eq. (A5) in [10]).

Just for completeness we mention here that a more alaborated model which has been considered in a large number of studies dealing with dynamic models is one example of the rate- and state-dependent friction laws, the so-called Dieterich Ruina (DR henceforth) law [36, 37]:

$$\begin{cases} \tau = \left[\mu_* + a \ln\left(\dfrac{v}{v_*}\right) + b \ln\left(\dfrac{\Psi v_*}{L}\right)\right] {\sigma_n}^{\text{eff}}, \\ \dfrac{\mathrm{d}}{\mathrm{d}t}\Psi = 1 - \dfrac{\Psi v}{L}, \end{cases} \tag{6}$$

which is also known as ageing law. Equation (6) possesses three governing parameters; a, which describes the slip-hardening phase (also named the direct effect), b, which accounts for the short-range evolution effect of traction and its long-range velocity strengthening and L, the characteristic length scale, which is the counterpart of d_0 in the SW model (3). From a more physical point of view, a and b describe the effects of thermally activated exponential creep occurring at the micro-asperity contacts level. The quantities μ_* and v_* are reference values for the friction coefficient and the fault slip, respectively; if the fault has an initial velocity $v_0 = v_*$, then μ_* formally defines the initial value of fault traction. The state variable Ψ (which in general is a multi-dimensional variable $\mathbf{\Psi} = (\Psi_I, \Psi_2, \ldots, \Psi_K)$) accounts for the different states of the fault surface and it represents a sort of memory of the fault of the previous slipping episodes. In the case of DR model (eq. (6)) the single variable Ψ has the physical meaning of the average contact time of the micro-asperities.

3. – Numerical solutions

There is no reason to emphasize that the spontaneous, 3D, dynamic problem cannot be solved analytically in closed form, even in homogeneous conditions (where all the medium and governing parameters are constant in time and spatially uniform). Remarkably, the only exception is represented by the 2D, pure mode II solution proposed by [38], although some integrals have to be evaluated numerically. Therefore we solve eq. (1) coupled with (3) numerically.

For the 2D case, we use the finite difference code described in [10], originally developed by [39], which uses a mesh of triangles and the leap-frog scheme. The code has been made more efficient by us using parallelization through the OpenMP paradigm (see [40]).

For the 3D case we use two OpenMP-parallel, 2nd-order accurate in space and in time, finite difference codes. For the investigations on the fault (see sects. **4** and **5**) we adopt the conventional grid method (all components of the different quantites are defined in the same grid node), implementing the traction-at-split node fault boundary condition, which is described in details in [13] and [41]. For the results pertaining the off-fault features (see sect. **6**) we prefer the staggered-grid (the components of the different quantites are defined in the different grid nodes) code described in [42] and used in [27] and [26], which in the body surrounding the fault is 4th-order accurate in space. In this case the fault boundary condition is implemented with the staggered-grid split-node method (*e.g.*, [43]).

In both 2D and 3D cases the nucleation is imposed in a hypocenter point and then the rupture develops spontaneously and bilaterally (*i.e.*, in a symmetric way with respect to the imposed hypocenter) over the whole fault line or plane (in the 2D and in the 3D case, respectively). For sake of simplicity all the parameters are homogeneous, unless otherwise specified in the following discussions.

As stated above, the value of the rupture speed is a part of the solution of the dynamic problem, but it is an indirect quantity, in that it has to be computed from the rupture time t_r. The latter is defined as the first time instant when the fault slip velocity v, in a given node, exceeds the threshold value $v_l = 0.01\,\mathrm{m/s}$ ([29] and references cited therein). We remark here that this value is at least two orders of magnitude smaller than the typical peak slip velocity which is attained in the numerical results of dynamic models and therefore it is able to capture what happens in most of the breakdown zone in numerical experiments on homogeneous faults, where the rupture always accelerates to a seismic regime.

In 2D v_r in the generic location $x_1 = (i-1)\Delta x$ is computed by using the two-point central difference method:

$$v_r(i) = \frac{(i+1)\Delta x - (i-1)\Delta x}{t_r(i+1) - t_r(i)} = \frac{2\Delta x}{t_r(i+1) - t_r(i-1)} \tag{7}$$

(Δx is the spatial sampling, which is homogeneous over the whole computational domain), while in 3D, in each node of the fault, it is computed as the inverse of the

slowness:

$$v_r(x_1, x_3) = \frac{1}{\|\nabla_{(x_1,x_3)} t_r(x_1, x_3)\|}\,, \tag{8}$$

where the spatial derivatives of t_r in eq. (8) are given by (*e.g.*, [44])

$$\frac{\partial}{\partial x_1} t_r(x_1, x_3) = \frac{1}{\Delta x} \frac{\tilde{t}_r(i+1,k+1) - \tilde{t}_r(i-1,k+1) + \tilde{t}_r(i+1,k-1) - \tilde{t}_r(i-1,k-1)}{4} \tag{9}$$

and

$$\frac{\partial}{\partial x_3} t_r(x_1, x_3) = \frac{1}{\Delta x} \frac{\tilde{t}_r(i+1,k+1) - \tilde{t}_r(i+1,k-1) + \tilde{t}_r(i-1,k+1) - \tilde{t}_r(i-1,k-1)}{4}\,, \tag{10}$$

where the symbol $\tilde{q}$ indicates the discrete equivalent of a generic quantity q and the doublets (i, k) define a fault node located at the position $i\Delta x$ in the strike direction (x_1) and at the depth $x_3 = (k-1)\Delta x$ (spatial sampling is constant in all directions, again for simplicity).

4. – Frequency content

The results presented here pertain to a 3D model with linear SW governing model (eq. (3)); the parameters are listed in table 1 (Model A) of [24].

In fig. 3a we plot the rupture speed v_r on the fault plane, computed through eq. (8); due to the symmetries of the problem only a quarter of fault plane is displayed; moreover, for clarity of presentation, we plot v_r only up to time $t = 1.29\,\mathrm{s}$, in order to better emphasize the region where rupture front accelerates to supershear rupture velocities. This transition is inded expected, since the value of strength parameter S is low (in the present case $S = 0.8$) and below the critical threshold which discriminate between subshear and supershear rupture propagation (see for instance [23, 45] and sect. **7**). S, sometimes called seismic ratio, is defined as follows:

$$S \underset{\mathrm{df}}{=} \frac{\tau_u - \tau_0}{\tau_0 - \tau_f} \tag{11}$$

[8, 46, 47]. We also note that in the direction of the pre-stress (namely in the in-plane direction, x_1 for the adopted fault mechanism) the rupture accelerates up to supershear velocity, reaching a value ($4209\,\mathrm{m/s}$) which is very close the Eshelby speed ($v_E = 4243\,\mathrm{m/s}$ for our parameters). On the contrary, in the anti-plane direction (x_3 for the adopted fault

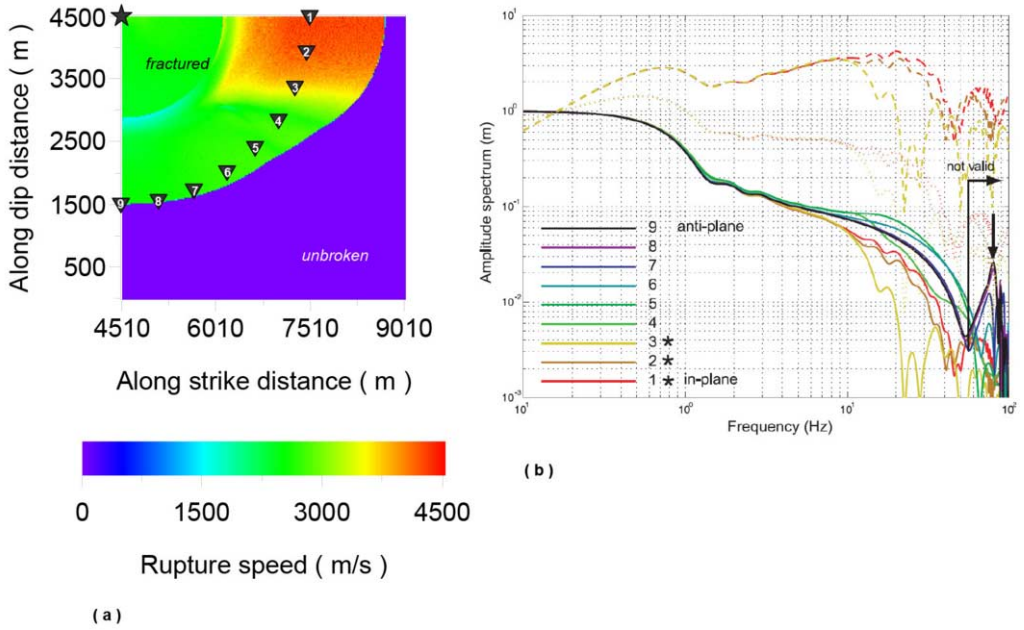

Fig. 3. – (a) Rupture speed on the fault plane in the case of homogeneous 3D fault governed by the linear slip-weakening model (eq. (3)), calculated from eq. (8). Blue portions of the fault identify the unbroken areas, while the black star denotes the earthquake hypocenter; black triangles indicate the locations where Frequency Amplitude Spectra (FAS) of fault slip velocity is calculated. Due to the symmetry of the problem, only a quarter of the fault plane is reported in the figure. Only for graphical clarity, the rupture speed is calculated not in the whole temporal window of the computation but only up to time $t = 1.29\,\mathrm{s}$. The parameters are reported in table 1 of [24] (their Model A). (b) Resulting FAS of the fault slip velocity time series. Asterisks indicate locations where rupture speed is supershear. Solid lines show unmodified FAS. Dashed and dotted lines show FAS of supershear locations multiplied by ω and $\omega^{1/2}$, respectively. Vertical arrow shows the lowest frequency peak caused by numerical oscillation in slip velocity. "Not valid" shows the range of frequencies in which antiplane and in-plane FAS cannot be compared. Reproduced from [24] with permission of John Wiley and Sons.

mechanism) v_r always remains subshear, as already numerically demonstrated by [13]. Moreover, it is evident from fig. 3a that there are intermediate regions where v_r increases from sub- to supershear rupture velocity, passing through the rupture velocity interval which has been considered as forbidden in 2D (*e.g.*, [23]). We will discuss in more details this important issue in sects. **5** and **7**.

In fig. 3b we plot the magnitude of the Fourier amplitude spectra (FAS) of the fault slip velocity time series at nine locations (black triangles in fig. 3a). All locations in this numerical experiment are at a distance of 3 km from the imposed hypocenter H (the black star in fig. 3a) and at different azimuths with respect to H. As a consequence of the linear SW governing law with constant effective normal stress, all the locations

experience the same stress drops (both static stress drop, $\Delta\tau_s \underset{\text{df}}{=} \tau_0 - \tau_f$, and breakdown stress drop, $\Delta\tau_b \underset{\text{df}}{=} \tau_u - \tau_f$), but they have different rupture velocities (basically due to the different oupling between the two modes of propagation, II and III). The FAS formally is the spectrum of the magnitude of the fault slip velocity time series. Namely, all locations' slip acceleration time series were terminated by a cosine-taper of duration t_{dur} starting at a delay t_{start} after the first non-zero value (*i.e.*, the onset time at that given fault node). The termination of the acceleration time series was chosen to exclude the back-propagating healing phases from unslipped parts of the models. The tails of the tapered accelerations were then padded with zeros and integrated to velocity. The tails of these velocities were gradually cosine-tapered to zero and the tapered slip velocities were then normalized to have one meter of total cumulative slip, a typical value that may be associated with a $M \sim 7$ earthquake. In this model we used $t_{start} = 0.5\,\text{s}$ and $t_{dur} = 0.1\,\text{s}$ for the acceleration taper and $t_{start} = 0.3\,\text{s}$ and $t_{dur} = 0.7\,\text{s}$ for the velocity taper.

From fig. 3a we can see that the spectra (solid lines) agree at low frequency but they diverge above 10 Hz. Moreover, we also see that a numerical oscillation occurs at some frequency, that frequency always being the lowest for anti-plane locations (see the arrow at 80 Hz for locations 7, 8, and 9 in fig. 3b) and highest for in-plane locations (about 180 Hz for location 1, not visible in fig. 3b). Because of the numerical oscillation, the in-plane and anti-plane locations' spectra cannot be compared in the band marked "not valid" on the figure, although the in-plane spectra are usually valid well into that band.

The most relevant result in fig. 3b is that in the band where the FAS diverge (10–40 Hz), the FAS of the pure in-plane location (1) is in the middle of the group, the location closest to the sub- to supershear transition (3) has the lowest FAS, and the FAS of the subshear locations (4 to 9) exceed those of the supershear [24]. This verifies the predictions of [2] and [23] that supershear crack tips should have less abrupt slip velocity onsets than subshear tips. We also remark here that the location with the lowest FAS experiences the largest rake rotation within the breakdown zone.

The dotted and dashed FAS in fig. 3b are the FAS of supershear locations (solid lines for 1, 2, and 3) multiplied by $\omega^{1/2}$ and ω, respectively, just to simulate the spectral enhancement of the radiated S waves expected for supershear rupture speed compared to subshear ruptures in case of slip heterogeneity spectra that follow $k^{-1.5}$ and k^{-2} at high wave number, respectively. They show that the spectral enhancement expected from supershear propagation exceeds the diminution of spectral amplitude caused by supershear reduction of the crack tip singularity.

It is important to emphasize that the results presented here are valid also in case of different governing models; esamples are reported in figs. 8 and 10 of [24]. Moreover, also for heterogeneous models (where the frictional properties are not homogeneous over the whole fault plane) it holds that the average FAS amplitude of subshear locations has about twice the amplitude of the supershear FAS in the 6–30 Hz band (see fig. 11d of [24]).

5. – The penetration of the forbidden zone

The results discussed in this section pertain to a 3D model with linear SW governing model (eq. (3)); the parameters are listed in table 1 of [29].

Self-similar calculations, in which a 2D, pure anti-plane (mode II) crack suddenly appears and starts extending at a constant speed showed that speeds between the Rayleigh speed v_R and the v_S are not possible, based on energy considerations [23, 48, 49]. Moreover, Andrews [50], starting from [2], founds self-similars solution in between v_R and v_S (non-spontaneous solutions) which are not physically realistic for pure mode-II spontaneous ruptures and his solutions are singular at the crack tip. Moreover, their numerical calculations of a mixed-mode rupture (in which $\mathbf{u} = (u_1(x_1, t), 0, u_3(x_1, t))$) have poor resolution and therefore can not handle the question of the penetration of the "forbidden zone" properly.

In order to determine if the forbidden zone truly exists, as well as to understand its properties if it is not forbidden, and to better understand the supershear rupturing process, Bizzarri and Das [29] carried out numerical calculations using finer grids than had ever been used before (5 m square grids). This extraordinary spatial resolution, associated with a time step of 1.2×10^{-4} s, gives an unprecedented resolution of the cohesive zone; on average we have $\langle N_c \rangle = \langle X_b \rangle / \Delta x = 100$ (X_b is the breakdown zone length, *i.e.*, the spatial extension on the fault over which the traction degrates from the upper yield stress down to the residual level). Just for comparison, the best resolved model of [14] uses $\langle N_c \rangle = 0.9$.

The resulting supture speed [29] is reported fig. 4a, where we have shown the regions which remained subshear and those which reached supershear speeds. Note that the spatial scales are normalized by the fault length L^f and the fault width W^f. Also in this case, due to the symmetries of the problem, we report only one half of the rupture, which we recall is expanding bilaterally with respect to the imposed hypocenter H.

In fig. 4b we plot the rupture speed along the pure mode II and a chosen direction where the two modes II and III are mixed together (reported in panel (a) as dashed red line). The rupture velocity clearly passes through the "forbidden zone" in both directions, the change in gradient of the curve on either side of the forbidden zone being particularly sharp for the mixed-mode case. Thus, though the crack front does pass through the so-called forbidden zone, it passes through it fast, as it emerges from fig. 5 [12] did proposed this idea, based on numerical simulations which did not have the same level of resolution compared to those discussed in this paper. The penetration of the forbidden zone was also shown in [13] (their fig. 2c), but for a special, non-dimensional set of parameters (that of [7] and [23]) which cannot be easily scaled to a real-world dimension and realistic conditions. We can clearly see that in the pure mode-II direction, the rupture then passes through the Eshelby speed without any perceptible change of gradient and it finally approaches v_P. The expected increase of the values of the supershear rupture speeds near the free surface is very clearly seen (see also [28, 35, 51]). However, we emphasize that in our simulations the penetration of the

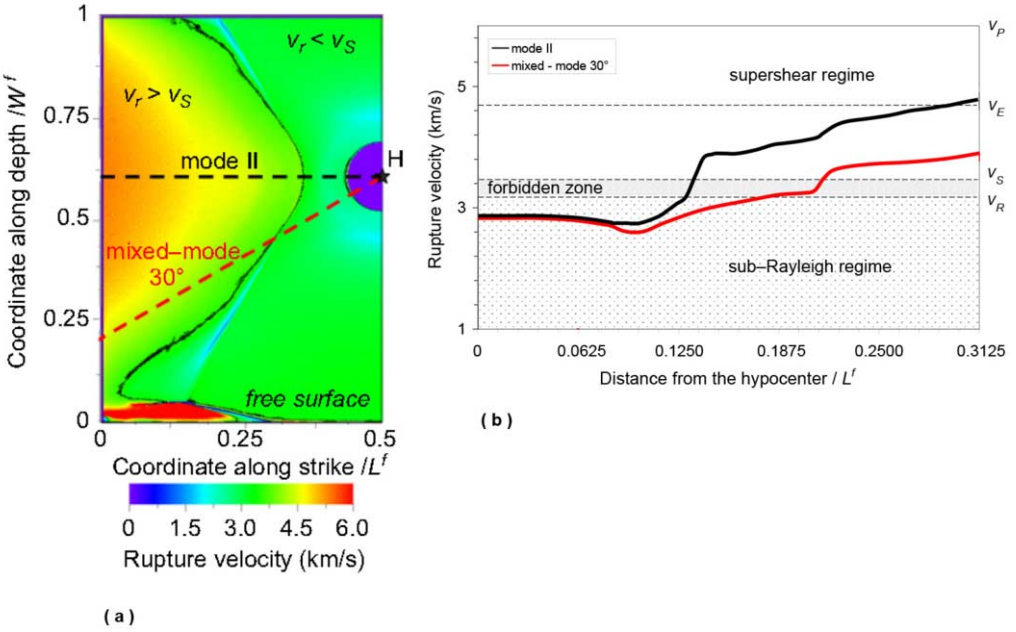

Fig. 4. – (a) Distribution of the rupture speed on the left half of the fault plane. The purple region denotes the initial patch where nucleation occurs. Spatial coordinates are normalized by the fault length L^f and the fault width W^f. The continuous black line represents the separation existing between regions experiencing sub- and supershear rupture speeds. The lines along which the rupture velocities v_r will be plotted in (b) are shown by red and black dashed lines. (b) Plot of v_r as a function of the hypocentral distance, along the two profiles shown in panel (a). The so-called forbidden zone is marked in grey. See sect. **5** for details. Modified from [29] with permission of Elsevier.

forbidden zone is not due to phase conversion along the free surface or to interactions with the stress field generated by the sliding near the free surface, as shown by [52] (their figs. 7 and 9c).

Finally, in fig. 4 we report a zoom of the so-called forbidden zone $[v_R, v_S]$. In this plot we superimpose the results pertaining to three different numerical experiments, when we only vary the spatial and temporal discretization. It is apparent that the number of points failing within the forbidden zone increases as the resolution becomes finer, as expected. The number of points within $[v_R, v_S]$ is also marked in the figure. The discrete jumps in the rupture speed do not depend on the adopted numerical scheme (see the discussion in [29]).

In sect. **7** we will see that also in pure mode II problems, under some conditions, the forbidden zone does disappear.

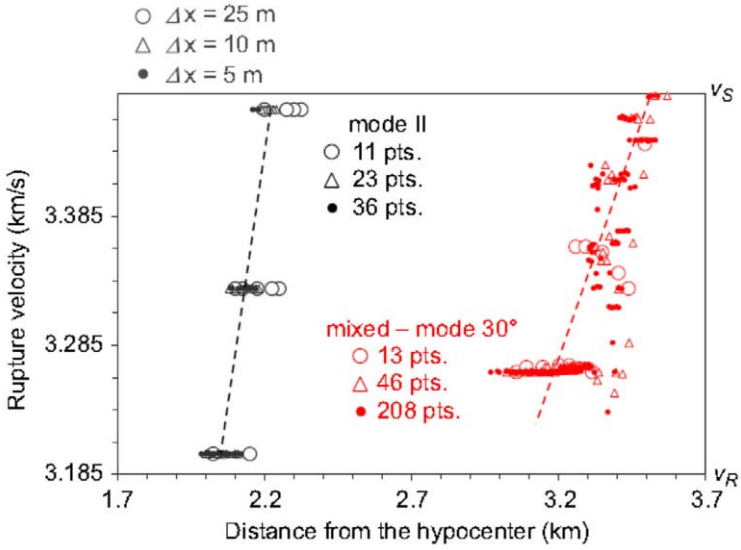

Fig. 5. – Zoom of the rupture speed in the so-called forbidden zone. The number of points failing in the range $[v_R, v_S]$ is also indicated for the different resolution of the models (listed in the topo of the panel). The maximum number of grid points lying within the forbidden zone are 36 and 208 for the pure mode II and the mixed-mode case, respectively. Even with a rougher discretization of 25 m grid size, we have 11 and 13 points in this zone, respectively, confirming that the forbidden zone is penetrated. Reproduced from [29] with permission of Elsevier.

6. – The shear-Mach and the Rayleigh-Mach cones

As for the previous section, the results presented here are from a 3D model with linear SW governing model (eq. (3)); the parameters are tabulated in table 1 of [26].

In the case of 2D steady state models [53] and [54] showed that supershear ruptures generate shear Mach (M_S henceforth) waves. Mach cones have been connected to the vapor cone generated by airplanes traveling at transonic speeds, just before reaching the speed of sound. For this reason, supershear earthquakes have been sometime, althought improperly, named "supersonic earthquakes". On the other hand, [27] showed that supershear ruptures having a straight rupture front generate not only M_S waves, but also Rayleigh Mach (M_R thereinafter) waves, which interfere and lead to complex velocity and stress fields (see their fig. 1 for a graphical sketch). Dunham and Bhat [27] also found that M_R fronts are most evident in the fault-normal and vertical components of particle velocity on the free surface and that they do not attenuate with distance from the fault trace (in a homogenous, ideally elastic medium). Finally, they also demonstrated that while high particle velocities are concentrated near the fault trace for subshear ruptures, in case of supershear ruptures they extend widely in the direction perpendicular to the fault trace. Additionally, they showed that when rupture velocity increases from sub- to supershear speeds, the dominant component of particle velocity changes from fault-normal to fault-parallel, as also shown by [28].

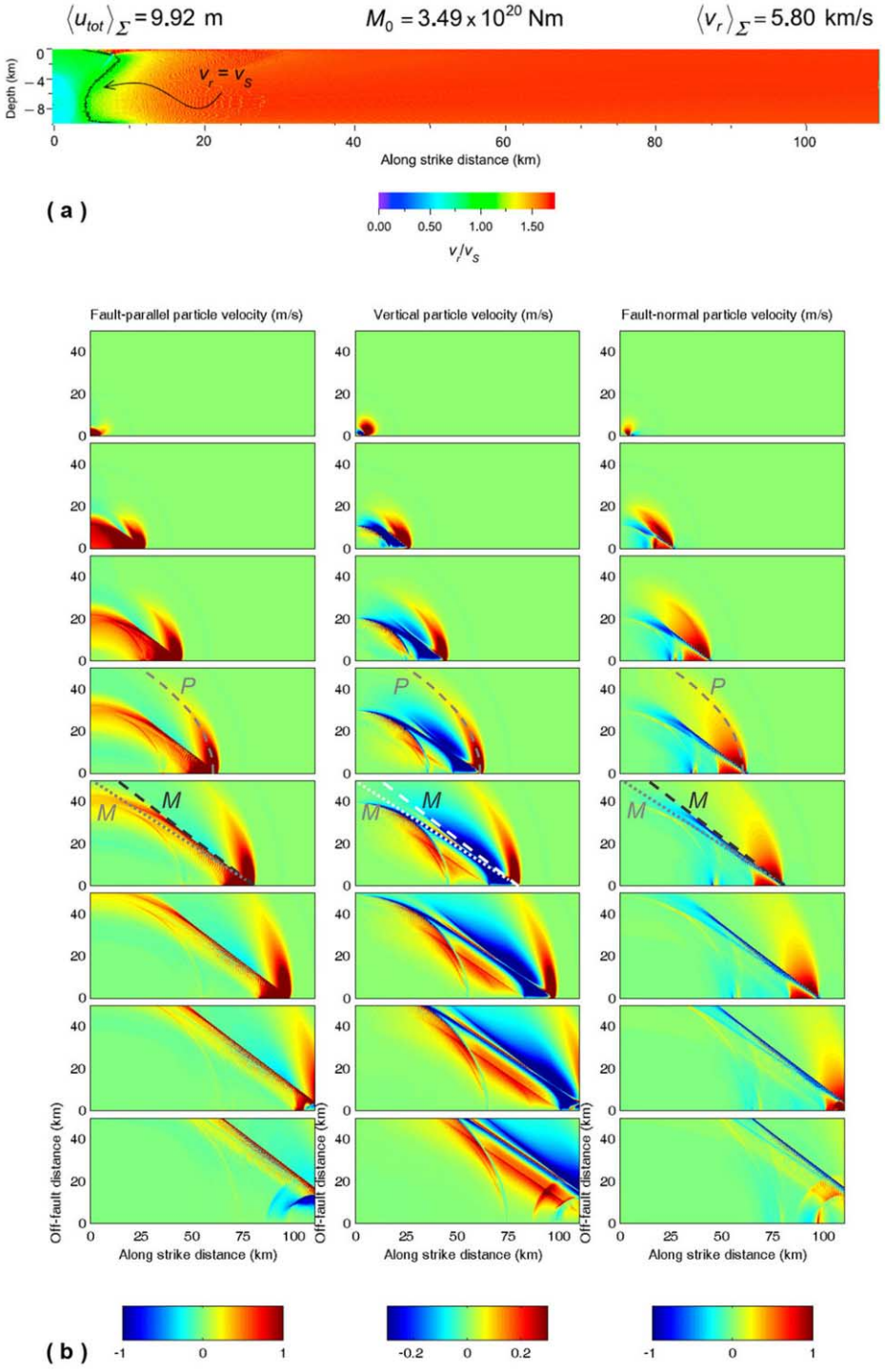

Fig. 6. – *Caption on top of fig. 8.*

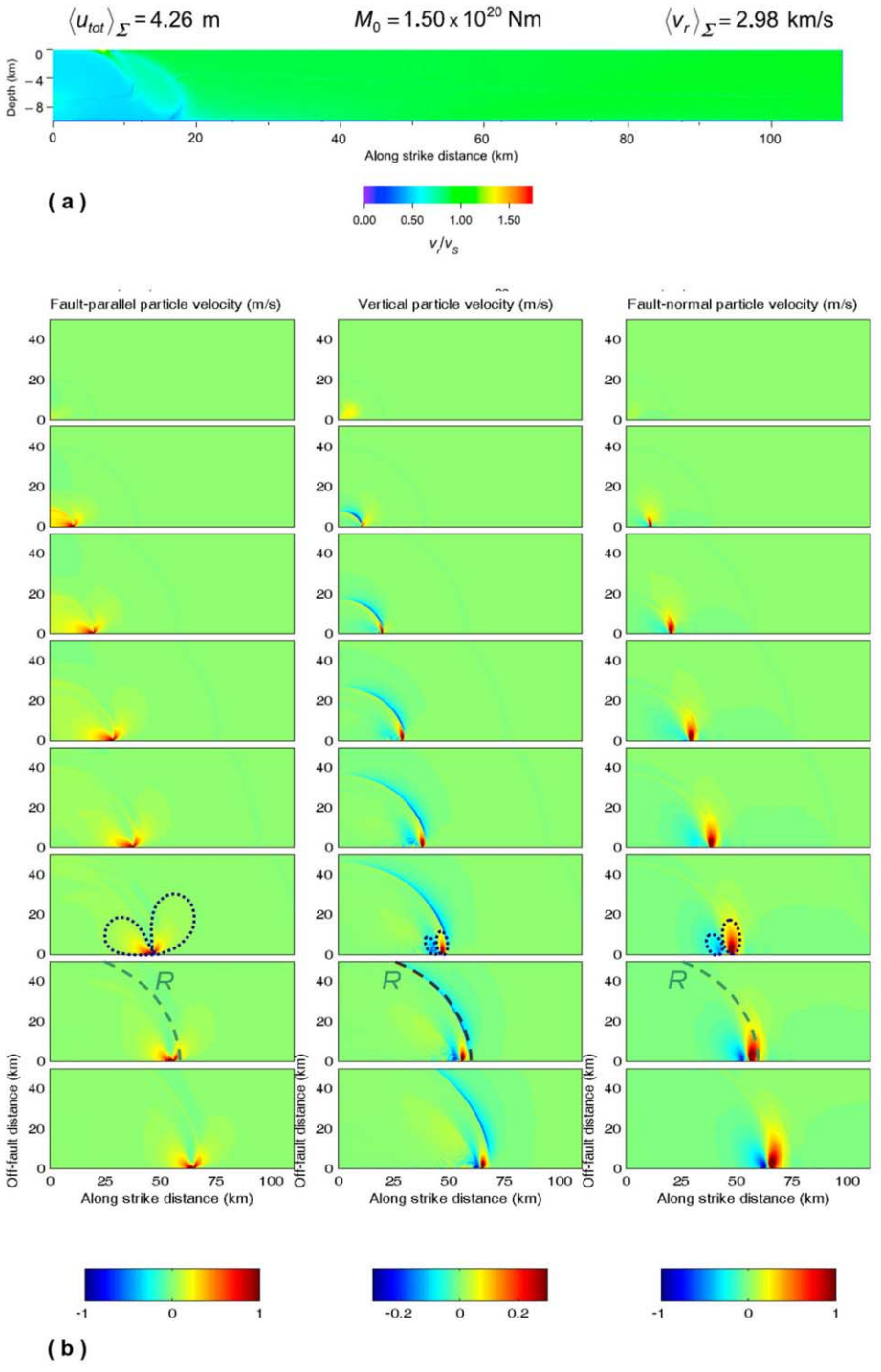

Fig. 7. – *Caption on top of fig. 8.*

Caption to fig. 6: (a) Rupture velocity normalized by the S-wave velocity on the fault plane in the case of supershear rupture. As usual, black line corresponds to $v_r = v_S$ contour. On the top of the panel we report the total seismic moment, M_0, and the spatial averages over the whole fault surfaces of the total cumulative fault slip and rupture velocity ($\langle u_{tot} \rangle_\Sigma$ and $\langle v_r \rangle_\Sigma$, respectively). (b) Snapshots at different times (indicated on the single plots) of the resulting free surface particle velocity $\mathbf{V}$ (with saturated color scale). M_S and M_R are the shear and Rayleigh wave Mach fronts, respectively, and P_1 denotes the first positive peak in particle velocity, associated with dilatational motion. Note in the last two snapshots the stopping phases generated from unbreakable barrier at $x_1 = 110\,\mathrm{km}$. Numerical dispersion of high-frequency waves is responsible for oscillations behind sharp wavefronts. See sect. **6** for further details. Modified from [26] with permission of John Wiley and Sons.

Caption to fig. 7: The same as fig. 6, but now in the case of homogeneous subshear rupture. In the present case R denotes the Rayleigh wavefront. Modified from [26] with permission of John Wiley and Sons.

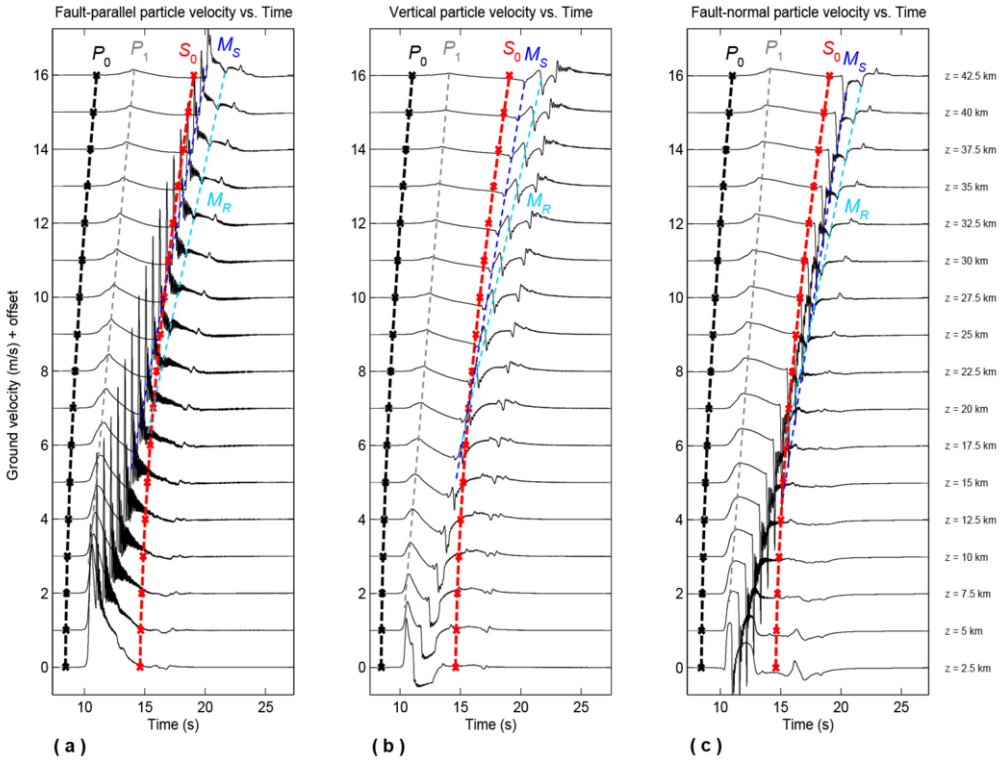

Fig. 8. – Time evolution, low-passed at 8 Hz, of the components of the normalized free surface particle velocity for the supershear model (fig. 6) at several receivers, all located 50 km along strike from the hypocenter and equally spaced by 5 km in the direction normal to the fault (the absolute location of each receiver is indicated, for each trace, to the right of panel (c)). Velocity is normalized by the multiplier factor $G/(v_S \Delta\tau_d)$, G being the rigidity of the medium and $\Delta\tau_d$ being the dynamic stress drop. P_0 and S_0 mark the theoretical arrival times of the direct P and S waves from the imposed hypocenter, respectively. M_S and M_R indicate the shear and Rayleigh Mach fronts, respectively, and P_1 denotes the first positive peak associated with dilatational motions, as in fig. 6a. The stopping wave fronts are outside the time window considered here for all free surface receivers. Reproduced from [26] with permission of John Wiley and Sons.

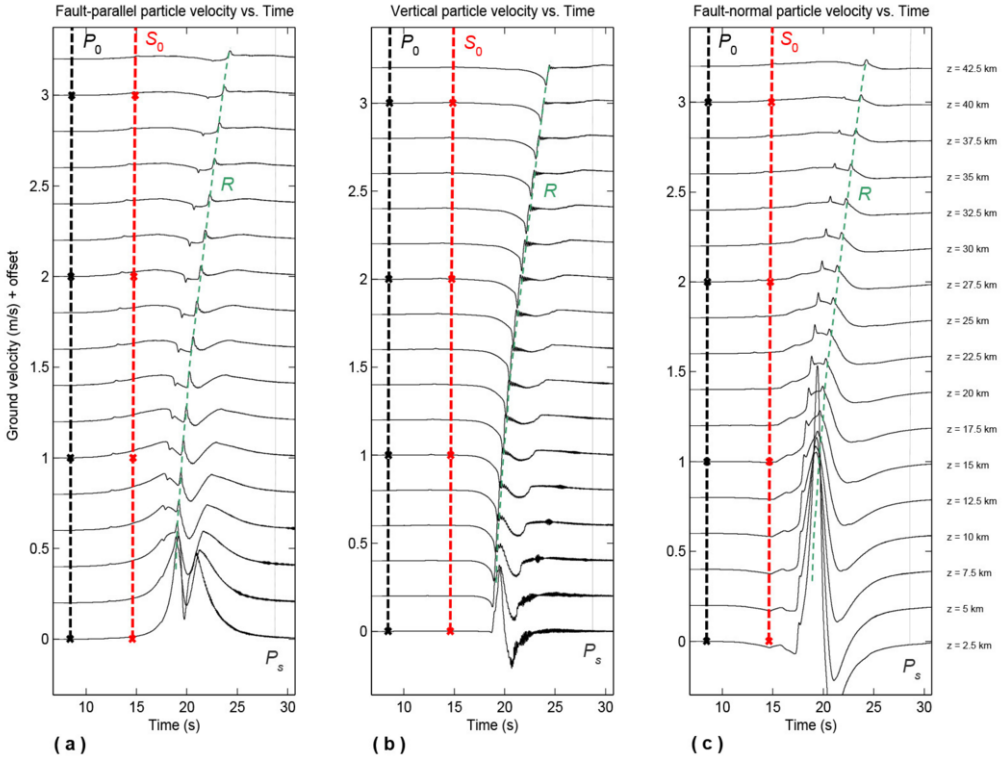

Fig. 9. – Same as fig. 8, but for the subshear configuration of fig. 7. Also in this case the stopping wavefronts are outside the considered time window considered. R again marks the Rayleigh wavefront. Reproduced from [26] with permission of John Wiley and Sons.

Bizzarri and coworkers [26] showed that in the truly 3D homogeneous case (in which the rupture fronts are curved due to interactions with the free surface and the finite fault width) still exist coherent M_S and M_R fronts. This is clearly visible from fig. 6b, where we report some time shapshots of the particle velocity $\mathbf{V}$ (its three components) pertaining to the supeshear case (the spatial distribution of the rupture speed is reported in fig. 6a). The comparison for the subshear configuration (fig. 7a) is reported in fig. 7b. The differences in S between super- and subshear models arise from differences in τ_0 only, since we keep τ_u and τ_f the same in both models; this results in a factor of two larger dynamic stress drop for first model compared with the second one (see table 1 of [26]).

From fig. 6b we can observe that the inclination of M_S with respect to the x_1-axis (which is expressed as $\beta_S = \arcsin(v_S/v_r)$) is constant through time, suggesting that the rupture velocity is constant; this prediction is in agreement with our numerical calculation of v_r (see fig. 6a). These results of [26] basically confirm what [27] found in their non-spontaneous model with a straight rupture front. Moreover, in agreement with [27], the comparison between figs. 6b and 7b confirms that in the steadily propagating homogeneous subshear case (fig. 7b) $\mathbf{V}$ is significant only near the fault trace, while in the

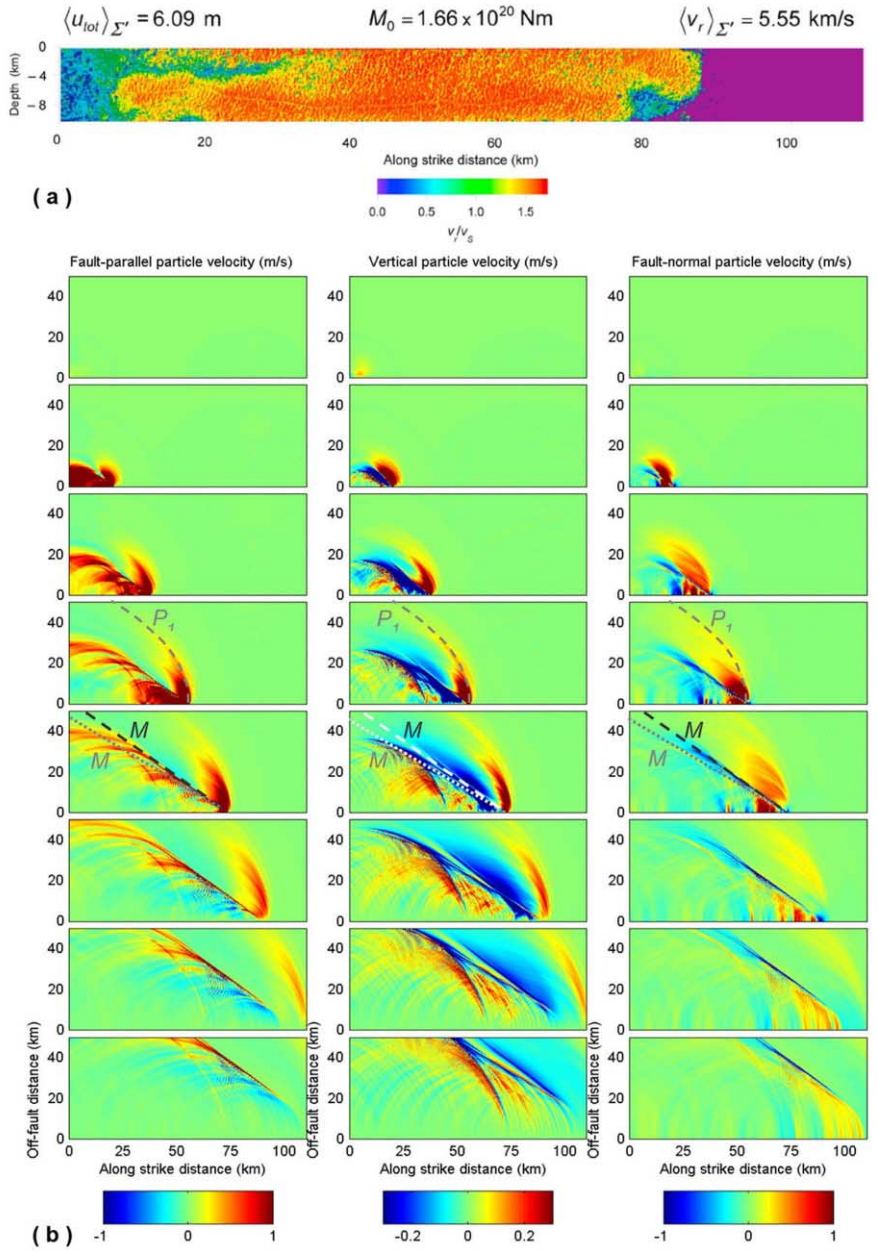

Fig. 10. – (a) Distribution of v_r/v_S for a heterogeneous model for which the initial shear stress is $\tau_0 = \Delta\tau^{(het)} + \tau_0^{(ref)}$, where $\tau_0^{(ref)} = 65.62\,\mathrm{MPa}$ (an intermediate value between super- and subshear models) and $\Delta\tau^{(het)}$ follows a k^{-1} distribution at high wave numbers k (see sect. 4 of [26] for additional details). As for previous figs. 6a and 7a, the total seismic moment and the spatial averages (over the fractured portion of the fault surface Σ') of the total cumulative fault slip and rupture velocity are reported on the top of panel. (b) Resulting vawe fields in the same receivers of figs. 6b and 7b. The shear (M_S) and Rayleigh (M_R) Mach fronts are not obscured by the presence of heterogeneities in the initial shear stress. Modified from [26] with permission of John Wiley and Sons.

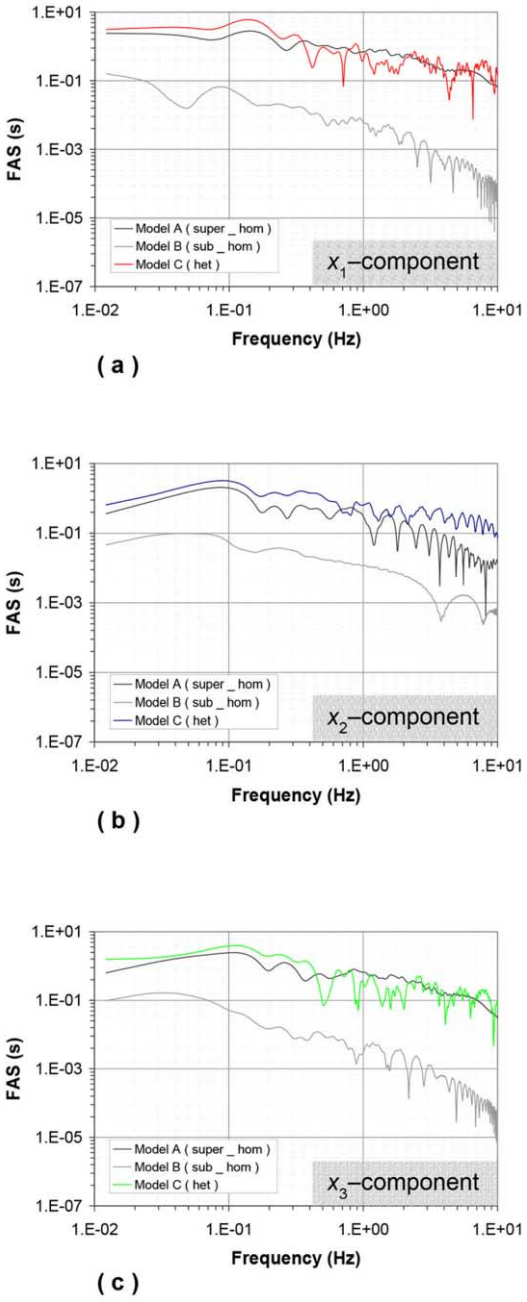

Fig. 11. – Spectral analysis of ground velocity at $(x_1, x_3) = (50, 35)$ km for the three models of figs. 6, 7 and 8. Frequencies above 8 Hz are affected by numerical oscillations. The omparison of FAS of three components of $\mathbf{V}$ indicate that the ground motions of a supershear rupture is richer in high frequencies with respect to that from a homogeneous subshear and that when a Mach pulse is present, its high-frequency content overwhelms the high frequencies introduced by stress/slip heterogeneity. Modified from [26] with permission of John Wiley and Sons.

supershear case (fig. 6b) large ground velocities extend to the end of the computational domain in the direction perpendicular to the fault [26].

The two Mach fronts (M_S and M_R) can be clearly recognized in the time evolution of $\mathbf{V}$ at different distance form the fault trace (see fig. 8). The distance along the strike distance is 50 km in order to be sure to capture all the features of the well-developed rupture and to minimize the potential effects of the imposed nucleation procedure. In agreement with [27], we can see that as the distance from the fault trace increases the amplitude of particle velocity (especially V_1 and V_3) decreases faster in the subshear model (see fig. 9) compared to the supershear one (see fig. 8) in these models having fairly uniform rupture speed. Another interesting feature which emerges from the comparison of figs. 8 and 9 is that in the supershear model $V_1 > V_2$ at most locations; on the contrary, in the subshear model the opposite is true (*i.e.*, $V_1 < V_2$ at most locations). This result [26] confirms the conclusions of [28] and [27].

If we introduce spatial heterogeneities in the distribution of the initial shear stress essentially we can confirm what we see in homogeneous models, in particular, the two Mach fronts still appear (fig. 10b), althougth the M_S front is less coherent in heterogeneous model than in the homogenesous one (this is an obvious consequence of the variability in rupture front history; see fig. 10a). The details of heterogeneous distribution is given in sect. **4** of [26]; we simply mention here that the heterogeneous initial shear stress is consistent with a specified power spectral density which attenuates with increasing radial wave number. Due to the heterogeneous value of the S parameter (eq. (11)), the distinction of the two speed regimes of propagation is not so strong as it was for previous homogeneous models; in this numerical experiments v_r generally exceedes v_S (see fig. 10a), but it exhibits some subshear patches. This model is characterized by a gradual, spontaneous (and probably more realistic) cessation of slip at various locations (*i.e.*, it stops at different times and distances along strike for each depth); when the rupture propagates into fault patches with negative stress drop (*i.e.*, stress increase), it stops gradually. It is apparent that in this case the event size was not predictable a priori (*i.e.*, before running the simulation). This configuration can be regarded as an interesting example of how artificial it probably is to stop ruptures so abruptly at the end of the fault, as we have done in the homogeneous simulations.

Calculations of the Fourier amplitude spectra (FAS) of ground velocity time histories corroborate the kinematic results of [24]: i) The ground motion of a supershear rupture is richer in high frequency with respect to a subshear one and ii) when a Mach pulse is present, its high-frequency content overwhelms that arising from stress heterogeneity. Numerical experiments of [26] indicate that a Mach pulse causes approximately an $\omega^{-1.7}$ high-frequency falloff in the FAS of ground displacement. This is visible from fig. 11.

7. – The two transition styles: the direct transition and the mother-daughter mechanism

In the present section we will consider a pure in-plane 2D fault subject to the linear SW law (eq. (3)); the parameters are the same as those of sect. **5**.

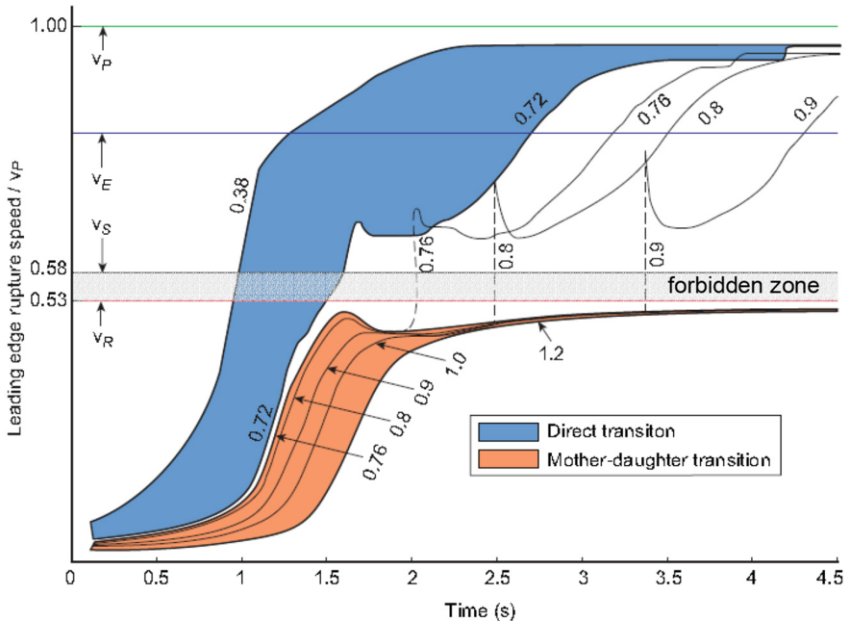

Fig. 12. – Rupture speeds for the 24 values of the streneght parameter S used for a homogeneous 2D, pure in-plane rupture (see sect. **7**). The spatial grid size Δx is 40 m and the starting velocity is 0.5 km/s. The so-called forbidden zone is marked (as in fig. 4). The two kinds of transition behavior for the smaller and larger S values are clearly visible (light blue and light orange, respectively). The vertical dashed lines indicate the birth of the daughter rupture in the case of the mother-daughter mechanism. For values of S greater than 0.9 the jump to the supershear speed (associated with the presence of the forbidden zone) occurs after $t = 4.5$ s (and thus out of the reported scale). When S reaches the critical value of 1.77 [23] the rupture asymptotically reaches v_R and remains in the sub-Rayleigh regime. Modified from [40] with permission of John Wiley and Sons.

Motivated by the results discussed in sect. **5**, Liu and coworkers [40] carried out one hundred and twenty six numerical experiments in order to scrutinize the features of the penetration of the so-called forbidden zone. For each configuration they investigate the relation existing between the rupture speed and the strength parameter S; they consider 24 values of S in the range between 0.38 and 1.2, and 6 values larger than 1.2. To obtain different values of S, they change the upper yield stress τ_u and they keep the other parameters unchanged. Contrary to the 3D case, where the absolute values of the stresses affect the behavior of the propagating rupture (they indeed control the level of rake rotation; [13]), in the 2D case only the value of S controls the rupture behavior. For values of S greater than the critical value of $S_{\max} = 1.77$ the rupture speed remains below the Rayleigh wave speed [8, 23, 55], so most of the values chosen ensure that supershear rupture speeds are attained.

Liu and coworkers [40] found there are two rather different mechanisms which control the supershear transition, discriminated through a threshold value of the strength

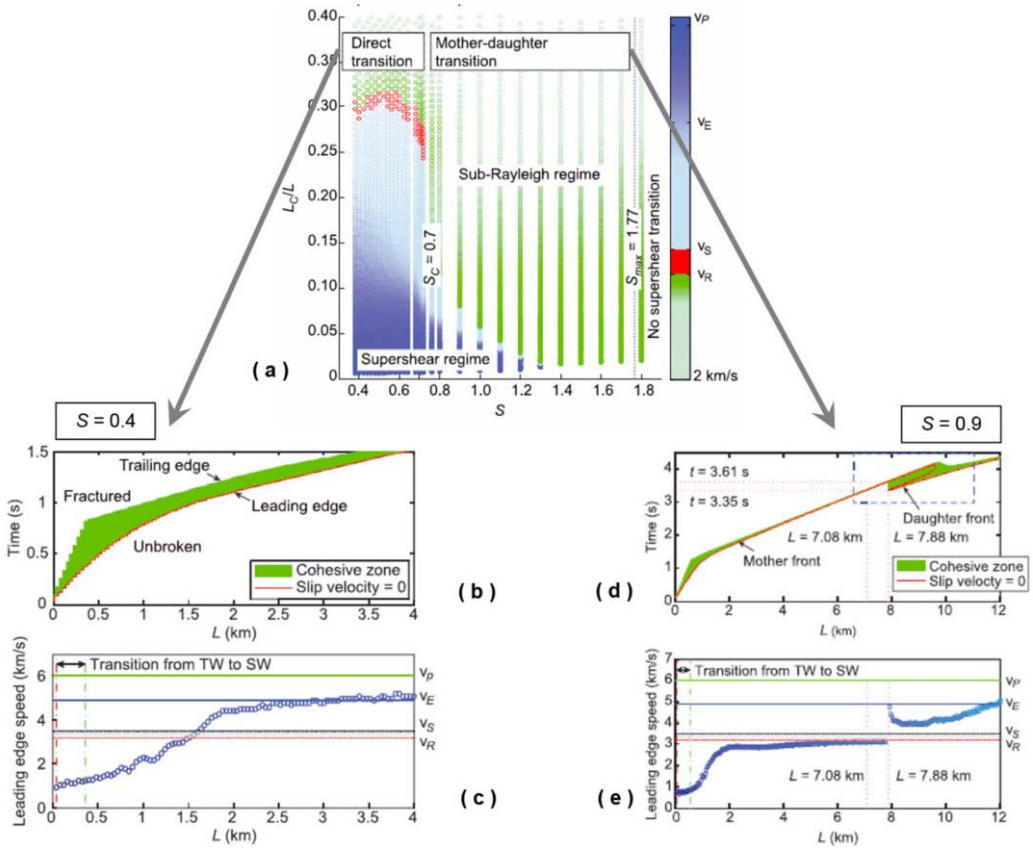

Fig. 13. – (a) Phase diagram summarizing the behavior of the dynamic system; we plot the values of v_r (in a color scale) as a function of the strength parameter S (on the abscissa) and the ratio between the half-critical length L_c and the location of the rupture front L (on the ordinate; L_c, first introduced by [23], is defined as $L_c^{(\mathrm{II})} = \frac{2}{\pi} G \frac{\lambda+G}{\lambda+2G} \frac{\tau_u - \tau_f}{(\tau_0-\tau_f)^2} d_0$, where λ and G are the two Lamé's constants). The penetration of the forbidden zone is emphasized in red. (b) Shape of the cohesive zone in case of direct transition ($S = 0.4$). The red line indicates where slip velocity is zero (*i.e.*, the nominal boundary between the unbroken and the broken parts of the fault). Leading edge and trailing edge of the cohesive zone are also indicated, in agreement with [29]. (c) Corresponding rupture speed as a function of the distance from the hypocenter. The red and green vertical dashed lines denotes the beginning of slip-weakening (SW) and the end of time-weakening (TW) used to obtain the rupture nucleation. Region between red vertical line and green vertical line denotes the transition from TW to SW. For distances greater than the green vertical line the propagation is fully spontaneous and governed by the SW model. (d) and (e) The same of panels (b) and (c), respectively, by now for $S = 0.9$, failing in the mother-daughter mechanism. Modified from [40] with permission of John Wiley and Sons.

parameter, $S_c \sim 0.7$. It is important to mention that, due to the numerical nature of the problem, it is virtually impossible to find an *exact, arbitrarily accurate* value which distinguishes the two regimes, and this is the reason why [40] gave the value "~ 0.72" as

upper bound for S in the direct transition (DT thereinafter) mechanism and the value of "~ 0.76" as lower bound for the mother-daughter (MD thereinafter) mechanism. When $S < S_c$ (so that we deal with "weak" faults) the DT mechanism (see also [56, 57]) dominates (light blue in fig. 12). There is no peak in the shear stress field traveling ahead of the main rupture front and therefore no daughter rupture appears. More importantly, the rupture penetrates and then passes smoothly through the formerly considered forbidden zone [40]. It then approaches the v_P speed, which indeed is the terminal, limiting speed for this rupture mode. Remarkably, the "forbidden zone" $[v_R, v_S]$ can disappear in this case. As pointed out by [40], the results are accurate and robust; the phenomenon we observe is not an artefact of the numerical method, the numerical resolution, or the method employed to nucleate the rupture.

On the other hand, when $S > S_c$ (so we deal with "strong" faults), the MD mechanism (also referred to as the Burridge-Andrews mechanism; [3, 23, 45, 56-59]) dominates. This family of configurations is marked in orange in fig. 12; in these cases the forbidden zone does really exist, as the transition to the intersonic regime involves a rupture speed jump. We recall here that the pioneering model of [23] fails in this cathegory, since he used $S = 0.8$ (see his fig. 3).

In fig. 13a a phase diagram is reported summarizing the behavior of the different ruptures considered in the present work. As S increases and approaches the critical value $S_{\max} = 1.77$, the rupture tends to remain in the sub-Rayleigh regime, as expected. On the other hand, when S decreases, the supershear transition can occur sooner. Figure 13a also reports the distance from the imposed nucleation point at which the supershear transition occurs (namely the quantity indicated as transitional length $L_{trans}^{(2\text{-D})}$ of [29]).

Two end-member cases are reported in figs. 13b and 13c (direct transition mechanism; $S = 0.4$) and in figs. 13d and 13e (mother-daughter mechanism; $S = 0.9$). The green region in figs. 13b and 13d emphasizes shape of the cohesive zone, where the fault traction degrades from the upper yield stress τ_u down to the kinetic level τ_f (or analogously, where the fault slip increases from 0 to d_0). From fig. 13b it is clear that no daughter rupture develops ahead of the main rupture, which indeed is a single continuous line, without any jump. The position of the leading edge and rupture time increase smoothly during the transition. The penetration of the so-called forbidden zone is evident from fig. 13c, in which we report the values of the rupture speed as a function of the distance from the imposed hypoceter. In the mother-daughter case (figs. 13d and 13e) we can see that overall behavior of the rupture below v_R is similar to that seen above. One interesting result of [40] is that, as v_R is approached, a major change in the behavior occurs; the rupture speed no longer crosses v_R but approaches it asymptotically (see fig. 13e). Then a secondary fracture is initiated ahead of the main rupture front; the daughter rupture now starts to propagate at a speed which is already supershear (as expected; see [23]), but it exhibits negligible fault slip and fault slip velocity. The mother rupture then merges with the daughter rupture and it is only after this time that the fault slip and the fault slip velocity of the daughter rupture become appreciable. In fact, the increase in the speed of the daughter rupture mentioned above actually occurs after the merging of the two ruptures and eventually itself approaches the P wave speed (the limiting speed

of this rupture mode). Thus, as observed by [40], the daughter rupture is essentially a "pseudo-rupture", where the two sides of the fracture have broken apart, but do not have significant motion and no appreciable stress drop, a feature seen in [23].

8. – Different ground motions

As in sect. **7**, we will consider here a pure in-plane 2D fault governed by the linear SW law (eq. (3)); the parameters are the same as those of sects. **5** and **7**.

Given the fact that two different transition mechanisms exist, as discussed in previous section [60, 61], it is natural to investigate whether they correspond to different ground motions; this has been done by [31]. According to that paper, in the following we will refer to $V_1(x_1, x_2, t)$ and to $V_2(x_1, x_2 t)$ as the fault-parallel (FP henceforth) and the fault-normal (FN henceforth) component of the particle velocity fields, respectively. Moreover, we freely speak of "ground motions" although, namely, there is no the free-of-traction condition in the present model. Namely, V_1 and V_2 are particle motions excited by the earthquake source. Indeed, we know that the Mach cone originated by the supershear rupture propagation does not depends on the presence of the free surface (see, *e.g.*, [27]; their fig. 1); the latter is known only to produce the additional Rayleigh-Mach waves ([26, 27]; see also sect. **6**) and it tends to enhance the supershear propagation once the rupture front interacts with it [29, 35, 51, 52, 62-65].

The two cases are the same reported in fig. 13; while Model A has $S = 0.4$ (DT mechanism), Model B has $S = 0.9$ (MD mechanism); both the configurations have the same initial shear stress τ_0 and the same τ_f (so that the dynamic stress drop is also the same; $\Delta\tau_d = \tau_0 - \tau_f = 18.6\,\mathrm{MPa}$). In such a way the amplitudes of the ground velocity of Models A and B reported in the following are directly comparable. However, the former has $\tau_u = 81.24\,\mathrm{MPa}$ (which correspond to an upper friction coefficient $\mu_u = 0.677$), while the latter has $\tau_u = 90.54\,\mathrm{MPa}$ ($\mu_u = 0.755$).

We report in fig. 14 the snapshots of the spatial distribution of the particle velocity field in the whole medium. As expected, we can clearly recognize the presence of the shear Mach (M_S) waves, that are generated by the two supershear ruptures (see sect. **6**). Shear Mach waves are preceded by a first peak in particle velocity (the arc denoted with the symbol P_1 in fig. 14), which is associated with dilatational motion [26]. In general, we have that the M_S wavefront is more relevant at large distances from the fault for ruptures experiencing the DT mechanism with respect to those experiencing the MD mechanism. As pointed out by [31], this is physically reasonable, because DT is characterized by a smaller value of the S parameter and thus by a higher level of fault instability (namely, since in our simulations τ_0 and τ_f are kept unchanged, Model A has a greater breakdown stress drop, $\Delta\tau_b$). This conclusion holds for both FP and FN components of particle velocity [31].

Remarkably, there is a more relevant difference between the wavefields of DT and MD mechanisms found by [31]; from fig. 14 we see that in the MD mechanism it emerges another wavefield (the trailing Rayleigh field or trailing Rayleigh pulse), which has been first mentioned by [66] in explaining the Denali, Alaska, PS10 record, has been experi-

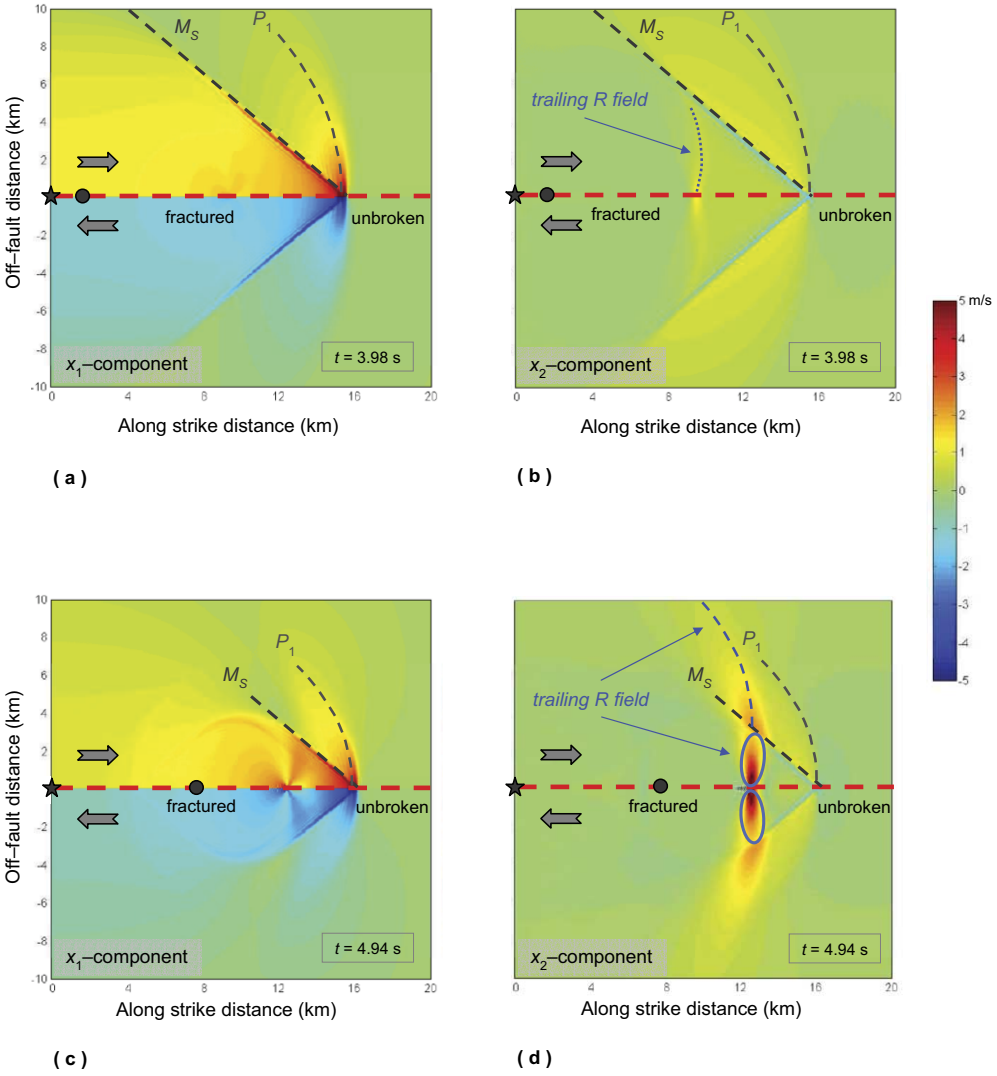

Fig. 14. – Spatial distribution of the particle velocity fields from homogeneous 2D, pure in-plane ruptures. Top panels pertain to direct transition (DT) mechanism ($S = 0.4$, figs. 13b and 13c), bottom panels pertain to mother-daughter (MD) mechanism ($S = 0.9$, figs. 13d and 13e). Left panels report the fault-parallel (FP) component (namely, V_1), right panels report the fault-normal (FN) component (namely, V_2). As usual, the star indicates the imposed epicenter. Due to the symmetry of the problem, only the positive part of the x_1-axis is reported. The red dashed line denotes the fault trace and the big dots indicates the strike distances at which the supershear transitions occur ($x_1 = 1.66$ km for the DT case and $x_1 = 7.88$ km for the MD). The times of the snapshots (indicated in each panel) have been selected in order to have the same location of the rupture tip for both the models. Big arrows emphasize the relative motion of the parts of the elastic medium separated by the fault interface. All relevant fields are also indicated (only in the positive x_2 half-plane, for better clarity). Reproduced from [31] with permission of Elsevier.

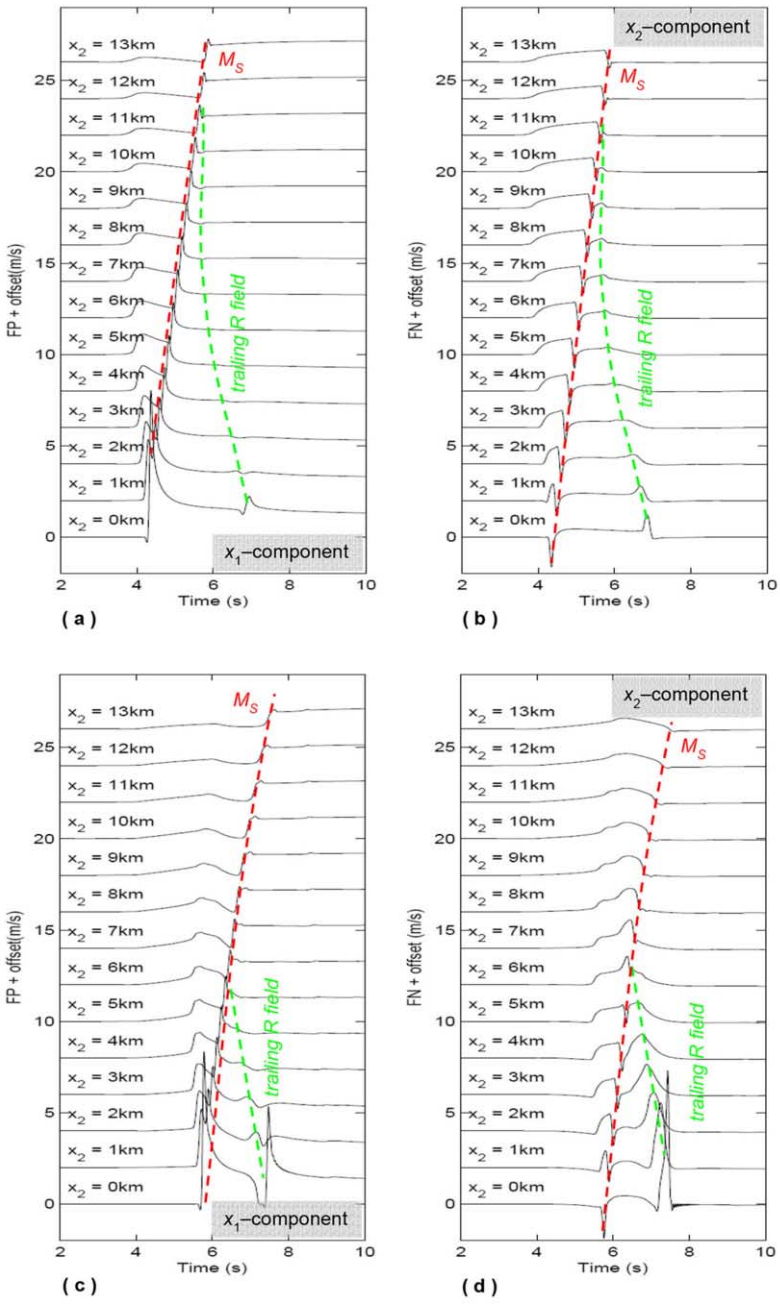

Fig. 15. – Synthetic signals pertaining to the two models of fig. 14 at a strike distance of 20 km from the hypocenter and for different off-fault distances (indicated near each trace). Again, top and bottom panels are for DT and MD mechanism, respectively; left and right panels report the FP and the FN component, respectively. As for figs. 8 and 9 data are low-passed at 8 Hz and the offset for n-th receiver is $(n-1)$. Reproduced from [31] with permission of Elsevier.

mentally identified by [67] and [68]. The trailing Rayleigh field does actually propagate at the Rayleigh wave speed. The trailing Rayleigh field is quite visible especially in the fault-normal (FN) component of ground motions (see fig. 14d); in the DT mechanism it is much lower (see fig. 14b) and it is practically absent in the fault-parallel (FP) component (see fig. 14a). The very small amplitude of the trailing Rayleigh field in the DT case is also confirmed by the results in a truly 3D model (pertaining to a configuration with $S = 0.4$) by [26] (see their figs. 3a and 3c from 3^{rd} to 5^{th} snapshots).

From fig. 14d, we can also see that in the MD case inside the shear Mach cone (*i.e.*, at off-fault distances up to about 5 km for the time snapshot reported in fig. 14d) the trailing Rayleigh field appears as a 8-shaped object in the FN component of $\mathbf{V}$. This 8-shaped object is not vertical, but its lobes have a forward curvature, in total agreement with the results of [67]. Far from the fault (namely, outside the shear Mach cone) the trailing Rayleigh field expands as an arcuate front, with a slightly lower curvature with respect to the P_1 arc.

In fig. 15 we plot the particle velocity time histories at different stations located at a distance along strike of 20 km from the hypocenter. Data are low-passed at 8 Hz in order to avoid the numerical noise due to grid dispersion. These records clearly indicate the differences in the trailing Rayleigh field in the DT and in the MD models (top and bottom panels, respectively). While the trailing Rayleigh field is feebly recognizable in the case of DT, it is firmly seen in the case of MD. In the latter situation its amplitude is paramount with respect to that of M_S waves. Once the rupture propagates along the fault the trailing Rayleigh field expands and intersects the Mach cone and persists at large distance from the fault trace. As observed in fig. 14d, also from figs. 15c and 15d it emerges that for stations close to the fault trace (namely, inside the Mach cone) the behaviour of the trailing Rayleigh field (marked as dashed green lines in fig. 14) has a forward curvature. Incidentally, we remark here that since our models do not incorporate any stopping or self-healing mechanism (*i.e.*, the rupture continues to propagates forever due to the homogeneities of the spatial distribution of the parameters), there is a permanent deformation in the x_1-direction, which corresponds to the fact that the particle velocity does not go back to zero.

9. – Concluding remarks

We have reviewed the prominent features of sesimogenic ruptures that sponetaneously propagate on a planar fault surfaces, governed by the linear slip-weakening governing law, for both 2D and truly 3D models. The numerical models presented in the recent literature highlight that earthquakes traveling at velocities greater than the S wave speed of the elastic medium in which the fault is embedded possess some special features, both in the solutions on the fault and in the solutions in the surrounding medium (and therefore on the free surface). A thorough analisys of the numerical solutions makes it possible to distinguish between sub- and supershear events, as well as to discriminate the style of the transition from the sub-Rayliegh and the supershear regimes.

* * *

The material presented here comes from scientific collaborations and papers with S. Das, E. M. Dunham, C. Liu and P. Spudich, which are greatly awknowledged. These results have been presented during Course 202 of the International School of Physics "Enrico Fermi" entitled "Mechanics of earthquake faulting", held in Varenna (Como, Italy) from 2 to 7 July, 2018, directed by A. Bizzarri, S. Das and A. Petri, under the sponsorship of the Italian Physical Society (SIF) and Istituto Nazionale di Geofisica e Vulcanologia (INGV).

REFERENCES

[1] BIZZARRI A., *Rev. Geophys.*, **49** (2011) RG3002, doi: 10.1029/2011RG000356.
[2] BURRIDGE R., *Geophys. J. R. Astron. Soc.*, **35** (1973) 439.
[3] FREUND L. B., *J. Geophys. Res.*, **84** (1979) 2199.
[4] BROBERG K. B., *Geophys. J. Int.*, **119** (1994) 706.
[5] BROBERG K. B., *Arch. Mech.*, **47** (1995) 859.
[6] SAMUDRALA O., HUANG Y. and ROSAKIS A. J., *J. Geophys. Res.*, **107** (2002) 2170, doi: 10.1029/2001JB000460.
[7] ANDREWS D. J., *J. Geophys. Res.*, **81** (1976a) 3575.
[8] DAS S. and AKI K., *Geophys. J. R. Astron. Soc.*, **50** (1977a) 643.
[9] DAS S., *Geophys. J. R. Astron. Soc.*, **67** (1981) 375.
[10] BIZZARRI A., COCCO M., ANDREWS D. J. and BOSCHI E., *Geophys. J. Int.*, **144** (2001) 656.
[11] DAY S. M., *Bull. Seismol. Soc. Am.*, **72** (1982) 1881.
[12] MADARIAGA R. and OLSEN K. B., *Pure Appl. Geophys.*, **157** (2000) 1981.
[13] BIZZARRI A. and COCCO M., *Ann. Geophys.*, **48** (2005) 279.
[14] DAY S. M., DALGUER L. A., LAPUSTA N. and LIU Y., *J. Geophys. Res.*, **110** (2005) B12307, doi: 10.1029/2005JB003813.
[15] OKUBO P. G., *J. Geophys. Res.*, **94** (1989) 12321.
[16] WU F. T., THOMSON K. C. and KUENZLER H., *Bull. Seismol. Soc. Am.*, **62** (1972) 1621.
[17] JOHNSON T., WU T. F. and SCHOLZ C. H., *Science*, **179** (1973) 278.
[18] ROSAKIS A. J., SAMUDRALA O. and COKER D., *Science*, **284** (1999) 1337.
[19] XIA K., ROSAKIS A. J. and KANAMORI H., *Science*, **303** (2004) 1859.
[20] HEATON T. H., *Phys. Earth Plan. Inter.*, **64** (1990) 1.
[21] ELLSWORTH W. L. *et al.*, *Earthquake Spectra*, **20** (2004) 597.
[22] BERNARD P. and BAUMONT D., *Geophys. J. Int.*, **162** (2005) 431.
[23] ANDREWS D. J., *J. Geophys. Res.*, **81** (1976b) 5679.
[24] BIZZARRI A. and SPUDICH P., *J. Geophys. Res.*, **113** (2008) B05304 doi: 10.1029/2007JB005146.
[25] SPUDICH P. and FRAZER L. N., *Bull. Seismol. Soc. Am.*, **74** (1984) 2061.
[26] BIZZARRI A., DUNHAM E. M. and SPUDICH P., *J. Geophys. Res.*, **115** (2010) B08301 doi: 10.1029/2009JB006819.
[27] DUNHAM E. M. and BHAT H. S., *J. Geophys. Res.*, **113** (2008) B08319, doi: 10.1029/2007JB005182.
[28] AAGAARD B. T. and HEATON T. H., *Bull. Seismol. Soc. Am.*, **94** (2004) 2064.
[29] BIZZARRI A. and DAS S., *Earth Plan. Sci. Lett.*, **357-358** (2012) 397, doi: 10.1016/j.epsl.2012.09.053.

[30] BIZZARRI A., *Ann. Geophys.*, **57** (2014) S0547, doi: 10.4401/ag-6582.
[31] BIZZARRI A. and LIU C., *Phys. Earth Planet. Inter.*, **261** (2016) doi: 10.1016/j.pepi.2016.05.013.
[32] IDA Y., *J. Geophys. Res.*, **77** (1972) 3796.
[33] BARENBLATT G. I., *Appl. Math. Mech.*, **23** (1959a) 622.
[34] BARENBLATT G. I., *Appl. Math. Mech.*, **23** (1959b) 1273.
[35] BIZZARRI A., *Bull. Seismol. Soc. Am.*, **100** (2010) 923, doi: 10.1785/0120090179.
[36] DIETERICH J. H., in *Solid Earth Geophysics and Geotecnology*, edited by NEMAT-NASSER S. (American Society of Mechanical Engineers, New York) 1980, pp. 21–30.
[37] DIETERICH J. H., in *Mechanical Behavior of Crustal Rocks, Geophysical Monograph*, edited by CARTER N. L., FRIEDMAN M., LOGAN J. M. and STEARNS D. W. Vol. **24** (Am. Geophys. Union, Washington, DC) 1981, pp. 103–120.
[38] KOSTROV B. V., *J. Appl. Math. Mech.*, **38** (1974) 551.
[39] ANDREWS D. J., *Bull. Seismol. Soc. Am.*, **63** (1973) 1375.
[40] LIU C., BIZZARRI A. and DAS S., *J. Geophys. Res.*, **119** (2014) doi: 10.1002/2014JB011187.
[41] BIZZARRI A., *Geophys. Res. Lett.*, **36** (2009) L11304, doi: 10.1029/2009GL037335.
[42] FAVREAU P., CAMPILLO M. and IONESCU I. R., *J. Geophys. Res.*, **107** (2002) .
[43] DALGUER L. A. and DAY S. M., *J. Geophys. Res.*, **112** (2007) B02302 doi: 10.1029/2006JB004467.
[44] LAPIDUS L. and PINDER G. R., *Numerical Solution of Partial Differential Equations in Science and Engineering* (Wiley-Interscience) 1999.
[45] DUNHAM E. M., *J. Geophys. Res.*, **112** (2007) B07302, doi: 10.1029/2006JB004717.
[46] HAMANO Y., *Eos Trans. AGU*, **55** (1974) 352.
[47] DAS S. and AKI K., *J. Geophys. Res.*, **82** (1977b) 5658.
[48] BURRIDGE R., CONN G. and FREUND L. B., *J. Geophys. Res.*, **84** (1979) 2210.
[49] BROBERG K. B., *Cracks and Fracture* (Academic Press, San Diego, CA) 1999.
[50] ANDREWS D. J., *Bull. Seismol. Soc. Am.*, **84** (1994) 1184.
[51] OLSEN K. B., MADARIAGA R. and ARCHULETA R. J., *Science*, **278** (1997) 834.
[52] KANEKO Y. and LAPUSTA N., *Tectonophysics*, **493** (2010) 272, doi: 10.1016/j.tecto.2010.06.015.
[53] DUNHAM E. M. and ARCHULETA R. J., *Geophys. Res. Lett.*, **32** (2005) L03302.
[54] BHAT H. S. *et al.*, *J. Geophys. Res.*, **112** (2007) B06301, doi: 10.1029/2006JB004425.
[55] DAS S., *A numerical study of rupture propagation and earthquake source mechanism* (PhD thesis, Massachusetts Institute of Technology, Mass.) 1976.
[56] LIU Y. and LAPUSTA N., *J. Mech. Phys. Solids*, **56** (2008) 25.
[57] LU X., LAPUSTA N. and ROSAKIS A. J., *Geopys. J. Int.*, **177** (2009) 717.
[58] ABRAHAM F. F. and GAO H., *Phys. Rev. Lett.*, **84** (2000) 3113.
[59] ROSAKIS A. J., *Adv. Phys.*, **51** (2002) 1189.
[60] GEUBELLE P. H. and KUBAIR D. V., *J. Mech. Phys. Solids*, **49** (2001) 571.
[61] FESTA G. and VILOTTE J. P., *Geophys. Res. Lett.*, **33** (2006) L15320, doi: 10.1029/2006GL026378.
[62] CHEN X.-F. and ZHANG H.-M., *Pure Appl. Geophys.*, **163** (2006) 267.
[63] ZHANG H.-M. and CHEN X.-F., *Geophys. J. Int.*, **167** (2006) 917.
[64] DAY S. M., GONZALEZ S. H., ANOOSHEHPOOR R. and BRUNE J. N., *Bull. Seismol. Soc. Am.*, **98** (2008) 1186.
[65] ZHANG Z., ZHANG W. and CHEN X.-F., *Geophys. J. Int.*, **199** (2014) 860.
[66] DUNHAM E. M. and ARCHULETA R. J., *Bull. Seismol. Soc. Am.*, **94** (2004) S256, doi: 10.1785/0120040616.

[67] BIZZARRI A., *Earthquake dynamics and fault interactions* (PhD thesis, Università degli Studi di Bologna) 2003.
[68] MELLO M. *et al.*, *Tectonophysics*, **493** (2010) 297.
[69] MELLO M. *et al.*, *Earth Plan. Sci. Lett.*, **387** (2014) 89.
[70] SONG S. G., BEROZA G. C. and SEGALL P., *Bull. Seismol. Soc. Am.*, **98** (2008) 823.
[71] ARCHULETA R. J., *J. Geophys. Res.*, **89** (1984) 4559.
[72] BOUCHON M. *et al.*, *Geophys. Res. Lett.*, **28** (2001) 2723.
[73] BOUCHON M. and VALLÉE M., *Science*, **301** (2003) 824.
[74] WANG D. and MORI J., *Bull Seismol. Soc. Am.*, **102** (2012) 301, doi: 10.1785/0120110034.
[75] WANG D. MORI J. and UCHIDE T., *Geophys. Res. Lett.*, **39** (2012) doi: 10.1029/2012GL053622.
[76] YUE H. *et al.*, *J. Geophys. Res.*, **118** (2013) 5903, doi: 10.1002/2013JB010594.

This page intentionally left blank

Proceedings of the International School of Physics "Enrico Fermi"
Course 202 "Mechanics of Earthquake Faulting", edited by A. Bizzarri, S. Das and A. Petri
(IOS, Amsterdam; SIF, Bologna) 2019
DOI 10.3254/978-1-61499-979-9-33

Unusual large earthquakes on oceanic transform faults

Shamita Das(*)

Department of Earth Sciences, University of Oxford
South Parks Road, Oxford, OX1 3AN, UK

Summary. — According to the classical theory of plate tectonics, oceanic transform faults do not usually have "large" or "great" earthquakes. In this paper, we discuss several transform fault earthquakes, some now moved into unusual tectonic settings due to plate motion, which did have earthquakes lying in the magnitude range $7.8 \leq Mw \leq 8.1$. The 2004 M_w8.1 earthquake occurred on a fossil fracture zone in the Tasman Sea. The 2000 M_w7.8 earthquake occurred in the Wharton Basin and ruptured two conjugate faults simultaneously. The largest known strike-slip earthquake in 2012 (M_w8.6) occurred off the coast of Sumatra and ruptured cross-cutting faults. An oceanic strike-slip earthquake in 1998 with M_w8.0 occurred on the Antarctic plate, but on a fault parallel to the ridge and nearly normal to the transform faults that is, it occurred on the ridge fabric! All these earthquakes together with the 2012 twin earthquakes (M_w8.6 and 8.2) in the Wharton Basin, the 1987–1992 ($6.8 \leq M_w \leq 7.8$) Gulf of Alaska sequence and the M_w7.9 2018 Gulf of Alaska earthquakes, show that the oceanic lithosphere is breaking up along the ridge-transform conjugate fault systems under tectonic stresses.

(*) E-mail: das@earth.ox.ac.uk

1. – Introduction

One of the key pieces of evidence that supported the theory of plate tectonics in the 1960s, was the explanation of how plates move along mid-oceanic transform faults, and was first given by Wilson in 1965 [1]. Figure 1(a) shows the six possible types of dextral (right-lateral) transform faults that he discussed. Six sinistral (left-lateral) transform faults, which are mirror images of the ones shown, also exist. Figure 1(b) shows the appearance of the right-lateral systems of fig. 1(a), after a period of growth. Note that length of the active transform fault is constant in some cases, growing in other cases and decreasing in one case. Some of these will be seen for the earthquakes discussed in detail later in this paper.

In the ridge-ridge configuration (fig. 1(a)), oceanic transform faults are bounded at both ends by spreading ridges, with the portion of the previously active transform fault beyond the ridges, called "fracture zones" being practically aseismic. In regions where the spreading ridge is no longer active, the fracture zones are termed "fossil fracture zones".

Explanation of the focal mechanisms along the ridge and transform faults along mid-ocean ridges was first given by Sykes in 1967 [2], and a schematic is shown in fig. 2. Very occasionally earthquakes do occur on the fracture zone, and have focal mechanisms with reversed polarity from the nearby oceanic transform fault [3]. This very useful fact can be used to identify such earthquakes. Figure 2 also shows that the situation is even more complex with other kinds of mechanisms occuring at the "inner corners" (fig. 2).

That fracture zones are essentially aseismic can be seen by examining earthquakes large enough to have a centroid moment-tensor (CMT, which can be accessed at `http://www.globalcmt.org/CMTsearch.html`) solution. By counting such earthquakes located within $\sim 1000\,\mathrm{km}$ of, as an example, the Mid-Atlantic Ridge between the Equator and $70\,^{\circ}\mathrm{N}$ (just North of Iceland), for the 34-year period from 1976–2009 inclusive, Robinson [4] showed that of the 1002 CMT solutions reported, 266 are strike-slip. Of these 266, only 8 are unambiguously identified as having occurred on the fracture zone by virtue of having focal mechanisms with reversed polarity relative to the nearest transform fault. These rare fracture zone earthquakes had negligible seismic moment compared to the strike-slip earthquakes on the nearby transform faults.

In this paper, I will discuss several unusual cases of large or great earthquakes on oceanic transform faults, including a $M_w 8.1$ on a fossil fracture zone and a $M_w 8.0$ pure strike-slip earthquake, which is nearly normal to the existing oceanic transform faults (*i.e.*, fractures along the pre-existing ridge fabric) as well as several large mid-oceanic earthquakes with simultaneous conjugate faulting. Tables I, II and III list of all earthquakes discussed in this paper.

2. – Pre-existing zones of weakness on the ocean floor

Earthquakes can occur on either of the nodal planes of an earthquake. Stress component τ_{xy} in elastic media implies that either the plane x or the plane y, or both, could

(a)

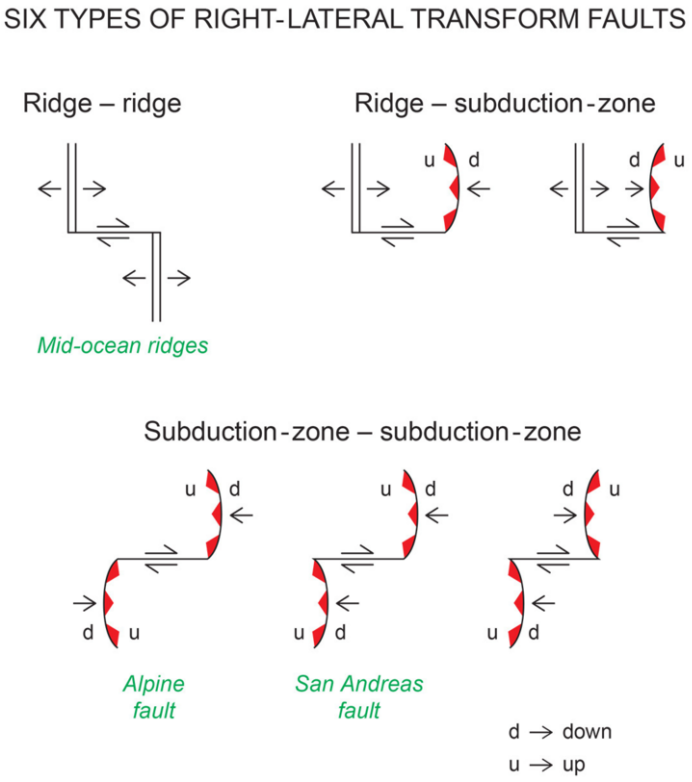

(b)

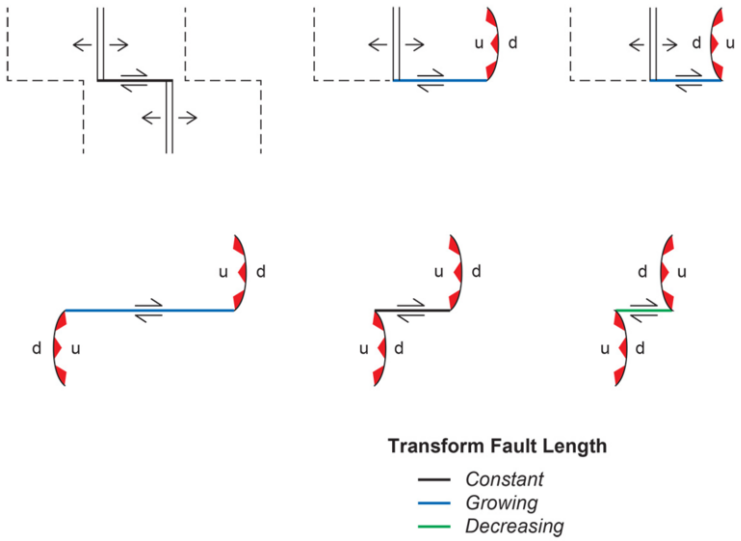

Fig. 1. – (a) Illustration of the six kinds of right-lateral transform faults. (b) The same as (a) but after some period of growth.

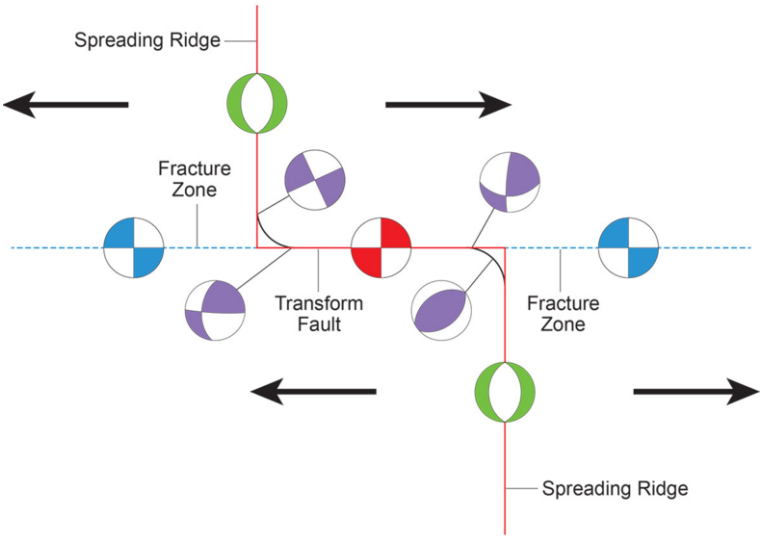

Fig. 2. – Schematic representation of the classical picture at mid-ocean (spreading) ridges, showing the focal mechanisms. Black arrows indicate relative plate motions and red lines the active plate boundary. The red focal mechanism shows the typical expected on the (active) transform fault, and the green ones the typical ones on the spreading ridges. The dashed blue line are the continuations of the transform fault which are usually visible in bathymetric surveys of the seafloor. The blue focal mechanisms are the ones for the rare earthquakes on these and have strike-slip mechanism reverse to that on the active transform. Both strike-slip and thrust earthquakes are seen in the inner corners and are in purple.

rupture. On land this is uncommon, though two such examples are known (see table I). This is because generally though either one of the nodal planes x or y can rupture due to tectonic stress, usually one of them is much weaker than the other, for example due to there being a pre-existing plane of weakness. The earthquake therefore usually only chooses to rupture the weaker plane. This is generally the normal situation on land, though aftershocks often cluster on the conjugate plane [5]. Table I gives two counterexamples on land in which both nodal planes ruptured, one simultaneously and the other over some period. In some cases, the two conjugate planes rupture in a single earthquake; in some cases, one nodal plane ruptures and a few hours or days later the other

TABLE I. – *Earthquakes with conjugate faulting on land.*

	Date	Location	Magnitude	Fault type	Faulting mode
1)	March 7, 1927	Tango, Japan	$M_w 8.0$	Strike-slip	Simultaneous
2)	November 23, 1987	Superstition Hills, Ca.	$M_s 6.2$	Strike slip	First earthquake
	November 24, 1987	″	$M_s 6.6$		≈ 11 h later

TABLE II. – *Earthquakes with conjugate faulting in oceanic environments.*

	Date	Location	M_w	Fault type	Faulting mode
1)	May 23, 1989	Macquarie Ridge	8.2	subd.-subd.	conjugate fault reactivated by aftershocks
2)	1987–1992	Gulf of Alaska	7.2, 7.8, 7.7, 6.8	ridge-transform	conjugate faulting over the period
3)	June 18, 2000	Wharton Basin	7.8	transform-ridge	Simultaneous rupture on transform fault and ridge fabric
4)	April 11, 2012	″	8.6, 8.2	transform-ridge fabric	″
5)	Jan. 23, 2018	Gulf of Alaska	7.9	transform-ridge	conjugate fault reactivated by aftershocks

ruptures. In some cases, the main earthquake activates high aftershock concentration on the conjugate fault. An example of the plane of slip in some of these off-fault aftershocks being in a direction normal to the main shock fault was given by Yamashina in 1980 [6], based on field observations.

The 1927 Tango, Japan earthquake (table I) was known to have initiated on the Gomura fault and ruptured it and its perpendicular Yamada fault near its eastern end simultaneously. Of the rupture on the conjugate fault, Richter ([7], p. 576) wrote that "either it was initiated by the arrival of the fracture progressing along the Gomura fault, or it was triggered by the shaking from the elastic waves arriving a little sooner. In fact, there are reports to the effect that the Yamada scarp was seen forming after the first violent shaking in its vicinity." A M_s6.2 earthquake occurred on the Elmore Ranch fault in the 1987 Superstition Hills, Ca. earthquake sequence (table II), and was followed about 11 hours later by a M_s6.6 earthquake on the Superstition Hills main fault. These two strike-slip faults are nearly orthogonal to each other [8]. Both these earthquakes were

TABLE III. – *Great under-water earthquakes in unusual tectonic environments.*

	Date	Location	M_w	Fault type	Faulting mode
1)	March 25, 1998	Antarctic Plate	8.0	Pure strike-slip	Cuts across pre-existing ridge fabric
2)	December 23, 2004	Tasman Sea	8.1	″	Great earthquake on a fossil fracture zone

on land, and hence had the advantage that their strikes were clearly seen from either the fault trace (in Tango) or by the fault trace and the concentration of aftershocks on the conjugate fault. The rest of the earthquakes discussed below were all under water.

Along mid-oceanic ridge-transform regions, there are two, nearly normal to one another, planes of weakness. These are the ridge itself together with the ridge fabric and the transform fault. (The ridge fabric is the location of where the ridge was in the past and its trace is a weak zone.) Matthews *et al.* [9] give a comprehensive discussion of the tectonic fabric in oceans. So, mechanically an earthquake can rupture either one or both planes in such tectonic settings. Examples of earthquakes known to have ruptured on conjugate planes are given in table II.

3. – Re-activation of old transform faults: earthquakes with conjugate faulting in oceanic environments

It is now known that old transform faults and even fossil fracture zones can be reactivated by nearby large earthquakes, due to stress increase after a major earthquake. The reactivation is generally been found to produce earthquakes of smaller magnitudes ($M_w < 6$). Some of the earthquakes discussed below are examples in which the earthquakes due to the reactivation are larger ones.

3˙1. *The 1989 great Macquarie Ridge earthquake reactivated a dormant conjugate fault.* – At the time of its occurrence, the May 23, 1989 Macquarie Ridge earthquake (M_w8.2) was the largest seismic event to have occurred globally for about twelve years and the largest on the India/Australia-Pacific plate boundary South of New Zealand in more than seventy years. Using arrival times at worldwide stations compiled by the International Seismological Centre (ISC), Das [10] relocated all earthquakes in the vicinity of the main shock for which at least seven stations reported P-wave readings in the period between January 1, 1964 and December 31, 1989, using the method of joint hypocenter determination JHD89 [11, 12]. Figure 3(a) shows the aftershocks with their CMT solutions superimposed on the bathymetry.

The aftershock map shows that there are two linear zones along which the aftershocks are concentrated. One is a 220 km segment of the India/Australia-Pacific plate boundary on which the main shock occurred. The other is a linear feature to its West, trending in the Northwest-Southeast direction, nearly 175 km long and lying close to the 4000 m bathymetric contour. The bathymetric data shows that the seafloor to the West of this feature is deeper and relatively smooth. In the area to the East and up to the Macquarie Ridge, the seafloor is shallower and rougher, suggesting a discontinuity in its nature (*e.g.*, age) of the seafloor on the two sides of the 4000 m bathymetric contour. The relocated background seismicity [10] for the 25-year period prior to the earthquake showed that this linear feature was not active prior to the earthquake, the first aftershocks appearing on it about $2\frac{1}{2}$ hours after the main shock.

It is interesting to note that for an earthquake of its size, the Macquarie Ridge earthquake had unusually few and unusually small aftershocks —a property I later noted for

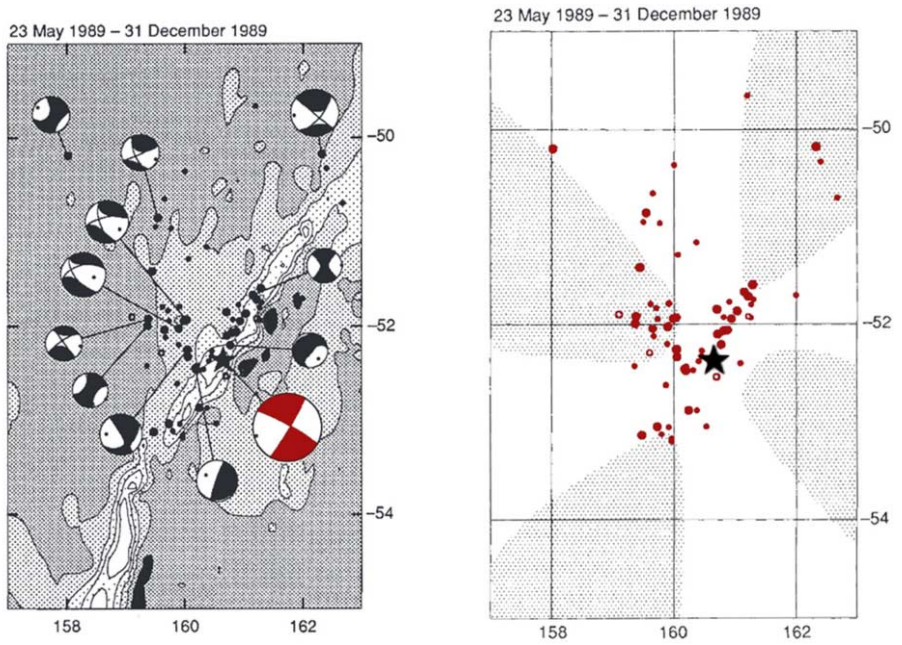

Fig. 3. – (a) $\approx$ 7 months of aftershocks with their CMT solutions for the 1989 Macquarie Ridge earthquake, superimposed on the bathymetry. (b) The shaded area indicates the zone of increased shear stress, both at the ends of the fault as well as in the off-fault regions, due to the occurrence of the main shock.

many strike-slip earthquakes. In the seven-month period following the earthquake, 79 aftershocks were reported with 44 occurring within the first 7 days and only 17 in the 5 months since August 1, 1989. Twenty-nine of the aftershocks were associated with the linear feature to the West of the plate boundary. Moreover, the largest aftershock ($m_b = 5.6$) occurred about 38 hours later, not on the main fault plane but on this second feature. Only 12 events were large enough for CMT solutions to be reliably obtained and of these, three of the smallest were on the main fault.

The CMT mechanisms show that the main fault plane rupture was pure right lateral strike-slip, but for the secondary feature, assuming that the fault plane is the nodal plane with strike similar to the trend defined by the aftershocks, the motion is seen to be primarily left-lateral strike-slip. The magnetic anomaly data for this area [10] shows that there is a left-lateral offset of magnetic anomalies 12, 13 and 18 on the two sides of a Northwest-Southeast trending feature at this place. The trend of the seismically defined feature follows the trend of a fracture zone inferred from this magnetic anomaly data and is seen to be parallel to other fracture zones to its West. This fracture lies largely within the zone of increased off-fault shear stress that is expected to the West of the ridge for this earthquake (fig. 3(b)).

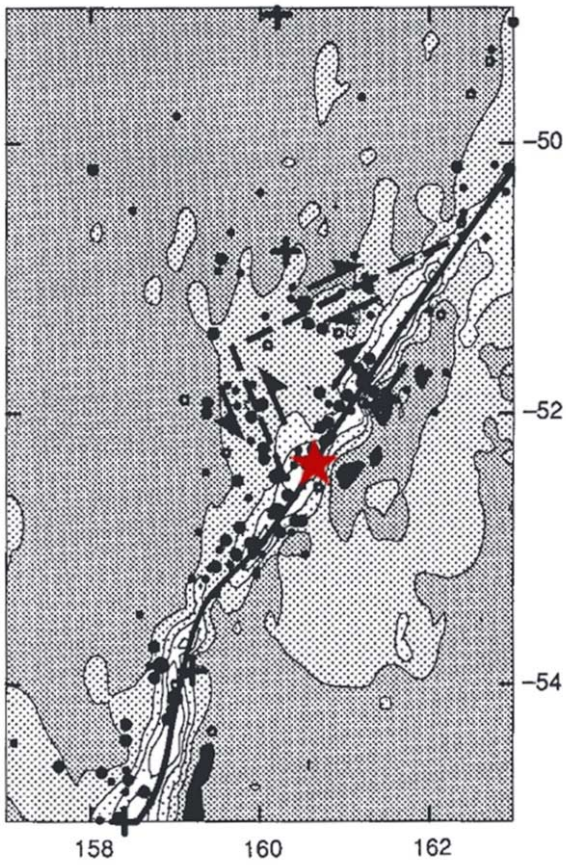

Fig. 4. – Tectonic interpretation of the earthquake mechanisms for the 1989 Macquarie Ridge earthquake.

Figure 4 shows the tectonic interpretation of the earthquake mechanisms combined with the locations of all known events in the area. It suggests that the triangular area between the plate boundary, the reactivated fracture and a fault to the North on which an earthquake of magnitude ($M_s = 7.7$) occurred in 1982 is being "squeezed" towards the North and West. This triangular feature is also clearly seen in the free air gravity anomaly map.

3˙2. *The 1987–1992 and the January 23, 2018 Gulf of Alaska earthquake sequences.* – At the time of its occurrence, the 1987–1992 Gulf of Alaska earthquakes provided a rare opportunity for a detailed study of three oceanic intra-plate earthquakes of $M_w >$ 7.0. Figure 5 shows the tectonic setting of these earthquakes, where the Pacific plate is subducting under Alaska. The four main earthquakes, all pure strike-slip occurred on November 17, 1987 (M_w7.2), November 30, 1987 (M_w7.8), March 6, 1988 (M_w7.7)

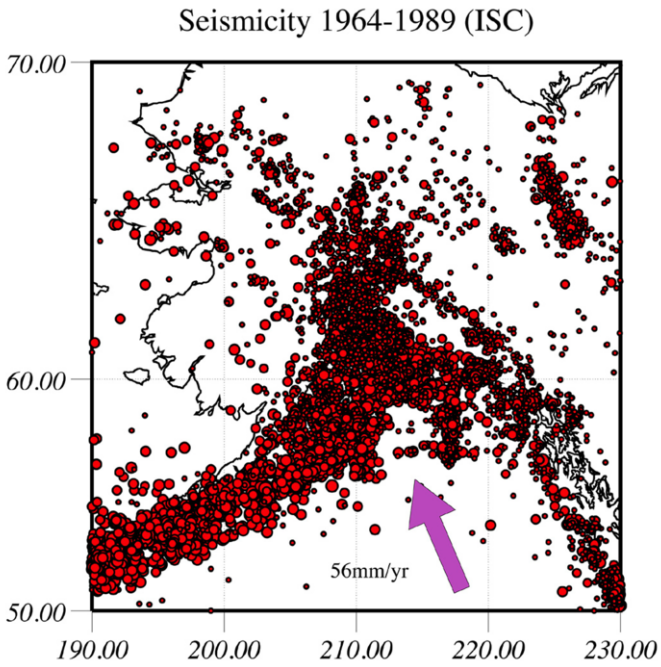

Fig. 5. – Tectonic setting of the Gulf of Alaska earthquakes. The arrow shows the direction in which the Pacific plate is subducting under Alaska.

and August 7, 1992 (M_w6.8). Pegler and Das [13] examined the seismicity from 1964 to the day before the earthquake and showed that there were no known earthquakes in the region for this period. The earthquakes and their aftershocks were relocated using the JHD method and fig. 6 shows these relocated epicenters together with the CMT solutions for the first three large earthquakes. For the first earthquake, the plane of faulting is clearly the E-W plane, as seen from the aftershocks, as well from the analysis of P and SH waves [13]. The second earthquake, the largest of the sequence occurred at the easternmost end of the fault of the first one and the aftershocks and the body wave analysis showed that the main plane of faulting was the N-S plane. The plane of rupture for the third one was more difficult to see clearly from the aftershock pattern. The aftershocks of the second were still occurring and the aftershocks gave a cross-like pattern. Analysis of the P and SH waves for the third earthquake, the second largest of the sequence, showed that the N-S plane was indeed the plane of rupture. Temporal development of the aftershock pattern following this earthquake is shown in fig. 7, and re-inforces this conclusion. The aftershocks in the E-W direction are interpreted as "off-fault" aftershocks. Magnetic anomaly and bathymetric data were used to conclude that the North-South portion sequence lies along magnetic anomaly 13, and the East-West fracture and aftershock concentrations along related fossil fracture zones —that is, pre-exisiting zones of weakness.

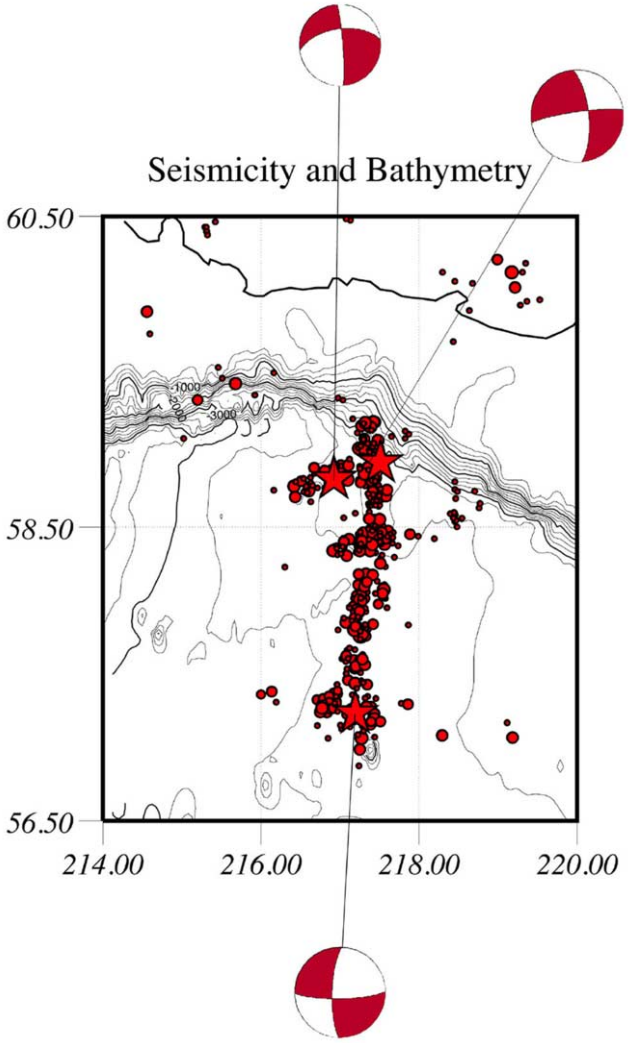

Fig. 6. – Relocated epicenters together with the CMT solutions for the first three large earthquakes [13].

The M_w7.9 in January 23, 2018 occurred to the West of the 1987–1992 sequence. The aftershock map from the USGS (`earthquake.usgs.gov/earthquakes/eventpage/us2000cmy3`) shows a cross-hatched pattern similar to that of the 1987–1992 sequence.

3˙3. *The M_w7.8 18 June 2000 Wharton Basin earthquake: simultaneous rupture of conjugate faults in an oceanic setting*. – This was the first example of such an earthquake. Figure 8 shows the tectonic setting, the known seismicity from 1904 till the day of this earthquake, with the main shock CMT in red. Analysis of broadband teleseis-

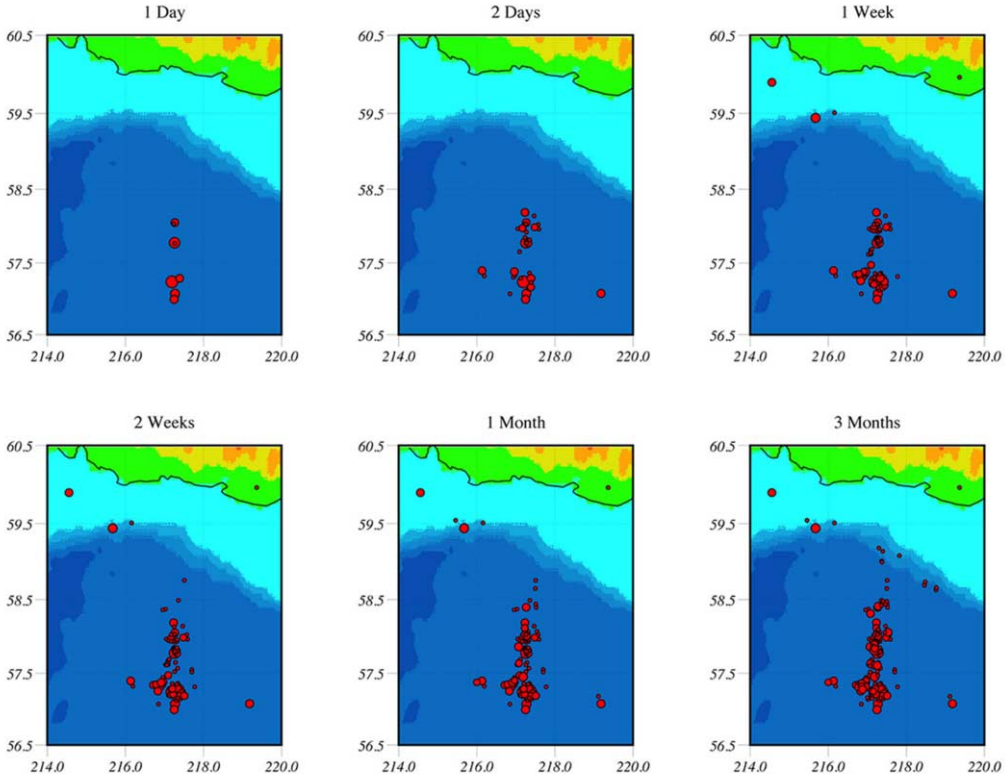

Fig. 7. – Temporal development of the aftershock pattern following the March 6, 1988 (M_w7.7) earthquake, reinforcing the conclusion that the plane of faulting is the N-S nodal plane.

mic data and relocated seismicity was used by Robinson *et al.* [14] to show that this intraplate earthquake, in the region of diffuse deformation separating the Indian and Australian plates, consisted of two subevents that simultaneously ruptured two near-conjugate planes (fig. 9). This mode of rupture accommodates shortening by a mechanism different from that previously known elsewhere in the region. The larger subevent occurred on a fossil fracture zone, with a relatively high-stress drop of about 20 megapascals, showing that large stresses can accumulate in regions of distributed deformation.

3˙4. *The January 11 and 12, 2012 twin Sumatra earthquake (M_w8.6, 8.2).* – Singh *et al.* ([15], their fig. 1) summarizes the main earthquakes in this region. Meng *et al.* [16] interpreted the 2012 twin earthquakes as "earthquakes in a maze", with simulataneous rupture on multiple conjugate planes. Satriano *et al.* [17] studied the same earthquake using essentially similar data but a different method of analysis and concluded that the two main episodes of energy release in this earthquake occurred on two parallel NNE striking planes. Marine exploration in the Wharton Basin [15] does show a system of

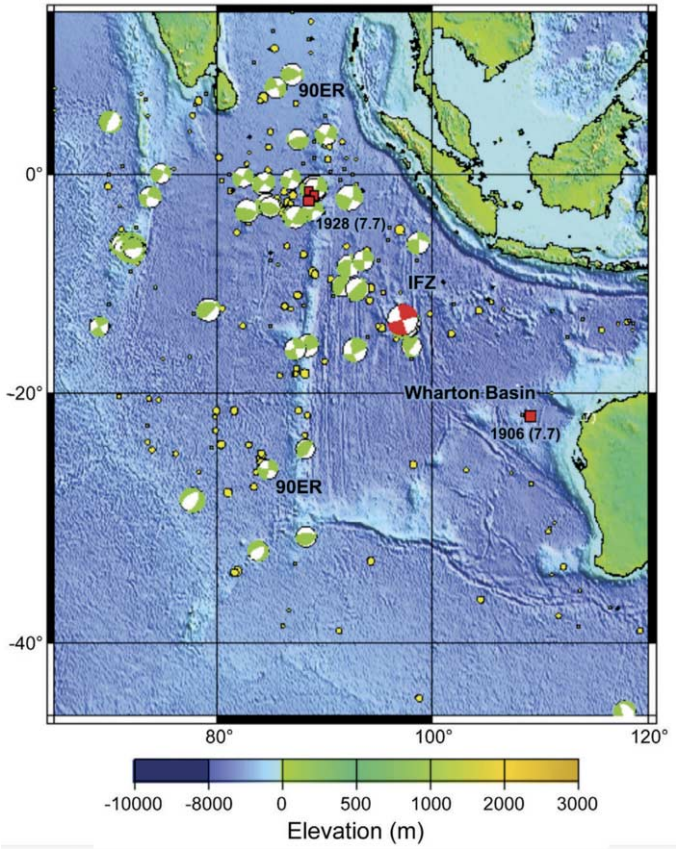

Fig. 8. – Tectonic setting and known seismicity from 1904 till the occurrence of the 2000 Wharton Basin earthquake, superimposed on the relief map of the region. The CMT of the main shock of the earthquake, obtained by [14] is in red, with other CMTs in green. The locations of two historical earthquakes in the region (in 1906 and 1928) are shown by red squares. Two foreshocks of the 1928 are also plotted as smaller red squares.

conjugate faults in the region, supporting both the results of Robinson *et al.* [4] for the 2000 Wharton Basin earthquake and of Meng *et al.* [16] for the twin Sumatra earthquakes.

The above cases suggest that the subducting oceanic crust is breaking up along nearly conjugate fault planes, which are pre-existing zones of weakness.

4. – A great earthquake on a fossil fracture zone: the 2004 Tasman Sea earthquake

Reactivation of fossil fracture zones by nearby large earthquakes had generally been found to produce earthquakes of smaller magnitudes ($M_w < 6$). So the $M_w 8.0$ earthquake in 2004 in the South Tasman Sea, well away from the Australia-Pacific plate boundary

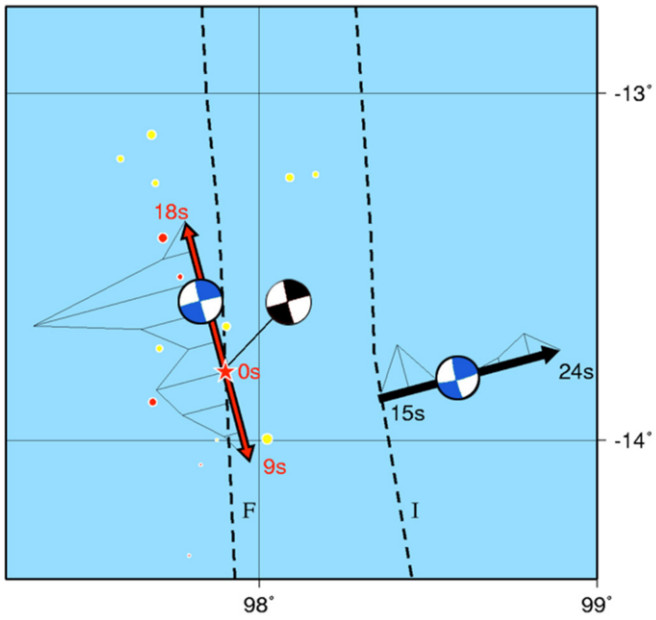

Fig. 9. – Schematic rupture history of the 2000 Wharton Basin earthquake. The red star is the epicenter where rupture initiated. It then propagated for 9 s. to the South and 18 s to the North before starting to rupture the E-W plane with a delay of 15 s.

was very surprising. It is also the 5th largest strike-slip earthquake worldwide since 1900 (see table 1 of Robinson [4], to which 2012 M_w8.6 Sumatra earthquake [16], the largest known strike-slip earthquake, now needs to be appended at the top of that table). The plate tectonic history of this region is extremely complex [18, 19]. Figure 10 gives the current tectonic setting of the earthquake, superposed on a gravity map of the region and shows how the originally straight "fossil fracture zones" have now been distorted into an arcuate shape. This indicates that large intraplate deformation is now occurring in the region. This earthquake was studied in detail by Robinson [4], including relocation of prior seismicity and aftershocks, and inversion of P- and SH-body wave data to analyse the rupture process.

The relocated aftershocks form an approximately linear feature striking $\sim$ 170° (fig. 11). The aftershocks on December 24, 2004 (04/12/24) with M_w4.9 and on January 3, 2005 (05/01/03) with M_w6.0 (the largest in the sequence) respectively lie near the northernmost and southernmost extent of the aftershock zone (fig. 12). These two aftershocks are $\sim$ 150 km apart, the main shock epicenter being located equidistant between them. Only 3 aftershocks large enough to have CMT solutions occurred in the 6-month period after the main shock, this small number being a property consistent with other recent large strike-slip earthquakes in the region.

Broad-band P- and SH-wave data were inverted [4] to obtain the full time history of the earthquake rupture process. Due to the fact that the rupture occurred on a curved

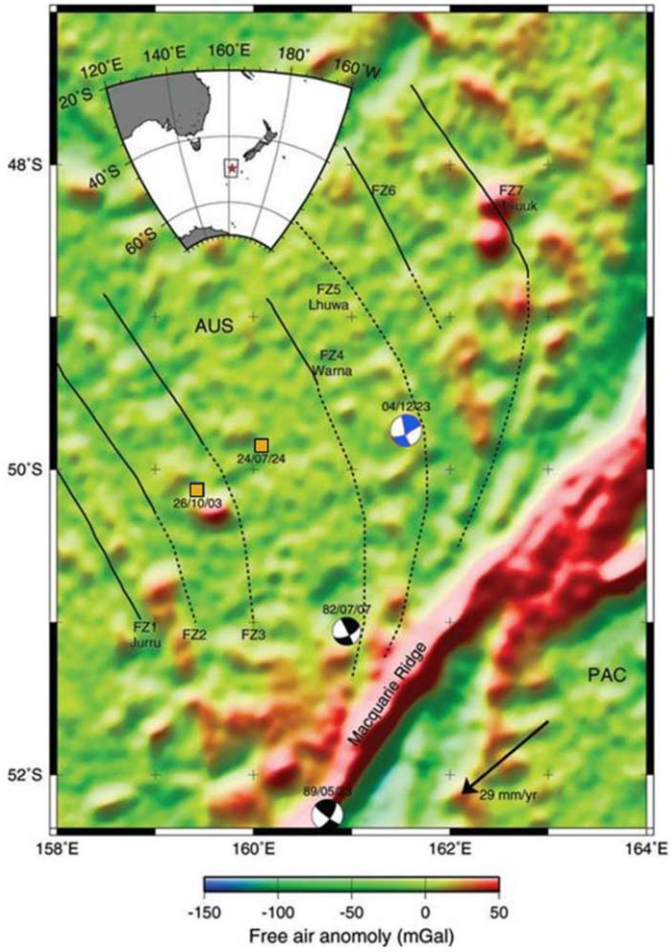

Fig. 10. – Tectonic setting of the 2004 Tasman Sea earthquake, superposed on a gravity map of the region. Note how the originally straight "fossil fracture zones" have now been distorted due to tectonic motions.

fault, more than 7500 inversions in total, using both SH-wave data by itself as well as P- and SH-wave data simultaneously were performed, to best estimate the rupture planes, the rupture length and the rupture width. The preferred solution, tested for robustness, has two faults, with a strike of 160°, dip of 86°, and rake of 5° on the northern fault, and a strike of 178°, dip of 54°, and rake of 65° on the southern fault. The southern fault with its marked change in dip and rake relative to the northern one shows that there is a change in the source mechanism to the North and to the South of the epicenter. The rupture process (fig. 12) shows that the main slip was confined to ~ 70 km North and South of the epicenter, in agreement with the aftershock data, most of the total moment

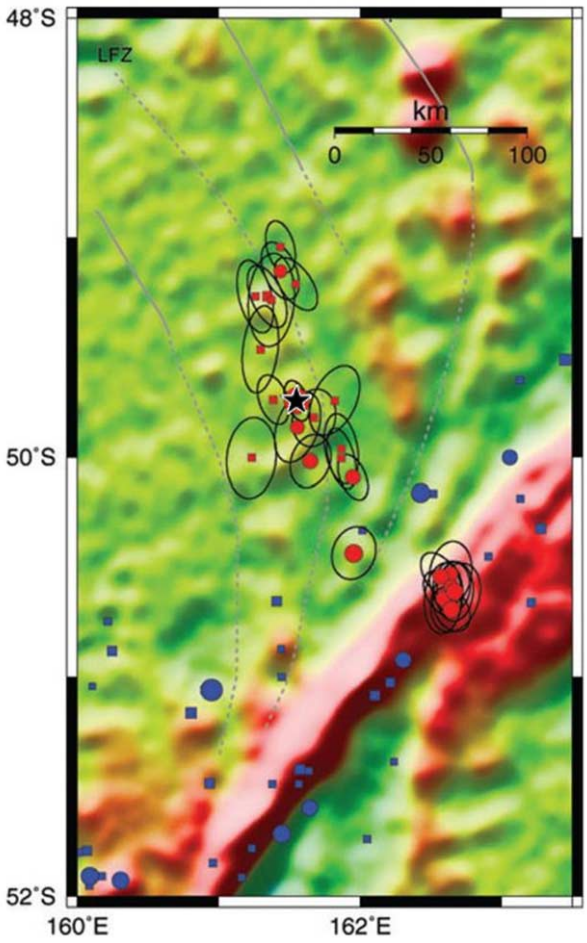

Fig. 11. – Relocated aftershocks of the 2004 Tasman Sea earthquake. Color key same as in fig. 10.

occurring on the northern section. The rupture started slowly and propagated towards the North at an average speed of about 1.7 km/s ($\sim 40\%$ of the local shear wave speed of 3.9 km/s in the crust). Rupture propagation to the South was much faster, the average rupture speed nearly reaching the local shear wave speed. A first-motion solution was performed to investigate the very early portion of the rupture and showed that rupture initiated on a fault with strike and dip very close to that of the northern fault. The source time function for the northern and southern faults are essentially triangular in shape [4]. The average stress drop on the northern section, using a fault length (L) of 100 km and permitting slip down to a depth of 15 km is about 30 MPa. On the southern 50 km section, the stress drop is about 10 MPa. The overall average slip is 9.5 m and, using an

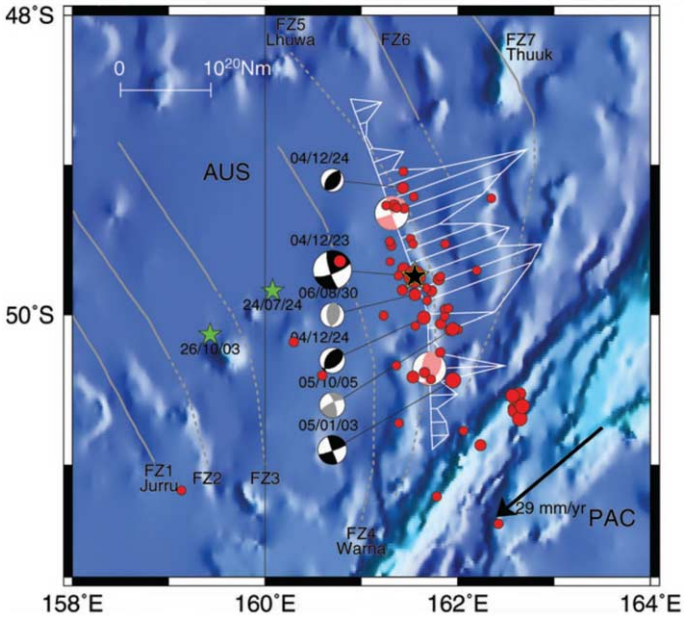

Fig. 12. – Rupture process of the 2004 Tasman Sea earthquakes, superimposed on the bathymetry taken from the British Oceanographic Data Centre (GEBCO). See [4] for details.

L of 150 km with slip allowed down to 15 km depth, the stress drop is 22 MPa. If slip is constrained to a depth of 12 km, the values for these stress drops would approximately double.

The width of the fault indicates that slip penetrated well below the Moho, located around 7.5 km depth here. In some of the many inversions that we carried out, we restricted the fault slip to occur only up to the local Moho depth, but this required unrealistically high slip and stress drop. In fact, simply using the seismic moment, a fault length of 150 km and a fault width of 7.5 km would require an average slip on the fault of about 30 m. In this region, the 400° isotherm is located at about 18 km depth. Thus, though slip occurs below the Moho, it is still confined to the brittle part of the asthenosphere. Examination of the rise times in grid cells above and below the Moho show that they are comparable.

The 2004 great South Tasman Sea earthquake shows that dead fracture zones can be reactivated in regions of very complex tectonic history with large internal deformation of the plate, to produce stresses required to generate great earthquakes. This might imply that similar behavior might be expected on land where old zones of weakness may be reactivated to produce great earthquakes. The older age of continental compared with oceanic crust implies that they should contain more old zones of weakness and consequently may be more liable to such behavior.

4·1. *Slip below the Moho during earthquakes.* – Even though slip below the Moho during earthquakes has been predicted in theoretical models [20, 21], there is only one, somewhat tenuous, example of this. Analysis of long-period surface waves had indicated that the 1989 Macquarie Ridge earthquake may have ruptured into the mantle [22], but the body wave data did not require such behavior [23] and hence this was not universally accepted. Consequently, the 2004 South Tasman Sea earthquake is the first where sub-Moho fault displacement best fits the body wave data. The 1998 Antarctic plate earthquake [24] (listed in table III, and discussed in the next section) in a nearby region, but located on a different plate, did not require slip below the Moho to fit the data. The 2000 Wharton Basin earthquake, the only other known earthquake to occur on an old fracture zone, also did not require slip below the Moho to fit the data [14].

Table 1 of Robinson [4] shows that with the exception of the two Mongolian earthquakes in the early 1900s, all the other strike-slip earthquakes with magnitude > 8 occurred underwater, and in the same part of the world. It is even more interesting that the only other earthquake with possible slip below the Moho is located only 250 km away from the one studied here.

The 2004 great South Tasman Sea earthquake shows that dead fracture zones can be reactivated in regions of very complex tectonic history with large internal deformation of the plate, not only to produce small earthquakes, but can generate great ones as well. This might imply that similar behavior might be expected on land where old zones of weakness may be reactivated to produce great earthquakes. The older age of continental compared with oceanic crust implies that they should contain more old zones of weakness and consequently may be more liable to such behavior.

5. – A great earthquake with the main fault plane normal to regional transform faults: the 1998 M_w8.1 Antarctic plate earthquake

At the time of its occurrence, this was the largest crustal submarine intraplate earthquake ever recorded, and the largest strike-slip earthquake as well as the fifth largest of any type worldwide since 1977. It has now been overtaken by the 2012 twin Sumatra earthquakes discussed above. It occurred in a region where no seismicity has previously been recorded, and was the largest known on the entire Antarctic plate (fig. 13). Its occurrence is still puzzling as its rupture zone does not coincide with any known feature on the ocean floor, all of which are nearly N-S trending in this region. Even more puzzling, the rupture is nearly E-W trending and actually cuts across these features at right angles, that is, close to the ridge fabric. Henry *et al.* [24] showed that the earthquake consisted of two subevents (fig. 14). The first subevent is a simple, primarily westward propagating ~ 140 km rupture, of ~ 45 s duration, with $M_w = 8.0$, and a stress drop of ~ 24 MPa, this stress drop being an order of magnitude larger than most earthquakes of this size. The earthquake then jumped over a 70–100 km unbroken region (perhaps a barrier) and, after a time delay of ~ 40 s, propagated for another 60 km, resulting in

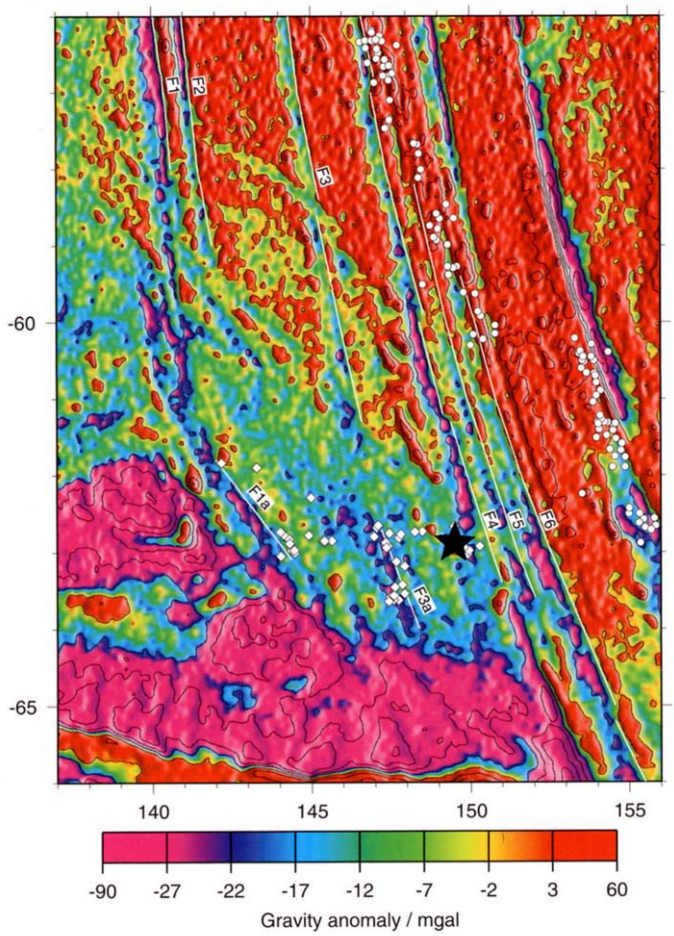

Fig. 13. – Tectonic setting of the 1998 Antarctic Plate earthquake, superimposed on the gravity anomaly. The black star shows the epicenter, and the white diamonds the aftershocks. Transform faults F1, F1a, F2, F3, F3a, F4–6 are shown in white, and the background seismicity as white dots.

a second subevent with $M_w = 7.6$–7.8, also having an unusually large stress drop. Each subevent propagated at an average speed just below the shear wave speed of the medium. This was an example of dynamic stress triggering over the largest separation distance ever found [24].

There were relatively few aftershocks on the main fault plane, only two being in the magnitude range $5 < M_w < 6$, and large enough to have CMT solutions. No significant aftershocks occurred within the region of greatest slip, nor within the unbroken region separating the two subevents of the earthquake. Figure 14 shows that the aftershock pattern, including all the significant clusters, was firmly established in the first 24-hour

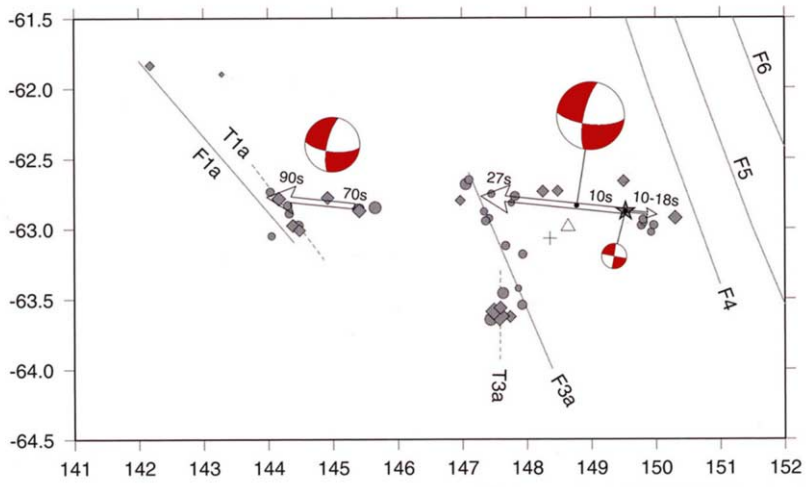

Fig. 14. – Schematic representation of the main features of the rupture history of the 1998 Antarctic Plate earthquake. The main shock epicenter is the star, and relocated aftershock epicenters [24], having semi-major axis of the 90% confidence ellipse of < 20 km, are shown as diamonds. Available International Seismological Centre (ISC) epicenters for the period January 1, 1964 to July 31, 1997 are shown as circles. Arrows show the location and directivity of the two subevents, labelled at each end with the start and end times of the two rupture segments. Focal mechanisms of the two events are shown. The cross represents the centroid location of the moment tensor, obtained in [24], the open triangle that obtained in the CMT solution. Linear gravity features (F1a, T1a, T3a, F3a, F4–6) discussed in [24] are shown as solid lines.

period following the main shock. Henry *et al.* [24] showed that the first subevent was terminated at both ends by pre-existing fossil fracture zones F3a and F4, and the second one terminated on F1a. The slip has a rapid fall-off at both ends of the first, and larger, subearthquake. By our criterion this means that we have sharp stress concentration at both these ends. Aftershock clusters did occur at both these ends, confirming this identification. We conclude that for this earthquake, aftershocks occurred where there is a sharp gradient in the slip, that is, most aftershocks occurred at the edges of regions of high slip, mainly at the ends.

6. – Conclusions

In conclusion, the occurrence of several large earthquakes in oceans shows that the oceanic crust is crumbling by fracture of nearly normal conjugate fault planes —the old planes of weakness related to the ridge fabric and transform faults, even in regions where the transform fault is no longer active.

REFERENCES

[1] WILSON J. T., *Nature*, **207** (1965) 343.
[2] SYKES L. R., *J. Geophys. Res.*, **72** (1967) 2131.
[3] ENGELN J. F., WIENS D. A. and STEIN S., *J. Geophys. Res.*, **91** (1986) 548.
[4] ROBINSON D. P., *Geophys. J. Int.*, **186** (2011) 1121.
[5] DAS S. and SCHOLZ C. H., *Bull. Seismol. Soc. Am.*, **71** (1981) 1669.
[6] YAMASHINA K., *Eos Trans. Am. Geophys. Union.*, **61** (1980) 292.
[7] RICHTER C. F., *Elementary Seismology* (W. H. Freeman and Co., San Francisco) 1958.
[8] HUDNUT K. W., SEEBER L. and PACHECO J., *Geophys. Res. Lett.*, **16** (1989) 199.
[9] MATTHEWS K. J., MÜLLER R. D., WESSEL P. and WHITTAKER J. M., *J. Geophys. Res.*, **116** (2011) B12109.
[10] DAS S., *Nature*, **357** (1992) 150.
[11] DEWEY J. W., *Seismic studies with the method of joint hypocenter determination*, PhD Thesis, University of California, Berkeley (1971).
[12] DEWEY J. W., *Relocation of instrumentally recorded pre-1974 earthquakes in the South Carolina region*, in *Studies Related to the Charleston, South Carolina, Earthquake of 1886–Tectonics and Seismicity, U. S. Geol. Surv. Prof. Pap. 1313*, Q1-Q9 (1983).
[13] PEGLER G. and DAS S., *Tectonophysics*, **257** (1996) 111.
[14] ROBINSON D. P., HENRY C., DAS S. and WOODHOUSE J. H., *Science*, **292** (2001) 1145.
[15] SINGH S. C. *et al.*, *Sci. Adv.*, **3** (2017) e1601689.
[16] MENG L. *et al.*, *Science*, **337** (2013) 724.
[17] SATRIANO C., KIRALY E., BERNARD P. and VILOTTE J.-P., *Geophys. Res. Lett.*, **39** (2012) L15302.
[18] WEISSEL J. K., HAYES D. E. and HERRON E. M., *Mar. Geol.*, **25** (1977) 231.
[19] CANDE S. C. and STOCK J. M., *Geophys. J. Int.*, **157** (2004) 399.
[20] DAS S., *Bull. Seismol. Soc. Am.*, **72** (1982) 1911.
[21] SHAW B. E. and WESNOUSKY S. G., *Bull. Seismol. Soc. Am.*, **98** (2008) 1633.
[22] ANDERSON H. J. and ZHANG J., *J. Geophys. Res.*, **96** (1991) 19853.
[23] DAS S., *Geophys. J. Int.*, **115** (1993) 778.
[24] HENRY C., DAS S. and WOODHOUSE J. H., *J. Geophys. Res.*, **105** (2000) 16097.

Proceedings of the International School of Physics "Enrico Fermi"
Course 202 "Mechanics of Earthquake Faulting", edited by A. Bizzarri, S. Das and A. Petri
(IOS, Amsterdam; SIF, Bologna) 2019
DOI 10.3254/978-1-61499-979-9-53

The evolution of fault slip rate prior to earthquake: The role of slow- and fast-slip modes

Aitaro Kato

Earthquake Research Institute, the University of Tokyo
113-0032, Yayoi 1-1-1, Bunkyo-ku, Tokyo, Japan

Summary. — The earthquake nucleation process is inherently complex, due to an involvement of several deformation mechanisms with multiple spatial and time scales. Natural fault hosts a wide spectrum of slip rate from fast- to slow-slip. Before large earthquakes, the number of smaller magnitude events often increases, retrospectively named foreshocks. Foreshock can be interpreted to be a physical process implying unlocking of fault by fast-slip mode. Recent seismic and geodetic studies of foreshock sequences suggest that partial unlocking of fault took place episodically through interplay between fast- and slow-slip modes before some large earthquakes such as the 2011 Tohoku-Oki, the 2014 Iquique and the 2016 Kumamoto earthquakes. The partial unlocking causes stress loading onto the nearby critically loaded fault segments, resulting to triggering of subsequent dynamic and unstable slip. Alternatively, the partial unlocking of fault enhances the strength weakening of the earthquake nucleation area through slip invasion or fluid migration, that ultimately initiates the subsequent dynamic rupture. However, the manner of the unlocking is "episodic", not "smooth acceleration" which has been typically observed as nucleation phase in laboratory experiment and numerical simulation model having simple fault zone structure. This episodic manner precludes a possibility of forecasting the subsequent large earthquake with a high degree of accuracy. The triggering of a subsequent large earthquake on nearby fault segments depends on the areal extent of the critically loaded seismic patches and how close these areas are to failure, even though the partial unlocking by both fast- and slow-slip processes is observed. An important research area is the development of methods for assessing the degree of criticality within fault segments adjacent to already ruptured portions. In addition, earthquake triggering probability by slow-slip transient shall be incorporated into operational earthquake forecasting scheme as future challenge, especially during the latter phase of the inter-seismic periods.

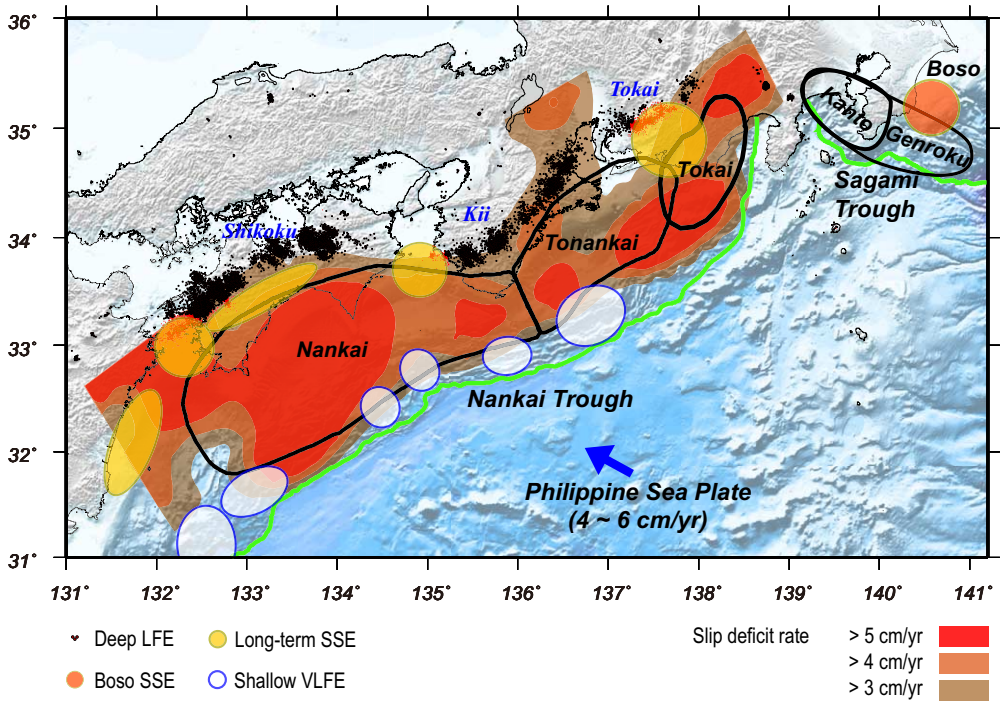

Fig. 1. – Map of slow earthquakes in southwest Japan (modified from Obara and Kato [5]; reprinted with permission from AAAS). Deep low-frequency earthquake is denoted by red dots, where short-term SSEs are also taking place within a narrow belt-like zone along the downdip edge of the megathrust seismogenic zone. Yellow and white shade denote locations where long-term SSEs and shallow VLF earthquakes occur. The contour map shows the distribution of the slip deficit rate obtained from onshore and seafloor geodetic measurements [7]. The megathrust seismogenic zones along the Nankai subduction zone are outlined in thick black curves.

1. – Wide spectrum of slip rate from fast- to slow-slip

A primary cause of earthquake is recognized to fast fault movement, resulting to sudden release of elastic energy which has been accumulated during inter-seismic period. This idea is referred to an elastic rebound theory of earthquake occurrence, proposed by H. F. Reid, following the 1906 San Francisco earthquake. Due to a friction exerting on fault surfaces at brittle deformation regime (typically, temperature is less than about 400 degrees), fault has been locked (the fault slip velocity is close to zero) during inter-earthquake time, leading to an accumulation of elastic energy around the fault. Regular earthquakes typically invoke fast-slip velocity $\sim 1\,\mathrm{m/s}$ along the fault, producing high-frequency seismic waves. The recent advent of improved geophysical instrumentations such as modern seismometers and geodetic measurements have unveiled that there is a wide spectrum of slip modes from fast- to slow-slip rate, to accommodate the elastic energy stored in Earth's crust [1, 2].

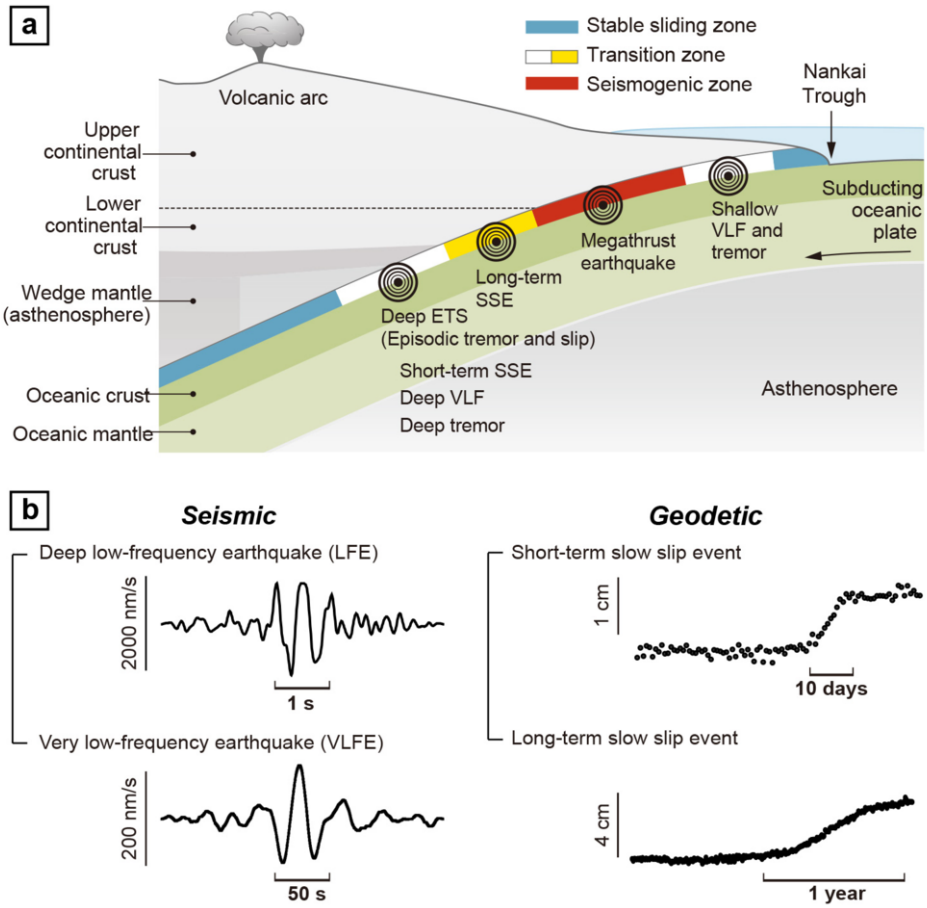

Fig. 2. – (a) Cross section of a subduction zone (based on the Nankai subduction zone) showing various types of slow earthquakes (modified from Obara and Kato [5]; reprinted with permission from AAAS). (b) Examples of signals observed for seismic and geodetic slow earthquakes; Deep low-frequency earthquake, Very low-frequency earthquake, Short-term slow-slip event, Long-term slow-slip event. Note the different horizontal and vertical scales.

1˙1. *Various types of slow earthquakes*. – After about 20 years from the discovery of non-volcanic tremors at downdip zone along Nankai Trough, SW-Japan [3], a family of slow earthquakes has been detected in many plate boundaries along the Pacific Rim [4,5]. Slow earthquakes show an intermediate type of fault slip that is transitional between fast rupture of regular earthquakes and stable sliding along a fault interface. In the Nankai subduction zone, slow earthquakes tend to be distributed at partially coupled areas, like downdip extensions of the strongly locked seismogenic zone (fully locked area) as well as several shallow spots near trench-axis (figs. 1 and 2) [5-8]. Thus, the slow earthquake provides us phenomenological evidence for the existence of a transition zone of slip modes along the megathrust fault.

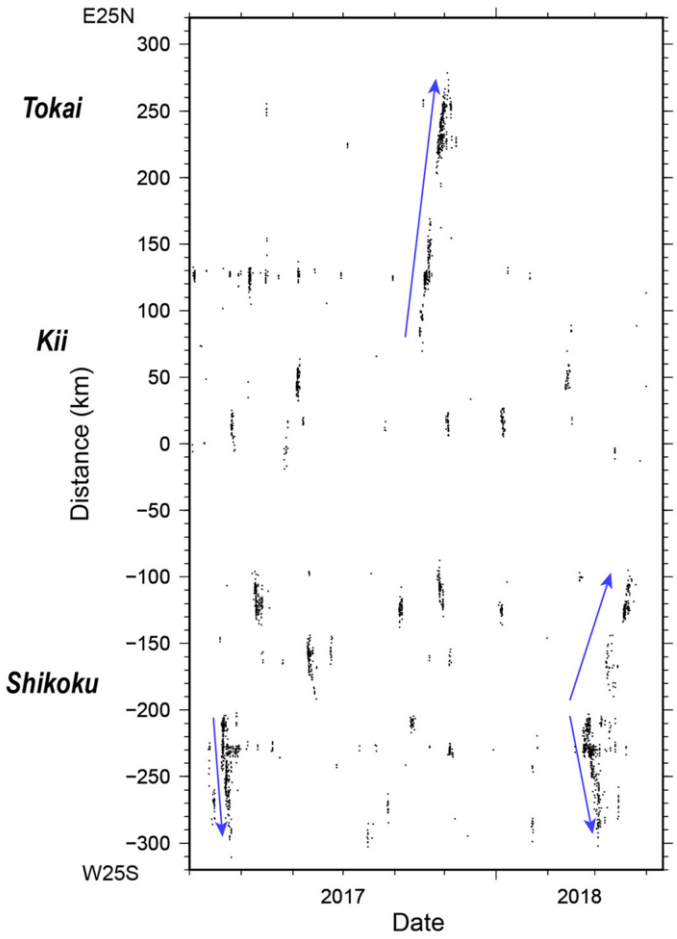

Fig. 3. – A space time diagram of deep LFEs determined by JMA along the downdip edge of the megathrust seismogenic zone in the Nankai subduction zone from 2017 to 2018. Blue arrows denote major propagations of LFEs over multiple segments.

Various types of slow earthquakes in Japan have been discovered and well documented using the dense geodetic and seismic observation networks such as GEONET [9] and Hi-net [10]. In the Nankai subduction zone, the slow earthquakes have been categorized according to their characteristic time scale [5]; from shorter to longer time scale, low-frequency earthquake (LFE), very low-frequency earthquake (VLF), short-term slow-slip event (SSE) and long-term SSE (fig. 2). Deep tectonic tremors can be explained by a successive or swarm-like occurrence of small LFEs, each of which occurs as shear faulting on the subduction-zone plate interface [11]. The duration of each slow earthquake proportionally increases with moment magnitude and is longer than regular earthquake with the same moment magnitude [1, 12]. In the case of short-term SSE, the fault

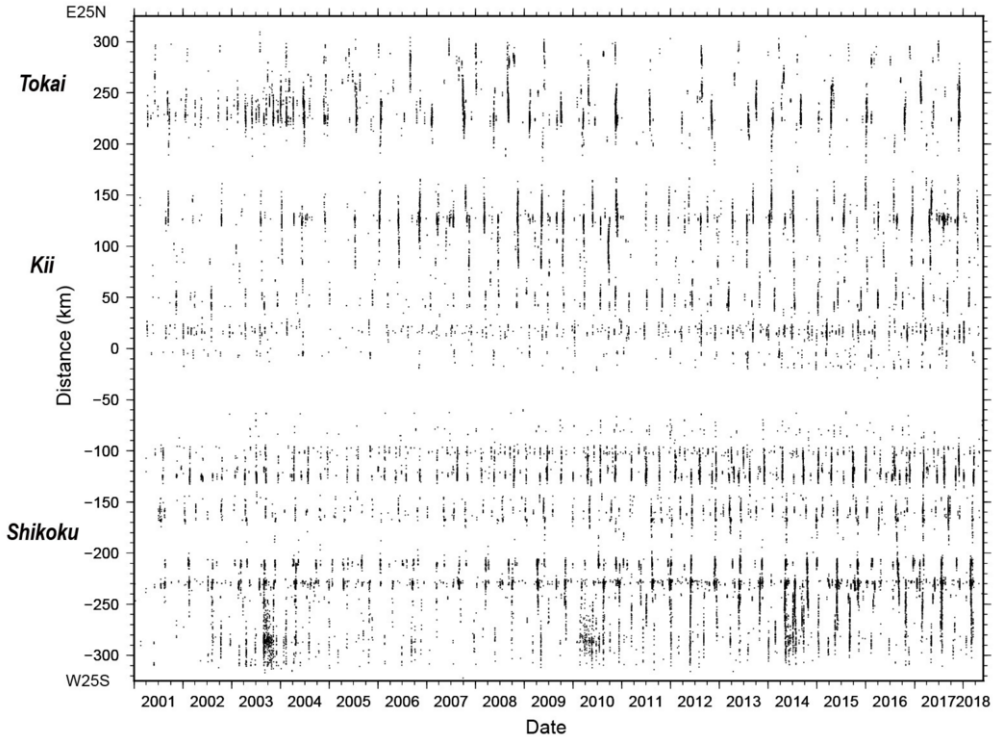

Fig. 4. – A space time diagram of deep LFEs determined by JMA along the downdip edge of the megathrust seismogenic zone in the Nankai subduction zone from 2001 to 2018.

slip velocity ranges from 10^{-8} to 10^{-7} m/s, which is tens or hundreds of times faster, compared with the plate convergence rate.

As common prominent feature, these slow earthquakes show clear spatiotemporal evolution, namely, "migration" (fig. 3). As the migration speed of slow earthquake decreases, the duration of each event becomes longer, suggesting that migrations of slow earthquakes are controlled by a diffusion process [13-15]. Often, both short-term SSEs and tremors migrate along-strike as well as along-dip directions at average speeds of approximately 10 km/day. The synchronization of short-term SSEs with tremor was first discovered in Cascadia and referred to as episodic tremors and slip (ETS) [16, 17]. Afterward, ETS was also identified in the Nankai subduction zone [18], and sometimes accompanied with VLFEs [19]. The migration pattern of ETS shows some diversity in terms of initiation and termination areas, propagation direction, and speed [20].

Figure 4 shows a space-time diagram of deep LFEs along the Nankai subduction zone determined by Japan Meteorological Agency (JMA) from 2001 to May in 2018. These LFEs are almost continuously distributed within a narrow belt-like zone along the downdip edge of the Nankai megathrust seismogenic zone over a length of 600 km (fig. 1).

Each streak along fault-strike corresponds to a migration of ETS episode with durations from several days to weeks [21]. The recurrence interval of major ETS episodes are approximately 6 months along the belt [20]. A streak of tremors/LFEs with minor SSE, of which detectability is close to noise level of geodetic data, takes place more frequently at the intervals from 70 to 150 days which are dependent on tectonic environment [22]. These observations indicate that ETS repeats with relatively periodic cycle compared with ordinary earthquakes, while there is certainly some variability of the recurrence time intervals.

As another prominent feature of slow earthquakes, the belt-like tremor zone is divided into segments bounded by spatial gaps [20]. Most of ETS activity are confined within each segment, however, some migrating ETSs extend over the gap, and continue to propagate toward the nearby segment. Within the gap, it seems that only slow-slip transient propagates without detectable tremors/LFEs [19]. Sequential ruptures of multiple segments lead to an event with larger moment release than isolated episode. One remarkable example can be seen recently during an episode at Shikoku island from Feb. to Mar. in 2018 (fig. 3), where LEEs initiated from the center of the Shikoku island and migrated along the total distance of about 100 km.

1˙2. *Complexity of slow earthquakes.* – Most slow earthquakes are characterized by their relatively regular, periodic occurrence. However, the manner in recurrence shows complex behavior in some cases. For example, repetitive long-term SSEs have been monitored in the Bungo channel, SW Japan, since the deployment of geodetic network (GEONET) (fig. 5). During the 1997 and 2010 episodes, three long-term SSEs recurred with similar slip parameters, including moment magnitude ($M_{\mathrm{w}} \sim 7$), slip area, duration and propagation direction of slip [23, 24]. These SSEs resemble a characteristic earthquake, which is a unique earthquake rupturing at approximately the same source size with a regular interval. However, the most recent long-term SSEs in 2014 and 2016 show quite smaller magnitude with M_{w} 6.0–6.2 than the previous ones, and the recurrence intervals become shorter compared with the previous events [25]. A likely explanation of the temporal changes in behavior of these SSEs is an interaction among SSEs occurring at the Bungo-channel and off-Miyazaki in Kyushu region. From 2013 to 2016, two sequences of long-term SSEs off-Miyazaki occurred, and propagated from south to north (fig. 5). The northward propagation of these SSEs might bring about increase in loading rate onto the Bungo-channel area, facilitating the slow-slip occurrence with minor and shorter recurrence interval than the previous three characteristic sequences. This observation may be a fingerprint of the interaction between different types of SSEs [5]. But since this is one of possible interpretations, a sustained effort of geodetic monitoring has been required to understand the interaction between SSEs.

It has been well known that a few SSEs drive a swarm of moderate earthquakes, *i.e.*, there is an interplay between small/moderate ordinary earthquakes (fast-slip) and slow sliding by SSEs. These synchronizations of fast and slow earthquakes have been reported at Japan, New Zealand and Ecuador [26-28]. Near the eastern coast of Boso Peninsula, Central Japan, SSEs with $M_{\mathrm{w}} \sim 6.6$ has repetitively took place along the top of the

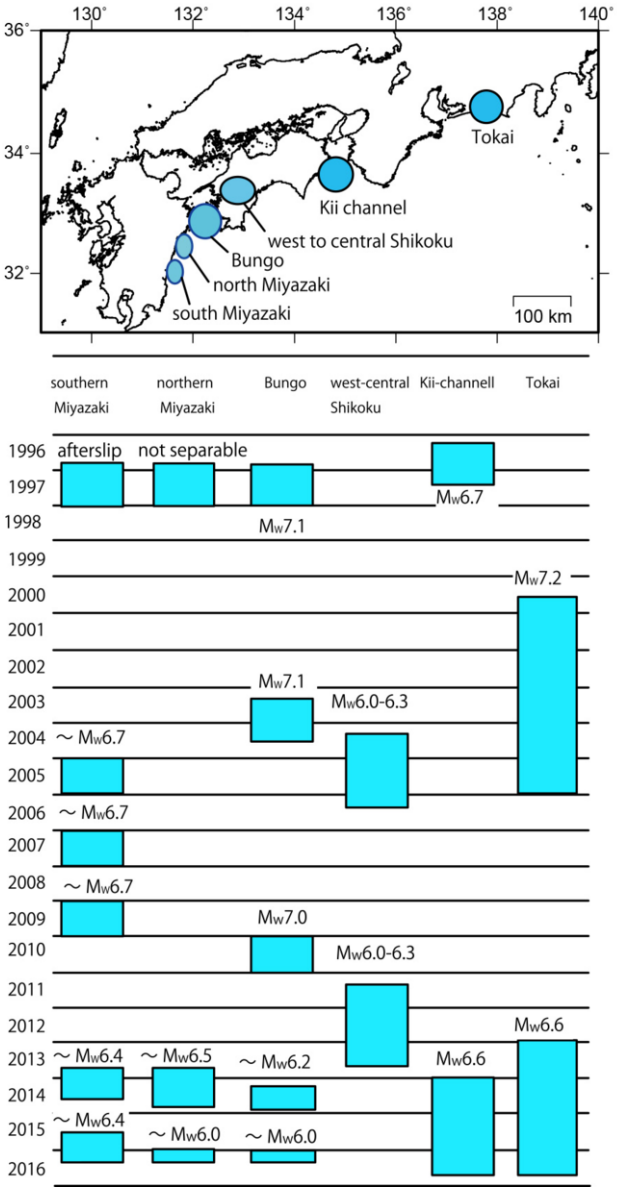

Fig. 5. – Spatiotemporal distribution of long-term slow-slip events along the Suruga and Nankai troughs together with the moment magnitudes [25]. The estimate of the moment magnitude for the 1997 northern Miyazaki slow-slip is quite difficult, due to contamination of the afterslip of the 1996 Hyuga-nada earthquakes and the 1997 Bungo channel SSE.

subducting Philippine Sea Plate, every 4 to 7 years (fig. 6) accompanying with a burst of ordinary earthquakes at the downdip side of the major slow-slip patch (the recorded largest earthquake is M_{w} 5.3). The most recent SSE has just occurred from the early part

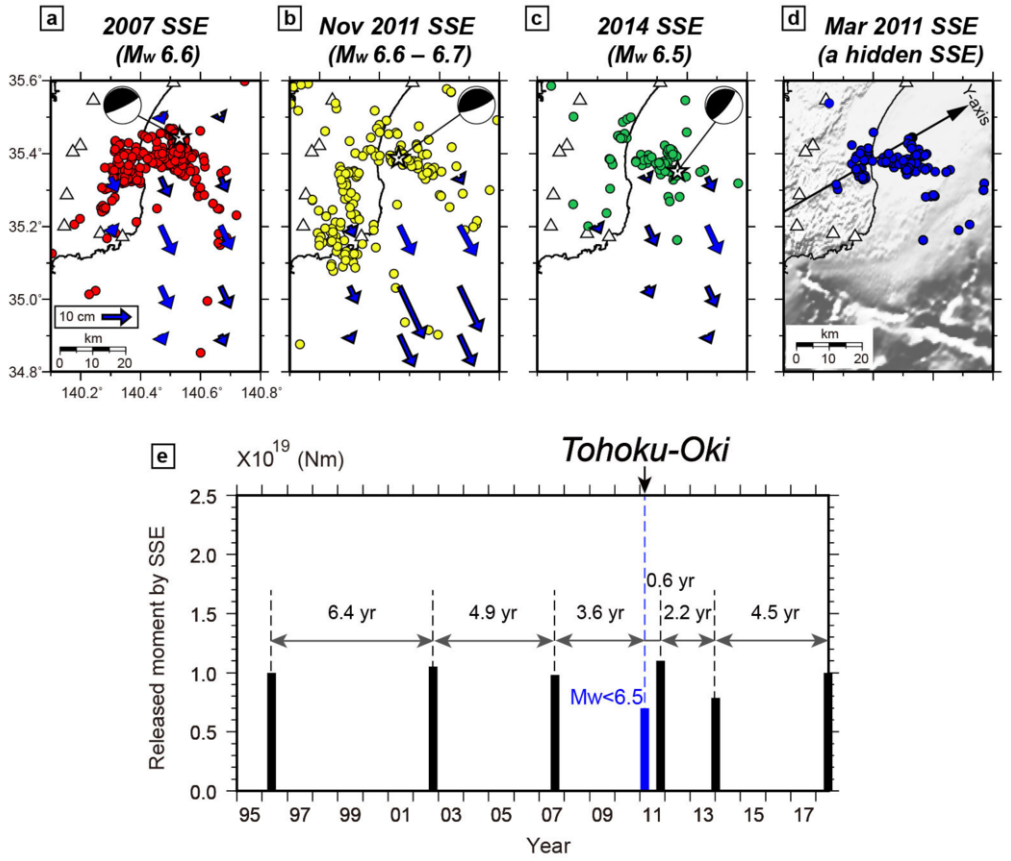

Fig. 6. – Map of the epicenters of earthquakes associated with Boso SSEs, including (a) the 2007 SSE, (b) the November 2011 SSE, and (c) the 2014 SSE (modified from Kato *et al.* [32]; reprinted with permission from John Wiley and Sons). The circles denote the earthquakes accompanied by the recently known SSEs. The blue vectors are the estimates of interplate slip made by geodetic measurements. (d) Epicentral distributions of all detected events in March 2011. (e) Revised history of the Boso SSEs, showing the newly detected hidden SSE that occurred immediately after the Tohoku-Oki earthquake.

of June in 2018. The triggering of downdip events during SSE resembles an increased rate of tremors at the deep side of the long-term SSE in the Bungo channel [29]. Therefore, the mechanism to drive earthquake swarms might be like that which drives tremor related to the Bungo channel SSE. However, the source area of the Boso SSE source is quite shallower than that of the Bungo channel SSE, and so the thermal regime in Boso is colder than that in Bungo. Because the cooler thermal regime enhances brittleness or slip-instability of fault movement, the slip rate in the triggered events may be dependent on the thermal regime therein [5].

This enhancement of brittleness may allow strong temporal variations of moment magnitude, slip area and spatiotemporal evolution during each Boso SSE, as determined

from the longest observed repetition history of SSEs derived from GNSS and swarm-like seismicity (almost 30 years) [30-32]. For example, Kato *et al.* [32] suggests that a small SSE might be hidden by substantial afterslip following the 2011 Tohoku earthquake, based on the seismicity analysis including repeating earthquakes off Boso Peninsula. The static and dynamic stress transfer imposed by the 2011 Tohoku earthquake plays a role to trigger the small SSE immediately after the Tohoku rupture. If we take this small SSE triggered by an external perturbation into account, the recurrence interval shows a more complex pattern than previously supposed (fig. 6e) [32, 33].

Similarly, SSE can be triggered by external stress change on the source area as observed in Nankai, New Zealand and Ecuador subduction zones [8, 34, 35]. The triggered SSE enhances stress loading onto a nearby seismogenic zone, pushing the subsequent event, like cascading trigger through interplay between fast- and slow-slip modes. Cascading trigger by mixed modes of fast- and slow-slip has been observed by seismic and geodetic data along a weakly coupled part of the Andean subduction zone in northern Peru [36]. It is therefore of crucial importance to understand the interactions between fast- and slow-slip modes through stresses transferred via elastic, quasi-static deformations or seismic waves.

1˙3. *The early acceleration phase of slow-slip event.* – Despite the widespread detection of SSEs, there has been little constraint on the spatiotemporal evolution of each SSE episode, especially during the early acceleration phase. For example, the relative timing between the onsets of SSEs and of their associated tremor or regular earthquake has been inferred in only a few cases [21, 37, 38]. However, it is quite difficult to demonstrate whether slow-slip takes place before the onset of tremors or not. Elucidating the detailed spatiotemporal evolution of SSEs may help constrain the physics of SSEs and driving mechanism for their synchronous seismic activity. Fukuda *et al.* [39] examine the spatiotemporal evolution of a slow-slip event (SSE) near Boso Peninsula, central Japan, from December 2013 to January 2014 applying the modified Network Inversion Filter to GNSS data. During the early phase with duration of 10 days, the slow-slip front slowly propagated to west at speeds of $\sim 1\,\mathrm{km/day}$ or less, without any detectable seismicity (fig. 7). Then, this slow-slip front suddenly accelerated with higher slip rate and propagated at higher speed ($\sim 10\,\mathrm{km/day}$), exciting an intensive migrating seismicity. The seismicity was highly correlated in space and time with slip rate, suggesting that the seismic swarm could be triggered by stress loading due to the slow-slip. This result implies that the associated seismicity is controlled by the evolution of the slip rate or migration speed of the SSE front.

Based on the above observations, the loading rate is an important factor to induce unstable fast-slip during the SSE accompanied with seismic swarm. A laboratory experimental study [40] suggests that abrupt increases in the loading rate can shrink the spatial and temporal extent of the earthquake nucleation zone, making seismic patch to close to be a condition of brittle slip-failure. Therefore, the abrupt change of slow-slip rate has a potential to generate earthquakes, as far as seismic asperities close to failure exist in the nearby area.

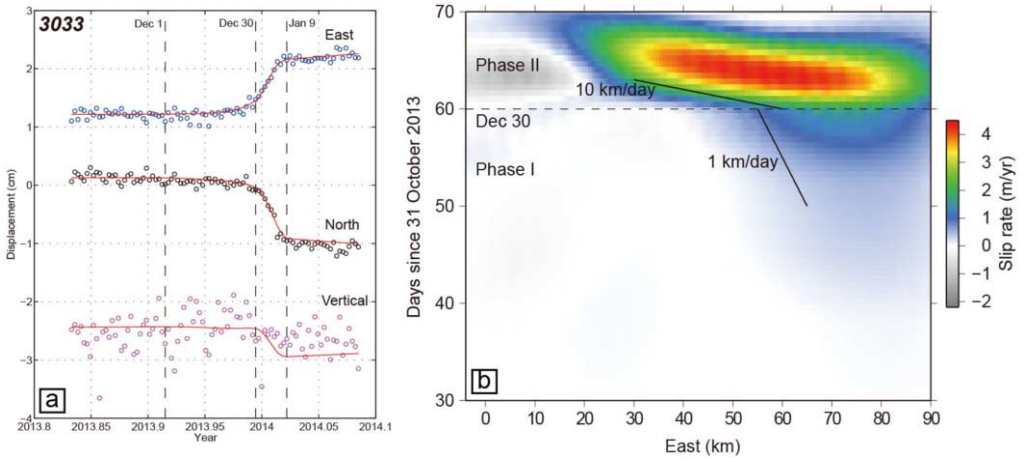

Fig. 7. – The 2013–2014 Boso slow-slip event (from Fukuda *et al.* [39]. Reprinted with permission from John Wiley and Sons). (a) Observed (circles) and predicted (red lines) displacement time series from a selected GNSS station. Circles represent the observed displacement time series, corrected for steady deformation, seasonal variations, postseismic deformation following the 2011 Tohoku-oki earthquake, and common mode errors. (b) Temporal evolution of slip rate along 35.26 °N latitude. The horizontal axis represents the east-west distance measured from (140.0 °E, 35.26 °N). Solid lines denote slopes corresponding to propagation speeds of 1 and 10 km/day.

To characterize the early phase of the SSE evolution, a systematic research about a suite of Boso SSEs has been conducted [41]. It has been elucidated that the SSEs in 1996 and 2013–2014 nucleated more slowly, with moment increase and slip rate lower than those of the 2002, 2007, and 2011 SSEs. These results indicate that there is a variability in the nucleation style, space-time slip histories and moment magnitude of the SSEs from event to event. We suppose that SSE accompanied with seismic swarm shows more complex slip behavior than ETS along the deeper extension of the strongly locked seismogenic zone in Nankai, because areas hosting slow- and fast-slip modes are in proximity to each other and are easily perturbated by the stress transferred between them. In some cases, fault weakening can be enhanced by an invasion of a locked patch by slow-slip transient. The interplay between slow- and fast-slip may produce more heterogeneity of stress field and fault strength, compared with that among families of slow earthquakes.

2. – Episodic unlocking of fault prior to large earthquake

The earthquake nucleation process *in situ* has remained enigmatic for a long time, despite vigorous laboratory and theoretical studies to understand the nucleation process. The nucleation process has been discussed actively in association with the occurrence of foreshocks, those are close in time and space to subsequent larger earthquakes [42, 43].

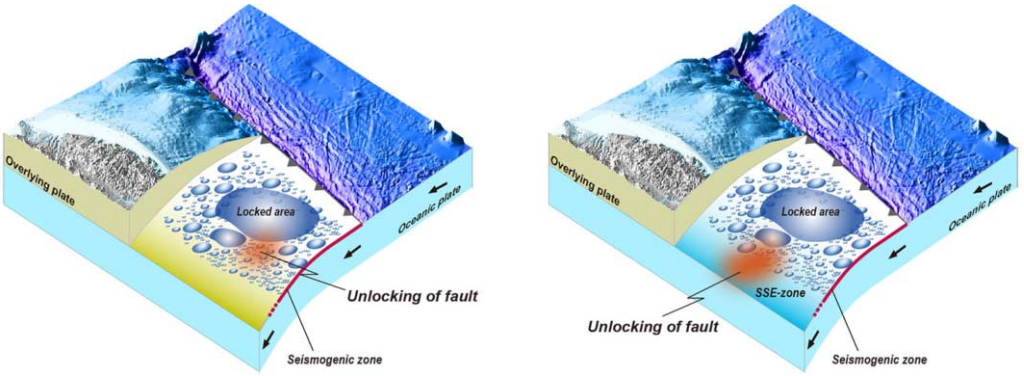

Fig. 8. – Schematic figures showing unlocking of fault within locked seismogenic zone (left) and distinct slow earthquake zone (right).

However, it has been unclear how these foreshocks relate to the nucleation process of the mainshock.

Most large earthquakes are not signaled by easily recognized foreshock sequences. In some cases, there are no foreshocks, while in others the foreshocks are small in magnitude and not distinguishable from the many naturally occurring clusters of events that do not lead to larger earthquakes [44]. Even in the retrospective investigation of seismicity, the incidence rate of foreshocks prior to a large earthquake has been reported to range from 20 to 40% [45-47], depending on tectonic setting, the period and completeness magnitude of the analyzed earthquake catalog, as well as the method to define mainshock (declustering scheme). For more than a half of major earthquakes, the dynamic rupture initiates without any foreshocks.

As described in the previous section, natural fault hosts a wide spectrum of slip rate from fast- to slow-slip modes [2]. We thus expect possible occurrence of slow-slip transient during foreshock sequence that is a representative of fast-slip mode. In the case when the fault slips at relatively faster speed than ordinary state (locked or sliding at very slow-slip rate), this means that unlocking of fault proceeds albite on wide range of slip rate. Prior to some major earthquakes, the unlocking of fault has been driven by mixed modes of faster (seismic) and slower (aseismic) slip along fault, resulting to that fault slip rate evolves in complex manner (fig. 8). Faster and slower slip modes may interact with each other and promote gradual accommodation of elastic energy stored in crust during a preparatory stage of large earthquake. Here, we briefly explain about a few foreshock sequences of large earthquakes, those are explained by step-like unlocking of fault enhanced by mixed modes of slow- and fast-slip.

2˙1. *Foreshock sequence of the 2011 M_w 9.0 Tohoku-Oki, Japan earthquake.* – Prior to the 2011 Tohoku-Oki earthquake, a bunch of seismicity took place at the northern side of the rupture initiation point of the mainshock. More precise earthquake catalog of the foreshocks revealed that two distinct sequences of earthquake migration occurred

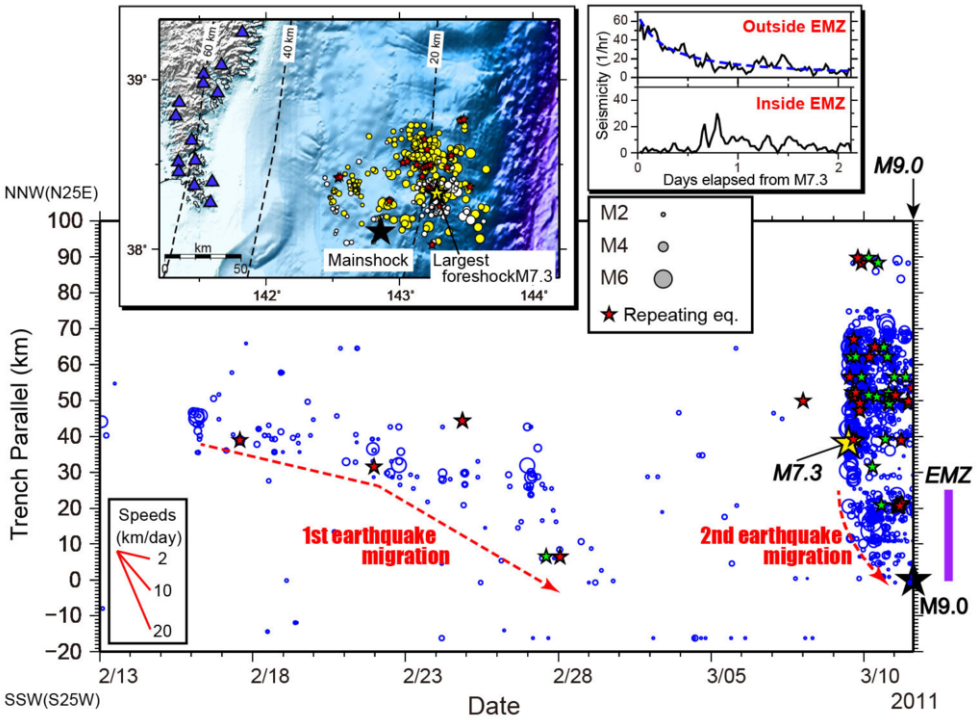

Fig. 9. – Spatiotemporal evolution of earthquakes (blue circles) prior to the 2011 Tohoku-Oki earthquake (modified from Kato *et al.* [48]; reprinted with permission from AAAS). Red dashed lines show approximate locations of earthquake migration fronts. Red stars denote repeating earthquakes, and green stars are identified to resemble those repeating earthquakes. Black and yellow stars denote epicenters of the Tohoku-Oki mainshock and the largest foreshock, respectively. The inset at the right shows temporary changes of seismicity rates inside and outside the EMZ after the M_{w} 7.3 largest foreshock. The blue dashed curve denotes least-squares fitting of the modified Ohmori law. The inset at the left shows the location of the study area off Miyagi Prefecture.

along the trench-parallel direction toward the epicenter of the mainshock [48], during final ~ 30 days before the mainshock rupture (fig. 9). The two sequences of earthquake migrations overlapped considerably in space. The migration speeds ranged from 2 to 10 km/day and slows down over time. The second migration front is well approximated by a parabolic curve without any final acceleration.

Most of the focal mechanisms during foreshock sequences with moderate-to-large magnitude are characterized by low-angle thrust faulting, which resembles with the mainshock type. This observation indicates that fast-slip caused by foreshocks took place along the subducting plate interface. Interestingly, the foreshock sequences included small repeating earthquakes that had identical focal mechanisms and identical locations, resulting in very similar waveforms. The repeating earthquakes can be interpreted to result from

recurrent rupture of seismic patch surrounded by aseismic creep on the plate interface. In addition to the foreshock migration, an episodic increase in the aseismic creep propagated toward the M_{w} 9.0 epicenter and coincided roughly with the area of earthquake migrations [48]. These observations clearly show that the accumulated elastic strain along the plate interface was accommodated by fast- and slow-slip processes, resulting to the episodic unlocking of the fault during the foreshock sequence.

The unlocking of the fault during the final two days before the Tohoku-Oki earthquake was confirmed by geodetic measurements on land (GNSS) and off-shore (ocean bottom pressure gauges) [49, 50]. From the middle of February to the onset of the largest M_{w} 7.3 foreshock, it has been inferred by ocean bottom pressure gauges that a slow-slip transient took place at depths shallower than the mainshock initiation point [51]. After the largest foreshock, a slow-transient deformation was detected at the updip in the coseismic slip of the largest M_{w} 7.3 foreshock and extended toward the south, where the two sequences of migrating foreshocks were observed. The maximum aseismic slip is estimated to be approximately 0.4 m and calculated moment magnitude released by aseismic slip ranged from 6.8 to 7.0. From the time series of geodetic measurement, the slow-slip transient appears to continue with gradual decay of the slip rate in the foreshock migration area until the mainshock rupture. However, we must pay a caution that there was no short-term acceleration of the slow-slip transient immediately before the mainshock rupture, above the detection threshold of ocean bottom pressure recorders (the minimum observable slow-slip magnitude: M_{w} 6.0–6.2) [52]. This observation indicates that moment released by the short-term nucleation process (final acceleration phase) is smaller than that expected from a scaling of the nucleation zone proposed from an approach in the framework of fracture mechanics [53].

In addition to the above daily and monthly time scales, an evolution of aseismic creep in decadal scales along the plate interface has been reported by several studies using on-land GNSS network [54, 55]. It has been proposed that a long-term aseismic creep had started around 2005 and continued until the Tohoku-Oki mainshock, along the downdip and south area of the large coseismic slip zone of the Tohoku mainshock. The total moment released by this long-term aseismic creep has increased monotonically from 2005 until the mainshock time, finally reaching an equivalent seismic moment of $\sim M_{\mathrm{w}}$ 7.7. This long-term aseismic creep implies that the fault hosting megathrust rupture slowly and partially slipped during around 7 years before the Tohoku-Oki earthquake. Adding the repeating earthquake data to the geodetic measurements, it has been inferred that the slow-slip rates on the plate interface slowly increased during the same time periods [56]. Furthermore, an analysis of very-low-frequency earthquakes off-Tohoku reveals that the activity of the VLFs at the south of the Tohoku-Oki rupture area slightly increased around 2008 [57]. These phenomena indicate that some aseismic creeps would result in increasing the stressing rate on the locked parts of the megathrust in decadal scales. The increasing stressing rate might contribute to promoting the generation of moderate-to-large earthquakes off-Tohoku region after 2003 [58].

There seems to be a direct correlation between periodic slow-slip occurrences and some moderate/larger earthquakes off-Tohoku region, Japan [59]. This observation indi-

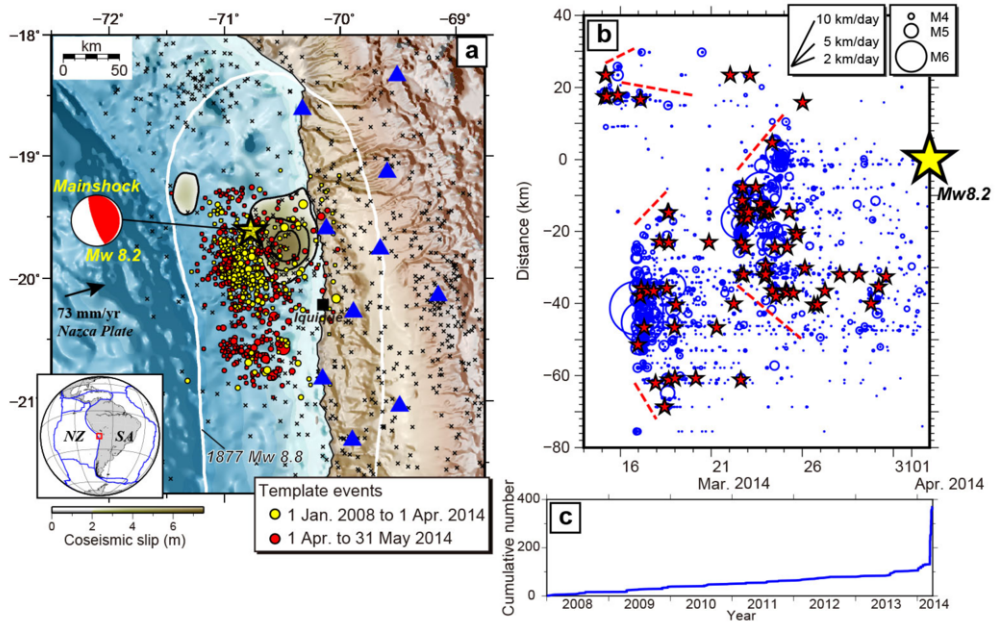

Fig. 10. – (a) Tectonic map of the 2014 Iquique, Chile M_w 8.2 earthquake (modified from Kato *et al.* [64]). The yellow star denotes the epicenter of the mainshock with the moment tensor solution by the USGS. The color scale and black contour lines show the coseismic slip distribution estimated by teleseismic waveform inversion. Yellow and red circles are epicenters before and after the mainshock, respectively. Crosses show USGS catalog epicenters from 1 January 1990 to 31 May 2014. The white outline denotes the approximate rupture area of the 1877 M_w 8.8 earthquake. The inset shows the location of the studied region. (b) Short-term evolution of seismicity during the final 17 days before the 2014 mainshock. Space-time diagram of all detected events (blue circles) and repeating earthquakes (red stars). Yellow star denotes the hypocenters of the mainshock. Red dashed lines represent the approximate locations of the fronts of earthquake migrations. (c) Observed cumulative number of earthquakes with magnitude ≥ 3.8 in decadal scale.

cates that the periodic unlocking of fault has caused stress loading onto seismic patches on the plate boundary fault, leading to temporal increase in earthquake generation probability. Although the monitoring of the slow-slip rate on plate interface has potential to help refine time-dependent earthquake forecasts, we must pay a caution to the fact that the maximum slip rate during slow-slip transient does not determine the final size of the subsequent earthquake. It is thus quite important to deepen our fundamental understanding about an interplay between slow- and fast-slip modes [60].

2˙2. *Foreshock sequence of the 2014 M_w 8.2 Iquique, Chile earthquake.* – The megathrust rupture of the 2014 Iquique, Chile M_w 8.2 earthquake occurred within the North Chile seismic gap, which stretches for $\sim$ 500 km along the plate boundary, where the Nazca Plate is subducting beneath the South American Plate. The mainshock was preceded by intensive foreshock sequences and geodetic signals lasting at least two

weeks [61-63], showing gradual unlocking of the plate boundary fault updip of the largest coseismic slip patch (fig. 10).

The space-time diagram of the seismic events shows that the seismicity rate off Iquique was almost constant before the summer of 2013. Similarly, the rate of aseismic slip derived from repeating earthquakes was nearly constant [64]. But it is inferred that the first crisis leading to the mainshock rupture started in summer 2013, accompanied by migrating seismic bursts at the southern edge of the largest coseismic slip patch. Following this seismic burst, repetitive sequences of seismic bursts migrated along dip as well as along strike. The frequency of earthquake migrations increased, and the migration speeds also tended to rise before the mainshock failure (fig. 11). These migrating seismic bursts were accompanied by the transient increase in aseismic slip derived from repeating earthquakes [61,64] and the background rate of seismicity. Furthermore, the lateral size of each seismic swarm area was considerably larger than the earthquake source dimensions. Based on these observations, a likely explanation for the earthquake migrations is a propagation of episodic aseismic slip transients; *i.e.*, slow-slip events.

During the final 17 days before the mainshock (15–31 March 2014), the continuous GNSS stations located along the coast near the source region started to move trench-ward. The trench-ward surface deformations indicate the gradual unlocking of the plate interface. It has been debated whether the unlocking of the plate interface was driven mainly by aseismic slip or cumulative seismic slip from M 5–6 class moderate/large foreshocks [62, 63]. This uncertainty arises because the detected surface deformations were too weak to be clearly separated into coseismic and aseismic slip. However, analyses of repeating earthquakes [64, 65] and GNSS data [66] suggest that a slow-slip transient took place during the final 17 days prior to the mainshock. The equivalent moment magnitude released by the slow-slip transient has been estimated to be 6.6–6.8, although the uncertainty is large.

The step-like increases in seismicity, the amount of aseismic slip inferred from repeating earthquakes, and the background seismicity rate, accompanied by an increasing frequency of earthquake migrations, started around 270 days before the mainshock occurrence at the updip of the largest coseismic slip patch (fig. 11). Due to the spatial-temporal evolution of fast- and slow-slip modes, repetitive sequences of migrating unlocking processes took place along dip as well as along strike, outlining the shallow rim of the largest coseismic slip patch (fig. 10) [64, 67].

Similar episodic unlocking was observed during the foreshock sequence prior to the 2017 Valparaíso M_{w} 6.9 Earthquake in Central Chile (at the northern extension of the rupture area of the 2010 Maule M_{w} 8.8 earthquake), accompanying the migrating seismicity and the slow-slip transient (M_{w} 6.5) within final 2 days [68]. Although geodetic measurements of the surface displacements are very limited and scatter, the trenchward displacements (meaning unlocking of fault) gradually increased with time until the mainshock rupture time. However, even in the time series of the high-rate GNSS, the unlocking of the plate boundary fault did not show any short-term acceleration. It is thus impossible to precisely predict the onset time of the mainshock occurrence using the geodetic measurement and seismicity at the current knowledge.

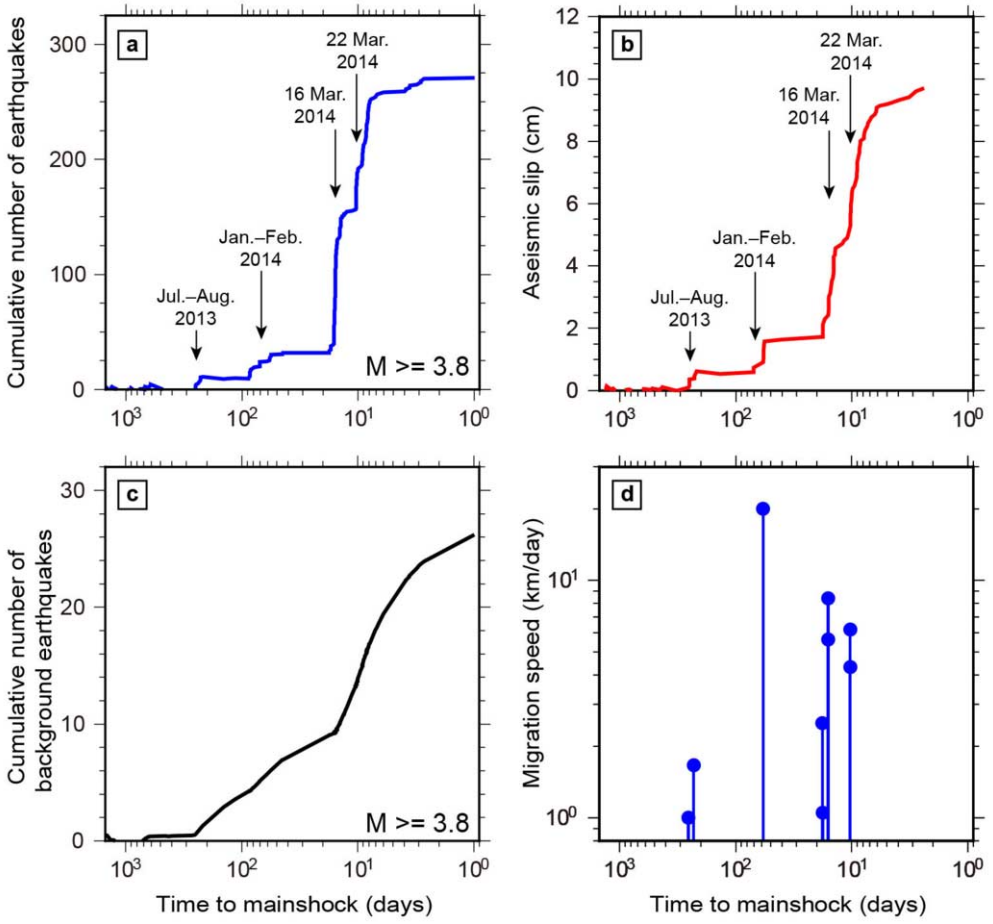

Fig. 11. – Episodically accelerated fast- and slow-slip during the foreshock sequence before the 2014 Iquique, Chile M_w 8.2 earthquake [64]. (a) Detrended cumulative number of earthquakes, (b) detrended aseismic slip averaged over all groups of repeating earthquakes, (c) detrended cumulative number of background seismicity, and (d) earthquake migration speeds, as a function of time to failure during the final 1200 days before the 2014 Iquique, Chile M_w 8.2 earthquake.

In laboratory experiments, fault displacements smoothly increased according to a power-law time-to-failure equation during the nucleation stage [69, 70]. However, the fault slip during each foreshock sequence shows not smooth change but step-like increase. This discrepancy clearly shows that the evolution of slip is more episodic and irregular in nature than in laboratory experiments. Even in the intensive foreshock sequence observed before the 2014 Chile Iquique earthquake, the slip rate estimated from repeating earthquakes has several discrete peaks with time [64]. This observation maybe attributed to the fact that the natural fault has more heterogeneous fault zone structure compared with well-prepared fault surfaces used in typical laboratory studies. Recent laboratory

experiments have found a reduction in nucleation duration and nucleation zone size with increasing the loading rate, which may be caused by the evolution of fault gouge layer as self-organized process [71]. An amount of production in the fault gouge increases with the loading rate. Thus, we suppose that local increase in loading rate imposed by fast-slip on the adjacent segment can shrink the classical nucleation zone size, resulting to difficulty in detection for nucleation phase of natural earthquake, based on seismic and geodetic observation from surface.

2˙3. *Triggering of the 2014 M_w 7.3 Papanoa, Mexico earthquake by a slow-slip event.* – As observed along Nankai Trough, Cascadia, Hikurangi and Mexico subduction zones, we have a distinct zone of slow earthquakes at the deeper extension of each seismogenic zone along a plate interface (fig. 8b). Soon after the discovery of slow earthquakes, it has been suggested that SSE could lead to an increased time-dependent probability of megathrust events [72]. However, there have been few observations to confirm or refute this hypothesis statistically.

Along subduction zones in Mexico and Costa-Rica, slow earthquakes preceding $M_w \sim 7$ class earthquakes have been observed recently by construction of geodetic network [73-75]. At the downdip extension of the Guerrero section in Mexico, the large-scale SSEs (released moment equivalent to $M_w \sim 7.5$) have occurred approximately every four years. The M_w 7.3 Papanoa (Mexico) earthquake took place on 18 April 2014 in the early stage of a long-term SSE with a total aseismic moment equivalent to M_w 7.6 (the largest moment magnitude ever recorded) [75]. The SSE started in February 2014 at the neighboring downdip side of the earthquake source fault and grew to the moment equivalent to M_w 7.1 before the onset of Papanoa earthquake. The spatiotemporal closeness between the mainshock and SSE occurrences allows to interpret that the Papanoa earthquake was triggered by the unlocking of the plate interface through the SSE. The ongoing SSE could transfer the Coulomb stress of 40 kPa on the source fault and prompt the mainshock rupture. Alternatively, the strength of the nucleation area might be weakened by an invasion of the slow-slip transient, leading to the subsequent dynamic rupture [76]. In either case, the slow-slip transient temporally increases the probability to enhance the generation of subsequent nearby large earthquake.

On the southern Mexico subduction plate boundary, the 2012 Ometepec M_w 7.4 earthquake occurred. At the downdip extension of the seismogenic zone, a slow-slip initiated by about 5 months before this earthquake, and migrated westward at ~ 2.6 km/day parallel to the trench-axis, and reached the eventual earthquake source region about one month before the mainshock rupture [74]. The mainshock rupture started during the SSE, of which moment magnitude grew to be 6.9. This moment magnitude is like that of each SSE observed in 2004 and 2006 along the same area of the subduction interface. The calculated Coulomb stress changes caused by the SSE on the mainshock area is small but positive values for the mainshock fault plane. Before the occurrence of the 2012 M_w 7.6 earthquake in Costa Rica, a slow-slip event was observed to migrate toward the eventual megathrust rupture [77]. The peak slip rate reached a maximum of 5 mm/day, 43 days before the earthquake, remaining high until the earthquake. However, the slip appears to

extend within the seismogenic zone, resulting in the very small positive value of Coulomb stress changes (0.01 MPa) imposed by the SSE on the mainshock hypocenter. In these cases, the stress increment imposed by the SSE on the mainshock area is insufficient to demonstrate causality. However, it is conceivable that the extended slow-slip in the focal region had weakened the fault strength, or the slow-slip allows the fluid to migrate updip toward the seismogenic zone along the plate interface, which facilitated the subsequent rupture [48, 77]. These results suggest that mainshock rupture can be enhanced by unlocking of the plate boundary fault through the propagation of SSE over the seismogenic zone.

2˙4. *Foreshock sequence of the 2016 M_w 7.0 Kumamoto, Japan earthquake.* – Albeit on a small scale, similar unlocking of fault prior to a mainshock rupture has been detected at shallow crustal fault. Beginning in April 2016, a series of powerful shallow earthquakes, including intensive aftershocks, struck the Kumamoto area of central Kyushu, Southwest Japan. After a first M_w 6.2 earthquake on 14 April 2016, a mainshock with M_w 7.0 occurred on 16 April 2016 (JST) close to the epicenter of the first event with a time delay of $\sim$ 28 hours. The source area is situated at a unique tectonic setting characterized as stress field composed of both strike-slip and north-south extensional regime, whereas the shallow crust of the Japanese islands is mainly affected by compressive regional stress. Based on recent geodetic measurements, a shear deformation zone, showing right-lateral strike-slip faulting with relatively high displacement rates of 7–8 mm/yr, has locally developed in the source area [78].

We have an advantage on determining more precise earthquake locations compared with the above earthquakes in subduction cases, because the source area has been well covered by a nationwide dense seismic network along the Japanese islands. The entire seismicity from the foreshock to the mainshock shows a clear spatiotemporal evolution (fig. 12) [79]. One example is that the seismicity immediately following the M_w 6.2 foreshock expanded toward northwest along the fault strike over time at the speed of around 20 km/day. The migration occurred both parallel to the fault-strike and along the slope of the dip (the updip and downdip), with indication of movement toward the rupture initiation point of the April 16 mainshock (fig. 12).

The foreshock area approaches its ultimate size (approximately double) within $\sim$ 9 hours after the initial M_w 6.2 foreshock. Similar migration of early aftershocks was observed immediately after some large events (the 2004 M_w 6.0 Parkfield earthquake on the San Andreas Fault, the 2007 M_w 6.7 Noto Hanto earthquake in Japan) [80,81]. These aftershock migrations are interpreted to result from propagation of afterslip (slow-slip transient) around the large slip-patch of each mainshock rupture [82].

To reveal the surface displacements associated with the aseismic-slip (afterslip) following the M_w 6.2 foreshock, subdaily GNSS data recorded at 30 s intervals was analyzed [79]. Transient surface displacements, which can be fit by a logarithmic function of time, were found out at two stations close to the foreshock fault (fig. 13), although the data has some scatters. These two surface vectors are consistent with those predicted by assuming a right-lateral slip motion along the foreshock fault plane with the aseismic

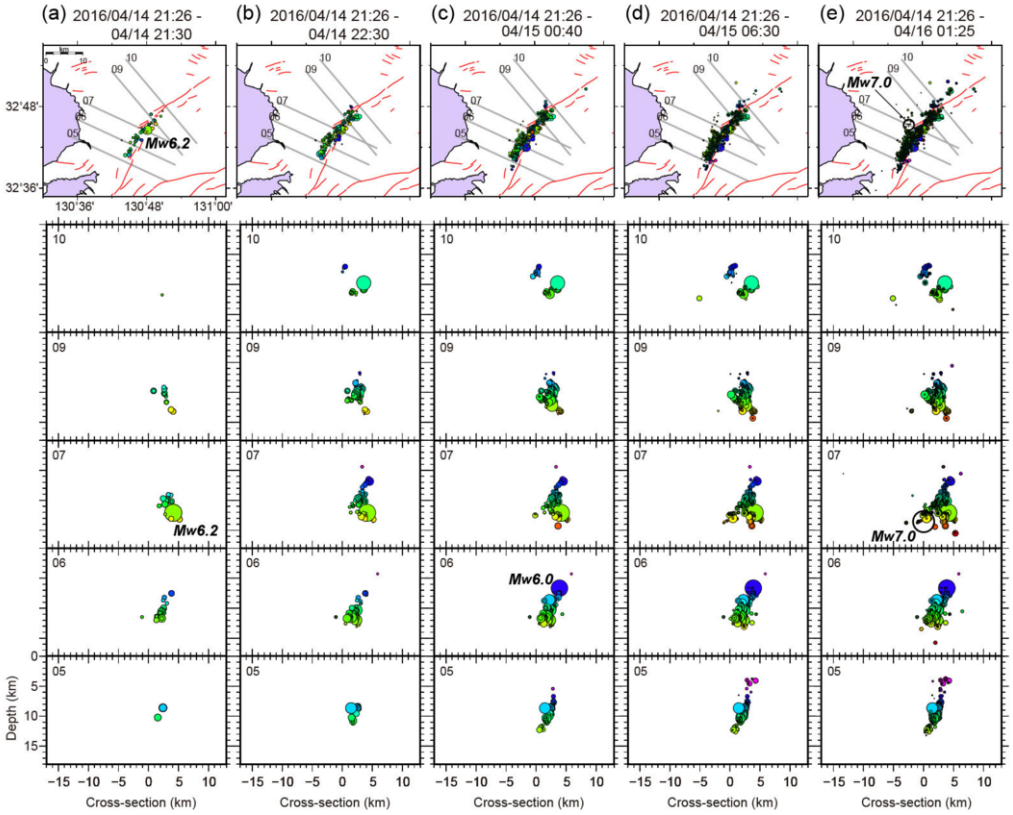

Fig. 12. – Spatial-temporal evolution of seismicity during the period between the foreshock and the 2016 Kumamoto mainshock rupture (from Kato *et al.* [79]; reprinted with permission from John Wiley and Sons). Plots of the cumulative distribution of epicentral locations over time, in map view and cross-section, are shown in the top and bottom panels, respectively. Events are colored according to hypocentral depth.

moment equivalent to M_w 5.8. Thus, the geodetic observations support that the slow-slip transient took place before the mainshock rupture.

Combining the evolution of seismicity with the geodetic signal, we suggest that aseismic slip propagated towards the nucleation point of the mainshock rupture. Because aseismic slip redistributes shear stress into the surrounding rock volume, the migration of aseismic slip effectively loaded the mainshock nucleation point, combined with static stress changes induced by the foreshock rupture itself (fig. 13). In addition, a very tiny earthquake cluster developed at the vicinity of the mainshock hypocenter just before the rupture initiation. This hints that the earthquake nucleation area might be locally weakened, that ultimately initiated the subsequent dynamic rupture. Similar interaction between earthquake faults was observed during the 2012 Emilia seismic sequence in northern Italy. An aseismic slip triggered by an initial M_w 6.1 earthquake propagated to a second fault nearby that then hosted an M_w 6.0 earthquake a week later [83]. Thus,

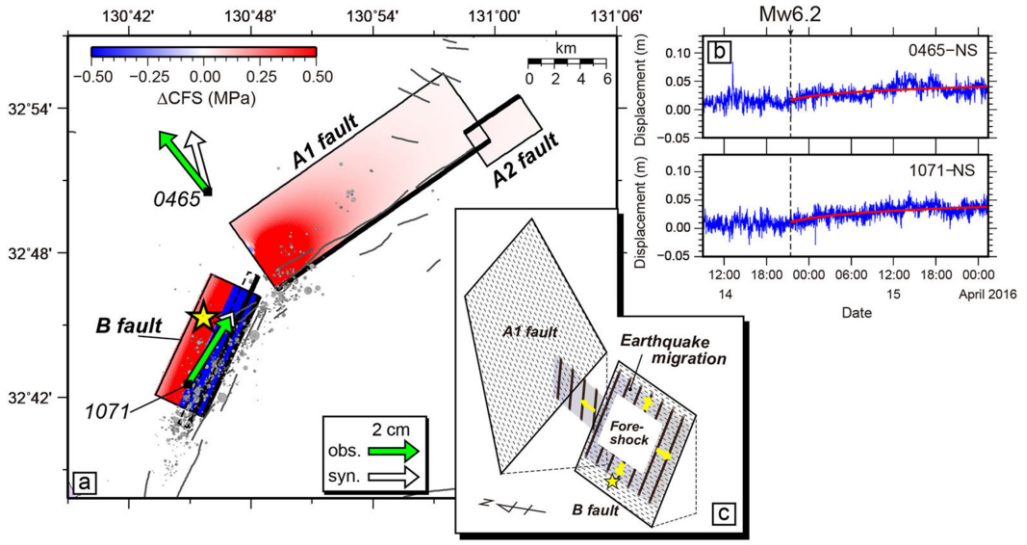

Fig. 13. – Fault interaction during the 2016 Kumamoto earthquake sequence (from Kato *et al.* [79]; reprinted with permission from John Wiley and Sons). (a) Static coulomb stress change caused by the M_w 6.2 foreshock and subsequent M_w 6.0 earthquake, resolved onto the three faults (A1, A2, and B) that failed in the M_w 7.0 mainshock. The coefficient of friction is assumed to be 0.4. The source-fault geometry for these foreshocks (dashed rectangle) was estimated from changes in surface displacement measured using both the GEONET GNSS network and InSAR data. The mainshock epicenter is shown by the yellow star; hypocenters of events occurring in the interval between the foreshock and mainshock ruptures are denoted by gray dots. The transient surface displacements recorded between the M_w 6.2 foreshock and the mainshock are shown by the green arrows; the open arrows denote synthetic displacements computed with a model assuming uniform slip on the foreshock fault plane. Gray lines represent the surface traces of active faults. (b) Time-series of displacement recorded at GNSS stations 1071 and 0465 (north-south component). The foreshock origin time is denoted by the dashed line. The logarithmic curve that best fits the transient deformation following the foreshock rupture is shown by the red line. (c) Perspective view of foreshock seismic slip and aseismic slip propagation on the mainshock rupture planes.

propagation of aseismic slip plays an important role in the buildup of shear stress onto nearby fault segments and in bringing them closer to failure.

3. – Discussion

The observation that the accumulated elastic strain was accommodated by both seismic and aseismic processes indicates that the transition zone from full coupling to creep was the site of fast- and slow-slip behaviors during the foreshock sequence [64, 65]. This means that the repeating sequences of fast- and slow-slip may have interacted with each other and promoted episodically accelerated unlocking of fault. The unlocking effectively caused stress loading on the largest slip patch of the mainshock rupture as the stress level approached the rupture threshold, thereby promoting the mainshock rupture. Alterna-

tively, if some displacement by slow-slip invades into the largest slip patch, the strength of the patch will be partially weakened and susceptible to rupture, which ultimately leads to unstable dynamic rupture, if the patch is close to failure [48, 75].

Even though the partial unlocking by fast- and slow-slip processes is observed, the triggering or enhancement of the subsequent large earthquake on nearby fault segments depends on the areal extent of the critically loaded seismic patches and how close these areas are to failure. To obtain information of the criticality, we need to understand the accumulated stress level (elastic energy) around the fault and the absolute strength level of the fault. An important research area is the development of methods for assessing the degree of criticality within fault segments adjacent to already slipped or ruptured portions. Therefore, it is essentially important to know spatiotemporal variations of stress and strength on fault through seismicity.

After the occurrence of M_{w} 7.8 Kaikōura earthquake in New Zealand in 2016 [84], a large-scale slow-slip event along the downdip side of the locked megathrust area were triggered by dynamic-stress changes derived from the passing seismic waves [85]. The large-scale slow-slip event with rupture length of about 300 km should cause rapid stress loading onto the shallow locked area during an ongoing few weeks, due to a geographical proximity. Furthermore, the Kaikōura earthquake induced an increase in static stress transfer of 20–200 kPa on the locked portion of the southern Hikurangi interface, which was further increased by $\sim$ 100 kPa over the year following the earthquake due to the subsequent long-term SSEs surrounding the locked zone [85]. However, despite the rapid stress loading onto the locked portion, the megathrust rupture has yet to occur at the current moment, while a swarm of seismicity including the largest M_{w} 6.0 earthquake was induced near the plate interface during the occurrence of the triggered SSEs.

In the Nankai subduction zone, more complex evolution of slip rate has been recently illuminated by development of a dense seismic and geodetic network at ocean floor. On 1 April 2016, an M_{w} 6.0 earthquake with low-dipping thrust faulting struck offshore the Kii Peninsula, SW Japan. The epicenter is located within the coseismic slip region of the 1944 Tonankai earthquake (M_{w} 8.1), namely within the locked seismogenic zone. Based on the seafloor network data, the rupture occurred on a landward dipping thrust fault at 9–10 km below the seafloor most likely on the plate interface [86, 87]. Since the occurrence of the last megathrust earthquake, earthquakes with magnitudes greater than 6 has been quite rare along the plate interface except for the aftershocks following the 1944 megathrust. After the occurrence of this plate interface earthquake, the afterslip near the coseismic slip area was observed by the ocean bottom geodetic measurement. Interestingly, following the afterslip, SSE, tremors and VLFEs simultaneously occurred with a slight time-delay at shallower depths close to the trench axis [8, 87]. The shallow VLEs showed clear migrations along the dip and strike directions, implying possible propagation of the shallow SSE toward trench. This observed sequence implies that unlocking of fault slightly proceeded at the relatively shallow side of the locked seismogenic zone. Furthermore, the interplay between the moderate earthquake and slow earthquakes highlights that the slip behavior hosting megathrust rupture has a wide range of time scales and a complex spatial distribution, even at the strongly locked seismogenic zone [86].

Based on these complexities of fault unlocking process, we are not able to predict the occurrence of large/megathrust earthquake with high accuracy, namely in a deterministic way at the current moment. Our current knowledge about the relationship between the onset of megathrust earthquake rupture and the fault unlocking process remains very limited. In addition, we do not have enough knowledge how the time scale of the fault unlocking prior to large earthquake varies from place to place, and from time to time. Therefore, it is quite important to focus on a scheme of operational earthquake forecasting as the principle means for estimation of time-dependent seismic hazards [88].

Over short time scales with durations of days and weeks, earthquake sequences often cluster in space and time, as illuminated by aftershocks triggered by large events as well as foreshocks prior to major events. Statistical models describing earthquake clustering like ETAS-model [89] well explains many features and diversities of observed seismic activity, that is representative of fast-slip on fault. These models can be used to construct forecasts that indicate how earthquake probabilities spatially change over the short time scale. Recently, this short-term probability model (ETAS) has been merged into long-term forecasting model of all fault-based supraseismogenic ruptures in the Southern California (UCERF3); elastic rebound statistics is explicitly adopted in modeling earthquake sequences including aftershocks [90]. Slow-slip transient also spatiotemporally increases triggering probability of the nearby earthquakes by releasing the accumulated strain energy around the slip area. Therefore, it is more desirable to incorporate the short-term probability derived from slow-slip transient into the operational earthquake forecasting model in the near future. To achieve this object, we must develop a more stable method to conduct real time monitoring of the wide spectrum of the slip rate (from fast- and slow-slip modes) on fault. In addition, it has been required to have more observational examples to figure out unlocking process prior to major earthquakes, and to deepen our fundamental understanding of earthquake generation mechanism.

4. – Conclusions

Here, we discuss the evolution of fault slip rate prior to large earthquake, focusing on the role of slow- and fast-slip modes. We review a wide spectrum of the slip rate from fast- to slow-slip on a natural fault, based on seismic and geodetic observations of various types of slow earthquakes. Complex variation of slow earthquakes can be recognized in time and space. Recent seismic and geodetic studies of foreshock sequences suggest that partial unlocking of fault took place episodically through the interplay between fast- and slow-slip modes before some large earthquakes. The partial unlocking causes stress loading to the nearby fault segments, resulting to triggering of subsequent dynamic and unstable slip. Alternatively, the partial unlocking of fault enhances the strength weakening of the earthquake nucleation area, that ultimately initiates a dynamic rupture. However, the manner of the unlocking is episodic, not smooth acceleration, which precludes a possibility of forecasting the subsequent large earthquake with a high degree of accuracy. The triggering of a subsequent large earthquake on nearby fault segments depends on the areal extent of the critically loaded seismic patches and how close these areas are to

failure, even though the partial unlocking of fault is observed. An important research area is the development of methods for assessing the degree of criticality within fault segments adjacent to already ruptured portions. Furthermore, the earthquake-triggering probability by slow-slip transient shall be incorporated into an operational earthquake forecasting scheme as future challenge.

* * *

We thank JMA for allowing us to use the earthquake catalog. This work was partially supported by JSPS KAKENHI Grant Number JP16H06473, and Earthquake and Volcano Hazards Observation and Research Program in MEXT.

REFERENCES

[1] GOMBERG J., WECH A., CREAGER K., OBARA K. and AGNEW D., "Reconsidering earthquake scaling", *Geophys. Res. Lett.*, **43** (2016) 6243. doi:10.1002/2016GL069967.
[2] BÜRGMANN R., "The geophysics, geology and mechanics of slow fault slip", *Earth Planet. Sci. Lett.*, **495** (2018) 112. doi:10.1016/j.epsl.2018.04.062.
[3] OBARA K., "Nonvolcanic deep tremor associated with subduction in southwest Japan", *Science*, **296** (2002) 1679. doi:10.1126/science.1070378.
[4] PENG Z. and GOMBERG J., "An integrated perspective of the continuum between earthquakes and slow-slip phenomena", *Nat. Geosci.*, **3** (2010) 599. doi:10.1038/ngeo940.
[5] OBARA K. and KATO A., "Connecting slowearthquakes to huge earthquakes", *Science*, **353** (2016) 253. doi:10.1126/science.aaf1512.
[6] ASANO Y., OBARA K., MATSUZAWA T., HIROSE H. and ITO Y., "Possible shallow slow slip events in Hyuga-nada, Nankai subduction zone, inferred from migration of very low frequency earthquakes", *Geophys. Res. Lett.*, **42** (2015) 331. doi:10.1002/2014GL062165.
[7] YOKOTA Y., ISHIKAWA T., WATANABE S. I., TASHIRO T. and ASADA A., "Seafloor geodetic constraints on interplate coupling of the Nankai Trough megathrust zone", *Nature*, **534** (2016) 374. doi:10.1038/nature17632.
[8] ARAKI E., SAFFER D. M., KOPF A. J., WALLACE L. M., KIMURA T., MACHIDA Y., IDE S. and DAVIS E., "Recurring and triggered slow-slip events near the trench at the Nankai Trough subduction megathrust", *Science*, **356** (2017) 1157. doi:10.1126/science.aan3120.
[9] SAGIYA T., "Interplate coupling in the Kanto district, central Japan, and the Boso Peninsula silent earthquake in May 1996", *Pure Appl. Geophys.*, **161** (2004) 2327. doi:10.1007/s00024-004-2566-6.
[10] OKADA Y., KASAHARA K., HORI S., OBARA K., SEKIGUCHI S., FUJIWARA H. and YAMAMOTO A., "Recent progress of seismic observation networks in Japan-Hi-net, F-net, K-NET and KiK-net-", *Earth, Planets Space*, **56** (2004) xv.
[11] SHELLY D. R., BEROZA G. C. and IDE S., "Non-volcanic tremor and low-frequency earthquake swarms", *Nature*, **446** (2007) 305. doi:10.1038/nature05666.
[12] IDE S., BEROZA G. C., SHELLY D. R. and UCHIDE T., "A scaling law for slow earthquakes", *Nature*, **447** (2007) 76. doi:10.1038/nature05780.
[13] ANDO R., TAKEDA N. and YAMASHITA T., "Propagation dynamics of seismic and aseismic slip governed by fault heterogeneity and Newtonian rheology", *J. Geophys. Res. B Solid Earth*, **117** (2012) 1. doi:10.1029/2012JB009532.
[14] OBARA K., MATSUZAWA T., TANAKA S. and MAEDA T., "Depth-dependent mode of tremor migration beneath Kii Peninsula, Nankai subduction zone", *Geophys. Res. Lett.*, **39** (2012) 1. doi:10.1029/2012GL051420.

[15] KANO M., KATO A., ANDO R. and OBARA K., "Strength of tremor patches along deep transition zone of a megathrust", *Sci. Rep.*, **8** (2018) 1. doi:10.1038/s41598-018-22048-8.

[16] DRAGERT H., WANG K. and JAMES T. S., "A silent slip event on the deeper Cascadia subduction interface", *Science*, **292** (2001) 1525. doi:10.1126/science.1060152.

[17] DRAGERT H., WANG K. and ROGERS G., "Geodetic and seismic signatures of episodic tremor and slip in the northern Cascadia subduction zone", *Earth, Planets Space*, **56** (2004) 1143. doi:10.1186/BF03353333.

[18] OBARA K., HIROSE H., YAMAMIZU F. and KASAHARA K., "Episodic slow slip events accompanied by non-volcanic tremors in southwest Japan subduction zone", *Geophys. Res. Lett.*, **31** (2004) 1. doi:10.1029/2004GL020848.

[19] ITO Y., OBARA K., SHIOMI K., SEKINE S. and HIROSE H., "Slow earthquakes coincident with episodic tremors and slow slip events", *Science*, **315** (2007) 503. doi:10.1126/science.1134454.

[20] OBARA K., "Phenomenology of deep slow earthquake family in southwest Japan: Spatiotemporal characteristics and segmentation", *J. Geophys. Res. Solid Earth*, **115** (2010) 1. doi:10.1029/2008JB006048.

[21] HIROSE H. and OBARA K., "Recurrence behavior of short-term slow slip and correlated nonvolcanic tremor episodes in western Shikoku, southwest Japan", *J. Geophys. Res. Solid Earth*, **115** (2010) 1. doi:10.1029/2008JB006050.

[22] NISHIMURA T., MATSUZAWA T. and OBARA K., "Detection of short-term slow slip events along the Nankai Trough, southwest Japan, using GNSS data", *J. Geophys. Res. Solid Earth*, **118** (2013) 3112. doi:10.1002/jgrb.50222.

[23] OZAWA S., YARAI H., IMAKIIRE T. and TOBITA M., "Spatial and temporal evolution of the long-term slow slip in the Bungo Channel, Japan", *Earth, Planets Space*, **65** (2013) 67. doi:10.5047/eps.2012.06.009.

[24] YOSHIOKA S., MATSUOKA Y. and IDE S., "Spatiotemporal slip distributions of three long-term slow slip events beneath the Bungo Channel, southwest Japan, inferred from inversion analyses of GPS data", *Geophys. J. Int.*, **201** (2015) 1437. doi:10.1093/gji/ggv022.

[25] OZAWA S., "Long-term slow slip events along the Nankai trough subduction zone after the 2011 Tohoku earthquake in Japan", *Earth, Planets Space*, **69** (2017) 56. doi:10.1186/s40623-017-0640-4.

[26] OZAWA S., MIYAZAKI S., HATANAKA Y., IMAKIIRE T., KAIDZU M. and MURAKAMI M., "Characteristic silent earthquakes in the eastern part of the Boso peninsula, Central Japan", *Geophys. Res. Lett.*, **30** (2003) 16. doi:10.1029/2002GL016665.

[27] WALLACE L. M., BEAVAN J., BANNISTER S. and WILLIAMS C., "Simultaneous long-term and short-term slow slip events at the Hikurangi subduction margin, New Zealand: Implications for processes that control slow slip event occurrence, duration, and migration", *J. Geophys. Res. B Solid Earth*, **117** (2012) 1. doi:10.1029/2012JB009489.

[28] VALLÉE M., NOCQUET J. M., BATTAGLIA J., FONT Y., SEGOVIA M., RÉGNIER M., MOTHES P., JARRIN P., CISNEROS D., VACA S., YEPES H., MARTIN X., BÉTHOUX N. and CHLIEH M., "Intense interface seismicity triggered by a shallow slow slip event in the Central Ecuador subduction zone", *J. Geophys. Res. Solid Earth*, **118** (2013) 2965. doi:10.1002/jgrb.50216.

[29] HIROSE H., ASANO Y., OBARA K., KIMURA T., MATSUZAWA T., TANAKA S. and MAEDA T., "Slow Earthquakes Linked Along Dip in the Nankai Zone Subduction Zone", *Science*, **330** (2010) 1502.

[30] HIROSE H., KIMURA H., ENESCU B. and AOI S., "Recurrent slow slip event likely hastened by the 2011 Tohoku earthquake", *Proc. Natl. Acad. Sci.*, **109** (2012) 15157. doi:10.1073/pnas.1202709109.

[31] REVERSO T., MARSAN D., HELMSTETTER A. and ENESCU B., "Background seismicity in Boso Peninsula, Japan: Long-term acceleration, and relationship with slow slip events", *Geophys. Res. Lett.*, **43** (2016) 5671. doi:10.1002/2016GL068524.
[32] KATO A., IGARASHI T. and OBARA K., "Detection of a hidden Boso slow slip event immediately after the 2011 M_w 9.0 Tohoku-Oki earthquake, Japan", *Geophys. Res. Lett.*, **41** (2014) 5868. doi:10.1002/2014GL061053.
[33] MITSUI Y., "Interval modulation of recurrent slow slip events by two types of earthquake loading", *Earth, Planets Space*, **67** (2015) 1. doi: 10.1186/s40623-015-0230-2.
[34] WALLACE L. M., KANEKO Y., HREINSDÓTTIR S., HAMLING I., PENG Z., BARTLOW N., D'ANASTASIO E. and FRY B., "Large-scale dynamic triggering of shallow slow slip enhanced by overlying sedimentary wedge", *Nat. Geosci.*, **10** (2017) 765. doi:10.1038/ngeo3021.
[35] ROLANDONE F., NOCQUET J. M., MOTHES P. A., JARRIN P., VALLÉE M., CUBAS N., HERNANDEZ S., PLAIN M., VACA S. and FONT Y., "Areas prone to slow slip events impede earthquake rupture propagation and promote afterslip", *Sci. Adv.*, **4** (2018) 2. doi:10.1126/sciadv.aao6596.
[36] VILLEGAS-LANZA J. C., NOCQUET J. M., ROLANDONE F., VALLEE M., TAVERA H., BONDOUX F., TRAN T., MARTIN X. and CHLIEH M., "A mixed seismic-aseismic stress release episode in the Andean subduction zone", *Nat. Geosci.*, **9** (2015) 150. doi:10.1038/ngeo2620.
[37] SEGALL P., DESMARAIS E. K., SHELLY D., MIKLIUS A. and CERVELLI P., "Earthquakes triggered by silent slip events on Kīlauea volcano, Hawaii", *Nature*, **442** (2006) 71. doi:10.1038/nature04938.
[38] BARTLOW N. M., MIYAZAKI S., BRADLEY A. M. and SEGALL P., "Space-time correlation of slip and tremor during the 2009 Cascadia slow slip event", *Geophys. Res. Lett.*, **38** (2011) 1. doi:10.1029/2011GL048714.
[39] FUKUDA J., KATO A., OBARA K., MIURA S. and KATO T., "Imaging of the early acceleration phase of the 2013-2014 Boso slow slip event", *Geophys. Res. Lett.*, **41** (2014) 7493. doi:10.1002/2014GL061550.
[40] MCLASKEY G. C. and YAMASHITA F., "Slow and fast ruptures on a laboratory fault controlled by loading characteristics", *J. Geophys. Res. Solid Earth*, **122** (2017) 3719. doi:10.1002/2016JB013681.
[41] FUKUDA J., "Variability of the Space-Time Evolution of Slow Slip Events Off the Boso Peninsula, Central Japan, From 1996 to 2014", *J. Geophys. Res. Solid Earth*, **123** (2018) 732. doi:10.1002/2017JB014709.
[42] DODGE D. A., BEROZA G. C. and ELLSWORTH W. L., "Detailed observations of California foreshock sequences: Implications for the earthquake initiation process", *J. Geophys. Res. Solid Earth*, **101** (1996) 22371. doi:10.1029/96JB02269.
[43] BOUCHON M., DURAND V., MARSAN D., KARABULUT H. and SCHMITTBUHL J., "The long precursory phase of most large interplate earthquakes", *Nat. Geosci.*, **6** (2013) 299. doi:10.1038/ngeo1770.
[44] SHEARER P. M., *Introduction to Seismology* (Cambridge University Press) 2009.
[45] JONES L. M. and MOLNAR P., "Some characteristics of foreshocks and their possible relationship to earthquake prediction and premonitory slip on faults", *J. Geophys. Res.*, **84** (1979) 3596. doi:10.1029/JB084iB07p03596.
[46] REASENBERG P. A., "Foreshock occurrence rates before large earthquakes worldwide", *Pure Appl. Geophys.*, **155** (1999) 355. doi:10.1007/s000240050269.
[47] TAMARIBUCHI K., YAGI Y., ENESCU B. and HIRANO S., "Characteristics of foreshock activity inferred from the JMA earthquake catalog", *Earth, Planets Space*, **70** (2018) 90. doi:10.1186/s40623-018-0866-9.

[48] KATO A., OBARA K., IGARASHI T., TSURUOKA H., NAKAGAWA S. and HIRATA N., "Propagation of slow slip leading up to the 2011 M_w 9.0 Tohoku-Oki earthquake", *Science*, **335** (2012) 705. doi:10.1126/science.1215141.

[49] MIYAZAKI S., MCGUIRE J. J. and SEGALL P., "Seismic and aseismic fault slip before and during the 2011 off the Pacific coast of Tohoku Earthquake", *Earth, Planets Space*, **63** (2011) 637. doi:10.5047/eps.2011.07.001.

[50] OHTA Y., HINO R., INAZU D., OHZONO M., ITO Y., MISHINA M., IINUMA T., NAKAJIMA J., OSADA Y., SUZUKI K., FUJIMOTO H., TACHIBANA K., DEMACHI T. and MIURA S., "Geodetic constraints on afterslip characteristics following the March 9, 2011, Sanriku-oki earthquake, Japan", *Geophys. Res. Lett.*, **39** (2012) 4. doi:10.1029/2012GL052430.

[51] ITO Y., HINO R., KIDO M., FUJIMOTO H., OSADA Y., INAZU D., OHTA Y., IINUMA T., OHZONO M., MIURA S., MISHINA M., SUZUKI K., TSUJI T. and ASHI J., "Episodic slow slip events in the Japan subduction zone before the 2011 Tohoku-Oki earthquake", *Tectonophysics*, **600** (2013) 14. doi:10.1016/j.tecto.2012.08.022.

[52] HINO R., INAZU D., OHTA Y., ITO Y., SUZUKI S., IINUMA T., OSADA Y., KIDO M., FUJIMOTO H. and KANEDA Y., "Was the 2011 Tohoku-Oki earthquake preceded by aseismic preslip? Examination of seafloor vertical deformation data near the epicenter", *Mar. Geophys. Res.*, **35** (2014) 181. doi:10.1007/s11001-013-9208-2.

[53] OHNAKA M., "A physical scaling relation between the size of an earthquake and its nucleation zone size", *Pure Appl. Geophys.*, **157** (2000) 2259.

[54] OZAWA S., NISHIMURA T., MUNEKANE H., SUITO H., KOBAYASHI T., TOBITA M. and IMAKIIRE T., "Preceding, coseismic, and postseismic slips of the 2011 Tohoku earthquake, Japan", *J. Geophys. Res. Solid Earth*, **117** (2012) B07404. doi:10.1029/2011JB009120.

[55] YOKOTA Y. and KOKETSU K., "A very long-term transient event preceding the 2011 Tohoku earthquake", *Nat. Commun.*, **6** (2015) 1. doi:10.1038/ncomms6934.

[56] MAVROMMATIS A. P., SEGALL P., UCHIDA N. and JOHNSON K. M., "Long-term acceleration of aseismic slip preceding the M_w 9 Tohoku-oki earthquake: Constraints from repeating earthquakes", *Geophys. Res. Lett.*, **42** (2015) 9717. doi:10.1002/2015GL066069.

[57] MATSUZAWA T., ASANO Y. and OBARA K., "Very low frequency earthquakes off the Pacific coast of Tohoku, Japan", *Geophys. Res. Lett.*, **42** (2015) 4318. doi:10.1002/2015GL063959.

[58] SATO T., HIRATSUKA S. and MORI J., "Precursory seismic activity surrounding the high-slip patches of the 2011 M_w 9.0 Tohoku-Oki earthquake", *Bull. Seismol. Soc. Am.*, **103** (2013) 3104. doi:10.1785/0120130042.

[59] UCHIDA N., IINUMA T., NADEAU R. M., BÜRGMANN R. and HINO R., "Periodic slow slip triggers megathrust zone earthquakes in northeastern Japan", *Science*, **351** (2016) 488. doi:10.1126/science.aad3108.

[60] MATSUZAWA T., UCHIDA N., IGARASHI T., OKADA T. and HASEGAWA A., "Repeating earthquakes and quasi-static slip on the plate boundary east off northern Honshu, Japan", *Earth, Planets Space*, **56** (2004) 803.

[61] KATO A. and NAKAGAWA S., "Multiple slow-slip events during a foreshock sequence of the 2014 Iquique, Chile M_w 8.1 earthquake", *Geophys. Res. Lett.*, **41** (2014) 5420. doi:10.1002/2014GL061138.

[62] RUIZ S., METOIS M., FUENZALIDA A., RUIZ J., LEYTON F., GRANDIN R., VIGNY C., MADARIAGA R. and CAMPOS J., "Intense foreshocks and a slow slip event preceded the 2014 Iquique M_w 8.1 earthquake", *Science*, **1165** (2014) 1165. doi:10.1126/science.1256074.

[63] SCHURR B., ASCH G., HAINZL S., BEDFORD J., HOECHNER A., PALO M., WANG R., MORENO M., BARTSCH M., ZHANG Y., ONCKEN O., TILMANN F., DAHM T., VICTOR P., BARRIENTOS S. and VILOTTE J. P., "Gradual unlocking of plate boundary controlled initiation of the 2014 Iquique earthquake", *Nature*, **512** (2014) 299. doi:10.1038/nature13681.

[64] KATO A., FUKUDA J., KUMAZAWA T. and NAKAGAWA S., "Accelerated nucleation of the 2014 Iquique, Chile M_w 8.2 Earthquake", *Sci. Rep.*, **6** (2016) 1. doi:10.1038/srep24792.

[65] MENG L., HUANG H., BÜRGMANN R., AMPUERO J. P. and STRADER A., "Dual megathrust slip behaviors of the 2014 Iquique earthquake sequence", *Earth Planet. Sci. Lett.*, **411** (2015) 177. doi:10.1016/j.epsl.2014.11.041.

[66] HERMAN M. W., FURLONG K. P., HAYES G. P. and BENZ H. M., "Foreshock triggering of the 1 April 2014 M_w 8.2 Iquique, Chile, earthquake", *Earth Planet. Sci. Lett.*, **447** (2016) 119. doi:10.1016/j.epsl.2016.04.020.

[67] SOCQUET A., VALDES J. P., JARA J., COTTON F., WALPERSDORF A., COTTE N., SPECHT S., ORTEGA-CULACIATI F., CARRIZO D. and NORABUENA E., "An 8 month slow slip event triggers progressive nucleation of the 2014 Chile megathrust", *Geophys. Res. Lett.*, **44** (2017) 4046. doi:10.1002/2017GL073023.

[68] RUIZ S., ADEN-ANTONIOW F., BAEZ J. C., OTAROLA C., POTIN B., DEL CAMPO F., POLI P., FLORES C., SATRIANO C., LEYTON F., MADARIAGA R. and BERNARD P., "Nucleation Phase and Dynamic Inversion of the M_w 6.9 Valparaíso 2017 Earthquake in Central Chile", *Geophys. Res. Lett.*, **44** (2017) 10,290. doi:10.1002/2017GL075675.

[69] OHNAKA M. and SHEN L., "Scaling of the shear rupture process from nucleation to dynamic propagation: Implications of geometric irregularity of the rupturing surfaces", *J. Geophys. Res. Solid Earth*, **104** (1999) 817. doi:10.1029/1998JB900007.

[70] MCLASKEY G. C. and KILGORE B. D., "Foreshocks during the nucleation of stick-slip instability", *J. Geophys. Res. Solid Earth*, **118** (2013) 2982. doi:10.1002/jgrb.50232.

[71] XU S., FUKUYAMA E., YAMASHITA F., MIZOGUCHI K., TAKIZAWA S. and KAWAKATA H., "Strain rate effect on fault slip and rupture evolution: Insight from meter-scale rock friction experiments", *Tectonophysics*, **733** (2018) 209. doi:10.1016/j.tecto.2017.11.039.

[72] MAZZOTTI S. and ADAMS J., "Variability of near-term probability for the next great earthquake on the Cascadia subduction zone", *Bull. Seismol. Soc. Am.*, **94** (2004) 1954. doi:10.1785/012004032.

[73] DIXON T. H., JIANG Y., MALSERVISI R., MCCAFFREY R., VOSS N., PROTTI M. and GONZALEZ V., "Earthquake and tsunami forecasts: Relation of slow slip events to subsequent earthquake rupture", *Proc. Natl. Acad. Sci. U.S.A.*, **111** (2014) 17039. doi:10.1073/pnas.1412299111.

[74] GRAHAM S. E., DEMETS C., CABRAL-CANO E., KOSTOGLODOV V., WALPERSDORF A., COTTE N., BRUDZINSKI M., MCCAFFREY R. and SALAZAR-TLACZANI L., "GPS constraints on the 2011-2012 Oaxaca slow slip event that preceded the 2012 March 20 Ometepec earthquake, southern Mexico", *Geophys. J. Int.*, **197** (2014) 1593. doi:10.1093/gji/ggu019.

[75] RADIGUET M., PERFETTINI H., COTTE N., GUALANDI A., VALETTE B., KOSTOGLODOV V., LHOMME T., WALPERSDORF A., CABRAL CANO E. and CAMPILLO M., "Triggering of the 2014 M_w 7.3 Papanoa earthquake by a slow slip event in Guerrero, Mexico", *Nat. Geosci.*, **9** (2016) 829. doi:10.1038/ngeo2817.

[76] SEGALL P. and BRADLEY A. M., "Slow-slip evolves into megathrust earthquakes in 2D numerical simulations", *Geophys. Res. Lett.*, **39** (2012) 2. doi:10.1029/2012GL052811.

[77] VOSS N., DIXON T. H., LIU Z., MALSERVISI R., PROTTI M. and SCHWARTZ S., "Do slow slip events trigger large and great megathrust earthquakes?", *Sci. Adv.*, **4** (2018) 1. doi:10.1126/sciadv.aat8472.

[78] MATSUMOTO S., NAKAO S., OHKURA T., MIYAZAKI M., SHIMIZU H., ABE Y., INOUE H., NAKAMOTO M., YOSHIKAWA S. and YAMASHITA Y., "Spatial heterogeneities in tectonic stress in Kyushu, Japan and their relation to a major shear zone", *Earth, Planets Space*, **67** (2015) 0. doi:10.1186/s40623-015-0342-8.

[79] KATO A., FUKUDA J., NAKAGAWA S. and OBARA K., "Foreshock migration preceding the 2016 M_w 7.0 Kumamoto earthquake, Japan", *Geophys. Res. Lett.*, **43** (2016) 8945. doi:10.1002/2016GL070079.

[80] PENG Z. and ZHAO P., "Migration of early aftershocks following the 2004 Parkfield earthquake", *Nat. Geosci.*, **2** (2009) 877. doi:10.1038/ngeo697.

[81] KATO A. and OBARA K., "Step-like migration of early aftershocks following the 2007 M_w 6.7 Noto-Hanto earthquake, Japan", *Geophys. Res. Lett.*, **41** (2014) 3864. doi:10.1002/2014GL060427.

[82] PERFETTINI H., FRANK W. B., MARSAN D. and BOUCHON M., "A Model of Aftershock Migration Driven by Afterslip", *Geophys. Res. Lett.*, **45** (2018) 2283. doi:10.1002/2017GL076287.

[83] CHELONI D., GIULIANI R., D'AGOSTINO N., MATTONE M., BONANO M., FORNARO G., LANARI R., REALE D. and ATZORI S., "New insights into fault activation and stress transfer between en echelon thrusts: The 2012 Emilia, Northern Italy, earthquake sequence", *J. Geophys. Res. Solid Earth*, **121** (2016) 4742. doi:10.1002/2016JB012823.

[84] HAMLING I. J., HREINSDÓTTIR S., CLARK K., ELLIOTT J., LIANG C., FIELDING E., LITCHFIELD N., VILLAMOR P., WALLACE L., WRIGHT T. J., D'ANASTASIO E., BANNISTER S., BURBIDGE D., DENYS P., GENTLE P., HOWARTH J., MUELLER C., PALMER N., PEARSON C., POWER W., BARNES P., BARRELL D. J. A., VAN DISSEN R., LANGRIDGE R., LITTLE T., NICOL A., PETTINGA J., ROWLAND J. and STIRLING M., "Complex multifault rupture during the 2016 M_w 7.8 Kaikōura earthquake, New Zealand", *Science*, **356** (2017) eaam7194. doi:10.1126/science.aam7194.

[85] WALLACE L. M., HREINSDÓTTIR S., ELLIS S., HAMLING I., D'ANASTASIO E. and DENYS P., "Triggered Slow Slip and Afterslip on the Southern Hikurangi Subduction Zone Following the Kaikōura Earthquake", *Geophys. Res. Lett.*, **45** (2018) 1. doi:10.1002/2018GL077385.

[86] WALLACE L. M., ARAKI E., SAFFER D., WANG X., ROESNER A., KOPF A., NAKANISHI A., POWER W., KOBAYASHI R., KINOSHITA C., TOCZKO S., KIMURA T., MACHIDA Y. and CARR S., "Near-field observations of an offshore M_w 6.0 earthquake from an integrated seafloor and subseafloor monitoring network at the Nankai Trough, southwest Japan", *J. Geophys. Res. Solid Earth*, **121** (2016) 8338. doi:10.1002/2016JB013417.

[87] NAKANO M., HYODO M., NAKANISHI A., YAMASHITA M., HORI T., KAMIYA S., SUZUKI K., TONEGAWA T., KODAIRA S., TAKAHASHI N. and KANEDA Y., "The 2016 M_w 5.9 earthquake off the southeastern coast of Mie Prefecture as an indicator of preparatory processes of the next Nankai Trough megathrust earthquake", *Prog. Earth Planet. Sci.*, **5** (2018) 30. doi:10.1186/s40645-018-0188-3.

[88] JORDAN T. H., CHEN Y. T., GASPARINI P., MADARIAGA R., MAIN I., MARZOCCHI W., PAPADOPOULOS G., SOBOLEV G., YAMAOKA K. and ZSCHAU J., "Operational earthquake forecasting: State of knowledge and guidelines for utilization", *Ann. Geophys.*, **54** (2011) 319. doi:10.4401/ag-5350.

[89] OGATA Y., "Statistics of Earthquake Activity: Models and Methods for Earthquake Predictability Studies", *Annu. Rev. Earth Planet. Sci.*, **45** (2017) 497. doi:10.1146/annurev-earth-063016-015918.

[90] FIELD E. H., MILNER K. R., HARDEBECK J. L., PAGE M. T., VAN DER ELST N., JORDAN T. H., MICHAEL A. J., SHAW B. E. and WERNER M. J., "A spatiotemporal clustering model for the third uniform California earthquake rupture forecast (UCERF3-ETAS): Toward an operational earthquake forecast", *Bull. Seismol. Soc. Am.*, **107** (2017) 1049. doi:10.1785/0120160173.

Proceedings of the International School of Physics "Enrico Fermi"
Course 202 "Mechanics of Earthquake Faulting", edited by A. Bizzarri, S. Das and A. Petri
(IOS, Amsterdam; SIF, Bologna) 2019
DOI 10.3254/978-1-61499-979-9-81

The spectrum of fault slip modes from elastodynamic rupture to slow earthquakes

Chris Marone(*)

Department of Geosciences and Energy Institute, Penn State University
University Park, PA 16802, USA

Summary. — Earthquake science is in the midst of a revolution. Our understanding of tectonic faulting has been shaken to the core by the discovery of seismic tremor, low frequency earthquakes, slow slip events, and other modes of fault slip. These phenomena represent modes of failure that were thought to be non-existent and theoretically impossible only a few years ago. Despite the growing number of observations of slow earthquakes and the fact that they can trigger catastrophic large earthquakes their origin remains unresolved. Basic questions remain regarding how slow ruptures can propagate quasi-dynamically, at speeds far below the Rayleigh wave speed, and how tectonic faults can host both slow slip and dynamic earthquake rupture. Here, I summarize results from laboratory experiments showing repetitive slow slip, describe friction laws for slow earthquakes, and discuss implications of the work for earthquake scaling laws. The lab results suggest that slow earthquakes occur for conditions near the stability boundary defined by the critical fault rheologic weakening rate K_c and that the spectrum of fault slip behaviors can be described with a single frictional mechanism. Other processes may contribute to the origin of slow earthquakes but the work summarized here shows that slow and quasi-dynamic fault slip can occur entirely as a result of frictional processes and fault zone heterogeneity.

(*) E-mail: cjm38@psu.edu

1. – Introduction

Slow earthquakes represent one mode of the spectrum of fault slip behaviors ranging from steady aseismic slip to ordinary (fast) earthquakes [1-7]. Like ordinary earthquakes, slow earthquakes can accommodate a significant fraction of a fault's slip budget, with equivalent magnitudes of 8 or larger; yet this slip occurs slowly, over days to months, rather than the few 10's of seconds for ordinary earthquakes [8-13]. Geodetic and seismic data show that slow slip events propagate along tectonic faults as *quasi-dynamic* ruptures with fault slip speed and propagation velocity controlled by unknown processes [14]. How are these phenomena related to normal earthquakes? Why do slow earthquakes appear to exhibit a different scaling law between size and duration compared to ordinary earthquakes? What processes limit the slip velocity and rupture propagation speed of slow earthquakes? Here, I suggest an explanation for slow earthquakes that draws on recent breakthroughs in our ability to produce repetitive, slow stick-slip in the laboratory [15-24]. The work follows the connection between frictional stick-slip and earthquakes [25] and provides insights on slow earthquakes and the spectrum of fault slip behaviors.

Since the discovery of tectonic tremor [4] and slow slip events [5, 6] evidence for a spectrum of fault slip behaviors has been observed along tectonic faults worldwide [26-31]. Slow slip and tremor have been observed in subduction zones and on transform faults such as the San Andreas Fault in California [32-37]. Although tremor and slow slip are often difficult to locate, it is now widely accepted that they represent frictional slip at the plate interface [35, 36].

A growing number of numerical models can simulate quasi-dynamic fault slip with characteristics that are similar to those observed in nature [38-48]. Many of these models have focused on observations from the downdip limit of the seismogenic zone in subduction settings, where the *in situ* conditions are difficult to reproduce in the laboratory. This is perhaps one reason for the paucity of laboratory data on repetitive, slow stick-slip until very recently (but see refs. [49-52]) and related studies of slow rupture or the onset of slip [53-59]. However, we have recently learned how to produce repetitive, slow stick-slip events under controlled conditions [15-22]. Here, I describe the mechanics of slow slip, drawing on lab observations, and applications to tectonic faulting.

2. – Mechanics of slow slip

Although there are now numerous instrumental observations of slow earthquakes, the underlying processes that produce these self-sustaining ruptures remain poorly understood. Several mechanisms have been proposed, including dilatant hardening, elevated fluid pressure, (*e.g.*, refs. [37, 42-44, 47, 60-65]), a transition in frictional behavior with increasing slip speed, and fault zone heterogeneity as imaged by geologic and geophysical techniques [65-68]. In the context of some of these models, slow earthquakes represent prematurely arrested ordinary earthquakes. However, laboratory observations of slow slick-slip and associated measurement of candidate processes are scarce. Moreover, if

slow earthquakes indeed initiate like ordinary earthquakes, they may be particularly good targets for exploration of precursors to failure [15, 19]. The duration of precursory behaviors such as accelerating fault slip or elastic wave-speed reduction may scale with slip duration and thus be easier to observe for slow events.

2˙1. *Friction laws for slow slip.* – Frictional instability and earthquake nucleation are often evaluated using rate- and state-dependent friction laws [69-72]. Within this framework and using 1-D elastic coupling, the criterion for slip instability is derived from a force balance, in which the elastic stiffness of the loading system K (units of stress/length) must be smaller than a rheologic, critical stiffness K_c defined by the frictional properties [39]:

$$K_c = \frac{\sigma_n(b-a)}{D_c}\left[1 + \frac{m{V_o}^2}{\sigma_n a D_c}\right], \tag{1}$$

where σ_n is the effective normal stress, D_c is a critical slip distance over which fault strength evolves, m is mass, and the parameters a and b are the friction direct effect and evolution parameter, respectively, of the rate and state friction laws. For nucleation of failure, when slip velocity is low, the inertial term of eq. (1) can be ignored. The change in steady-state sliding friction $\Delta\mu$ with a change in slip velocity from V_o to V is given by $(a-b)$

$$(a-b) = \frac{\Delta\mu}{\Delta \ln V}\,. \tag{2}$$

Positive values of $a-b$ represent velocity-strengthening behavior, in which an increase in sliding velocity results in an increase in steady-state sliding friction $\Delta\mu$, and indicates that stable frictional sliding should be expected. Negative values of $a-b$ (velocity-weakening) are a necessary condition for frictional slip instability, with $K < K_c$ (eq. (1)) representing the sufficient condition [39].

Equation (1) suggests that dynamic instability will occur if the elastic unloading stiffness K is minimally below K_c. However, this result is for an extremely simplified case with 1-D elasticity and uniform frictional properties that are independent of slip velocity. Other forms of the stability parameter have been developed for more complex elastic interactions and to account for important aspects of earthquake nucleation [73]. Laboratory data and theoretical models indicate more complex slip behaviors for more complex friction laws [38-44, 54-56], however, there are relatively few detailed laboratory studies that document these conditions.

2˙2. *Laboratory observations of the full spectrum of slip modes from fast to slow.* – Recent works document repetitive stick-slip motion for the complete spectrum of fault slip behaviors observed in nature, with systematic measurements that range from transient slow slip to fast stick-slip [15, 17, 22]. The laboratory experiments reproduce the full spectrum of fault slip behaviors, from fast to slow (fig. 1). These data are from fault zones

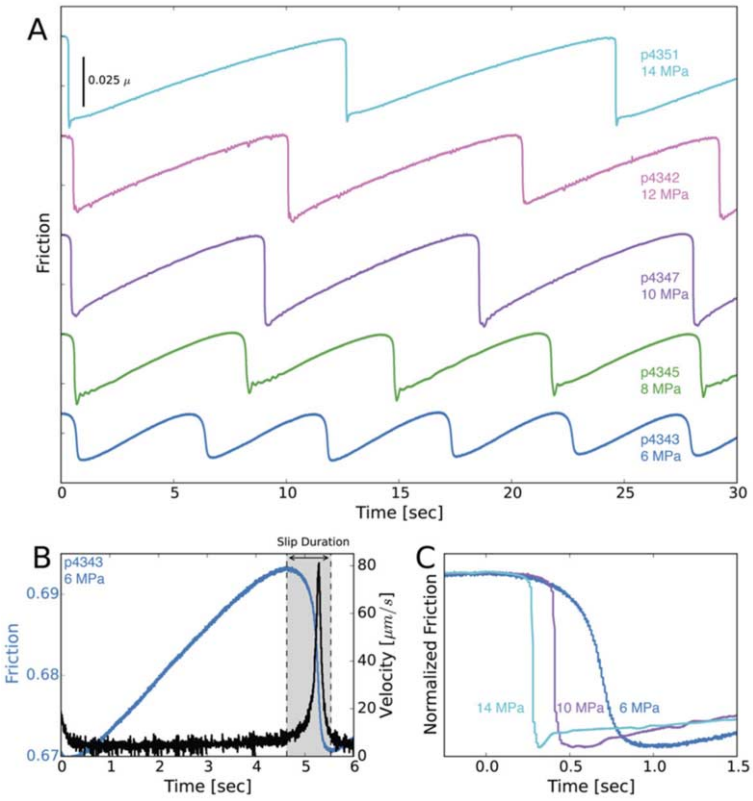

Fig. 1. – Data for simulated faults composed of quartz powder. A) Friction data are plotted at the same scale (note scale bar) and offset for comparison. Annotations on the right give experiment number and normal stress. Stick-slip friction drop is smaller and events have systematically longer duration at lower normal stresses. B) Detail of friction and fault slip for a slow slip event; maximum slip rate during failure is $80\,\mu$m/s. C) Comparison of slip events at three normal stresses. Time is set to zero at maximum friction for each curve. Slip accelerates more slowly at lower normal stress and event durations are systematically longer than at higher normal stress, where the main slip pulse occurs in $\ll 1$ s. (Data from Leeman *et al.*, ref. [18].)

composed of quartz powder and sheared in the double-direct shear configuration [18]. Shear is imposed at constant fault normal stress and load point velocity. Normal stress is varied over a range of values to produce a range of effective shear loading stiffnesses K/σ_n (fig. 1). These results show that stick-slip instability and fault zone failure occurs when the fault weakening rate, given by K_c, exceeds the rate at which elastic unloading can occur K. In the lab, K_c typically increases with fault zone shear strain because D_c decreases with strain [74] and the friction rate parameter $(b-a)$ increases with strain [71, 72, 74-76].

For many fault rocks and granular materials, the parameter $(b-a)$ is initially negative (indicating velocity strengthening behavior) and transitions to velocity weakening with

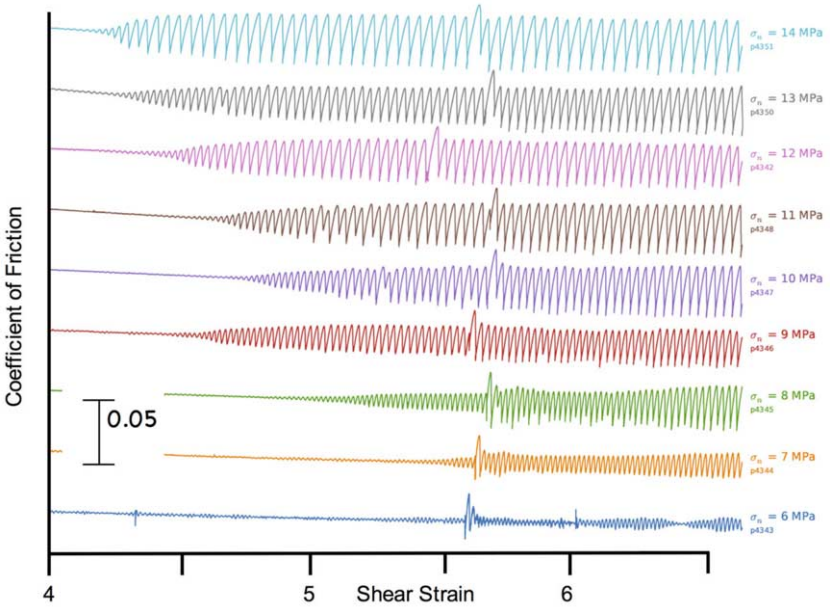

Fig. 2. – Friction data from experiments at a series of normal stresses. Annotations on the right give experiment number and normal stress. Data are plotted at the same scale and offset for comparison. Note that the transition from stable sliding to unstable slip occurred at smaller values of shear strain for experiments conducted at higher normal stress. Anomalous peak values near shear strain of 5.5 are associated with short periods when sliding was stopped. Note that these slide-hold-slide periods cause friction to increase transiently before returning to the initial behavior. (Data from Leeman *et al.*, ref. [18].)

increasing shear strain [72]. In experiments designed to explore the stability transition near $K/K_c = 1.0$, Leeman and co-workers [18] and Scuderi and co-workers [19] found a continuous transition from stable sliding to unstable creep-slip and stick-slip motion (fig. 2). They showed that the transition to unstable slip occurred at smaller values of shear strain for experiments conducted at higher normal stress (fig. 2). This is consistent with a higher value of the frictional weakening rate K_c at higher normal stress (eq. (1)). They also found that K increased with shear strain, but the increase in K_c with strain was larger and thus K_c exceeded K causing instability (fig. 2). The stick-slip events shown in fig. 2 exhibit a wide range of failure modes, spanning the spectrum from slow, creep-slip events to dynamic failure (fig. 3).

Linear stability analysis indicates that frictional motion governed by simple rate state friction should transition abruptly from stable to unstable motion at $K = K_c$ (*e.g.*, refs. [39, 77]). Furthermore, slip velocity in such failure events is predicted to increase without bound. However, the lab data indicate a spectrum of failure modes including slow slip (fig. 3). These data show that peak slip velocity during lab earthquakes varies systematically with $\kappa = K/K_c$, from slow slip for $\kappa > 1$ to dynamic, fast events for

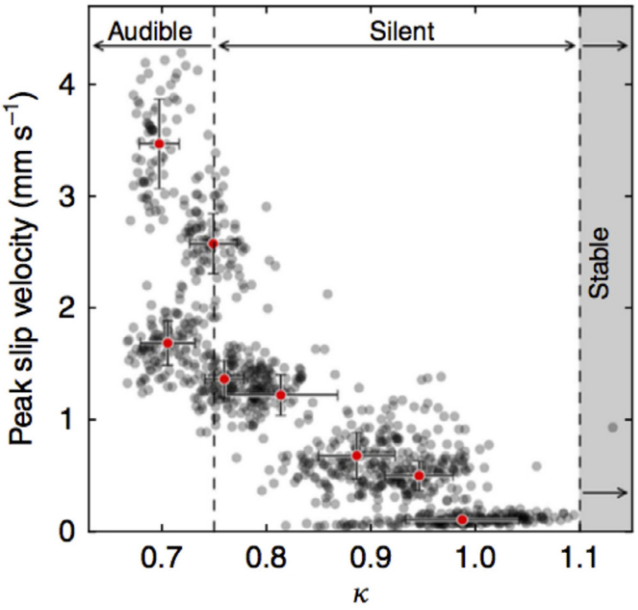

Fig. 3. – Data for lab earthquakes showing fault slip velocity during failure events as a function of the ratio K/K_c. Only stable sliding is observed for $K/K_c > 1.1$. Slow slip events occur for values near 1.0 and dynamic failure events occur for values of K/K_c below about 0.75. (Data from Leeman *et al.*, ref. [18].)

$\kappa < 1$ (fig. 3). The experiments show only stable sliding when the stability parameter κ exceeds 1.1, and that a broad region of slow slip occurs for values near 1.0. When the critical frictional weakening rate K_c becomes large and κ drops below about 0.75, the lab earthquakes become dynamic and are associated with loud acoustic coupling (fig. 3). The observed range of failure modes is consistent with the spectrum of fault slip modes observed in nature.

2˙3. *Mechanics of laboratory slow earthquakes.* – While the origin of slow earthquakes is still enigmatic, the lab work shows that slow slip occurs because the critical weakening rate depends on slip velocity [15, 19, 22]. For a range of loading stiffnesses, the lab work shows that K_c decreases with increasing slip velocity (fig. 4). For granular fault zones, the reduction in K_c is a product of an increase in D_c with slip velocity [78] and a reduction of $(b-a)$ with slip velocity [18,19]. The decrease in $(b-a)$ with increasing slip velocity has been proposed in previous work and similar ideas have been described in the context of more complex, two-state variable friction laws [45,46]. It has also been observed in a few other cases, including clays and serpentine [15, 79-82]. The fact that K_c decreases with slip velocity means that an unstable slip event may be quenched as it accelerates above a critical slip velocity (fig. 4). This effect has been documented previously for friction of technological materials [52] and requires additional study for geophysical conditions.

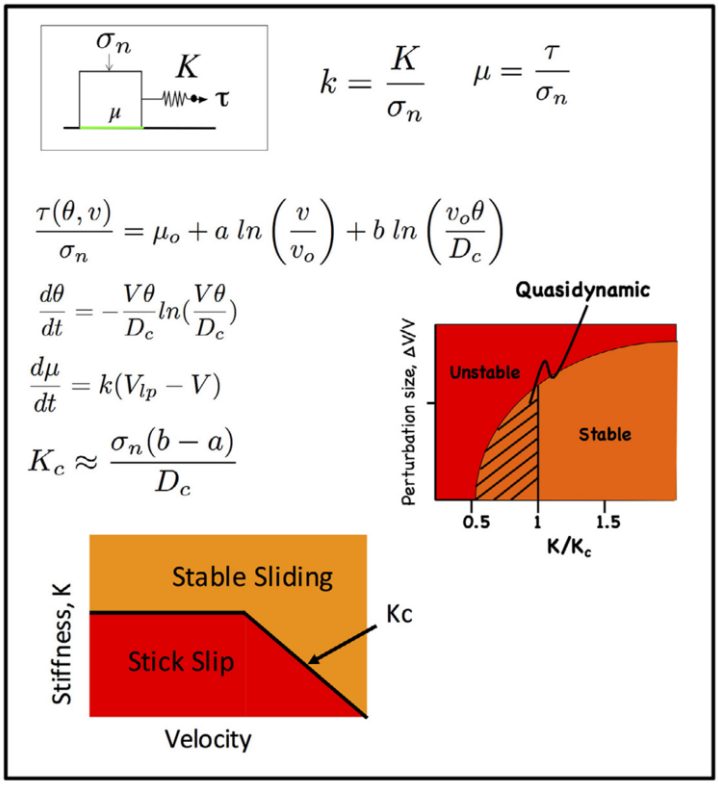

Fig. 4. – Stability of frictional sliding for a spring-slider system that obeys rate and state friction. Lab data indicate quasi-dynamic motion for values of K/K_c slightly below 1.0 and that K_c decreases with slip velocity. The decrease of K_c with slip velocity means that an unstable slip event may nucleate but then be quenched as it accelerates and slip velocity reaches a critical value.

3. – Earthquake scaling laws for dynamic rupture and slow slip

For ordinary earthquakes, the scaling relations between earthquake size and duration are consistent with elastodynamic rupture models and friction stability theory (fig. 5). Box A of fig. 5 shows the relation between stress drop $\Delta\sigma$ and rupture size for a circular fault patch in an elastic medium with shear modulus G and Poisson ratio of 0.25. Combining this with the definition of seismic moment M_o in terms of fault area A and average slip u yields the relation between moment, stress drop, and rupture radius (fig. 5, box A). Given that neither stress drop nor rupture velocity V_r are observed to scale with earthquake rupture size, this model predicts that seismic moment should scale with the cube of duration T (fig. 5), consistent with observations [7, 9]. Existing works have suggested that slow earthquakes may obey a different scaling law, such that seismic moment scales linearly with duration [7], although this interpretation has been questioned [83, 84].

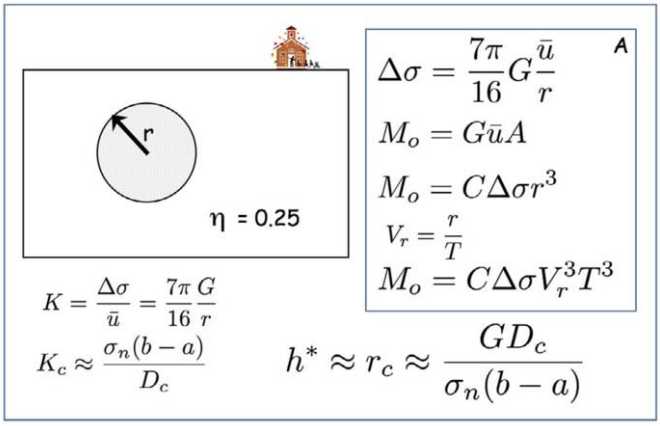

Fig. 5. – Earthquake nucleation and rupture model. Sketch at upper left shows slip patch of size r in a homogeneous elastic medium with shear modulus G and Poisson ratio of 0.25. Box A gives the relation between stress drop $\Delta\sigma$ and the ratio of average slip u to slip patch radius r. Combining this with seismic moment M_o yields a relation between M_o, stress drop and rupture dimension. Replacing rupture size with rupture velocity V_r and duration T yields a relation between M_o and the cube of duration. The equations in the lower left give the stiffness K around a slip patch, which when combined with K_c yields a critical slip patch size h^* or r_c for nucleation of unstable slip. Regions of slip that are smaller than h^* will creep stably, whereas those that grow quasi-statically to a size that exceeds h^* will accelerate into a dynamically propagating instability.

The rupture model and earthquake scaling law can be connected to a model for rupture nucleation (fig. 5). This model is based on the idea that earthquakes nucleate when a slip patch exceeds a critical dimension commonly referred to as h^* or r_c (fig. 5). In the context of the model for frictional stability (fig. 4), h^* and the critical patch size for nucleation can be estimated from the local stiffness K around the slip patch and the critical frictional weakening rate K_c (fig. 5). Note that the relation for h^* (fig. 5) is approximate because stiffness is derived from the average slip whereas nucleation would be derived from the maximum slip, at the center of the dislocation, which would require a small adjustment. The relation for h^* defines a minimum earthquake size [85] that depends on the friction parameters and the local elastic properties. An important implication for slow earthquakes is that dynamic rupture should occur for slip patches larger than h^*. Slow slip could occur for slip patches smaller than h^*, but the stiffness around larger patches would be smaller than K_c and thus slip should accelerate into a dynamic rupture.

The earthquake nucleation model outlined in fig. 5 involves several simplifications and approximations. For example, it assumes isotropic elastic properties, a homogeneous distribution of initial stress and frictional properties, and a simplistic friction law that is independent of slip velocity. If we incorporate the lab results summarized here showing that K_c varies with slip velocity, we would predict that h^* increases with fault slip

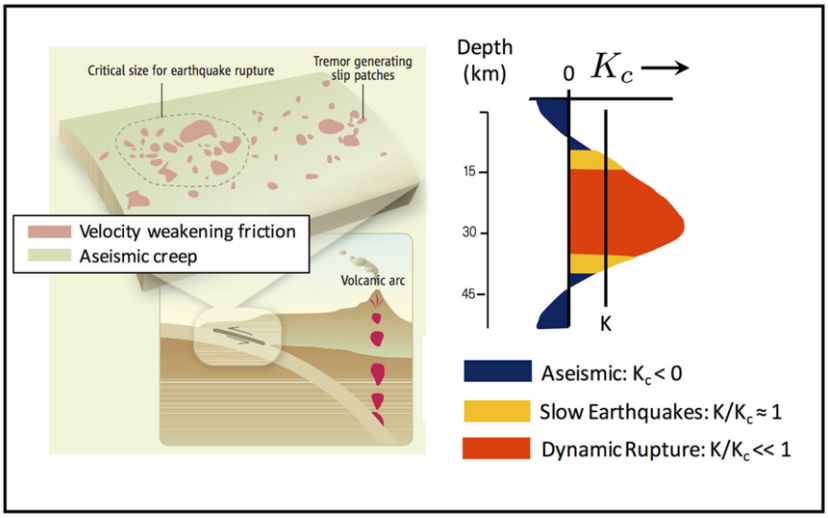

Fig. 6. – Earthquake nucleation model. Left: subduction zone with zoom to show fault zone heterogeneity. Note patches with velocity weakening frictional properties surrounded by regions of aseismic creep. For a heterogeneous fault zone, the critical size for earthquake rupture nucleation may exceed the size of velocity weakening frictional patches, which could produce slow slip and quasi-dynamic rupture. Right: depth variation of fault rheology showing the critical frictional weakening rate K_c in relation to fault zone stiffness K. Slow earthquakes would be expected in regions where $K/K_c \approx 1$.

velocity. Further, including heterogeneity of fault zone frictional properties [65] would effectively increase the nucleation patch size if velocity weakening patches were smaller than h^* (fig. 6). Earthquake nucleation on a heterogeneous fault might begin when slip reached a dimension equal to h^*, but then arrest until slip grew to a larger size, dictated by a combination of frictional properties and heterogeneity (fig. 6). It is interesting to note that if rupture patch size were limited by heterogeneity, such that propagation occurred at a fixed size, the resulting moment-duration relation would be linear, as reported in various works [7, 9]. For a range of heterogeneities, one could imagine a broad range of rupture propagation rates and rupture dimensions, dictated by frictional heterogeneity and the effective local stiffness around a patch that encompassed regions of aseismic/viscous creep and velocity weakening friction.

4. – Conclusions

Laboratory results show the complete spectrum of slip modes from fast to slow and provide an analogy for the spectrum of fault slip behaviors from ordinary (fast) elastodynamic rupture to slow earthquakes. I summarize results showing that slow earthquakes are expected near the threshold between stable and unstable failure, controlled by the interplay of fault zone frictional properties, including rate dependence of the critical rhe-

ologic friction parameter K_c, and elastic stiffness of the surrounding rock. In the context of this view, slow earthquakes and transient fault slip arise from the same governing frictional dynamics as ordinary earthquakes. This mechanism could act in concert with other mechanisms that have been proposed for slow earthquakes, including fault zone dilatancy, and is consistent with the broad range of geologic environments where slow earthquakes are observed.

REFERENCES

[1] SACKS I. S., SUYEHIRO S., LINDE A. T. and SNOKE J. A., Slow earthquakes and stress redistribution, *Nature*, **275** (1978) 599.

[2] GLADWIN M., GWYTHER R., HART R. and BRECKENRIDGE K., Measurements of the strain field associated with episodic creep events on the San Andreas fault near San Juan Bautista, California, *J. Geophys. Res.*, **99** (1994) 4559.

[3] BEROZA G. C. and JORDAN T. H., Searching for slow and silent earthquakes using free oscillations, *J. Geophys. Res.*, **95** (1990) 2485.

[4] OBARA K., Nonvolcanic deep tremor associated with subduction in southwest Japan, *Science*, **296** (2002) 1679.

[5] DRAGERT H., WANG K. and JAMES T. S., A silent slip event on the deeper Cascadia subduction interface, *Science*, **292** (2001) 1525.

[6] ROGERS G. and DRAGERT H., Episodic tremor and slip on the Cascadia subduction zone: The chatter of silent Slip, *Science*, **300** (2003) 1942.

[7] IDE S., BEROZA G. C., SHELLY D. R. and UCHIDE T., A scaling law for slow earthquakes, *Nature*, **447** (2007) 76.

[8] SCHWARTZ S. Y. and ROKOSKY J. M., Slow slip events and seismic tremor at circum-Pacific subduction zones, *Rev. Geophys.*, **45** (2007) RG3004.

[9] PENG Z. and GOMBERG J., An integrated perspective of the continuum between earthquakes and slow-slip phenomena, *Nature Geo.*, **3** (2010) 599.

[10] BEROZA G. and IDE S., Slow earthquakes and non-volcanic tremor, *Annu. Rev. Earth Planet. Sci.*, **39** (2011) 271.

[11] SAFFER D. M. and WALLACE L. M., The frictional, hydrologic, metamorphic and thermal habitat of shallow slow earthquakes, *Nat. Geosci.*, **8** (2015) 594.

[12] FRANK W. B., Slow slip hidden in the noise: The intermittence of tectonic release, *Geophys. Res. Lett.*, **43** (2016) 10, 125.

[13] BÜRGMANN R., The geophysics, geology and mechanics of slow fault slip, *Earth Planet. Sci. Lett.*, **495** (2018) 112.

[14] HOUSTON H., Low friction and fault weakening revealed by rising sensitivity of tremor to tidal stress, *Nat. Geosci.*, **8** (2015) 409.

[15] KAPROTH B. and MARONE C., Slow earthquakes, preseismic velocity changes, and the origin of slow frictional stick-slip, *Science*, **341** (2013) 1229.

[16] JOHNSON P. A., FERDOWSI B., KAPROTH B. M., SCUDERI M., GRIFFA M., CARMELIET J., GUYER R. A., LE BAS P.-Y., TRUGMAN D. T. and MARONE C., Acoustic emission and microslip precursors to stick-slip failure in sheared granular material, *Geophys. Res. Lett.*, **40** (2013) 5627.

[17] LEEMAN J. R., SCUDERI M. M., MARONE C. and SAFFER D. M., Stiffness evolution of granular layers and the origin of repetitive, slow, stick-slip frictional sliding, *Granular Matter*, **17** (2005) 447.

[18] Leeman J. R., Saffer D. M., Scuderi M. M. and Marone C., Laboratory observations of slow earthquakes and the spectrum of tectonic fault slip modes, *Nat. Commun.*, **7** (2016) 11104.
[19] Scuderi M. M., Marone C., Tinti E., Di Stefano G. and Collettini C., Precursory changes in seismic velocity for the spectrum of earthquake failure modes, *Nat. Geosci.*, **9** (2016) 695.
[20] Tinti E., Scuderi M. M., Scognamiglio L., Di Stefano G., Marone C. and Collettini C., On the evolution of elastic properties during laboratory stick-slip experiments spanning the transition from slow slip to dynamic rupture, *J. Geophys. Res. Solid Earth*, **121** (2016) 8569.
[21] Scuderi M. M., Viti C., Tinti E., Collettini C. and Marone C., Evolution of shear fabric in granular fault gouge from stable sliding to stick-slip and implications for fault slip mode, *Geology*, **45** (2017) 731.
[22] Leeman J. R., Marone C. and Saffer D. M., Frictional mechanics of slow earthquakes, *J. Geophys. Res. Solid Earth*, **123** (2018) 7931.
[23] Hulbert C., Rouet-Leduc B., Johnson P. A., Ren C. X., Rivière J., Bolton D. C. and Marone C., Machine learning predictions illuminate similarity of fast and slow laboratory earthquakes, *Nat. Geosci.*, **12** (2018) 69.
[24] Kyungjae I. m., Marone C. and Elsworth D., The transition from steady frictional sliding to inertia-dominated instability with rate and state friction, *J. Mech. Phys. Solids*, **122** (2018) 116.
[25] Brace and Byerlee, Stick-slip as a mechanism for earthquakes, *Science*, **153** (1966) 990.
[26] Ito Y. and Obara K., Very low frequency earthquakes within accretionary prisms are very low stress-drop earthquakes, *Geophys. Res. Lett.*, **33** (2006) L09302.
[27] Ito I., Obara K., Shiomi K. Sekine S. and Hirose H., Slow Earthquakes Coincident with Episodic Tremors and Slow Slip Events, *Science*, **315** (2007) 503.
[28] Wallace L. M. and Beavan J., Diverse slow slip behavior at the Hikurangi subduction margin, New Zealand, *J. Geophys. Res.*, **115** (2010) B12402.
[29] Kato K., Obara T., Igarashi H. and Tsuruoka S., Propagation of slow slip leading up to the 2011 M_W 9.0 Tohoku-Oki earthquake, *Science*, **335** (2012) 705.
[30] Bouchon M., Durand V., Marsan D., Karabulut H. and Schmittbuhl J., The long precursory phase of most large interplate earthquakes, *Nat. Geosci.*, **6** (2013) 299.
[31] Obara K. and Kato A., Connecting slow earthquakes to huge earthquakes, *Science*, **353** (2016) 253.
[32] Linde A. T., Gladwin M. T., Johnston M. J. S., Gwyther R. L. and Bilham R. G., A slow earthquake sequence on the San Andreas fault, *Nature*, **383** (1996) 65.
[33] Peng Z., Vidale J. E., Creager K. C., Rubinstein J. L., Gomberg J. and Bodin P., Strong tremor near Parkfield, CA, excited by the 2002 Denali Fault earthquake, *Geophys. Res. Lett.*, **35** (2008) L23305.
[34] Peng Z., Vidale J. E., Wech A. G., Nadeau R. M. and Creager K. C., Remote triggering of tremor along the San Andreas Fault in central California, *J. Geophys. Res.*, **114** (2009) B00A06.
[35] Shelly D. R., Migrating tremors illuminate deformation beneath the seismogenic San Andreas Fault, *Nature*, **463** (2010) 648.
[36] Shelly D. R., Periodic, chaotic and doubled earthquake recurrence intervals on the deep San Andreas Fault, *Science*, **328** (2010) 1385.
[37] Veedu D. M. and Barbot S., The Parkfield tremors reveal slow and fast ruptures on the same asperity, *Nature*, **532** (2016) 361.
[38] Rice J. R. and Gu J. C., Earthquake aftereffects and triggered seismic phenomena, *Pure Appl. Geophys.*, **121** (1983) 187.

[39] GU J. C., RICE J. R., RUINA A. L. and TSE S. T., Slip motion and stability of a single degree of freedom elastic system with rate and state dependent friciton, *J. Mech. Phys. Solids*, **32** (1984) 167.
[40] BLANPIED M. L. and TULLIS T. E., The stability and behavior of a frictional system with a two state variable constitutive law, *Pure Appl. Geophys.*, **124** (1986) 415.
[41] ROY M. and MARONE C., Earthquake nucleation on model faults with rate- and state-dependent friction: Effects of inertia, *J. Geophys. Res.*, **101** (1996) 13919.
[42] LIU Y. and RICE J. R., Aseismic slip transients emerge spontaneously in three-dimensional rate and state modeling of subduction earth- quake sequences, *J. Geophys. Res.*, **110** (2005) B08307.
[43] LIU Y. and RICE J. R., Spontaneous and triggered aseismic deformation transients in a subduction fault model, *J. Geophys. Res.*, **112** (2007) B09404.
[44] PERFETTINI H. and AMPUERO J.-P., Dynamics of a velocity-strengthening fault region: Implications for slow earthquakes and postseismic slip, *J. Geophys. Res.*, **113** (2008) B09411.
[45] RUBIN A. M., Episodic slow slip events and rate-and-state friction, *J. Geophys. Res.*, **113** (2008) B11414.
[46] RUBIN A. M., Designer friction laws for bimodal slow slip propagation speeds, *Geochem. Geophys. Geosys.*, **12** (2011) Q04007.
[47] SEGALL P., RUBIN A. M., BRADLEY A. M. and RICE J. R., Dilatant strengthening as a mechanism for slow slip events, *J. Geophys. Res.*, **115** (2010) B12305.
[48] KANEKO Y. and AMPUERO J.-P., A mechanism for preseismic steady rupture fronts observed in laboratory experiments, *Geophys. Res. Lett.*, **38** (2011) L21307.
[49] SCHOLZ C., MOLNAR P. and JOHNSON T., Detailed studies of frictional sliding of granite and implications for earthquake mechanism, *J. Geophys. Res.*, **77** (1972) 6392.
[50] VOISIN C., RENARD F. and GRASSO J.-R., Long term friction: from stick-slip to stable sliding, *Geophys. Res. Lett.*, **34** (2007) L13301.
[51] VOISIN, GRASSO J.-R., LAROSE E. and RENARD F., Evolution of seismic signals and slip patterns along subduction zones: Insights from a friction lab scale experiment, *Geophys. Res. Lett.*, **35** (2008) L08302.
[52] BAUMBERGER T., HESLOT F. and PERRIN B., Crossover from creep to inertial motion in friction dynamics, *Nature*, **367** (1994) 544.
[53] BEN-DAVID O., COHEN G. and FINEBERG J., The dynamics of the onset of frictional slip, *Science*, **330** (2010) 211.
[54] BRANTUT N., SULEM J. and SCHUBNEL A., Effect of dehydration reactions on earthquake nucleation: Stable sliding, slow transients and unstable slip, *J. Geophys. Res.*, **116** (2011) B05304.
[55] SCHUBNEL A., NIELSEN S., TADDEUCCI J., VINCIGUERRA S. and RAO S., Photo-acoustic study of subshear and supershear ruptures in the laboratory, *Earth Planet. Sci. Lett.*, **308** (2011) 424.
[56] KATAYAMA I., IWATA M., OKAZAKI K. and HIRAUCHI K. I., Slow earthquakes associated with fault healing on a serpentinized plate interface, *Nat. Sci. Rep.*, **3** (2013) 1784.
[57] SELVADURAI P. A. and GLASER S. D., Laboratory-developed contact models controlling instability on frictional faults, *J. Geophys. Res.*, **120** (2015) 4208.
[58] SVETLIZKY I., KAMMER D. S., BAYART E., COHEN G. and FINEBERG J., Brittle fracture theory predicts the equation of motion of frictional rupture fronts, *Phys. Rev. Lett.*, **118** (2017) 125501.
[59] SVETLIZKY I., PINO MUNOZ D., RADIGUET M., KAMMER D. S., MOLINARI J.-F. and FINEBERG J., Properties of the shear stress peak radiated ahead of rapidly accelerating rupture fronts that mediate frictional slip, *Proc. Natl. Acad. Sci. U.S.A.*, **113** (2016) 542.

[60] Wong T.-F. and Zhao Y., Effects of load point velocity on frictional instability behavior, *Tectonophys.*, **175** (1990) 177.
[61] Samuelson J., Elsworth D. and Marone C., Influence of dilatancy on the frictional constitutive behavior of a saturated fault zone under a variety of drainage conditions, *J. Geophys. Res.*, **116** (2011) B10406.
[62] Thomas A. M., Bürgmann R., Shelly D. R., Beeler N. M. and Rudolph M. L., Tidal triggering of low frequency earthquakes near Parkfield, CA: Implications for fault mechanics within the brittle-ductile transition, *J. Geophys. Res.*, **117** (2012) B05301.
[63] Thomas A., Nadeau R. M. and Bürgmann R., Tremor-tide correlations and near-lithostatic pore pressure on the deep San Andreas Fault, *Nature*, **462** (2009) 1048.
[64] Kitajima H. and Saffer D., Elevated pore pressure and anomalously low stress in regions of low frequency earthquakes along the Nankai Trough subduction megathrust, *Geophys. Res. Lett.*, **39** (2012) L23301.
[65] Skarbek R. M., Rempel A. W. and Schmidt D. A., Geologic heterogeneity can produce aseismic slip transients, *Geophys. Res. Lett.*, **39** (2012) L21306.
[66] Fagereng A. and Sibson R. H., Mélange rheology and seismic style, *Geology*, **38** (2010) 751.
[67] Collettini C., Niemeijer A., Viti C., Smith S. A. F. and Marone C., Fault structure, frictional properties and mixed-mode fault slip behavior, *Earth Plan. Sci. Lett.*, **311** (2011) 316.
[68] Ghosh A., Vidale J. E. and Creager K. C., Tremor asperities in the transition zone control evolution of slow earthquakes, *J. Geophys. Res.*, **117** (2012) B10301.
[69] Dieterich J. H., Modeling of rock friction: 1. Experimental results and constitutive equations, *J. Geophys. Res.*, **84** (1979) 2161.
[70] Ruina A., Slip instability and state variable friction laws, *J. Geophys. Res.*, **88** (1983) 10359.
[71] Tullis T. and Weeks J., Constitutive behavior and stability of frictional sliding of granite, *Pure Appl. Geophys.*, **124** (1986) 10.
[72] Marone, Laboratory derived friction laws and their application to seismic faulting, *Annu. Rev. Earth Planet. Sci.*, **26** (1998) 643.
[73] Ampuero J.-P. and Rubin A. M., Earthquake nucleation on rate and state faults: Aging and slip laws, *J. Geophys. Res.*, **113** (2008) B01302.
[74] Marone C. and Kilgore B., Scaling of the critical slip distance for seismic faulting with shear strain in fault zones, *Nature*, **362** (1993) 618.
[75] Dieterich J. H., *Constitutive properties of faults with simulated gouge*, in *Mechanical Behavior of Crustal Rocks, AGU Monograph*, Vol. **24**, edited by Carter N. L., Friedman M., Logan J. M. and Sterns D. W. (American Geophysical Union, Washington) 1981, p. 103.
[76] Beeler N. M., Tullis T. E. and Weeks J. D., Frictional behavior of large displacement experimental faults, *J. Geophys. Res.*, **101** (2016) 8697.
[77] Rice J. R. and Ruina A. L., Stability of steady frictional slipping, *J. Appl. Mech.*, **105** (1983) 343.
[78] Mair K. and Marone C., Friction of simulated fault gouge for a wide range of velocities and normal stresses, *J. Geophys. Res.*, **104** (1999) 28, 899.
[79] Ikari M., Saffer D. M. and Marone C., Frictional and Hydrologic Properties of Clay-Rich Fault Gouge, *J. Geophys. Res.*, **114** (2009) B05409.
[80] Ikari M. J., Marone C. and Saffer D., On the relation between fault strength and frictional stability, *Geology*, **39** (2011) 83.
[81] Ikari M., Marone C., Saffer D. M. and Kopf A. J., Slip-weakening in tectonic fault zones: A potential mechanism for slow slip events, *Nat. Geosci.*, **6** (2013) 468.

[82] IKARI M. J., ITO Y., UJIIE K. and KOPF A. J., Spectrum of slip behaviour in Tohoku fault zone samples at plate tectonic slip rates, *Nat. Geosci.*, **8** (2015) 870.
[83] GOMBERG J., WECH A., CREAGER K., OBARA K. and AGNEW D., Reconsidering earthquake scaling, *Geophys. Res. Lett.*, **43** (2016) 6243.
[84] GOMBERG J., AGNEW D. C. and SCHWARTZ S. Y., Alternative source models of very low frequency events, *J. Geophys. Res.*, **121** (2016) 6722.
[85] AKI K., Magnitude-frequency relation for small earthquakes: A clue to the origin of $f_{\max}$ of large earthquakes, *J. Geophys. Res.*, **92** (1987) 1349.

Proceedings of the International School of Physics "Enrico Fermi"
Course 202 "Mechanics of Earthquake Faulting", edited by A. Bizzarri, S. Das and A. Petri
(IOS, Amsterdam; SIF, Bologna) 2019
DOI 10.3254/978-1-61499-979-9-95

From foreshocks to mainshocks: mechanisms and implications for earthquake nucleation and rupture propagation

W. L. Ellsworth(*)

Department of Geophysics, Stanford University - Stanford, CA, USA

Summary. — Earthquakes begin without any obvious sign of their coming. Two hypotheses have been advanced to describe the underlying physical processes that lead to their nucleation. These are the preslip and cascade models which take opposing views on the role of aseismic deformation in the nucleation process as well as the prospects for prediction. In this paper, foreshocks, the small earthquakes that sometimes precede larger ones, and the initial seismic wave radiation of the earthquake itself are used to examine how earthquakes nucleate and grow. Earthquake are found to begin abruptly and grow irregularly, consistent with laboratory-derived predictions for limited aseismic slip and in agreement with the predictions of the cascade model.

1. – Introduction

Earthquakes initiate deep underground, cloaked within solid rock and many kilometers below the nearest observation point. Our ability to "see" them is principally through the seismic waves radiated during the earthquake, as seismic waves can be easily detected at the Earth's surface and are rich in information content. The theory of elasticity

(*) E-mail: wellsworth@stanford.edu

has been exceptionally successful for extracting information from seismic waves about what happens in an earthquake, and there are many excellent books on the theory (*e.g.* [1, 2]). Earthquakes are produced by rapid shear slip on an approximately planar surface (fault). They begin from a very limited region, the hypocenter or locus of initial radiation of far field seismic waves. Once initiated the faulted area will grow in size as long as the mechanical energy supplied to the rupture front by the medium exceeds the energy consumed in advancing the rupture. Repeating the process over geologic time can displace the original configuration of the rocks astride the fault by great distances while accommodating the inelastic deformation in a very narrow zone. We observe fossil earthquakes when uplift and erosion bring the rocks to the surface. But interpreting the rock record is complex, due to the overprinting of multiple rupture episodes (see for example [3]).

Because the process we observe is ephemeral, revealing only what happens for the brief time when the fault is sliding rapidly, it raises a fundamental question of how and under what conditions earthquakes began. Is anything happening on the fault just before it radiates seismic waves? Fault slip that is too slow to radiate high-frequency waves is often regarded as the most probable answer, and if verified by observation would be of great importance. Such slow deformations, however, are exceptionally difficult to observe because of the rapid decay of their amplitudes ($1/\text{distance}^2$) compared to the radiated field ($1/\text{distance}$). The high background level of noise in the Earth at low frequency places strong limits on what can be observed from near the Earth's surface. As a consequence, much of what we know about how earthquakes begin comes from the study of the radiated field.

The pioneering theoretical work on the rate-and-state theory of frictional instability by Jim Dieterich [4], Jim Rice [5] and scores of collaborators introduced the concept of a minimum earthquake size through the recognition that slow slip in a nucleation zone with radius

$$h^* = G\, d_c/(b-a)\sigma$$

or larger is required for an earthquake instability to occur. In the expression for h^*, G is the shear modulus, d_c is the sliding distance over which friction evolves, $b-a$ is the velocity weakening parameter and σ is the effective normal stress. The model is supported by laboratory studies of frictional sliding scaled to conditions appropriate for the Earth's crust [6] in which slow slip occurs on the sample before a dynamic stick-slip occurs. Laboratory derived values for d_c and $b-a$ suggest that the minimum earthquake should have a magnitude well below $M_\text{w} = 0$ in the crust. Indeed, tectonic earthquakes with $M_\text{w} < -3$ have been observed in the SAFOD borehole and events with $M_\text{w} < -5$ have been observed in deep mines in South Africa.

Very small earthquakes clearly happen. Thus h^* must, in some places, be quite small. But do all earthquakes nucleate in the same way? If all earthquakes nucleate in a region governed by laboratory friction values the slow deformation process that precedes dynamic rupture would be much too small to be observed at the surface and would have

no predictive value. Alternatively, does the nucleation process change as the size of the earthquake grows? Or, are there other processes that accompany the nucleation process?

From an observational viewpoint, the beginning of earthquakes as recorded in the seismogram is commonly unsteady, not smooth as would be expected if rupture spreads uniformly outward from the nucleation point [7]. Two schools of thought have evolved on these questions, taking opposite views. One, the *cascade model*, asserts that earthquake initiate in a common way, independent of the final size and that complexity that we observe at the beginning of rupture arises from variability in fault geometry, state of stress and other factors [8-10]. Once initiated, the rupture can trigger secondary nucleations through stress transfer, leading to additional complexity. The alternate view, the *preslip model*, asserts that the slow sliding in the nucleation zone occurs over an area that scales with earthquake size [9, 11]. The preslip model envisions both foreshocks and the unsteady start of earthquakes are a consequence of aseismic slip in the region around the eventual hypocenter, while the cascade model considers foreshocks and mainshock initiation a stochastic process driven by stress interactions. The preslip model presents a possible path to prediction while the cascade model generally does not.

In this paper, I examine the initiation process of earthquakes through a series of case studies, first of earthquakes preceded by foreshocks, followed by an examination of the initial radiation from mainshocks and finally through considerations of the minimum earthquake magnitude implied by h^*.

2. – Foreshocks and mainshocks

It is well known that earthquakes cluster in both space and time. Sequences of related earthquakes are often divided into foreshocks and aftershocks, which are simply labels for origin times before and after the largest event, the mainshock. These labels can only be applied after the sequence has completed, as the occurrence of a new mainshock would relabel all earthquakes to that time as foreshocks. Retrospectively, foreshocks are common, occurring before approximately 1/3 of all mainshocks [12], while only one earthquake in 20 is followed by a larger event [13]. If there are properties of foreshocks that set them apart from ordinary earthquakes, they remain elusive, and from a global statistical point of view earthquake sequences are consistent with a single triggering mechanism of stress transfer (cascade model) [14].

Large earthquakes initiating along plate boundaries, however, show a tendency for seismic activity to increase as the time of the mainshock approaches [11], suggesting the presence of a precursory process driven by aseismic slip (preslip model). A precursory process is also suggested by detailed analysis of foreshock sequences in California [15].

Here we will review several well-studied crustal earthquakes in continental crust that were preceded by foreshocks. We will take advantage of the property of seismograms that they encode the convolution of the source process with the path and instrument. The geologic complexity of the Earth ensures that at high enough frequency each source/station pair produces a unique waveform that can be used to identify repeating earthquakes as well as discriminate between those that are true repeats or just close to one another.

2˙1. *1934 and 1966 Parkfield, California, USA.* – The Parkfield segment of the San Andreas Fault in central California has ruptured seven times since 1857 in earthquakes of about magnitude 6, most recently in 2004 [16]. It is located at the transition between the locked and virtually aseismic Cholame segment of the fault to the south that last ruptured in the great 1857 earthquake and the central San Andreas Fault that moves principally through aseismic fault creep but also produces a high rate of microearthquake activity, of which many are repeating earthquakes [17].

From the early 1930s on, Parkfield earthquakes with magnitudes of 3.5 and greater have been recorded by regional seismic stations in California, permitting comparative analysis of their waveforms. Bakun and McEvilly [18] discovered that the 1934 and 1966 earthquakes not only nucleated from the same hypocenter, but also shared a common foreshock, a M_{L} 5.1 event 17 minutes before each mainshock. The 1934 earthquake was also preceded by 3 days of foreshock activity, suggesting an extended nucleation process. The observation of repeating foreshocks led to the hypothesis that the next Parkfield earthquake could be predicted if the foreshocks recurred and led to the intensive instrumentation of the Parkfield region to trap the anticipated earthquake. When the next earthquake happened in 2004, it began at a different hypocenter and lacked any foreshocks, although it ruptured the predicted segment of the fault. This event is discussed in detail in sect. **3**˙2.

Of interest here are recurrences of the foreshocks at times other than in 1934 and 1966. By comparing seismograms recorded at the U.C. Berkeley Mount Hamilton station (MHC) by both Wood-Anderson analog and modern digital seismographs after conversion to Wood-Anderson response, it was found that the M_{L} 5.0 "three day" foreshock that initiated the 1934 sequence occurred at other times. One triggered public warning of an impending Parkfield earthquake in1993 that failed to materialize, demonstrating that the occurrence of this earthquake does not guarantee a Parkfield mainshock will follow. Another foreshock to the 1934 earthquake repeated multiple times between 1934 and 1966 and also as aftershock to the 2004 mainshock (fig. 1). The "17-minute" foreshock to both the 1934 and 1966 events, however, has only occurred these two times during the instrumental era.

2˙2. *1992 Joshua Tree, California, USA.* – The M_{w} 6.1 Joshua Tree, California earthquake was preceded by a brief foreshock sequence that produced just 5 detected events in 2.4 hours, including a M 4.3 event that initiated the sequence. Using a master event technique and earthquake source dimensions for typical San Andreas system earthquakes, Dodge *et al.* [15] computed the stress change at the mainshock hypocenter due to the foreshocks. They used resampling of the probability distributions on location, fault orientation, strike and stress drop for a circular crack slip model to determine the probability that the foreshocks increased or decreased the stress at the mainshock hypocenter. They found that it was highly likely ($P > 0.999$) that the shear stress and Coulomb stress decreased at the hypocenter, and concluded that preslip was likely a factor in the initiation of the main earthquake.

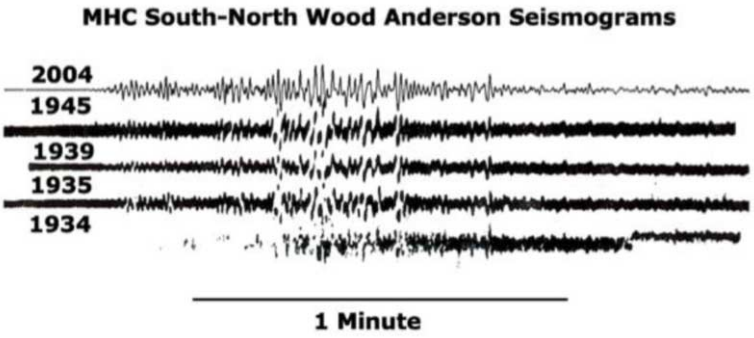

Fig. 1. – Seismograms of a repeating M_L 4.2 Parkfield, California earthquake recorded at the Mt. Hamilton (MHC) seismic station. This earthquake was a foreshock to the 1934 mainshock, a late aftershock in 1935, occurred at times unrelated to larger earthquakes in 1939 and 1945, and was an aftershock in 2004 (Wood Anderson seismogram synthesized from broad band seismometer).

The Joshua Tree earthquake was also studied using a different method by Mori [19]. He used a M 2.4 foreshock as an empirical Green's function, or proxy for the impulse response of the Earth, to correct the observed seismograms of the M 4.3 foreshock for wave propagation, yielding a displacement pulse of the source. The deconvolved displacement

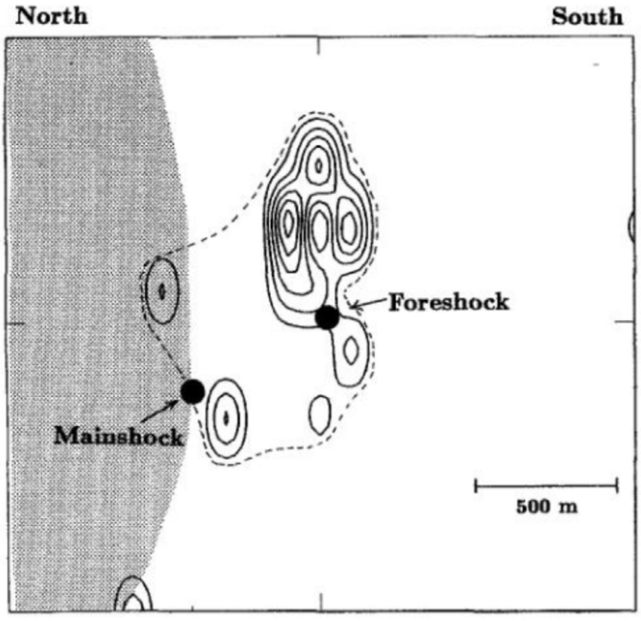

Fig. 2. – Contours of slip in the M 4.3 foreshock to the M 6.1 Joshua Tree, California earthquake from Mori [19]. Contour interval 10 cm. Dashed line indicates inferred limits of foreshock slip. Hypocenters of the foreshock and mainshock indicated. Shaded area corresponds to initial rupture direction of the mainshock. (Reproduced from fig. 7 of Mori [19].)

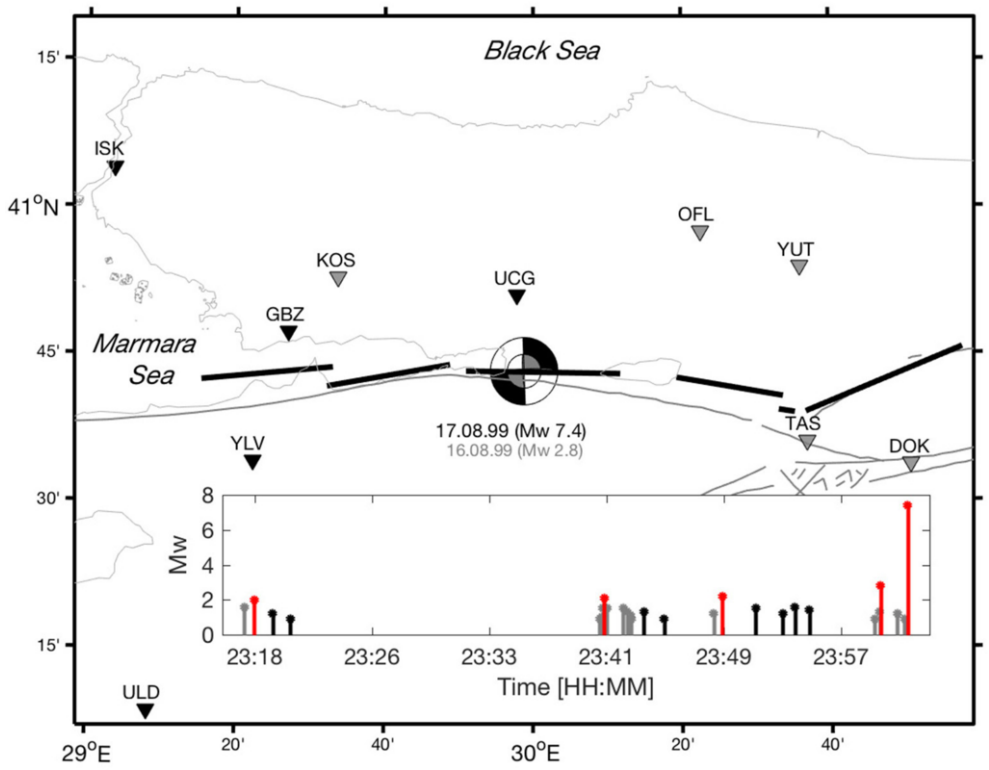

Fig. 3. – Location map of the Izmit earthquake and generalized rupture of the North Anatolian Fault in the 1999 Izmit earthquake. Triangles identify seismic stations used by [21] (UCG) and [20] (all). First motion mechanisms of the largest foreshock and mainshock shown with compressional quadrants shaded. Inset magnitude-diagram with four largest foreshocks (red) and other events studied by [21] (gray) and additional foreshocks found by template matching [20] (black). (Reproduced from fig. 1 of Ellsworth and Bulut [20].)

seismograms were used to image the rupture of the foreshock and its source properties. Mori found it had a very high stress drop, locally over 87 MPa. The mainshock hypocenter located outside of the rupture, which according to this analysis makes the foreshock sequence compatible with the cascade model (fig. 2).

2˙3. *1999 Izmit, Turkey.* – The M_w 7.6 Izmit, Turkey earthquake and its foreshocks is one of the largest strike-slip earthquakes recorded at near distances. The mainshock hypocenter lies at a depth of 15 km in the middle of this long (120 km) bilateral rupture. A brief, 44 minute-long foreshock sequence initiated the event, which included 26 detected events with magnitudes between M 0.9 and 2.8 [20]. The foreshocks were initially studied by Bouchon *et al.* [21] using a single seismic station, UCG, located along a perpendicular to the North Anatolian Fault. They found that the foreshocks had very similar waveforms and on this basis concluded that they represented repeated movement

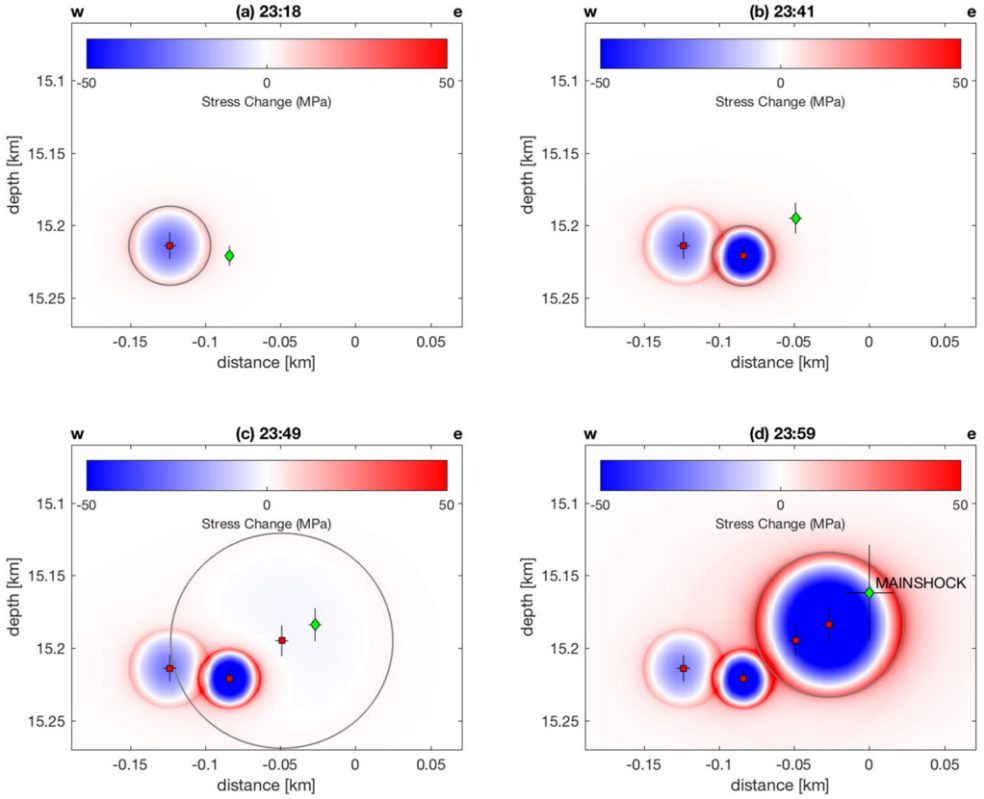

Fig. 4. – Longitudinal cross section along the North Anatolian Fault showing shear stress change on the fault from rupture in the four largest foreshocks. Each panel shows the cumulative stress change with the hypocentroid (point of initial rupture) for each earthquake identified (red square with 2σ error) and the hypocentroid of the next to occur foreshock or mainshock (green diamond with 2σ error). (Reproduced from fig. 3 of Ellsworth and Bulut [20].)

at the same position on the fault. They argued that for repeats to occur over such a short time span they must have been driven by fault preslip that rapidly accelerated in the final 2 minutes before the mainshock.

Ellsworth and Bulut [20] collected seismograms for the foreshocks at additional regional stations (fig. 3) and reanalyzed the sequence using a collection of precision methods. They searched for additional foreshocks in the year prior the earthquake, and found 8 additional events, all within the known 44 minutes of foreshock activity but no others. The highly similar foreshock waveforms at station UCG were decomposed by removing the principal component from each seismogram. The residual seismograms were then cross-correlated prior to application of cluster analysis. The maximum cross correlation coefficients between the residual seismograms barely exceeded 0.5 for the most similar pairs, indicating that none of the events were repeating earthquakes. The resulting fam-

ily tree naturally sorted the foreshocks in time into families for each of the four largest foreshocks, indicating that these largest foreshocks also had their own foreshocks and brief aftershock sequences (inset fig. 3).

Differential arrival times of P- and S-waves of the four larges foreshocks and mainshock were measured by cross correlation on the suite of stations and precisely relocated using hypoDD [22]. Spectral ratios were used to measure the source parameters of the foreshocks [23]. Using the source model of Madariaga [24] to interpret the spectral measurements through a constant stress drop crack model, the relationship between the foreshocks and the mainshock hypocenter could be determined. It was found that the four largest foreshocks and their clustered subordinate events ruptured progressively from west to east along the North Anatolian Fault (fig. 4).

A stress-transfer–driven cascade can explain the Izmit foreshocks sequence without the need to invoke an unobservable slow-slip mechanism. If aseismic slip accompanied any of the foreshocks within their rupture zones, it likely amounted to more than a few centimeters of slip since none of the foreshocks repeat. Accelerating preslip exterior to the ruptures is unlikely as well as the aftershocks of each of the four large foreshocks rapidly decayed in frequency (fig. 3). One external agent that we cannot rule out is the hypothesized entry of overpressured fluid into the fault once fault zone seals were broken by the foreshocks. This would reduce the effective normal stress and encourage the cascade to continue.

It is noteworthy that the largest foreshocks of both the Joshua Tree and Izmit earthquakes had stress drops in excess of 80 MPa. This is an order-of-magnitude higher stress drops considered typical of crustal earthquakes within strike-slip fault systems. Note also that not every foreshock of the Izmit earthquake had a high stress drop, indicating significant spatial variability in the state of stress.

2˙4. *1999 Hector Mine, California, USA.* – Recently, Clara Yoon [25, 26] analyzed the foreshock sequence of the 1999 M_{w} 7.1 Hector Mine, California earthquake using the same general approach of computing high-accuracy hypocentroids using cross correlation timing and spectral ratio measurements to determine source dimensions. The foreshock sequence lasted 20 hours and included 50 events with magnitudes between $M - 0.4$ and 3.7. The foreshocks form a tight cluster on the fault plane with minimal overlap. Growth of the cumulative foreshock rupture is more-or-less radial from the initiator, compared to the linear progression found for the Izmit earthquake. The mainshock hypocenter locates at an unruptured spot interior to the foreshocks and immediately next to the last foreshock. Yoon concluded that the "observations are consistent with a triggered cascade of stress transfer, where previous foreshocks load adjacent fault patches to rupture as additional foreshocks, and eventually the mainshock".

3. – Mainshock initial rupture process

Not every earthquake has foreshocks. For some, this could be simply a detection issue. For others, we can say with certainty that no foreshocks occurred within 6 mag-

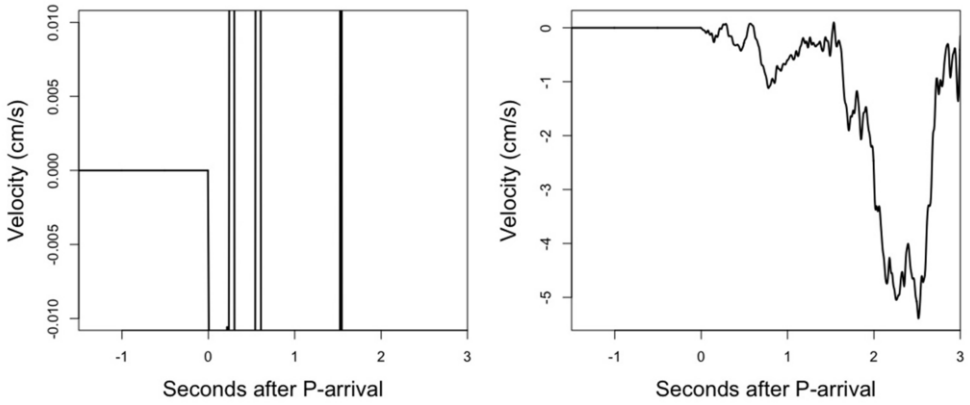

Fig. 5. – Initial P-waves of the M_w 7.2 Loma Prieta earthquake recorded by the vertical accelerometer at station Santa Teresa Hills, 25 km from the epicenter. Left panel shows details of arrival in which the velocity exceeded 0.005 cm/s in less than 0.01 s. Right panel shows on-scale record.

nitude units of the mainshock, a difference in seismic moment of 10^9. For some of these earthquakes with no foreshocks we can also show that there were no earthquakes closer than several kilometers to their hypocenters for several decades before their occurrence.

Despite the absence of seismicity near their initiation points, the beginnings of these foreshock-less earthquakes are not simple, and commonly display the unsteady rupture growth identified as the seismic nucleation phase [7,9]. Here we examine two such earthquakes in detail.

3˙1. *1989 Loma Prieta, California, USA.* – The M_w 7.2 (M_s 6.9) Loma Prieta earthquake initiated at a depth of 15.9 km depth on a blind thrust fault within the San Andreas Fault zone along the southern end of the 1906 earthquake rupture. In the 22 years preceding the earthquake, no microearthquakes (magnitude of completeness M_d 1.5) were detected within 2 km of the hypocenter. The nearest earthquake in the USGS Northern California catalog, M_d 1.3 occurred in 1973 at a distance of 2.3 km; no other events located within 3 km.

If the earthquake had any foreshock activity, it is represented by the waves arriving in the first 1.6 s (fig. 5). The abrupt beginning at the initiation of the earthquake is evident. While some suggested the initial 1.6 s represent a foreshock (see discussion in [27]), Beroza and Ellsworth [9] interpreted the initial event as the beginning of a continuous and unsteady rupture process.

A simple model of the rupture initiation process was developed by [27] using digital strong-motion records from the near field. To model the displacement seismograms, they used the complete synthetic seismogram for a point dislocation in a half-space and assume the fault orientation determined from the first-motion data. The seismograms were modeled by determining the seismic moment rate as a function of time for a point

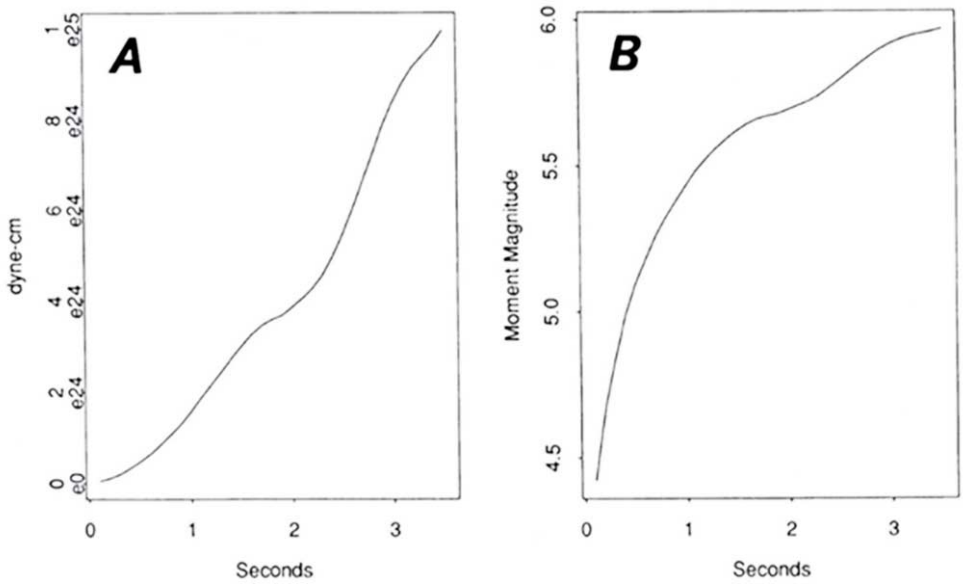

Fig. 6. – Cumulative seismic moment release *versus* time determined by inversion of near-field displacement seismograms. Both the total seismic moment (A) and the equivalent M_w (B) are shown. (Reproduced from fig. 15 of Dietz and Ellsworth [27].)

source. The best fit to the observed displacement seismograms shows a continuous growth in seismic moment beginning at the initial P-wave arrival. The total moment release by 1.6 s into the event is equivalent to M_w 5.5 earthquake (fig. 6) Thus the initial event appears to mark the beginning of a continuous and rapid slip in the earthquake.

Short-period seismometers close to the Loma Prieta earthquake had sufficient sensitivity to detect slow deformations that might have occurred as part of the nucleation process at periods of up to 10 s. None were observed [28]. This earthquake was also one of very few captured by borehole strainmeters located within a few focal depths distance. High sensitivity strain meters (10^{-10}) located 37 and 42 km from the epicenter detected no strain corresponding to slip in the hypocentral zone [29]. Assuming a maximum unobserved strain of 1 nanostrain in the weeks to minutes before the earthquake, steady preslip equivalent to a M_w 5.3 earthquake could have gone unobserved, but not accelerating slip.

The Loma Prieta earthquake is far from unique in initiating abruptly with rapid and unsteady slip. The M_w 6.7 1994 Northridge, California earthquake provides another clear example with neither foreshocks nor any detected activity in the decades leading up to the earthquake. Additional examples of earthquakes with sharp onsets and complex beginnings and possible interpretations of the seismic nucleation phase are discussed in [7] and [9].

3˙2. *2004 Parkfield, California, USA.* – The seventh known rupture of the Parkfield segment of the San Andreas Fault took place on September 28, 2004 and was captured by the dense arrays of geophysical sensors deployed in the 1980s to capture it [16]. The earthquake imitated along the southern portion of the segment, in contrast to the 1934 and 1966 events which shared a common hypocenter at the northern end of the segment. In contrast to the 1934 and 1966 events the 2004 event had no foreshocks. Seismicity regularly occurs on the San Andreas Fault at Parkfield. A search of the double difference catalog at the Northern California Data Center revealed 4 earthquakes within 500 m of the hypocenter, M_{d} 1.5 to 3.0 in the 20 years before the earthquake, the last 9 years before the event.

The initial rupture process shares many of the same growth characteristics with the Loma Prieta earthquake. The initiation process was studied in detail by Uchide *et al.* [30] who used the dense accelerometer network to image the rupture process. They found that the rupture started abruptly, growing to an equivalent of M_{w} 3.9 with a fault slip rate of 3 m/s in the first 0.2 s. There was no evidence of a transition from quasistatic rupture growth to dynamic rupture. They concluded that the initiation of the earthquake was consistent with the cascade model, and noted the difficulty of assessing the ultimate size of an earthquake from its initial stages.

The earthquake was captured by a wide variety of geophysical instruments in addition to accelerometers and seismometers. High-fidelity recordings at borehole strainmeters place very strong constraints on preslip [31]. Figure 7 compares the observed strains and displacements with the expectation of one nucleation model. Quoting Johnston *et al.* "Final prerupture nucleation slip in the hypocentral region is constrained to have a moment less than 2×10^{12} N m (**M** 2.2) and a source size less than 30 m" [31].

Some have criticized the Parkfield experiment for neither predicting the earthquake nor finding reliable precursors. What was found, however, strongly suggests that precursory behavior associated with hypothesized preslip, if it did indeed occur in 1934 and 1966, does not accompany every segment rupturing earthquake.

Magnetic- and electric-field monitoring sites in the Parkfield experiment also provided strong constraints on the precursory processes. Preseismic magnetic field variations measured by an array of seven proton magnetometers were unremarkable in the months, weeks and days leading to the earthquake and showed no short-term changes in the minutes leading to the earthquake [32]. Electric and magnetic fields were also monitored at a site close to the epicenter using a three-component very broad band magnetic coil induction system and two horizontal orthogonal electric dipole pairs. These sensors showed neither anomalous behavior in the ULF band nor changes in EM noise [32].

4. – Near source observations at SAFOD

The deployment of instrumentation deep within the San Andreas Fault as part of the NSF EarthScope San Andreas Fault Observatory at Depth (SAFOD) opened a new window for the study of the earthquake source by reducing the distance between source and receiver to a few hundred meters or less [33]. SAFOD is located at the northern end

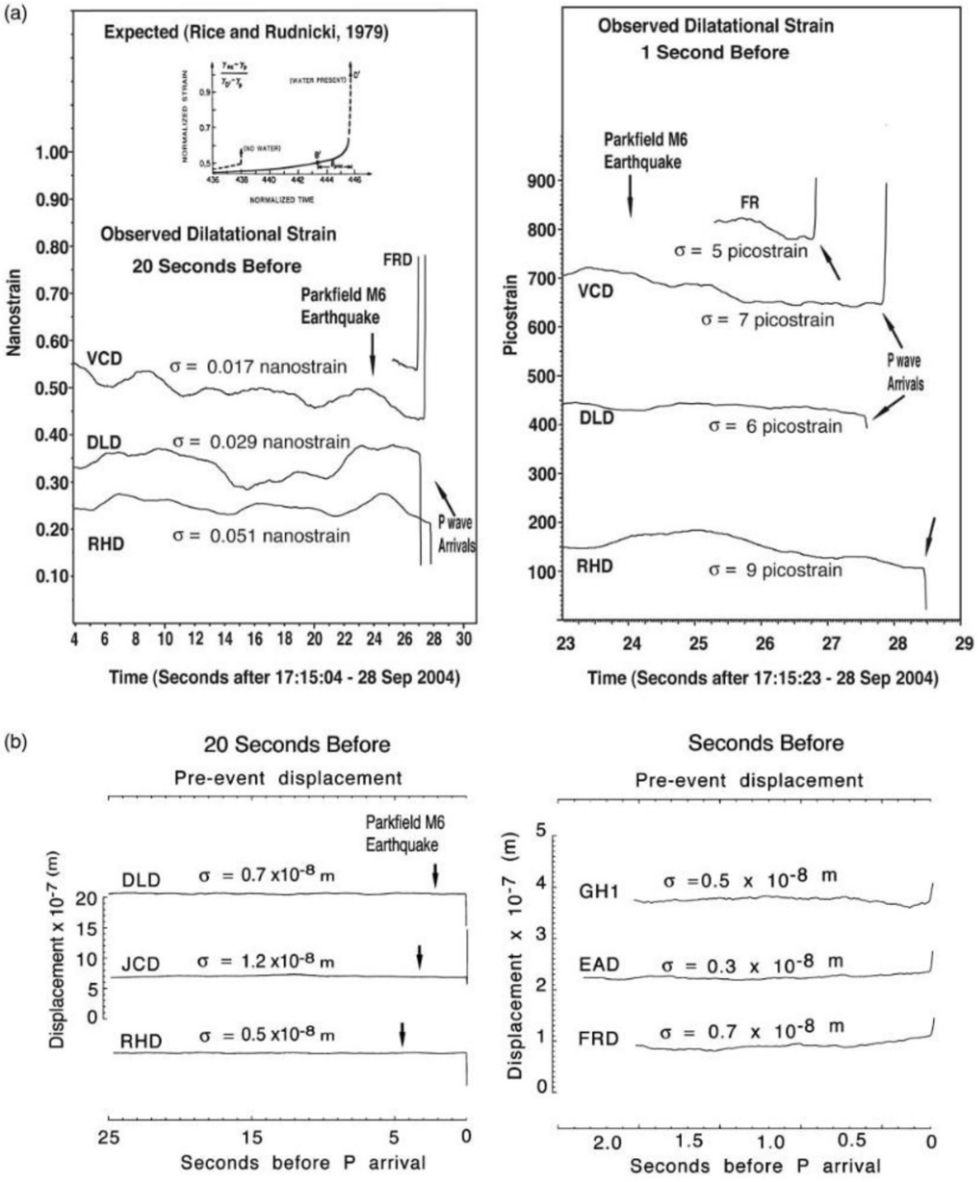

Fig. 7. – (a) Expected strain time history before rupture (top) and observed dilational strain during the final seconds before the M_w 6.0 Parkfield earthquake (bottom). Standard deviations of strain σ up to the time of the first P arrival are included on each plot. Strain changes immediately before the earthquake are less than 10 picostrain. Arrows show the occurrence times of earthquake. (b) Ground displacement derived from acceleration data during the last 20 seconds and 1 second before the M_w 6.0 Parkfield earthquake. Each trace has the peak change in displacement during these periods listed. (Reproduced from fig. 7 of Johnston *et al.* [31].)

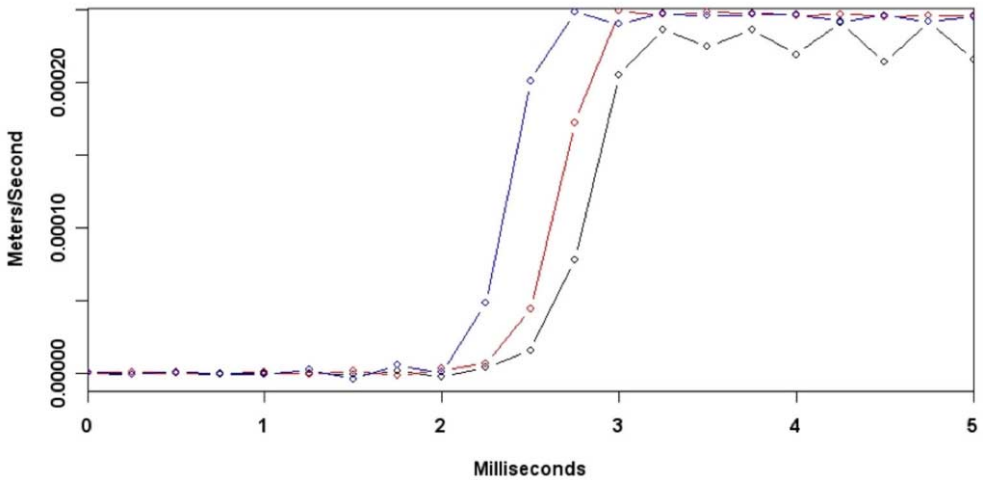

Fig. 8. – Three components velocity seismograms of the initial P-wave arrival for the $M_{\rm d}$ 1.8 August 11, 2006 "Hawaii" repeating earthquake recorded in the SAFOD borehole at 150 m hypocentral distance. A dynamic stress drop of 5 MPa was determined from the slope of the unclipped portion of the P-wave arrival in the first half millisecond of rupture, assuming the dynamic rupture model of Kostrov [2]. The linear dimension of the ruptured area is no larger than 2–3 m in diameter at this time.

of the Parkfield segment, and intersects the San Andreas Fault at a depth of 2.7 km. Key questions that can be addressed in the near-source region include scaling of apparent stress, static stress drop, dynamic stress drop, the minimum size of earthquakes, and potentially the evolution of friction during nucleation.

The rate of fault weakening can be studied using the earliest part of the P-wave arrival by applying Kostrov's model for self-similar crack growth to determine the dynamic stress drop [2]. Earthquakes very close to the SAFOD seismometers begin abruptly with the dynamic stress drop typically reaching 5 MPa within the first few milliseconds of rupture, pointing to a very small slip weakening length scale (fig. 8). The absence of a slow initial phase of the type described by Iio [34], the rapid release of stress when the rupture is 1–3 m in dimension, and the agreement between the early dynamic stress drop and static stress drop [23] all point to a d_c value (the slip weakening distance over which friction evolves from static to fully dynamic) in the range of 10s to 100s of microns, comparable to values measured in the laboratory.

How else might we constrain it or the underlying rate-and-state parameters d_c and $b - a$? If h^* has a finite minimum size, there should be a minimum size for earthquakes.

Seismometers in the SAFOD main hole detect earthquakes down to $M_{\rm w} - 3.5$ at distances of 150 m. Earthquake source parameters determined using a variety of methods indicate that there is no breakdown in apparent stress scaling or stress drop scaling for $M_{\rm w} \geq -1$ [23]. The highest stress drop values are comparable to the laboratory-derived frictional strength of faults at stress conditions measured at SAFOD. The smallest

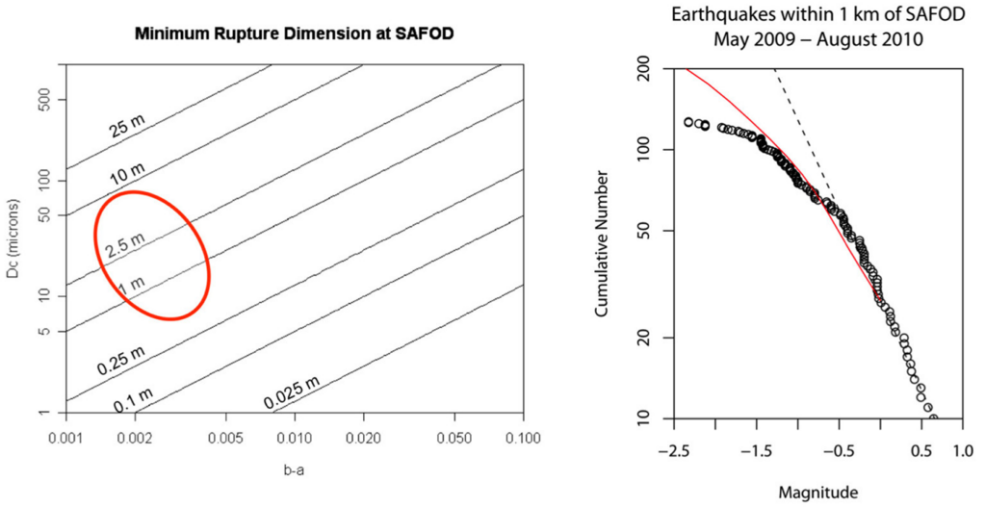

Fig. 9. – Left: Minimum rupture dimension for earthquakes as a function of rate-and-state parameters $b - a$ and d_c for conditions at SAFOD. Elliptical region indicates parameter ranges compatible with observed earthquake magnitude-frequency statistics. Right: Comparison between observed magnitude-frequency statistics (circles), Gutenberg-Richter distribution fit for completeness threshold of $M_w - 0.5$ (dashed line) and prediction of the dynamic rupture model of Chen and Lapusta [35] (solid line) with full dynamic rupture reached at M_w 0.

resolved events have source dimensions of about 3 m, indicating that if there is a minimum earthquake size, it must be at least this small.

To explore the question of the minimum rupture dimension, the frequency-magnitude distribution of earthquakes occurring within a 1 km radius of the SAFOD borehole was studied. Between May 2009 and August 2010 a total of 120 earthquakes with $M_w \geq -2.0$ were detected by a high-gain 15 Hz seismometer installed in the SAFOD main hole at a depth of 2550 m below the land surface. These earthquakes exhibit a linear Gutenberg-Richter frequency-magnitude relation for $M_w \geq -0.5$. Below $M_w - 0.5$, however, the G-R relation breaks down, as too few events were detected. The breakdown is not believed to be an artifact of incomplete detection of events, but rather reflects a change in earthquake population statistics (fig. 9).

At SAFOD, both the effective normal stress, σ, and shear modulus, G, are known from *in situ* measurement, leaving only the rate-and-state parameters d_c and $b-a$ as unknowns in the expression for h^*. Under the assumption that d_c has a distribution peaked between 20 μm and 100 μm, and that $b - a$ lies in the range between 0.001 and 0.005, a simple statistical model is developed for the distribution of minimum earthquakes growing out of the nucleation zone. Using this model, the observed frequency-magnitude distribution for events within 1 km of SAFOD can be modeled using laboratory-derived values for the rate-and-state friction parameters d_c and $b - a$. A comparison between a rate-and-state model [35] for an isolated repeating earthquake and the SAFOD magnitude-

frequency distribution provides a reasonable fit for $M_w - 1.5$, below which the magnitude-frequency statistics fall off faster than the model. Needless to say, the resulting match is neither unique nor required by the model. Instead, it points out the value of future work connecting the initiation of rupture to the physical processes that control the transition from only quasistatic slip to full dynamic rupture.

5. – Discussion

Earthquakes begin abruptly and grow irregularly from their earliest times [9]. The examples discussed above emphasize the value of observational data collected at high sample rate and at close distances to the rupture. There is, of course, ample room to improve on the available data, particularly for strain measurements made in close proximity to the hypocenter, a goal that could be achieved by selecting a place to make an earthquake by stimulating a fault to slip [36]. For now, we must chiefly rely on improvements to our data analysis methods and increased realism of numerical simulations. Repeating earthquakes provide a particularly important target for research, as they are one of the few opportunities to study the failure process through multiple cycles. Without them, we are in a sense just collecting postage stamps of this earthquake and that one.

The foreshock sequences discussed here all favor the cascade model and the view that a simple triggering mechanism controls the initiations of earthquakes, be they foreshocks, mainshocks or aftershock [10,14]. The preslip hypothesis [9,11], however, remains viable in other cases along with other triggering mechanisms such as fluid flow [40] as we cannot exclude what cannot be detected [29,31]. In situ experiments, such as those envisioned by Savage *et al.* [36], may be needed if we are to resolve the preslip/cascade question.

Comparisons between the beginnings of earthquakes of different sizes from small regions also show promise. For example, Uchide and Ide [37] analyzed the initial rupture of M_w 1.7 to 4.6 earthquakes at Parkfield. Their derived moment rate functions follow a common curve during the growth phase of the rupture. This common moment rate increases with the cube of time, implying a self-similar process. How might we reconcile a common growth curve with the complexities evident in the beginnings of earthquakes (*e.g.* fig. 5 and many examples from [7])?

In a pair of insightful papers, Joe Andrews [38, 39] recognized a deep connection between the nature of high-frequency radiation in earthquakes, the magnitude-frequency distribution of earthquake sizes and state of stress. He argued that the stress acting on the fault is not uniform in space, as had been frequently assumed, but fractal. Further, he argued that while an earthquake smooths the stress field at the length scales of the rupture, it roughens the stress at smaller scales [38]. Andrews also related the b-value of the magnitude-frequency distribution the roughness of the stress state. For a fault to maintain a statistically stationary stress distribution and produce earthquakes with a constant b-value, the stress spectrum needed to scale as 1/wavenumber raised to a power close to 1.

On human time scales, the stress heterogeneity spectrum from past slip events is frozen in place except at the longest wavelength where tectonic loading raises the overall

level. Thus, when an earthquake nucleates, it encounters a fractally rough stress field. It should be no surprise that the radiated seismic waves exhibit complexity.

6. – Conclusions

Our current understanding of how earthquakes nucleate leaves open the questions of value of foreshocks or preslip as precursors. If there is a property of foreshocks that makes them identifiable as such before the mainshock occurs, we have not yet found it. Can foreshock sequences be discriminated from more commonly occurring sequences and swarms that do no result in large earthquakes? The collection of methods discussed here, including the imaging of foreshock rupture can be usefully applied to many sequences, from which we may learn if there are indeed differences that set them apart from background earthquakes.

The examples presented here of the initial stages of rupture of earthquakes in transform environments in continental crust generally agree with the predictions of laboratory measurements of rock friction. Preslip will likely remain undetectable for these earthquakes so long as strain observations are restricted to hypocentral distances greater than 1 km. Oceanic subduction zones, however, are only now being instrumented offshore, such as in the NantroSEIZE project in Japan and in the Hikurangi subduction margin drilling project in New Zealand. Both are locations where slow-slip and low-frequency earthquakes occur. The challenges of working in these environments are great and the risks are high, but so can be the rewards.

* * *

Waveform data and earthquake for the Parkfield and Loma Prieta earthquakes were accessed through the Northern California Earthquake Data Center (NCEDC), doi:10.7932/NCEDC.

REFERENCES

[1] Keiiti Aki and Paul G. Richards, *Quantative seismology: Theory and methods* (W.H. Freeman, San Francisco) 1980.
[2] Boris V. Kostrov and Shamita Das, *Principles of earthquake source mechanics* (Cambridge University Press) 1988.
[3] Richard H. Sibson, *Geology of the earthquake source: a volume in honour of Rick Sibson* (Geological Society of London) 2011.
[4] James H. Dieterich, "Modeling of rock friction: 1. Experimental results and constitutive equations", *J. Geophys. Res.: Solid Earth*, **84** (1979) 2161.
[5] Rice J. R. and Ruina A. L., "Stability of steady frictional slipping", *J. Appl. Mech.*, **50** (1983) 343.
[6] James H. Dieterich and Brian Kilgore, "Implications of fault constitutive properties for earthquake prediction", *Proc. Natl. Acad. Sci. U.S.A.*, **93** (1996) 3787.
[7] Gregory C. Beroza and William L. Ellsworth, "Properties of the seismic nucleation phase", *Tectonophysics*, **261** (1996) 209.

[8] Yoshio Fukao and Muneyoshi Furumoto, "Hierarchy in earthquake size distribution", *Phys. Earth Plan. Inter.*, **37** (1985) 149.
[9] Ellsworth W. L. and Beroza G. C., "Seismic evidence for an earthquake nucleation phase", *Science*, **268** (1995) 851.
[10] Agnes Helmstetter and Didier Sornette, "Foreshocks explained by cascades of triggered seismicity", *J. Geophys. Res.: Solid Earth*, **108** (2003) 2457.
[11] Michel Bouchon *et al.*, "The long precursory phase of most large interplate earthquakes", *Nat. Geosci.*, **6** (2013) 299.
[12] Paul A. Reasenberg, "Foreshock occurrence before large earthquakes", *J. Geophys. Res.: Solid Earth*, **104** (1999) 4755.
[13] Annemarie Christophersen and Euan G. C. Smith, "Foreshock rates from aftershock abundance", *Bull. Seismol. Soc. Am.*, **98** (2008) 2133.
[14] Karen R. Felzer, Rachel E. Abercrombie and Göran Ekström, "A common origin for aftershocks, foreshocks, and multiplets", *Bull. Seismol. Soc. Am.*, **94** (2004) 88.
[15] Douglas A. Dodge, Gregory C. Beroza and Ellsworth W. L., "Detailed observations of California foreshock sequences: Implications for the earthquake initiation process", *J. Geophys. Res.: Solid Earth*, **101** (1996) 22371.
[16] Bakun W. H. *et al.*, "Implications for prediction and hazard assessment from the 2004 Parkfield earthquake", *Nature*, **437** (2005) 969.
[17] Felix Waldhauser *et al.*, "Streaks, multiplets, and holes: High-resolution spatio-temporal behavior of Parkfield seismicity", *Geophys. Res. Lett.*, **31** (2004) L18608.
[18] Bakun W. H. and McEvilly T. V., "Earthquakes near Parkfield, California: Comparing the 1934 and 1966 sequences", *Science*, **205** (1979) 1375.
[19] Jim Mori, "Rupture directivity and slip distribution of the M 4.3 foreshock to the 1992 Joshua Tree earthquake, southern California", *Bull. Seismol. Soc. Am.*, **86** (1996) 805.
[20] William L. Ellsworth and Fatih Bulut, "Nucleation of the 1999 Izmit earthquake by a triggered cascade of foreshocks", *Nat. Geosci.*, **11** (2018) 531.
[21] Michel Bouchon *et al.*, "Extended nucleation of the 1999 M_{w} 7.6 Izmit earthquake", *Science*, **331** (2011) 877.
[22] Felix Waldhauser and William L. Ellsworth, "A double-difference earthquake location algorithm: Method and application to the northern Hayward fault, California", *Bull. Seismol. Soc. Am.*, **90** (2000) 1353.
[23] Kazutoshi Imanishi and William L. Ellsworth, "Source scaling relationships of microearthquakes at Parkfield, CA, determined using the SAFOD pilot hole seismic array", in: *Earthquakes: Radiated Energy and the Physics of Faulting*, edited by Rachel Abercrombie, Art McGarr, Giulio DiToro and Hiroo Kanamori, Geophysical Monograph 170 (American Geophysical Union, Washington D.C.) 2006, pp. 81-90.
[24] Raul Madariaga, "Dynamics of an expanding circular fault", *Bull. Seismol. Soc. Am.*, **66** (1976) 639.
[25] Clara E. Yoon, "A fast data mining approach for similar earthquake detection", PhD Thesis, Stanford University (2018).
[26] Clara E. Yoon *et al.*, "Foreshocks and mainshock nucleation of the 1999 M_{w} 7.1 Hector Mine, California earthquake", *J. Geophys. Res.*, **124** (2019) 1569.
[27] Lynn D. Dietz and William L. Ellsworth, "Aftershocks of the Loma Prieta earthquake and their tectonic implications", *US Geol. Surv. Prof. Paper*, **1550-D** (1997) 5.
[28] Randall A. White and William L. Ellsworth, "Near-source short- to intermediate-period ground motions", *US Geol. Surv. Prof. Paper*, **1550-C** (1993) 31.
[29] Johnston M. J. S., Linde A. T. and Gladwin M. T., "Near-field high resolution strain measurements prior to the October 18, 1989, Loma Prieta M_{s} 7.1 Earthquake", *Geophys. Res. Lett.*, **17** (1990) 1777.

[30] Takahiko Uchide, Satoshi Ide and Gregory C. Beroza, "Dynamic high-speed rupture from the onset of the 2004 Parkfield, California, earthquake", *Geophys. Res. Lett.*, **36** (2009) L04307.
[31] Johnston M. J. S. *et al.*, "Continuous borehole strain and pore pressure in the near field of the 28 September 2004 M 6.0 Parkfield, California, earthquake: Implications for nucleation, fault response, earthquake prediction, and tremor", *Bull. Seismol. Soc. Am.*, **96** (2006) S56.
[32] Johnston M. J. S. *et al.*, "Seismomagnetic effects from the long-awaited 28 September 2004 M 6.0 Parkfield earthquake", *Bull. Seismol. Soc. Am.*, **96** (2006) S206.
[33] Mark Zoback, Stephen Hickman and William Ellsworth, "Scientific drilling Into the San Andreas Fault Zone–an overview of SAFOD's first five years", *Sci. Drill.*, **11** (2011) 14.
[34] Yoshihisa Iio, "Observations of the slow initial phase generated by microearthquakes: Implications for earthquake nucleation and propagation", *J. Geophys. Res.: Solid Earth*, **100** (1995) 15333.
[35] Ting Chen and Nadia Lapusta, "Scaling of small repeating earthquakes explained by interaction of seismic and aseismic slip in a rate and state fault model", *J. Geophys. Res.: Solid Earth*, **114** (2009) B01311.
[36] Heather M. Savage *et al.*, "Scientific Exploration of Induced SeisMicity and Stress (SEISMS)", *Sci. Drill.*, **23** (2017) 57.
[37] Takahiko Uchide and Satoshi Ide, "Scaling of earthquake rupture growth in the Parkfield area: Self-similar growth and suppression by the finite seismogenic layer", *J. Geophys. Res.: Solid Earth*, **115** (2010) B11302.
[38] Andrews D. J., "A stochastic fault model: 1. Static case", *J. Geophys. Res.: Solid Earth*, **85** (1980) 3867.
[39] Andrews D. J., "A stochastic fault model: 2. Time-dependent case", *J. Geophys. Res.: Solid Earth*, **86** (1981) 10821.
[40] Xiaowei Chen and Peter M. Shearer, "California foreshock sequences suggest aseismic triggering process", *Geophys. Res. Lett.*, **40** (2013) 2602.

Proceedings of the International School of Physics "Enrico Fermi"
Course 202 "Mechanics of Earthquake Faulting", edited by A. Bizzarri, S. Das and A. Petri
(IOS, Amsterdam; SIF, Bologna) 2019
DOI 10.3254/978-1-61499-979-9-113

Experimental statistics and stochastic modeling of stick-slip dynamics in a sheared granular fault

Alberto Petri

Istituto dei Sistemi Complessi - CNR
Dipartimento di Fisica, Università La Sapienza, Roma, Italy

Summary. — These lectures illustrate laboratory experiments investigating a spring-slider system shearing a granular bed. When the shear rate is low enough, the dynamics is intermittent, displaying a chaotic stick-slip motion which can only be described statistically. This is an instance, among many others, of systems exhibiting intermittent and erratic activity, in the form of *avalanches* characterized by self-similar fluctuations of physical quantities in a wide range of values. In analogy with equilibrium systems, it is thought that such properties originate from the vicinity of some critical transition, and therefore that systems microscopically very different could display similar and universal statistical properties. Investigation of such systems is thence not only interesting in itself, but can be of help in understanding the dynamics of a wider class of phenomena and in devising effective models.

1. – Motivations

Laboratory experiments on the response of a granular bed subjected to a shear stress can be performed in different ways and with different aims. One possibility is to aim at replicating what happens within real seismic faults, trying to reproduce analogous conditions, with inherent difficulties especially for what concerns fault pressure and extension.

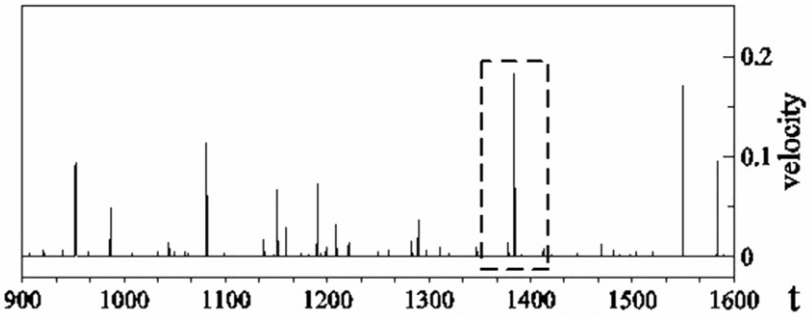

Fig. 1. – An example of intermittent signal supplied by the velocity time series of a spring-slider shearing a granular bed.

Another possibility, which is the one we explore, aims at finding whether the relevant mechanisms of the dynamics are general enough to be applied also to different systems whose phenomenology displays very similar features. This would allow to understand several situations of interest, including those not easily accessible. These lectures illustrate and discuss the results of laboratory experiments performed within this perspective, which is the one of statistical physics. For those who are not familiar with this area of physics, and perhaps with its language and basic concepts, we shall recall in the first part some notions and some methods that will also serve to introduce concepts useful to the second part, where we shall describe the experimental results. In the third part we shall try to better understand what is seen in experiments with the aid of some simple stochastic models.

1˙1. *Crackling noise*. – Many systems in the natural world react to solicitations in a discontinuous and impulsive manner, displaying random intermittence of the activity and strong fluctuations of physical quantities. Instances of this phenomenology are earthquakes, which share this feature with many natural phenomena such as fractures [1], crack propagation [2], plastic deformation [3], structural phase transitions [4], rain precipitation [5], and others. Besides intermittency, these diverse phenomena share several other statistical properties. In particular, physical quantities often display long-range correlations and self-similar distributions, *i.e.* power laws, in a wide range of values. Such common properties raise the question of whether some similar mechanism could trigger the occurrence of events. This is one main reason for investigating such systems, which have also been associated with their "crackling noise" [6]. Figure 1 shows the velocity of a spring-slider shearing a granular medium as a function of time. This is an example of crackling noise and will be the object of these lectures.

Another hint that similar dynamics could be at the basis of the phenomenology shared by different systems, comes from the study of the critical phase transitions. It is in this context that the concept of universality has been developed and observed: systems that are microscopically very different, can display similar and universal statistical features

in their critical properties. In this section the main properties characterizing critical phenomena will be shortly recalled, keeping in mind their possible connection with the "crackling noise" systems.

1˙2. *The point of view of the statistical physics*. – The study of critical phase transitions makes use of the tools of the statistical mechanics. This branch of physics is usually concerned with systems made by many components (*e.g.* molecules) whose trajectories are practically impossible to follow singularly, and that therefore are treated statistically.

To make these ideas clearer let us consider a concrete example. Many phenomena present Gaussian statistics. An instance is the diffusion, like that of a colloidal particle in a liquid, known as Brownian motion. For each spatial component the dynamics of the particle can in principle be described by a Newton equation like

$$m\frac{\mathrm{d}^2x}{\mathrm{d}t^2} = -\mu\frac{\mathrm{d}x}{\mathrm{d}t} + f(\vec{x}\,) + F(\mathbf{x},\mathbf{v}), \tag{1}$$

where m and μ are the mass and the viscous damping of the particle. $f(\vec{x}\,)$ are the external forces and $F(\mathbf{x},\mathbf{v})$ describes the interaction of the particle with the liquid molecules, depending on their coordinates and velocities $\mathbf{x}$ and $\mathbf{v}$. Being impossible to determine the motion of all the molecules, one can treat F like a random force with suitable properties [7]. One expects that such interaction force, describing the collision of the particle with the liquid molecules, has no preferred direction

$$\overline{F(t)} = 0 \tag{2}$$

and very short memory:

$$\overline{Fx} = 0, \tag{3}$$

where $\overline{\ldots}$ indicates time, or ensemble, averages. Using these assumptions, and the equipartition principle

$$m\overline{v^2} = \frac{RT}{N}\,,$$

where T is the absolute temperature, R the gas constant and N the Avogadro number, Langevin [7] determined the strength of the random force:

$$\overline{F^2} = 2kT\mu \tag{4}$$

(where $k = R/N$ is the Boltzmann constant).

From eq. (1) Fick's law for diffusion also follows. An easy way to see this is to consider eq. (1) in the simpler case when external forces and inertia can be neglected:

$$\mu v = F(t). \tag{5}$$

In modern language the Langevin assumptions amount to taking a force that only depends on time, with zero average

$$\overline{F(t)} = 0 \tag{6}$$

and no correlations

$$\overline{F_i(t')F_i(t)} = \Gamma\delta(t' - t), \tag{7}$$

i.e. a white spectrum, with $\Gamma = 2kT\mu$. By integrating eq. (5) it s straightforward to obtain (assuming the intial position in the origin)

$$\overline{x^2} = \frac{\Gamma}{\mu^2}t = Dt \tag{8}$$

with

$$D = \frac{\Gamma}{\mu^2} = \frac{2kT}{\mu}\,. \tag{9}$$

In fact, the most important result is this formula relating the diffusion coefficient to the absolute temperature and the viscous damping of the particle through Avogadro's number and the gas constant (it must be reminded that this relation was first derived by Einstein in a less straightforward way [8]). It can also be shown from eq. (1) that the coordinate of the particle obeys a Gaussian probability distribution whose variance is indeed Dt [9]. This example shows how a general results can be derived by exploiting the statistical features of a system.

1˙3. *Critical phenomena.* – Actually the crackling noise statistics of intermittent systems is very far from that of a Gaussian process. It is generally characterized by strongly asymmetric distributions of many physical quantities, usually close to power laws. We will see below that also the Gutenberg-Richter statistics for earthquakes magnitude and the Omori's law for the aftershocks number can be considered examples of this phenomenology. So the questions are where do power laws come from, and whether should they be universal.

In equilibrium critical phase transitions, some power laws are observed which originate from long-range correlations in the system. Power laws are self-similar, that is they have no characteristic scales, as opposite to, *e.g.*, exponential or Gaussian distributions, whose scales are characterized by some parameter. They generally describe self-similar (fractal) objects, Such an absence of characteristic scales was first observed in critical phase transitions and revealed the existence of universal behaviors in nature, *i.e.* not depending on many details of the system. This suggests the presence of some equivalent critical transition also in non-equilibrium systems.

To see how a critical behavior emerges in equilibrium systems let us consider a very familiar substance like water. In certain conditions of pressure and temperature, liquid

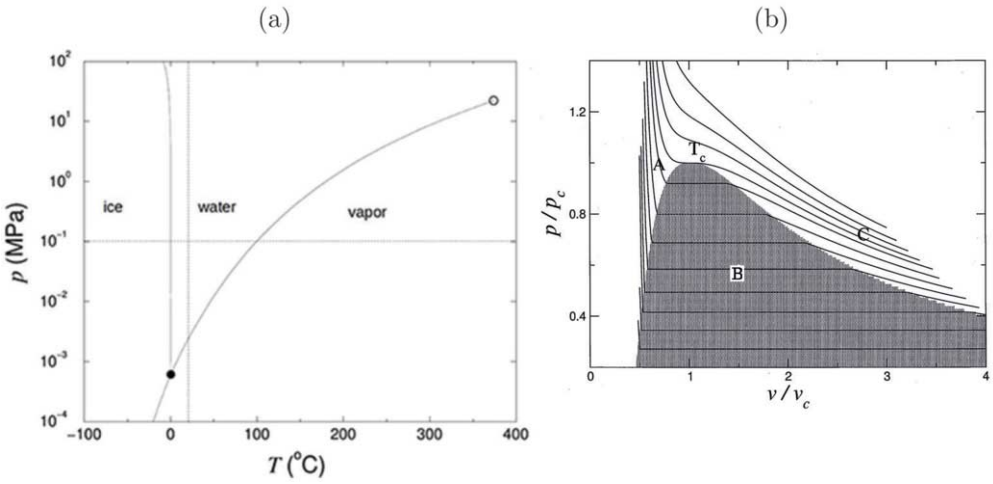

Fig. 2. – (a) Phase diagram of water. (b) Phase diagram drawn from van der Waals equation. Lines indicates isotherms. Within the shadowed region, B, the two pases A and C coexist. The region terminates above T_c.

and gaseous (vapor) phases, so as liquid and solid (ice) phases, can coexist. This situation is summerized in the phase diagram in fig. 2a), where the coexistence is marked by lines. There is also a point (black dot) where all the lines cross (the triple point) and another where the liquid-vapor line ends (open circle). This is the *critical point*, where the two phases merge into an opalescent fog. This special fog is made of vapor bubbles of any size containing liquid drops of any size, which in turn contain vapor and so on [10]. The system is a fractal, displaying the same landscape at every length scale.

The existence of a critical point is predicted by the van der Waals equation [11], relating temperature, pressure and volume at thermodynamic equilibrium. The coexistence curves derived by this equation (supplemented with the Maxwell construction) are shown in fig. 2b). Each line corresponds to a different temperature. The system is liquid in region A, gaseous in region C and the two phases coexist in region B. This region shrinks as temperature increases, until it reduces to a point at the critical temperature T_c.

1˙4. *Universality.* – The bell-shaped region of coexistence is common to many systems, which in fact display a critical point. Close to this point many thermodynamics quantities show power law dependences on its distance. For instance the temperature distance ΔT from the critical temperature, T_c, that is $\Delta T = T - T_c$, or from the specific critical volume v_c: $\Delta v = v - v_c$. The dependences of some standard thermodynamic quantities are reported in table I. The astonishing fact is that many different systems display very similar values of the exponents characterizing these dependences, which therefore appear to be *universal*, as can be seen in fig. 3 where the values for some substances are reported. Universality can also be seen in a famous plot by Guggenheim [12], fig. 4,

	α	β	γ	δ
^{3}He	0,11	0,36	1,19	4,1
^{4}He	0,13	0,36	1,18	
Ne		0,33	1,25	
Ar	0,13	0,34	1,21	
Kr		0,36	1,18	
Xe	0,11	0,33	1,23	
H_2		0,33	1,19	
O_2	0,12	0,35	1,25	
N_2		0,33	1,23	
CO_2	0,11	0,32	1,24	
SF_6	0,11	0,32	1,28	
C_2H_4		0,33	1,18	4,4
C_2H_6	0,12	0,34		

Fig. 3. – Critical exponents of table I for different phase transitions.

where experimental points for different substances on the coexistence line are reported. All points fall on the same bell-shaped curve. It is also seen that in nature many different kinds of transitions display a critical behavior [11]. After many contributions from several scholars, the concept of universality was definitely made clear by K. Wilson, who gained the Nobel prize in 1982 for identifying, by means of the renormalization group theory, which ingredients (like space dimensionality and symmetries in the interactions) make different systems fall into the same universality class.

The liaison between power laws and critical behavior strongly suggests that similar mechanisms can rule some different out of equilibrium, *e.g.* dissipative, systems and that universality classes could exist as well in this context. Simplifying a bit it could be said that when algebraic relations are observed, they could correspond to some fractal features due to the criticality of the system. However the identification of universality classes in out of equilibrium systems is still an open problem [13, 14] which is far from being solved even for simple model systems.

TABLE I. – *Critical behaviour of some thermodynamic quantities.*

Specific heat	Specific volume	Isothermal compressibility	Pressure
$c_v \propto \lvert\Delta T\rvert^{-\alpha}$	$v_G - v_L \propto \lvert\Delta T\rvert^{\beta}$	$\kappa_T \propto \lvert\Delta v\rvert^{-\gamma}$	$\lvert p - p_c\rvert \propto \lvert\Delta v\rvert^{\delta}$

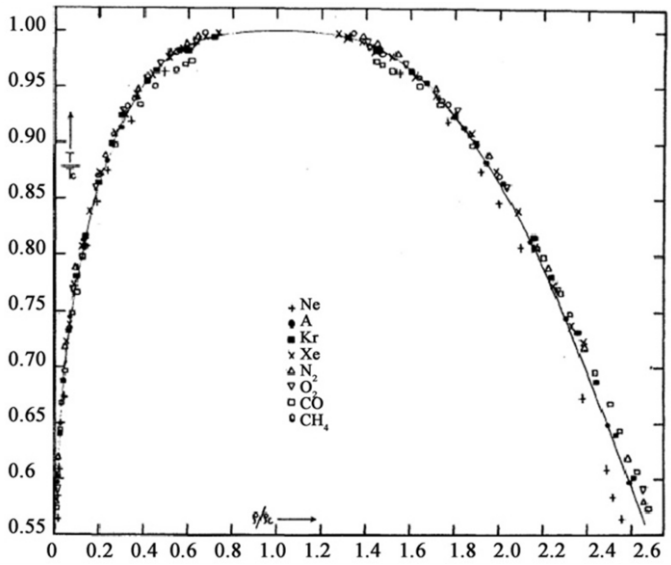

Fig. 4. – Region of coexistence. Reproduced from Guggenheim J., *Chem. Phys.*, **13** (1945) with the permission of AIP Publishing.

2. – Sheared granular matter in laboratory experiments

2˙1. *The laboratory set up.* – We have realized a laboratory version of the spring-slider system [15]. A circular geometry has been chosen because it allows for long-lasting experiments, and consequently large statistics. The system, in its present version, consists of a PPMI annular channel (see fig. 5) of inner radius $r = 12.5\,\text{cm}$ and outer radius $R = 19.2\,\text{cm}$. The channel is 12 cm high and filled almost completely with glass beads of diameter ranging between 1 and 2.5 mm, depending on the experiment. The beads can be sheared by a horizontal plate laying on their top and inserted in the channel. The plate has a few layer of grains glued to its lower face, in order to better drag the underlying granular medium, and is free to move vertically. This implies that in our experiments the medium can change volume under a nominal pressure of $p = Mg/[\pi(R^2 - r^2)]$, if M is the mass of the plate. The plate is put into rotation by a motor to which it is connected via a torsion spring, and two optical encoders supply the angular positions of motor, $\theta_0(t)$, and plate, $\theta(t)$, with a spatial resolution of $3 \cdot 10^{-5}\,\text{rad}$. From θ_0 and θ one derives the respective instantaneous velocities, $\omega_0(t)$ and $\omega(t)$. The instantaneous frictional torque $\tau(t)$ is obtained through the motion equation of the plate

$$\tau = -\kappa(\theta_0 - \theta) - I\dot{\omega}, \tag{10}$$

where κ is the spring constant and I the plate inertia. All quantities are acquired at a sampling rate between 10 and 1000 Hz, depending on the experiment, recorded by a computer and then processed and analyzed.

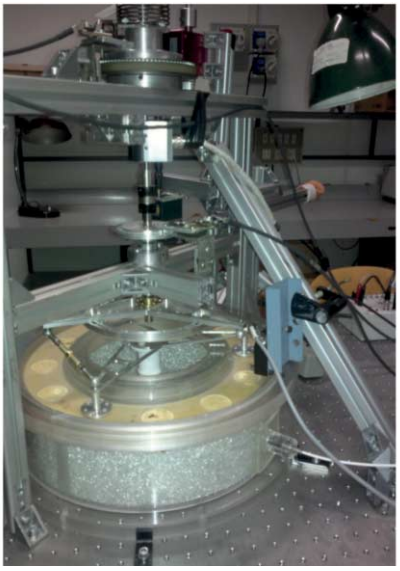

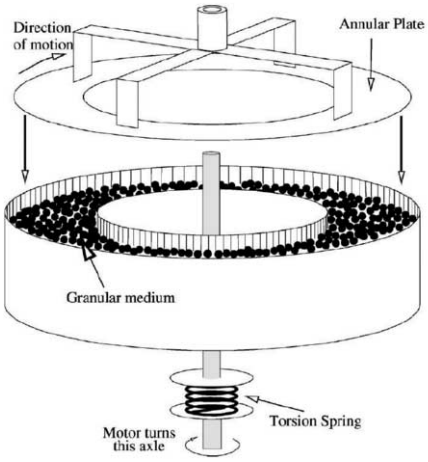

Fig. 5. – An image of the laboratory granular system and its schematic.

2˙2. *Distribution of dynamical quantities.* – When the motor speed and the spring constant are small enough, one observes high intermittent motion (fig. 1) where the plate alternates slipping, in which it explores a broad range of velocities, with sticking, in which it stays at rest for unpredictable times, as shown in fig. 1 More details of this *stick-slip* regime can be seen in the sample of plate velocity time series shown in fig. 6. The lower curve (red online) shows the instantaneous plate velocity for some slips. In the same figure the higher curve (black online) displays the velocity during continuous slide, occurring for larger values of driving speed and/or spring constant.

From these time series quantities such as slip extension, s, duration T and instantaneous velocity $\omega(t)$ can be extracted (see inset of fig. 7), and their statistical distribution estimated. An example of the resulting distribution for the slip size is reported in the main panel of fig. 7. It is seen that, as expected, it is not simply peaked around a typical value but, on the contrary, it is essentially monotonic. It is close to a power law and well described by

$$p(s) \simeq s^{\alpha} f\left(\frac{s}{s_0}\right).$$

Similar equations describe the distributions of T and ω. The function f represent a physical cut-off and for a purely critical dynamics is an exponential function. The present system sometimes also displays a bump in the distribution at high values of s and of other quantities. This is mainly related to the characteristic system time, proportional to $\sqrt{I/\kappa}$, but possibly also to other issues that can drive the system away from criticality. This possibility will be discussed below, talking about theoretical models.

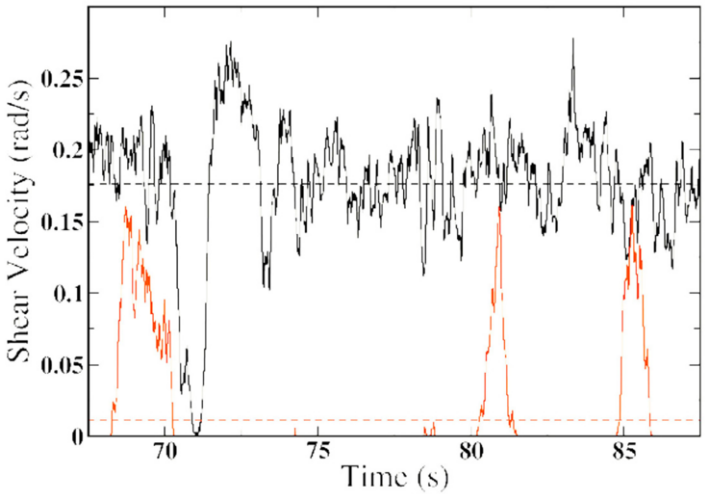

Fig. 6. – Velocity signal in stick-slip (red lower line) and continuous sliding (black upper line).

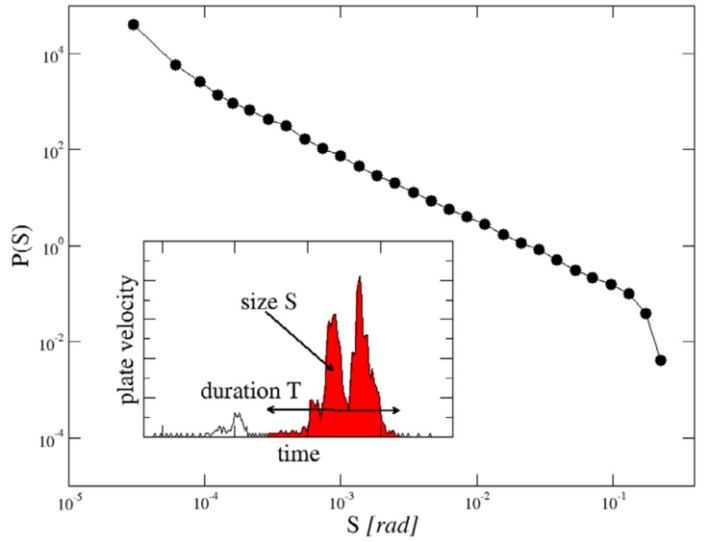

Fig. 7. – Experimental probability distribution of slip size s. In the inset an exemplification of the quantities s, T and ω.

It can be useful to remark that power laws underly also the celebrated Gutemberg-Richter law [16], relating the occurrence of seismic events to their magnitude:

$$P(m) \propto 10^{-bm},$$

where $P(m)$ is the probability of occurrence of an event with magnitude larger than m.

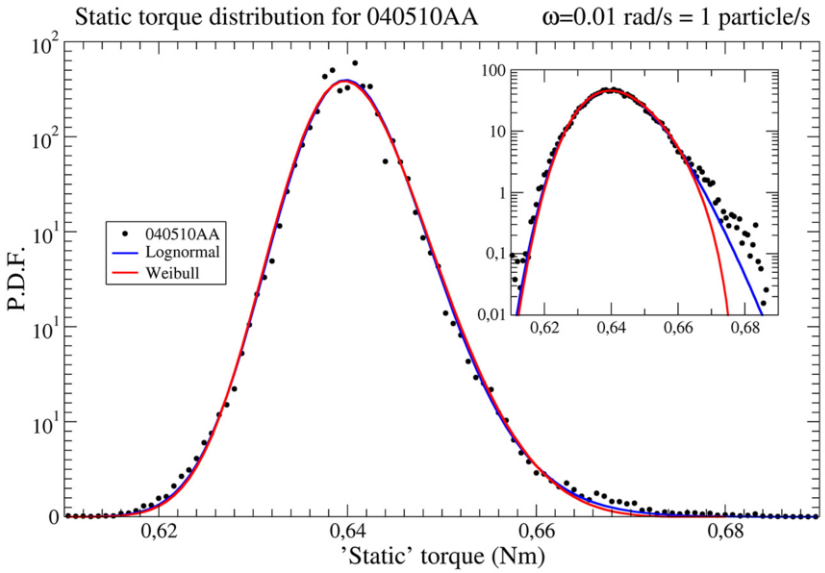

Fig. 8. – Static torque probability distribution in the stick regime.

In fact magnitude is related to the seismic moment M:

$$m = \frac{2}{3} \log M + c,$$

with $M \simeq \mu A s$, where A is the slipping area and μ the shear modulus. For given A and μ one gets from the above equations the cumulatative distribution of slips larger than s: $P(s) \propto s^{-\beta}$ with $\beta = \frac{2}{3} b$, and thus the density

$$p(s) = -\frac{\mathrm{d}P(s)}{\mathrm{d}s} \simeq s^{-(1+\beta)}.$$

For the typical value([1]) $b \approx 1$ this implies $\beta \approx 1.7$, not far from what observed in laboratory (see, *e.g.*, fig. 2 in [17]). This power law behavior is a manifestation of criticality in earthquakes, as it is Omori's law, and several other statistical regularities observed in seismic activity [16]. A recent review on this subject can be found in [18].

Another interesting quantity is the frictional torque. The first important thing to observe is that it is a fluctuating quantity. This aspect of friction is essential and is at the base of the observed critical behavior, as will be discussed below. Friction exhibits two phases: The loading one, in which the plate stills and the spring is stretched by the

([1]) Measured values have been criticized, *e.g.* Tinti and Mulargia *Bull. Seismol. Soc. Amer.*, **75** (1985) 1681 and revised, *e.g.* Y.Y. Kagan, *Tectonophysics*, **490** (2010) 103.

motor causing a linear increase of the torque, and the slipping one, where friction strongly fluctuates (examples of these fluctuations are shown in [19]). As a stochastic quantity the friction torque can only be characterized statistically. Figure 8 shows the experimental probability distribution for the static torque in the stick-slip regime. It is seen that, at variance with the previous quantities, it is not right winged. Nevertheless it is far from Gaussian and still asymmetric, with an exponential tail at large values. This signals the presence of strong correlations, as discussed in [20], which are not present in the continuous sliding phase, where the torque distribution shrinks and attains a Gaussian profile [15]. A similar behavior is observed for the dynamic friction [15].

3. – A stochastic model for the slider motion

Different models have been devised and investigated in the effort of understanding and reproducing the erratic and intermittent activity displayed by earthquakes and many other phenomena. The first of such models to our knowledge is that of Burridge and Knopoff [21]. The model is an idealization of a frictional elastic interface. It reproduces several features of earthquakes and has been extensively investigated [22]. A different approach to this kind of phenomena was devised at the end of the eighties by Bak, Tang and Wiesenfeld [23] who, using a sand-pile as a metaphor, proposed the concept of Self-Organized Criticality (SOC). The concept gained wide popularity and has been the subject of a huge quantity of work [24]. Nevertheless the concept of critical self-organization itself has been criticized [25] and still presents many open problems [13,14], like the existence of well-defined universality classes and the way it can be connected with real systems in terms of specific dynamics, parameter values, etc. The sand-pile, and the models inspired to it, belong to the category of stochastic cellular automata, to which belong even other kinds of models more directly related to real systems. For instance the Fiber Bundle Model and its derivations [26] which together with other statistical models [27] aim at the description of fractures or cracks [28]. There is no room here for reviewing these models in the due manner and in the following we shall focus on a different approach [29], which appears more suitable to describe the dynamics observed in the experiments.

3˙1. *The friction force.* – To model the experimental spring-slider system one can start from eq. (10). The friction torque, τ, however is known only through its experimental realization. It looks random and in principle can be a function of many variables such as position, velocity, acceleration, $F(\theta, \omega, \dot{\omega}, \ldots)$, and others, like state or memory variables. In analogy with other friction laws, one can first attempt to put into evidence a definite dependence on the instantaneous velocity. As seen above, friction is a fluctuating quantity and presents complicated trajectories as function of the instantaneous plate speed, (as shown for instance in fig. 2 of [17]). One possible way out is to average over many slips. That is to consider the mean value of friction for given instantaneous velocity. Despite the apparent chaoticity of the friction trajectories a regular pattern emerges, showing a well-defined dependence, also characterized by a velocity weakening, visible in fig. 9.

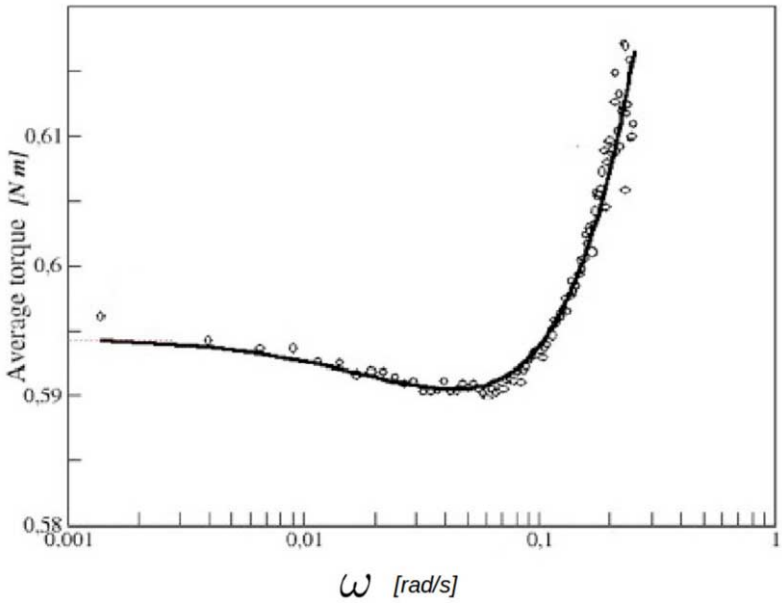

Fig. 9. – Average friction as function of the instantaneous velocity.

In order to account for the stochastic fluctuations one can be inspired by the Langevin dynamics discussed in sect. **1**, and assume that the friction is the sum of a deterministic velocity-dependent term, $\tau_d(\omega)$ and a random term, τ_r:

$$\tau = \tau_d(\omega) + \tau_r. \tag{11}$$

As for the Brownian motion the aim of the random term is to describe in an effective way the interaction of the probe, in this case the plate, with the medium, *i.e.* the granular bed, without resort to the motion of each individual particle. The friction exerted by the granular medium on the plate is mainly due to the action in the medium of force chains which transmit the stress. The strength of these chains evolves in a continuous manner along with the configuration during the motion, while in the stick phases it does not change sensibly. Thus in this case the time dependence of the random force is replaced by an angular dependence. The simplest assumption that can be made is that, along the plate trajectory, the strength variations result from the sum of independent increments. This can be formalized as

$$\frac{\mathrm{d}\tau_r}{\mathrm{d}\theta} = \eta(\theta), \tag{12}$$

where η is a white noise satisfying the usual properties (6) of zero average

$$\overline{\eta(\theta)} = 0, \tag{13}$$

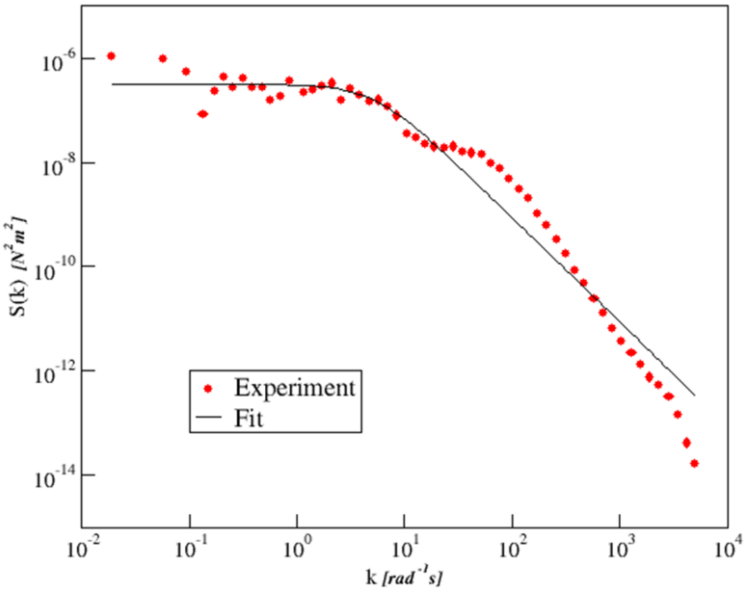

Fig. 10. – Spectrum of the dynamic random torque τ_r with a Lorentzian fit.

and δ correlation (7)

$$\overline{\eta(\theta')\eta(\theta)} = r\delta(\theta' - \theta), \tag{14}$$

while r is the strength of the fluctuations. This amounts to saying that the friction force performs a Brownian motion [29], like the one described in sect. **1**.

The above form is coherent with the fact that friction cannot be a white noise itself, since this would imply that its value at $\theta + \mathrm{d}\theta$ would be totally independent of its value at θ, which looks highly unphysical. On the other hand, a simple random walk can also lead to unphysical consequences since, as we also know from sect. **1**, the average fluctuations for this process diverge linearly with the parameter (which in this case is the angular coordinate θ). Forces must be limited, and this can be obtained by subjecting them to some bounding potential. At the lowest order it can be assumed to be harmonic so that the friction torque obeys the equation

$$\frac{\mathrm{d}\tau_r}{\mathrm{d}\theta} = \eta(\theta) - a\tau_r. \tag{15}$$

This process is named after Uhlembeck and Ornstein [9] and the parameter a represents the inverse of its correlation length (a correlation angle in the present case).

In order to test this hypothesis and determine the relevant parameters r and a one resorts to the experimental data. By subtracting $\tau_d(\omega)$ from the experimental time series

of $\tau(\omega)$, one obtains the series for $\tau_r(\theta)$. Performing a Fourier transform (in angle) one gets the power spectrum of the signal, as a function of the wave number, an instance of which is shown in fig. 10. It is seen that its shape is well described by a Lorentzian, and the values of r and a can be determined by a best fit.

3˙2. *Results from the model.* – Different forms can be equivalently assumed for describing the behavior of τ_d reproduced in fig. 9. We have resorted to one already employed in the literature for the solid-on-solid friction [30]:

$$\tau_d(\omega) = \tau_0 + \gamma \left\{ \omega - 2\omega_0 \ln\left(1 + \frac{\omega}{\omega_0}\right) \right\}, \tag{16}$$

where τ_0 is the constant dynamical friction and ω_0 a characteristic speed. With this expression and (15) in eqs. (10) and (11) one can simulate numerically the stick-slip motion of the plate employing the values of the parameters used in the experiment (plate inertia I, spring constant κ, motor driving angular speed ω_d) and those characterizing friction in eqs. (15) and (16).

By repeating on the resulting time series the same analysis performed on the experimental series one can compute distributions for slip extension, duration, etc. Some results are shown in fig. 11 together with experimental data. The different curves correspond to different driving speed of the plate and a good agreement is obtained in all cases.

4. – Criticality and its possible breakdown

4˙1. *Where does criticality come from?* – This question has not yet received definitive answers. It involves areas of non-equilibrium statistical physics which, at variance with thermodynamics, deals with systems where detailed balance is not observed and that usually include dissipative forces. As already recalled, a common feature of these systems is the existence of a non-equilibrium critical transition underlying the observed dynamics [6], that for granular matter could be the jamming transition [31, 32].

The model introduced above does not consider the motion of individual grains but only their global influence on the slider dynamics and is closely related to models for propagating fracture in disordered media [33, 27]. In this frame, a large class of models presenting common, and in some cases universal, critical features are the depinning models. These models describe the motion of an elastic line or surface, representing the crack front, driven by a uniform force: The motion takes place in the presence of a viscous force and of a disordered potential, which accounts for inhomogeneities and can exert a pinning force. When this force is larger than the driving force, the system stills, until the drive is made large enough. The depinnig transition presents all the features of criticality described above (power law distributions, correlations, etc.). These features are shared by other models describing different systems, and in certain cases give raise to identical critical exponents, distributions etc. (or at least compatible, when models can be studied only numerically). One instance of these cases is the so-called ABBM model.

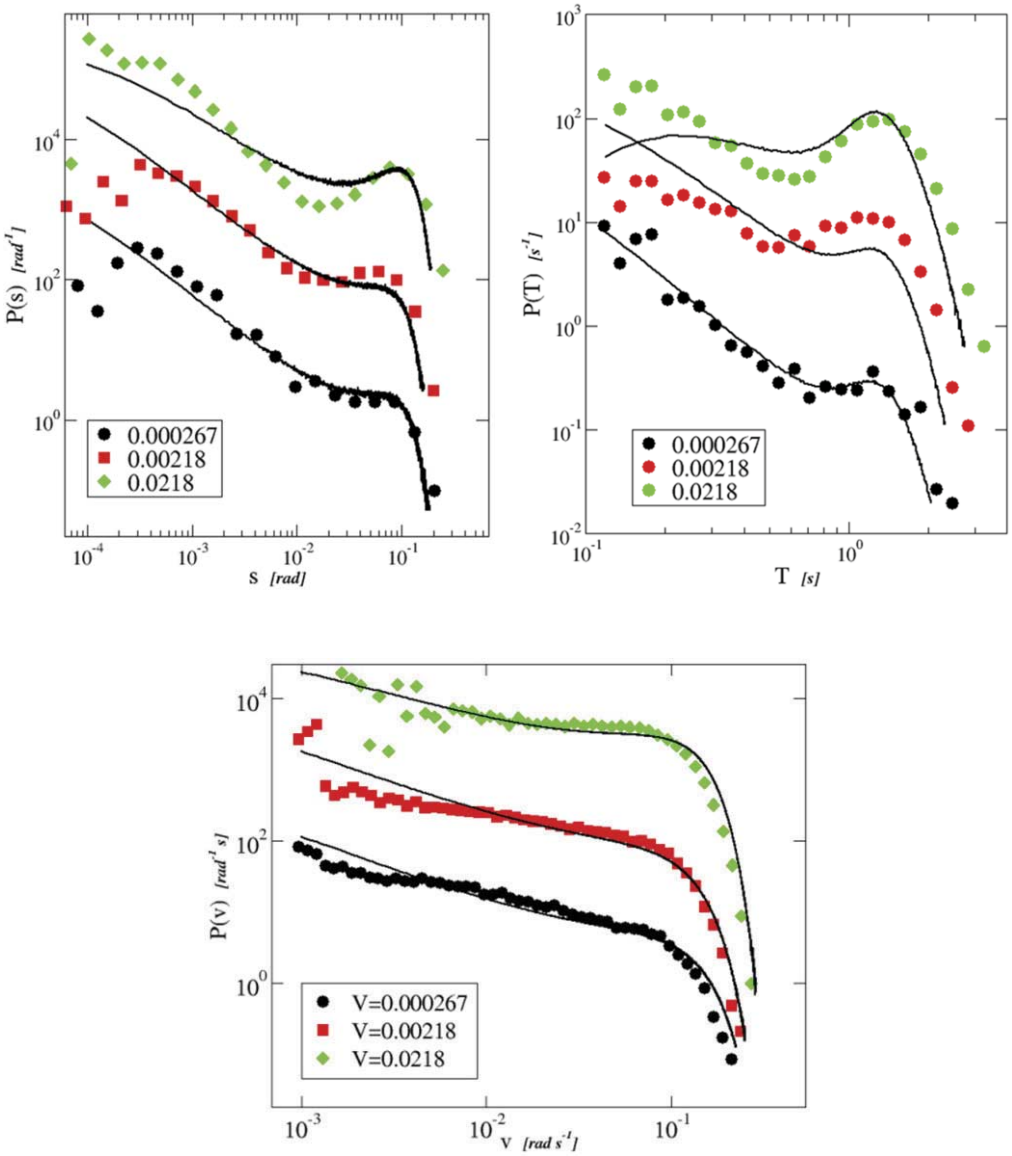

Fig. 11. – Distributions for slip size, velocity and duration from experiments (symbols) and simulation of the model (lines) from eqs. (10), (11), (15) and (16). Three different driving speeds are considered.

4˙2. *The ABBM model.* – A ferromagnet in an external magnetic field H is characterized by a certain amount of magnetization M. If the field changes, magnetization follows. However, on closer observation it can be seen that M as a function of H is not smooth but rather irregular, displaying jumps, *avalanches*, of magnetization. These jumps were

at first revealed by their induced electromagnetic flux and are known under the name of Barkhausen effect, or noise, see *e.g.* [34]. In order to describe the Barkhausen noise, in [35] a model was derived from microscopic considerations, known as $ABBM$ model. Besides the application to material science, a very interesting point of the model is that it has been shown to be directly related with the depinning models mentioned above [34] and, in certain cases, it is described by the same equation [36]. One of this case is the *mean field* case, in which the average position of the interface is considered.

The ABBM model in the mean-field formulation can be described by the equation

$$\frac{\mathrm{d}x}{\mathrm{d}t} = -(x - ct) + F \tag{17}$$

with x a quantity directly proportional to the magnetization and c the rate of variation of the external field H. F is a random perturbation given by

$$\frac{\mathrm{d}F}{\mathrm{d}x} = \eta(x),$$

where η has the usual properties of the white noise, eqs. (13) and (14). One can recognize the same evolution described by (12).

As anticipated, although not evident at first sight, the dynamics described by eq. (17) is critical. Motion occurs intermittently and many physical quantities characterizing the avalanches (duration, size, velocity) are distributed as power laws. The importance of the model comes also from the fact that it is analytically soluble and all quantities are known exactly. Moreover it is possible to identify the origin of criticality in the self-similar symmetry owned by the equation [34]. For all these reasons the model is considered paradigmatic and investigated in different contexts [37]. It also describes a kind of population dynamics (previously introduced by Feller [38]) and the price evolution of several financial products [39]. More recently, the same equations have been adopted for describing other items, such as concentration of pollutants [40].

Concerning the stochastic dynamics of the slider, ABBM is also a simplified model of this dynamics. In fact, by neglecting inertia in eq. (10), in analogy with what done to obtain eq. (5), using eq. (11) and then moving τ_d to the right-hand side, one has

$$\tau_d = -k(\theta - \omega_d t) + \tau_r.$$

It is easy to recognize that this equation assumes the aspect of eq. (17) if in eq. (16) one retains only the linear term in the velocity. The correspondence is exact by setting $a = 0$ in eq. (15).

4˙3. *Breakdown of criticality.* – Models for granular and earthquake dynamics directly mappable into the original ABBM have been proposed and investigated [41]. Nevertheless, how and to which extent the presence of different friction laws and inertia can affect the critical behavior and the universality properties of dynamics is still not clear and it is subject of investigation. The statistical distributions derived from our experiments, so

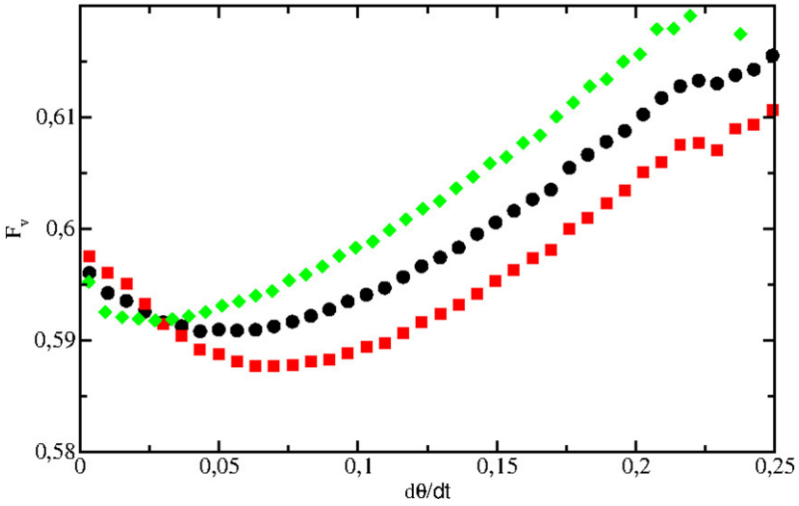

Fig. 12. – Friction torque measured in an experiment with imposed plate speed. Diamond (green on line) correspond to decreasing speed and square (red on line) to increasing speed. Bullets (black) are the average friction.

as those reproduced by the related model, are not clean power laws as those from the ABBM model [34]. Other deviations from criticality have been observed in [42] and [43].

In [37], some aspects of the effect of inertia on the original ABBM have been studied, while other aspects are under investigation [44]. In addition there are many features of the granular-slider dynamics that should be considered and that also the models discussed here do not take into consideration. One of these features is friction hysteresis. It is well known that in many instances dynamical friction is not a single-valued function of velocity. Different friction laws addressing these problem have been proposed, among the most widely adopted being those by Dieterich [45] and Ruina [46], also known as *rate-and-state* laws. These laws were at first deduced and validated for solid-on-solid friction, and then employed, together with some simplified versions, also for describing the friction of faults and granular gauges [47-49]. It is thus clear that a description of the systems must take into account suitable friction laws. Attempts to supply eq. (11) with a rate-and-state law have been done in [19], where the behavior of friction as function of controlled plate speed has been measured while imposing a velocity ramp. An example of the resulting dynamical friction si shown in fig. 12. It can be seen that, although exhibiting weakening, friction behaves very differently in the accelerating and decelerating phases, with a peculiar crossing value. Another important point concerns the correlation length a in eq. (15). Since the granular medium is quasi-solid near the jamming point, and quasi-liquid at high shear rate, it is clear that a is also a dynamical quantity that should be described by a suitable, shear rate dependent, constitutive equation. All these features can cause a breakdown of the critical behavior, at least for large avalanches, as emerging in recent experiments [42, 43].

5. – Summary and perspectives

These lectures have summarized some of the results produced in experiments on the stick-slip dynamics of a sheared laboratory fault, and some models aimed at describing and understanding the observed phenomenology. This has been done within a statistical physics approach and adopting simple stochastic models, because the very irregular and chaotic dynamics prevents detailed descriptions. At the same time, such approach is also an effort to understand whether alike elementary mechanisms might underly several different natural phenomena that display apparently similar phenomenologies.

It is clear that all the features listed in the last section, like friction hysteresis, variable correlation length in the random friction, scaling breakdown, etc., are important in determining the slider motion even in a simplified approach as the one reported here. Their influence deserves to be more systematically investigated in both experiments and theoretical models. Especially these latter seem to be still rather scarce and have very little evolved. At the same time the results discussed here show that also approaches based on general assumptions can be quite effective in the description of systems with irregular dynamics.

* * *

The author acknowledges A. Baldassarri, F. Dalton, F. Leoni and M. J. Oliveira for some pictures.

REFERENCES

[1] PETRI A., PAPARO G., VESPIGNANI A., ALIPPI A. and COSTANTINI M., *Phys. Rev. Lett.*, **73** (1994) 3423.
[2] CALDARELLI G., TOLLA F. D. and PETRI A., *Phys. Rev. Lett.*, **77** (1996) 2503.
[3] DIMIDUK D. M., WOODWARD C., LESAR R. and UCHIC M. D., *Science*, **312** (2006) 1188.
[4] CANNELLI G., CANTELLI R. and CORDERO F., *Phys. Rev. Lett.*, **70** (1993) 3923.
[5] NEELIN J. D. and PETERS O., *Nat. Phys.*, **2** (2006) 393.
[6] SETHNA J. P., DAHMEN K. A. and MYERS C. R., *Nature*, **410** (2001) 242.
[7] LANGEVIN P., *C. R. Acad. Sci. (Paris)*, **146** (1908) 530.
[8] EINSTEIN A., *Ann. Phys. (Leipzig)*, **7** (1905) 549.
[9] GARDINER C., *Handbook of stochastic methods* (Springer-Verlag, Berlin) 1997.
[10] HUANG K., *Statistical mechanics* (John Wiley & Sons) 1987.
[11] OLIVEIRA M. J., *Equilibrium Thermodynamics* (Springer) 2017.
[12] GUGGENHEIM J., *Chem. Phys.*, **13** (1945) 253.
[13] PRUESSNER G., *Self-Organised Criticality: Theory, Models and Characterisation* (Cambridge University Press) 2012.
URL `http://books.google.it/books?id=TXKcpGqMSDYC`
[14] PETRI A. and PONTUALE G., *J. Stat. Mech.*, (2018) 063201.
[15] DALTON F., FARRELLY F., PETRI A., PIETRONERO L., PITOLLI L. and PONTUALE G., *Phys. Rev. Lett.*, **95** (2005) 138001.
[16] TURCOTTE D. R., *Fractals and Chaos in Geology and Geophysics* (Cambridge University Press) 1997.

[17] Ciamarra M. P., Dalton F., de Arcangelis L., Godano C., Lippiello E. and Petri A., *Tribol. Lett.*, **48** (2012) 89.
[18] de Arcangelis L., Godano C., Grasso J. R. and Lippiello E., *Phys. Rep.*, **628** (2016) 1.
[19] Leoni F., Baldassarri A., Dalton F., Petri A., Pontuale G. and Zapperi S., *J. Non-Cryst. Solids*, **357** (2010) 749.
[20] Petri A., Baldassarri A., Dalton F., Pontuale G., Pietronero L. and Zapperi S., *Eur. Phys. J. B*, **64** (2008) 531.
[21] Burridge R. and Knopoff L., *Bull. Seismol. Soc. Am.*, **341** (1967) 57.
[22] Carlson J. M., Langer J. S. and Shaw B. E., *Rev. Mod. Phys.*, **66** (1994) 657.
[23] Bak P., Tang C. and Wiesenfeld K., *Phys. Rev. Lett.*, **59** (1987) 381.
URL `http://link.aps.org/doi/10.1103/PhysRevLett.59.381`
[24] Watkins N. W., Pruessner G., Chapman S. C., Crosby N. B. and Jensen H. J., *Space Sci. Rev.*, **198** (2016) 3.
[25] Dickman R., Muñoz M. A., Vespignani A. and Zapperi S., *Braz. J. Phys.*, **30** (2000) 27.
[26] Pradhan S., Hansen A. and Chakrabarti B. K., *Rev. Mod. Phys.*, **82** (2010) 499.
[27] Alava M. J., Nukala P. K. and Zapperi S., *Adv. Phys.*, **55** (2006) 349.
[28] Pontuale G., Colaiori F. and Petri A., *EPL*, **101** (2013) 16005.
URL `http://dx.doi.org/10.1209/0295-5075/101/16005`
[29] Baldassarri A., Dalton F., Petri A., Zapperi S., Pontuale G. and Pietronero L., *Phys. Rev. Lett.*, **96** (2006) 118002.
[30] Baumberger T. and Caroli C., *Adv. Phys.*, **55** (2006) 279.
[31] Dauchot O., Marty G. and Biroli G., *Phys. Rev. Lett.*, **95** (2005) 265701.
[32] Ciamarra M. P., Lippiello E., Godano C. and de Arcangelis L., *Phys. Rev. Lett.*, **104** (2010) 238001.
[33] Dalton F., Petri A. and Pontuale G., *J. Stat. Mech.*, (2010) P03011.
[34] Colaiori F., *Adv. Phys.*, **57** (2008) 287.
[35] Alessandro B., Beatrice C., Bertotti G. and Montorsi A., *J. Appl. Phys.*, **68** (1990) 2901.
[36] Bonamy D., Santucci S. and Ponson L., *Phys. Rev. Lett.*, **101** (2008) 045501.
[37] Le Doussal P., Petković A. and Wiese K. J., *Phys. Rev. E*, **85** (2012) 061116.
URL `http://link.aps.org/doi/10.1103/PhysRevE.85.061116`
[38] Feller W., *Ann. Math.*, **54** (1951) 173.
[39] Cox J., Ingersoll J. E. and Ross S., *Econometrica*, **53** (1985) 385.
[40] Pedersen A. R., *Scand. J. Stat.*, **27** (2000) 385.
[41] Dahmen K. A., Ben-Zion Y. and Uhl J., *Nat. Phyis.*, **7** (2011) 554.
[42] Barés J., Wang D., Wang D., Bertrand T., O'Hern C. S. and Behringer R. P., *Phys. Rev. E*, **96** (2017) 052902.
URL `http://arxiv.org/abs/1709.01012`
[43] Baldassarri A., Annunziata M., Gnoli A., Pontuale G. and Petri A., *Breakdown of scaling and friction memory in the critical granular flow*, arXiv:1811.02464.
[44] Baldassarri A. and Petri A., in preparation.
[45] Dieterich J., *J. Geophys. Res.: Solid Earth*, **99** (1994) 2601.
[46] Ruina A., *J. Geophys. Res.: Solid Earth*, **88** (1983) 10359.
[47] Scholz C. H., *Nature*, **391** (1998) 37.
[48] Marone C., *Ann. Revs. Earth & Plan. Sci.*, **26** (1998) 643.
[49] Bizzarri A. and Cocco M., *J. Geophys. Res.: Solid Earth*, **108** (2003) 2373.

This page intentionally left blank

Proceedings of the International School of Physics "Enrico Fermi"
Course 202 "Mechanics of Earthquake Faulting", edited by A. Bizzarri, S. Das and A. Petri
(IOS, Amsterdam; SIF, Bologna) 2019
DOI 10.3254/978-1-61499-979-9-133

Inversion of earthquake rupture process: Theory and applications

Yun-tai Chen(*)

College of the Earth and Planetary Sciences, University of Chinese Academy of Sciences Beijing 100049, China

School of the Earth and Space Sciences, Peking University - Beijing 100871, China

Yong Zhang

School of the Earth and Space Sciences, Peking University - Beijing 100871, China

Institute of Geophysics, China Earthquake Administration - Beijing 100081, China

Li-sheng Xu

Institute of Geophysics, China Earthquake Administration - Beijing 100081, China

Summary. — We present the theory and methods of earthquake rupture process inversion by using seismic and geodetic data, and their applications to scientific researches and earthquake emergency responses. It is shown that the knowledge obtained from these studies has much improved our understanding of the complexities of the earthquake source and causative mechanism of the earthquake disaster, and is of important reference value in earthquake disaster mitigation such as rapid earthquake emergency response. Especially since the 2008 $M_{\rm w}7.9$ ($M_{\rm S}8.0$) Wenchuan, Sichuan, earthquake, fast and routine determination of the earthquake rupture process has been performed for significant earthquakes ($M_{\rm S} \geq 6.5$ in China and $M_{\rm S} \geq 7.5$ worldwide), and the results obtained are timely reported to the authorities and released to the public on the web site. The time consumed by the inversion has been reduced from more than 5 hours in 2009 to approximately 1-3 hours at present. The timely released rupture model was routinely used by the China Earthquake Administration and other authorities during the earthquake emergency responses period for destructive earthquakes, such as the 2010 $M_{\rm w}6.9$ Yushu earthquake, the 2013 $M_{\rm w}6.6$ Lushan earthquake, the 2014 $M_{\rm w}6.1$ Ludian earthquake, and the 2015 $M_{\rm w}7.8$ Gorkha, Nepal, earthquake, among the others.

(*) E-mail: chenyt@cea-igp.ac.cn

1. – Introduction

As the continuous developments in digital seismic network and earthquake source theory [1-3], it has been feasible to investigate the rupture process on a finite fault since the 1980s. Many significant earthquakes were studied and their rupture models have been determined. A detailed rupture model of an earthquake provides important source information, *i.e.*, the fault dimension, the source duration, the rupture directivity, the slip distribution, and the source time function, etc. The source information renews and improves our understanding of the earthquake source physics, and is necessary to constrain the source dynamic process. In addition, the rupture model is valuable in the simulation of strong ground motion and thus is useful in the estimation of intensities which are critical in earthquake emergency response (EER) [4] and even in earthquake early warning (EEW) [5].

The pioneering works of rupture process inversion can be referred to Kikuchi and Kanamori [6], Hartzell and Heaton [7], and Das and Kostrov [8], who estimated the rupture models by inverting local strong motion and/or teleseismic seismograms. The techniques were further developed by the subsequent researchers (*e.g.*, [9]). An alternative method is to invert the apparent source time functions (ASTFs), which should have been obtained by deconvolving the Green's function (sometimes a small shock served as the empirical Green's function) from the mainshock seismograms [10-13]. In principle, the seismogram inversion and the ASTF inversion are equally effective to estimate the rupture model [14-17].

The fault slip model can be also determined by inverting geodetic deformation data. Compared with the seismic data inversion, geodetic inversion of the co-seismic deformation data has fewer unknown parameters and thus has a higher stability. Meanwhile, the disadvantage is that it cannot constrain the temporal evolution of slip accumulation. Combination of the seismic and geodetic data can synthesize their advantages and results in a better resolution power at different depths. In the past two and more decades, joint inversion of seismic and geodetic data has been a powerful tool to study the earthquake source process. All seismic and geodetic datasets, *e.g.*, strong-motion data, broad-band data at local, regional and teleseismic distances, high-rate/campaign GNSS (Global Navigation Satellite System) data, InSAR (Interferometric Synthetic Aperture Radar) data, and leveling data, have been used and inverted for that purpose (*e.g.*, [18, 19]). The joint inversion much expands the frequency band of source inversions, and provides better estimates of source parameters, such as magnitude, source dimension and duration, rupture velocity and rupture directivity, etc.

On the other hand, as large and disastrous earthquakes frequently occurred in the 21st century, more and more needs have been raised for the source inversion by disaster mitigations. Fast estimation of earthquake sources can effectively provide valuable information for intensity estimation especially at near-fault distances. An example is the 12 May 2008 Wenchman earthquake. The two meizoseismal areas of intensity XI, which are located around the epicenter and the Beichuan County, are closely associated with the two slip-concentrated patches [20, 21]. However, it is regrettable that should the meizo-

seismal area in the Beichuan County as identified by the inverted fault slip distribution be noticed and corresponding measurements adopted at that time, the casualties in that area would be able to be greatly reduced. Another example is the 2011 $M_{\rm w}9.1$ Tohoku earthquake. Although the earthquake early warning (EEW) system of Japan was well operated, the fast measured magnitude stabilized at $M_{\rm S}8.1$ rather than $M_{\rm w}9.1$ two minutes after the earthquake initiation (`http://www.eqh.dpri.kyoto-u.ac.jp/~masumi/ecastweb/110311/index.htm`), from which the height of the tsunami wave approaching the coast was empirically estimated to be 3 m to 6 m [22]. Actually, the $M_{\rm w}9.1$ shock caused a height of the tsunami wave as large as 37.9 m in Miyako. The unexpected big wave caused the majority of loss of life during the earthquake. The problem, as has been widely discussed by the international seismological community, is that the EEW system of JMA treated the earthquake as a point source, rather than a finite-sized fault plane (`https://www.nature.com/news/2011/110329/full/471556a.html`). Therefore, to well estimate the intensity at near-source distance and the height of the tsunami wave, the finite-fault rupture model should be considered.

In this paper, we first summarize the theory and methods of finite-fault source inversions. We will derive the equations of seismogram inversion and ASTF inversion. In application to the 2009 $M_{\rm w}6.3$ L'Aquila, Italy, earthquake, we will compare and discuss the advantages and disadvantages of the two kinds of the inversion methods. The method of joint inversion with seismic and geodetic data is also presented. By also taking the 2009 $M_{\rm w}6.3$ L'Aquila earthquake as an example, we will show the improved resolution power of the joint inversion. Then in the following, we present the source studies of three significant earthquakes occurred around the Tibet Plateau, *i.e.*, the 2011 $M_{\rm w}7.8$ Kunlun earthquake, the 2008 $M_{\rm w}7.9$ Wenchuan earthquake, and the 2010 $M_{\rm w}6.9$ Yushu earthquake. In addition, we will introduce the progress we have made in fast-source inversion for earthquake emergency responses. The success in prediction of the rupture direction and even the meizoseismal area has provided valuable information for intensity estimation. This suggests that at the present time the earthquake source inversion has been able to play an important role in earthquake disaster mitigations.

2. – Theory and methods

2˙1. *Seismic inversion.* – The seismic waves radiated from a finite-fault can be represented as (fig. 1)

$$U_n(P,t) = \iint_{\Sigma} G_{np,q}(P,t;Q,0) * m_{pq}(Q,t)\mathrm{d}\Sigma', \tag{1}$$

where $U_n(P,t)$ is the seismogram on the n-th component observed at $\boldsymbol{P}$, $G_{np,q}(P,t;Q,0)$ is the Green's function at P caused by a force couple (p, q) at Q, $m_{pq}(Q,t)$ is the time history of the force couple (moment tensor element). Equation (1) is the basis of the source inversion.

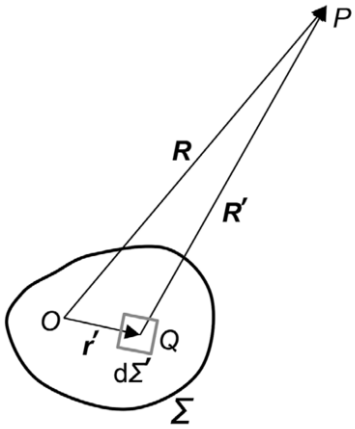

Fig. 1. – The finite fault model. The origin of coordinates is taken on the finite fault plane. $\boldsymbol{O}$ is a reference point (*e.g.*, the hypocenter) on the fault $\boldsymbol{\Sigma}$. $\boldsymbol{R}$ and $\boldsymbol{R}'$ are the position vectors $\overline{OP}$ and $\overline{QP}$, of the observation point P, respectively. $\boldsymbol{r}'$ is the position vector $\overline{OQ}$.

2˙1.1. Inversion with fixed rake. If a purely shear dislocation is assumed and the double-couple mechanism is known, we have

$$m_{pq}(Q,t) = M_0(Q,t)(e_p v_q + e_q v_p), \tag{2}$$

where M_0 is the scalar seismic moment, $\boldsymbol{e}$ and $\boldsymbol{v}$ are the slip vector and the normal direction on the fault plane, respectively. By putting eq. (2) into eq. (1), we can get

$$U_n(P,t) = \iint_{\Sigma} G_{np,q}(P,t;Q,0) * [M_0(Q,t)(e_p v_q + e_q v_p)]\mathrm{d}\Sigma'. \tag{3}$$

If assuming

$$g_n(P,t;Q,0) = G_{np,q}(P,t;Q,0) \cdot (e_p v_q + e_q v_p), \tag{4}$$

where $g_n(P,t;Q,0)$ is the Green's functions caused by a point source with a given focal mechanism. Then eq. (3) becomes

$$U_n(P,t) = \iint_{\Sigma} g_n(P,t;Q,0) * M_0(Q,t)\mathrm{d}\Sigma'. \tag{5}$$

In eq. (5), the unknown is $M_0(Q,t)$, *i.e.*, spatial and temporal variations of the scalar seismic moment.

For a case of spatial point source ($R \gg L$, L is the source dimension), a path approximation can be assumed

$$g_n(P,t;Q,0) \cong g_n(P,t-\tau;O,0), \tag{6}$$

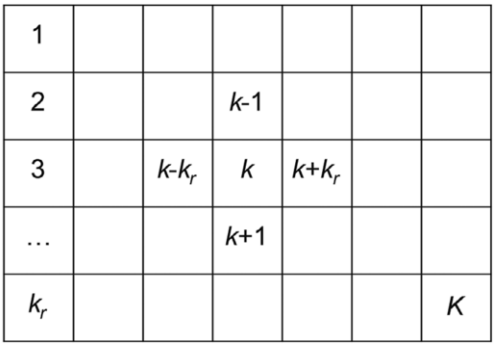

Fig. 2. – Discretization of a fault plane. Here k_r is the number of sub-fault along the down-dip direction of the fault.

where O is a reference point on the fault (*e.g.*, the hypocenter), τ is the difference of travel time between Q-P and O-P, and equals $(R - R')/c$, where c is the phase velocity. Sometimes for convenience, $R-R'$ is approximated as $\boldsymbol{r}' \cdot \boldsymbol{e}_R$ when the minimum wavelength λ, the hypocentral distance R, and the source dimension L satisfy $\lambda R/2 \gg L^2$ (notice $R \gg L$ is also demanded here).

By putting eq. (6) into eq. (5), we get

$$U_n(P,t) = \iint_\Sigma [g_n(P, t-\tau; O, 0) * M_0(Q,t)] \mathrm{d}\Sigma'. \tag{7}$$

It can be rewritten as

$$U_n(P,t) = g_n(P,t;O,0) * \iint_\Sigma [\delta(t-\tau) * M_0(Q,t)] \mathrm{d}\Sigma', \tag{8}$$

the integration on the right-hand side actually the apparent source time function (ASTF)

$$S_A(P,t) = \iint_\Sigma [\delta(t-\tau) * M_0(Q,t)] \mathrm{d}\Sigma'. \tag{9}$$

From eq. (7), we can estimate the rupture process by calculating only one Green's function for each station, which much reduce the calculation cost. Equations (8) and (9) suggest another way to determine the rupture model: First determine the ASTF at each station by deconvolving the Green's function from the observation, and then invert the ASTFs for rupture process based on eq. (9). Two important issues should be noted for the path approximation described in eq. (6) and used in eq. (7) to eq. (9). First, it works at only far-field distances ($R \gg L$). And second, single phase should be considered since the lengths of ray path (R and R') and the phase velocity c are needed in calculation of the travel time difference $\tau = (R - R')/c$.

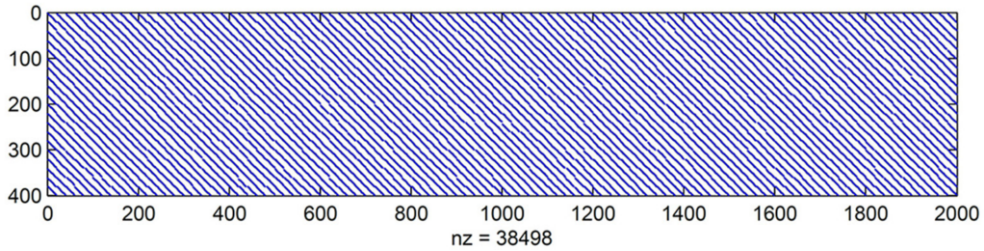

Fig. 3. – An example of the matrix $[\boldsymbol{\delta}]$. Blue dots denote the non-zero elements.

To determine spatio-temporal rupture process of an earthquake, it is common to discretize a finite fault into sub-faults (fig. 2). The unknowns to be solved are sub-fault source time functions or moment rate functions. Because the Green's function is calculated based on a point source, the sub-faults should be reasonably small enough. This point source approximation is only tenable when both the hypocentral distance (R) and the minimum wavelength (λ) are very much larger than the sub-fault size (L_S), where $R \gg L_S$ means Green's functions from different places on the sub-fault to the station are similar in waveform (*i.e.*, the spatial point source), and $\lambda \gg L_S$ means the phase differences of the Green's functions are negligible (*i.e.*, the temporal point source). With the point source approximation, the integrations in eqs. (7) to (9) can be replaced as summations

$$U_n^m(t) = \sum_k [g_n^m(t - \tau^{mk}) * M_0^k(t)], \tag{10}$$

$$U_n^m(t) = g_n^m(t) * S_A^m(t), \tag{11}$$

$$S_A^m(t) = \sum_k [\delta(t - \tau^{mk}) * M_0^k(t)], \tag{12}$$

where the superscripts m and k are indexes of the station and sub-fault, respectively. They suggest that the spatio-temporal rupture process can be imaged by inverting either the station waveforms $U_n^m(t)$ or the ASTFs $S_A^m(t)$. In the following, these two kinds of inversions will be introduced, respectively.

1) Apparent Source Time Function Inversion

Equation (12) can be also rewritten as the matrix equation

$$[\mathbf{S}_A] = [\boldsymbol{\delta}][\mathbf{M}_0], \tag{13}$$

where $[\mathbf{S}_A]$ is the vector of all ASTFs, and $[\boldsymbol{\delta}]$ is a sparse matrix, which consists of block diagonally dominant matrices. An example of the sparse matrix $[\boldsymbol{\delta}]$ is shown in fig. 3. The matrix $[\boldsymbol{\delta}]$ consists of equal-sized block matrices $[\boldsymbol{\delta}_B]$. For each block matrix $[\boldsymbol{\delta}_B]$,

there would be an identity matrix if $\tau^{mk} = 0$, that is

$$[\boldsymbol{\delta}_B(t)] = \begin{bmatrix} 1 & & & \\ & 1 & & \\ & & \cdots & \\ & & & 1 \end{bmatrix}.$$

When τ^{mk} is not equal to 0, the non-zero elements will be moved upward or downward, *e.g.*

$$[\boldsymbol{\delta}_B(t-1)] = \begin{bmatrix} 0 & & & \\ 1 & 0 & & \\ & \cdots & \cdots & \\ & & 1 & 0 \end{bmatrix},$$

and

$$[\boldsymbol{\delta}_B(t+1)] = \begin{bmatrix} 0 & 1 & & \\ & 0 & \cdots & \\ & & \cdots & 1 \\ & & & 0 \end{bmatrix}.$$

2) Waveform Inversion

Equation (10) can be rewritten as the matrix equation

$$[\mathbf{U}] = [\mathbf{g}][\mathbf{M}_0], \tag{14}$$

where $[\mathbf{U}]$ is the vector of all waveform seismograms, $[\mathbf{M}_0]$ is the sub-fault source time functions, and $[\mathbf{g}]$ consists of block matrices as

$$[\mathbf{g}] = \begin{bmatrix} \mathbf{g}^{11} & \mathbf{g}^{12} & \cdots & \mathbf{g}^{1K} \\ \mathbf{g}^{21} & \mathbf{g}^{22} & \cdots & \mathbf{g}^{2K} \\ \cdots & \cdots & \mathbf{g}^{mk} & \cdots \\ \mathbf{g}^{M1} & \mathbf{g}^{M2} & \cdots & \mathbf{g}^{MK} \end{bmatrix}, \tag{15}$$

where $[\mathbf{g}^{mk}]$ is the convolution matrix for $g_n^{mk}(t - \tau^{mk})$, *i.e.*, a lower triangular matrix,

$$[\mathbf{g}^{mk}(t)] = \begin{bmatrix} g^{mk}(1) & & & \\ g^{mk}(2) & g^{mk}(1) & & \\ \cdots & & \cdots & \\ g^{mk}(L_g) & \cdots & g^{mk}(2) & g^{mk}(1) \end{bmatrix}. \tag{16}$$

Equation (16) is for the case that the maximum source duration is equal to the length of Green's functions (L_g). For more general cases, a shorter source duration (T_S) is assumed for the inversion, then only the first T_S columns of $[\mathbf{g}^{mk}(t)]$ are preserved. Because over half of the elements are occupied, $[\mathbf{g}]$ is generally a dense matrix.

2˙1.2. Inversion with rake variation. In some case, the rake variation is considered in the inversion. The rake variation case represents the case that the slip vector on the fault plane $\boldsymbol{e}$ is allowed to change with space and time:

$$m_{pq}(Q,t) = M_0(Q,t)[e_p(t)v_q + e_q(t)v_p]. \tag{17}$$

By putting eq. (17) into eq. (1), we get

$$U_n(P,t) = \iint_\Sigma G_{np,q}(P,t;Q,0) * \{M_0(Q,t)\cdot[e_p(t)v_q + e_q(t)v_p]\}\mathrm{d}\Sigma'. \tag{18}$$

The projections of the slip vector and normal direction of the fault can be made in any coordinate system. Without loss of generality, we define a coordinate system on the fault plane (fig. 4) as: x_1-axis is the strike-slip direction, x_2-axis is the reverse-slip direction, x_3-axis is the normal direction of the fault plane. For a purely shear dislocation, $e_3 = 0$, $v_1 = v_2 = 0$. This makes eq. (18) become

$$U_n(P,t) = \iint_\Sigma [g_{n1}(P,t;Q,0) * M_{01}(Q,t) + g_{n2}(P,t;Q,0) * M_{02}(Q,t)]\mathrm{d}\Sigma', \tag{19}$$

where

$$\begin{aligned} g_{n1}(P,t;Q,0) &= G_{n1,3}(P,t;Q,0)\cdot v_3, \qquad & M_{01}(Q,t) &= M_0(Q,t)\cdot e_1(t), \\ g_{n2}(P,t;Q,0) &= G_{n2,3}(P,t;Q,0)\cdot v_3, \qquad & M_{02}(Q,t) &= M_0(Q,t)\cdot e_2(t), \end{aligned} \tag{20}$$

$M_{01}(Q,t)$ and $M_{02}(Q,t)$ are moment histories along the strike-slip and reverse-slip directions, respectively. Similar to eq. (14), eq. (18) can be also written as

$$[\mathbf{U}] = [\mathbf{g}_1\ \mathbf{g}_2]\begin{bmatrix} \mathbf{M}_{01} \\ \mathbf{M}_{02} \end{bmatrix}. \tag{21}$$

If $M_{01}(Q,t)$ and $M_{02}(Q,t)$ are solved, the rake angle and its variations will be obtained. Compared with the inversion with fixed rake, the rake variation inversion has double unknown parameters.

Equations (13), (14) and (21), correspond to the ASTF inversion, seismogram inversion with fixed rake, and seismogram inversion with rake variation, respectively. It is worth noticing that the unknown parameters in the three equations are the history of scalar seismic moment. When the Green's functions are calculated by considering the step response, the unknowns become the moment rate function or the far-field source time function. The unknowns of moment rate can be transferred into fault slip-rate by multiplying the Green's functions with the shear modulus and the sub-fault area.

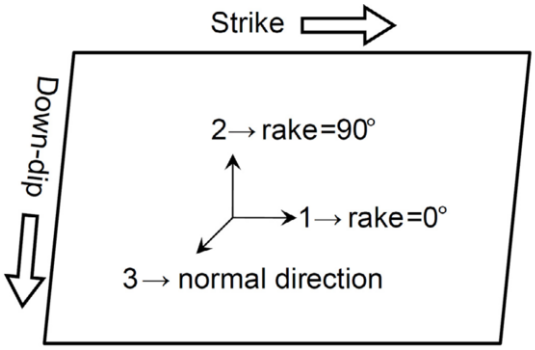

Fig. 4. – The coordinate system on the fault plane used in the inversion of earthquake rupture process.

2˙1.3. Limitations and constraints. Since the ill-conditioning of matrix of Green's functions, and the usually poorly distributed seismic stations, directly solving eqs. (13), (14) or (21) is likely to result in a misleading rupture model. Hence it is necessary to introduce some effective limitations or constraints during the inversion. Commonly, several constraints are considered.

1) Limitation of maximum rupture velocity

In the inversions with far-field data, especially teleseismic data, it is difficult to well constrain the rupture velocity. A limitation would be helpful to make the rupture velocity more reasonable. In principle, the rupture velocity does not exceed P-wave velocity, and usually less than 0.85 times of shear wave velocity. For a sub-fault d km away from the hypocenter, the maximum rupture velocity v_{r} means it does not rupture until $\tau_{\mathrm{r}} = d/v_{\mathrm{r}}$ (see fig. 5).

2) Limitation of maximum rupture duration of sub-fault

The number of unknowns is largely decided by the sub-fault rupture duration, that is, the time differences between the rupture initiation and stop of a sub-fault. In principle,

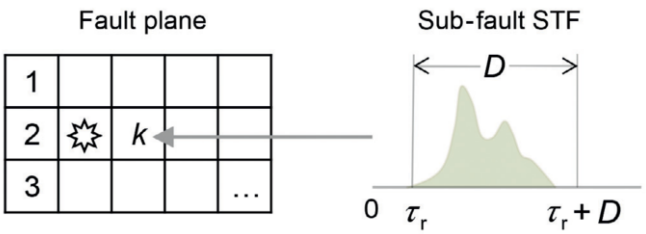

Fig. 5. – A sketch showing the rupture initiation time (τ_{r}) and rupture duration (D) of a sub-fault STF.

a larger duration leads to better data fit, but also causes more instabilities. A reasonable limitation of maximum rupture duration (D, see fig. 5) is usually needed for an inversion. It needs to be reasonably large when there exist multiple ruptures.

3) Non-negative constraint

Earthquake fault slips occur at depth under a high level of confining pressure. The friction is likely to prevent the stress from being fully released. It makes the fault hard to slip reversely. Therefore, non-negative constraint is commonly imposed to the fault slips.

4) Spatial smoothing

Based on the assumption that the residual stress after an earthquake is homogeneous to some extent, the fault slips should be reasonably smooth. A Laplace equation is often preferred for this purpose (*e.g.*, [23]). For the k-th sub-fault, the equation is

$$4s^k(t) - [s^{k-1}(t) + s^{k+1}(t) + s^{k-k_r}(t) + s^{k+k_r}(t)] = 0, \tag{22}$$

where $s(t)$ is the slip velocity.

5) Temporal smoothing

In the inversion, the point source approximation demands that the minimum wavelength is much more than the sub-fault size, and the high-frequency waves are hard to be well modeled in the Green's functions due to our relatively poor knowledge on the 3D Earth structure. Only low-frequency waveform data are inverted, and thus the resulted source time functions of sub-faults (moment rate history or slip-rate function) should be smooth enough. A Laplace equation is also applied to the k-th sub-fault source time functions

$$2s^k(t) - [s^k(t-1) + s^k(t+1)] = 0. \tag{23}$$

6) Scalar moment minimization

The ideal case for the source inversion is that the seismic stations evenly distribute on both the azimuthal and take-off angles. Sometimes in real data inversions, however, the station distribution is usually uneven. It causes the inversion problem ill-conditioned. A feasible way to solve this problem is to suppress the solution norm by using a scalar moment minimization [24].

2˙1.4. Equations for the three kinds of inversions. The constrain conditions of the spatial and temporal smoothing, and the scalar moment minimization can be formulated.

Together with eqs. (13), (14), and (21), the equations of the three kinds of inversions are

$$\begin{bmatrix} \mathbf{S}_A \\ 0 \\ 0 \end{bmatrix} = \begin{bmatrix} \boldsymbol{\delta} \\ \kappa_1 \mathbf{D} \\ \kappa_2 \mathbf{T} \end{bmatrix} [\mathbf{s}], \tag{24}$$

$$\begin{bmatrix} \mathbf{U} \\ 0 \\ 0 \\ 0 \end{bmatrix} = \begin{bmatrix} \mathbf{g} \\ \kappa_1 \mathbf{D} \\ \kappa_2 \mathbf{T} \\ \kappa_3 \mathbf{Z} \end{bmatrix} [\mathbf{s}], \tag{25}$$

and

$$\begin{bmatrix} \mathbf{U} \\ 0 \\ 0 \\ 0 \end{bmatrix} = \begin{bmatrix} \mathbf{g}_1 & \mathbf{g}_2 \\ \kappa_1 \begin{bmatrix} \mathbf{D} & \\ & \mathbf{D} \end{bmatrix} \\ \kappa_2 \begin{bmatrix} \mathbf{T} & \\ & \mathbf{T} \end{bmatrix} \\ \kappa_3 \begin{bmatrix} \mathbf{Z} & \\ & \mathbf{Z} \end{bmatrix} \end{bmatrix} \begin{bmatrix} \mathbf{s}_1 \\ \mathbf{s}_2 \end{bmatrix}, \tag{26}$$

where the unknowns $[\mathbf{s}]$ are sub-fault slip-rate functions, $[\mathbf{D}]$, $[\mathbf{T}]$ and $[\mathbf{Z}]$ are matrices of spatial smoothing, temporal smoothing, and scalar moment minimization, respectively, κ_1, κ_2 and κ_3 are the corresponding weights, which can be optimized by the Bayesian criterion or with experience. No scalar moment minimization appears in the ASTF inversion since $[\boldsymbol{\delta}]$ is a sparse matrix which has a small condition number.

2·1.5. An Example: The 2009 M_w6.3 L'Aquila, Italy, earthquake. We take the 6 April 2009 M_w6.3 L'Aquila, Italy, earthquake as an example to compare the three kinds of inversions of eqs. (24) to (26). We used P-waves on vertical components of 24 teleseismic stations (fig. 6a) for these analysis. The ASTFs were retrieved by using the Projected Landweber Deconvolution (PLD) [13, 25] method and based on the fault parameters strike $\phi = 132°$/dip $\delta = 53°$/rake $\lambda = -103°$ [26]. The azimuth-dependent ASTFs are shown in fig. 6b. Two sub-events can be clearly identified. The first one appears at almost the same time (~ 2 s) at all stations, suggesting that it is around the hypocenter. The peak value of the second sub-event appears earliest at azimuth of approximately 150°, indicating that it is located to the southeast of the epicenter. The rupture directions of the two sub-event imply that the earthquake was a unilateral rupture event.

With the ASTFs and the P-wave seismograms, three rupture models were estimated by solving eqs. (24) to (26), respectively, (figs. 7 to 10). They are basically consistent

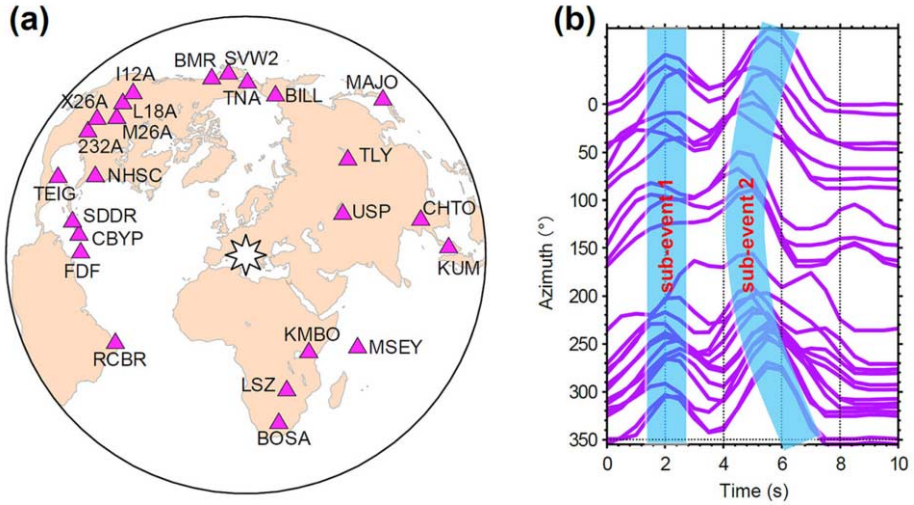

Fig. 6. – Teleseismic stations (triangles) and epicenter (star) of the 2009 L'Aquila, Italy, earthquake (a). Azimuth-dependent ASTFs retrieved (b).

with each other, suggesting that both the ASTF inversion and seismogram inversion are effective to estimate the source rupture processes. However, because of the difference in inversion workflow, the two inversion ways are somewhat different in the following aspects (see table I).

1) Stability

For ASTF inversion, the instability mainly exists in the deconvolution for ASTFs. When inverting ASTFs for rupture process, since the condition number of the matrix $[\boldsymbol{\delta}]$ is not very large, the inversion is basically stable. However, in the inversion of the seismograms, the matrix $[\mathbf{G}]$ is usually ill-conditioned, leading to the instabilities in the inversion.

2) Efficiency

In case of the ASTF inversion, the coefficient matrix is a sparse matrix. We can use the multiplication of sparse matrix to solve the equation very efficiently. In the application to the L'Aquila earthquake, the computation time for the three kinds of the inversion are 0.8 s (including 0.05 s for retrieving ASTFs), 3.6 s and 7.3 s, respectively (performed on a laptop with Intel CPU T9300). The computation time of the ASTF inversion is almost one order less than the seismogram inversions.

3) Scope of application

In the ASTF inversion, an approximation of spatial point source (the hypocentral distance is much larger than the source dimension) is needed, and waveform data of single phase are demanded. These limit the scope of its application. In the seismogram inversion these limitations are not needed, thus the seismogram inversion technique is suitable for more general cases.

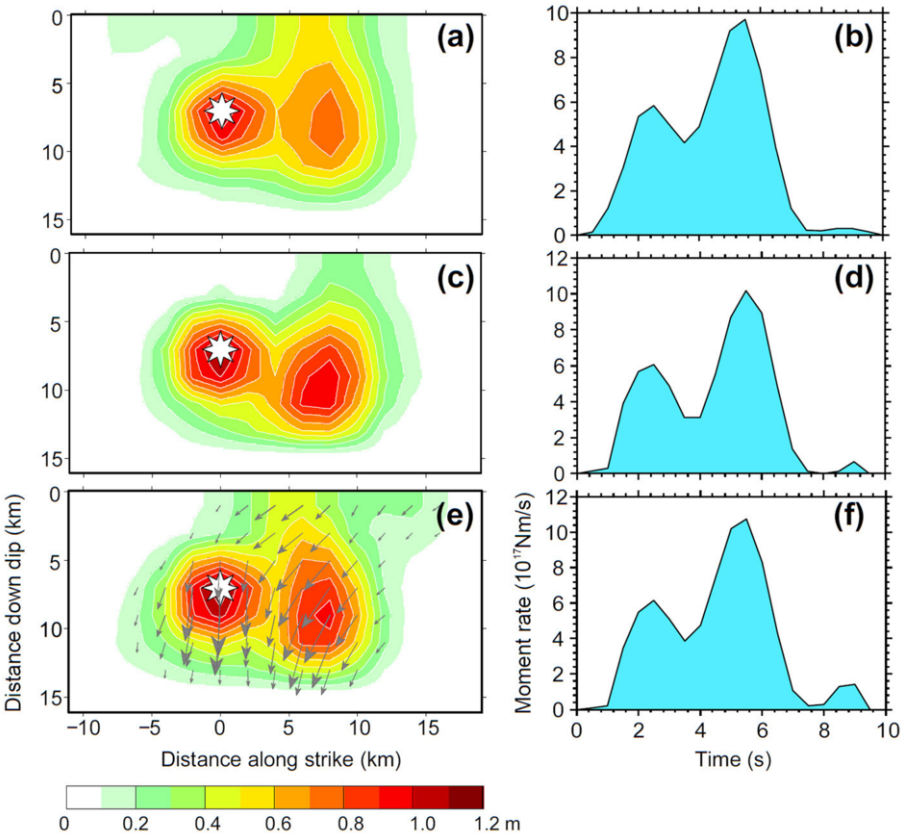

Fig. 7. – Static-slip distributions and STFs obtained by solving eqs. (23) to (25), respectively, *i.e.*, the results by the ASTF inversion (a, b) and by the seismogram inversion with fixed rake (c, d), and with variable rake (e, f).

4) Since the ASTF deconvolution is performed separately for each station, any misestimate on the ASTF duration may cause the rupture behaviors loss or some errors introduced. In contrast, the rupture behaviors were determined by inverting all waves simultaneously in the seismogram inversion. It would help to minimize the problems existing in the ASTF inversion (table I).

TABLE I. – *Comparison of the ASTF and seismogram inversions.*

	ASTF inversion	Seismogram inversion
Stability	√	
Efficiency	√	
Scope of application		√
Misleading of rupture behaviors		√

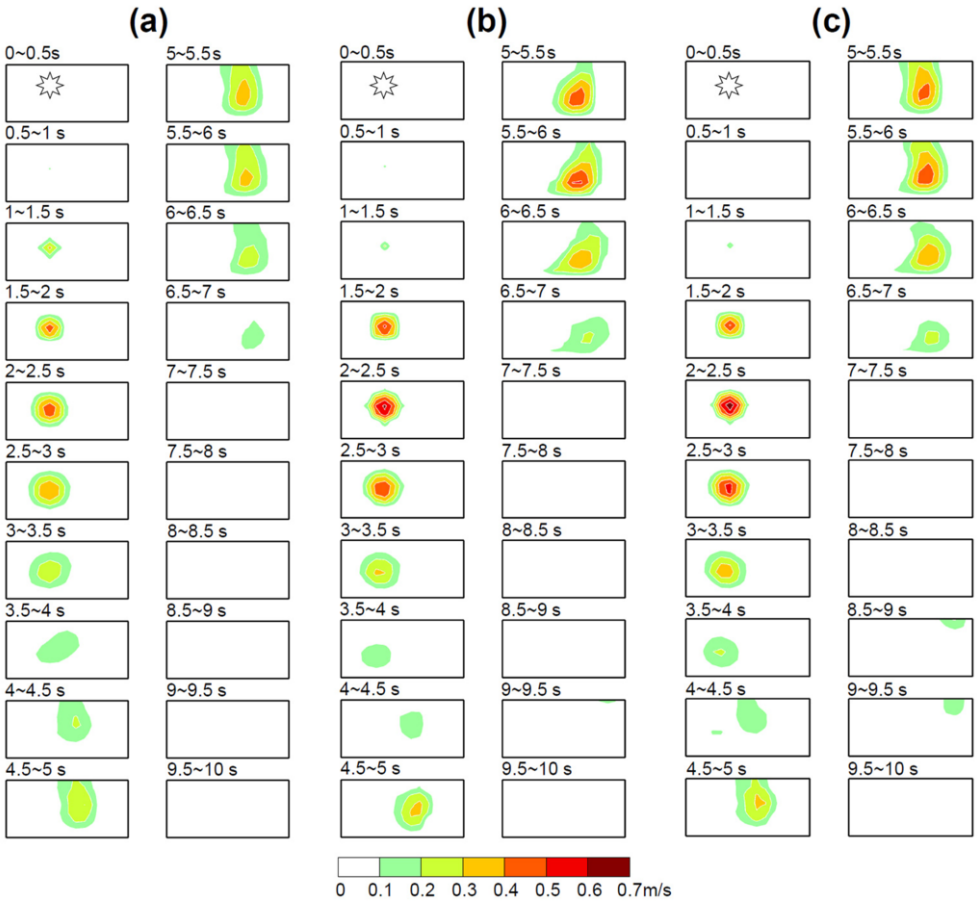

Fig. 8. – Snapshots showing spatio-temporal variations of fault slip-rate obtained by solving eqs. (23) to (25), respectively, *i.e.*, the results by the ASTF inversion (a) and by the seismogram inversion with fixed rake (b), and with variable rake (c).

By synthesizing the advantages of ASTF and seismogram inversions, we suggest a technical flow to effectively and robustly determine the rupture model. The first is to retrieve the ASTFs through deconvolution, which helps to get the overall estimates on the source duration and rupture direction. Then based on the overall estimates, we can invert the seismograms directly for the detailed rupture model.

2˙2. *Joint inversion of seismic and geodetic data.* – Source inversion with seismic data solely often shows instabilities. A major reason is the trade-off between the rupture velocity and fault slips. The geodetic co-seismic deformation data have no resolution on the temporal rupture process, but can strongly constrain the fault slip distribution. Therefore, the combination of seismic and geodetic data can help to better estimate the spatio-temporal rupture process.

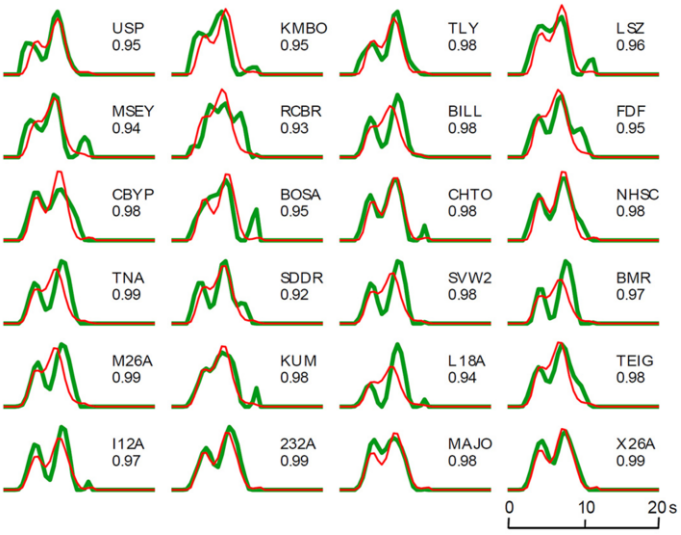

Fig. 9. – Comparison of the observed (green) and synthetic (red) ASTFs. In each sub-graph, the station codes (top) and correlation coefficients (bottom) between the observed and synthetic ASTFs are labeled, respectively.

By considering the variable-rake case, the equation of co-seismic deformation data inversion can be represented as

$$[\mathbf{E}] = [\mathbf{B}_1\ \mathbf{B}_2] \begin{bmatrix} \mathbf{f}_1 \\ \mathbf{f}_2 \end{bmatrix}, \tag{27}$$

where $[\mathbf{E}]$ is the co-seismic deformation data, $[\mathbf{B}]$ is the Green's function, *i.e.*, surface deformation cause by an unit slip on the rectangular sub-fault, $[\mathbf{f}]$ is the fault slips. The fault slip $[\mathbf{f}]$ is equal to the integration of the slip-rate $[\mathbf{s}]$, which can be approximately written as summations:

$$\begin{bmatrix} \mathbf{f}_1 \\ \mathbf{f}_2 \end{bmatrix} = \begin{bmatrix} \mathbf{J} & 0 \\ 0 & \mathbf{J} \end{bmatrix} \begin{bmatrix} \mathbf{s}_1 \\ \mathbf{s}_2 \end{bmatrix}, \tag{28}$$

where $[\mathbf{J}]$ consists of row vectors with elements equal to 1, *i.e.*, $[1, 1, \ldots, 1]$.

Putting eq. (28) into eq. (27), we can get

$$[\mathbf{E}] = [\mathbf{H}_1\ \mathbf{H}_2] \begin{bmatrix} \mathbf{s}_1 \\ \mathbf{s}_2 \end{bmatrix}, \tag{29}$$

where $[\mathbf{H}_1] = [\mathbf{B}_1] * [\mathbf{J}]$, $[\mathbf{H}_2] = [\mathbf{B}_2] * [\mathbf{J}]$.

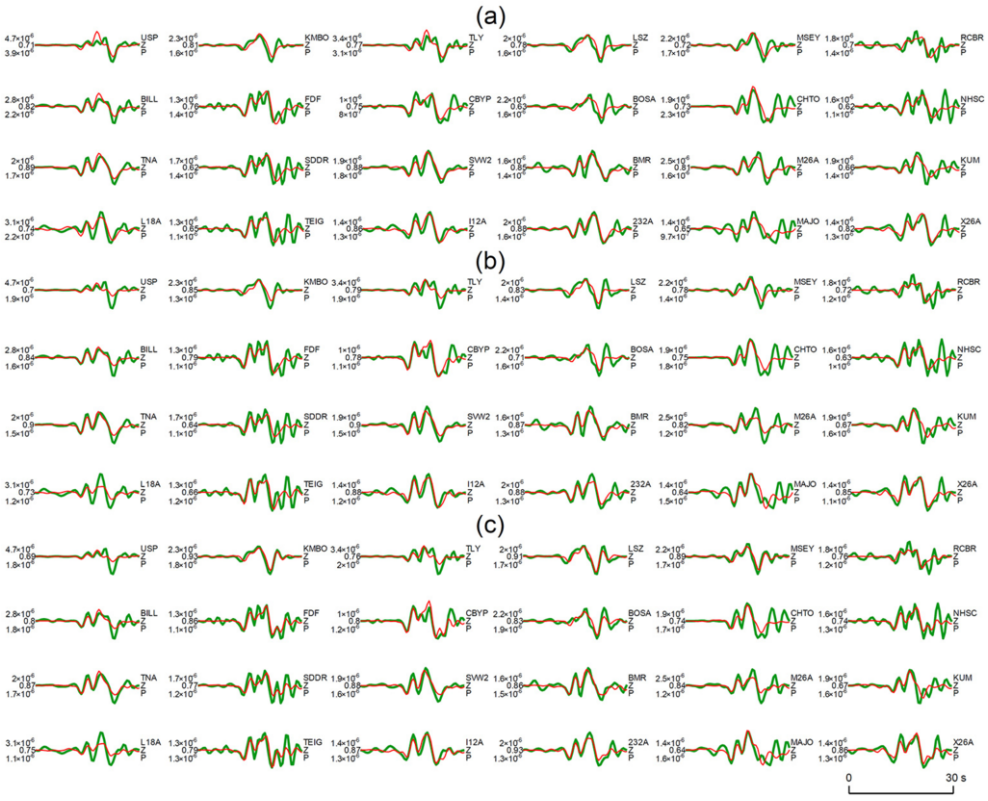

Fig. 10. – Comparison between the observed and synthetic seismograms of the three kinds of inversions. (a) The results by the ASTF inversion; (b) the results by the seismogram inversion with fixed rake; (c) the results by the seismogram inversion with variable rake.

The equation of joint inversion can be obtained by putting eqs. (26) and (29) together

$$\begin{bmatrix} \mathbf{U} \\ 0 \\ 0 \\ 0 \\ \kappa\mathbf{E} \end{bmatrix} = \begin{bmatrix} \mathbf{g}_1 & \mathbf{g}_2 \\ \kappa_1 \begin{bmatrix} \mathbf{D} & \\ & \mathbf{D} \end{bmatrix} \\ \kappa_2 \begin{bmatrix} \mathbf{T} & \\ & \mathbf{T} \end{bmatrix} \\ \kappa_3 \begin{bmatrix} \mathbf{Z} & \\ & \mathbf{Z} \end{bmatrix} \\ \kappa[\mathbf{H}_1 \quad \mathbf{H}_2] \end{bmatrix} \begin{bmatrix} \mathbf{s}_1 \\ \mathbf{s}_2 \end{bmatrix}, \tag{30}$$

where κ is the relative weight of the co-seismic deformation data compared with the seismic data. Since the difference in values of the seismic data [**U**] and the deformation

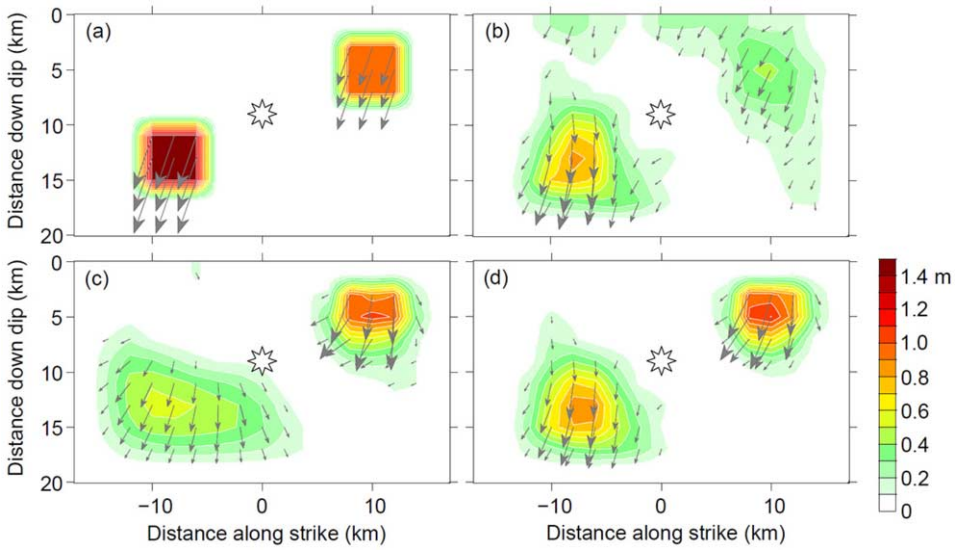

Fig. 11. – Numerical test for the case of two slip patches with identical area but different slips and depths. The shallower patch has smaller slip than the deeper one. Fault slip distributions (a) obtained by teleseismic data inversion (b); InSAR data inversion (c); and joint inversion (d).

data may reach several orders of magnitude, a normalization is necessary to ensure that they are comparable in the joint inversion. Usually we normalize them by their square root of energy, *i.e.*

$$U = \frac{U}{\sqrt{\int U^2 \mathrm{d}t}}, \qquad E = \frac{E}{\sqrt{\int E^2 \mathrm{d}t}}. \tag{31}$$

This makes the two datasets be equally weighted in the least-square optimizations if $\kappa = 1$.

There may be not an objective criterion to choose the best relative weight κ. For our experiences, equally weighting the datasets is usually enough to recover the major rupture behaviors for most cases.

In addition to the constraint on the static fault slip distribution, the co-seismic deformation data can better constrain the shallow slip. In contrast, seismic data may have better resolution in depth since some seismic waves are radiated downward away from the source. Here we demonstrate two numerical tests for the 2009 L'Aquila earthquake by use of teleseismic data and Interferometric Synthetic Aperture Radar (InSAR) deformation data. In the first test, two slip patches with the identical area but different slips and depths are assumed: the shallow patch slips less than the deep one (fig. 11a). Seismic data inversion mainly recovers the deep slip patch which has larger seismic moment (fig. 11b). In contrast, the InSAR slip model has better resolution at shallow

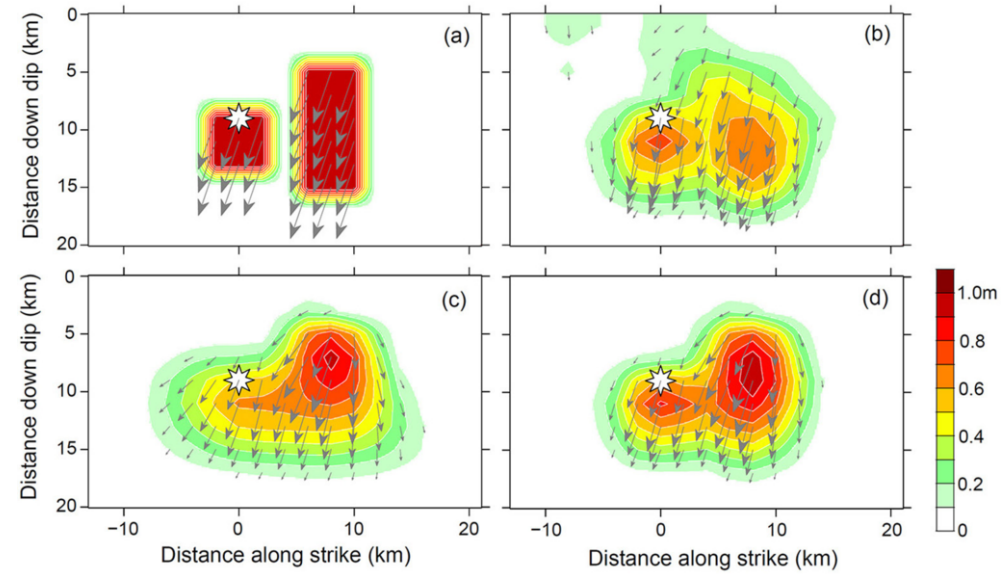

Fig. 12. – Two adjacent slip patches which have different extensions along the down dip direction. Fault slip distributions (a) obtained by teleseismic data inversion (b); InSAR data inversion (c); and joint inversion (d).

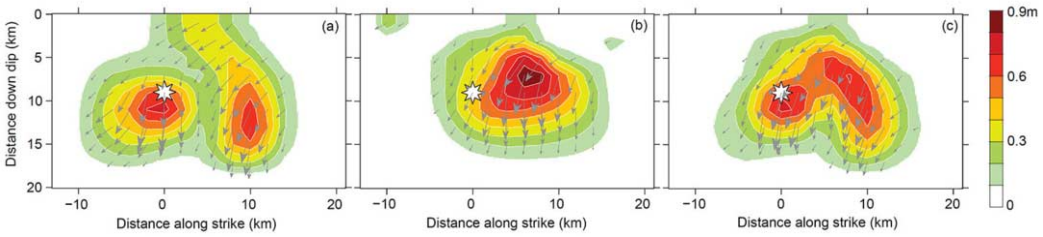

Fig. 13. – Fault slip distributions of the 2009 L'Aquila earthquake obtained by teleseismic data inversion (a), by InSAR data inversion (b), and by joint inversion (c), respectively.

depth (fig. 11c). The joint inversion synthesizes the advantages of both the two datasets (fig. 11d).

In the second test (fig. 12), we assumed two adjacent slip patches which have different extensions along the down dip direction (fig. 12a). Seismic data inversion well distinguishes the two slip patches, but losses some details of shapes of the patches (fig. 12b). InSAR data inversion well recovers the shallow slips but cannot distinguish the slip gap (fig. 12c). The joint inversion provides the best estimates compared with the single data inversion (fig. 12d).

The fault slips of the 2009 L'Aquila earthquake may be similar to the slip model shown in fig. 12a. Seismic data inversion, as well as the ASTF analysis, clearly finds 2 sub-events and 2 slip patches (fig. 13a). However, InSAR data inversion only results in 1 slip patch (fig. 13b). The reason may be that the smaller patch causes little surface deformation and thus can hardly be distinguished. Through joint inversion, the two slip patches are well imaged (fig. 13c).

3. – Applications

During the last three decades, several significant earthquakes occurred around the boundaries of the Bayan Har Block (table II; fig. 14). By significant earthquake we mean the earthquake of magnitude 7.5 or greater or the one that caused fatalities, injuries or substantial damage. These include the $M_{\rm w}$7.8 Kunlun Mountain Pass earthquake (KMPE) of 14 November 2001, the $M_{\rm w}$7.9 Wenchuan, Sichuan, earthquake of 12 May 2008, and the $M_{\rm w}$6.9 Yushu, Qinghai, earthquake of 14 April 2010 [27-30]. In the following these earthquakes will be taken as examples to illustrate briefly how the knowledge on the earthquake source rupture process retrieved from seismic recordings be used in the studies of earthquake rupture complexities and the earthquake disaster emergency response [31].

3·1. *The $M_{\rm w}$ 7.8 Kunlun Mountain Pass earthquake of 14 November 2001.*

3·1.1. Tectonic settings. The first example is the $M_{\rm w}$7.8 Kunlun Mountain Pass earthquake (KMPE) of 14 November 2001. This earthquake occurred on the northern margin of the Bayan Har Block of the eastern Tibetan Plateau. The epicenter of this earthquake was located at the west-to-east striking, left-lateral strike-slip Kunlun Mountain Fault (KMF) (fig. 15).

3·1.2. Aftershocks. Despite its large magnitude of $M_{\rm w}$7.8, the 2001 KMPE caused no casualty or major damage, because it occurred in a nearly uninhabited mountainous area with elevation ranging from 4500 m to 6860 m. This earthquake was followed by a large number of aftershocks. Till 27 November 2001 there had been more than 2000 aftershocks with magnitude $M_L \geq 1.0$ recorded and located by the local seismograph network of Qinghai Province Earthquake Administration. These aftershocks mainly distributed about 100 km away to the east of the mainshock epicenter along the KMF (fig. 16).

3·1.3. Focal mechanism. The focal mechanism of the KMPE was determined by moment tensor inversion and with first motions of P-waves. The inversion results show that this earthquake has a focal mechanism with a strike of 290°, a dip of 85° and a rake of −10° (fig. 16), and a moment released of 3.5×10^{20} Nm ($M_{\rm w}$7.6). These results indicate that the KMPE ruptured a left-lateral strike-slip and nearly vertical fault. The mechanism is consistent with the southeastward movement of the Bayan Har Block relative to the East Kunlun-Qaidam Block (fig. 14).

TABLE II. – *Catalog of the focal mechanisms of recent significant earthquakes in the Tibetan Plateau. Symbols ϕ, δ and λ denote strike, dip and rake, respectively.*

No.	Date	Time	Lat.	Long.	h	M_W	M_S	M_0	NP1			NP2			Place	Source
	a:m:d	h:min:s	(°)	(°)	(km)			(Nm)	ϕ (°)	δ (°)	λ (°)	ϕ (°)	δ (°)	λ (°)		
1	1990-04-26	17:37:15	35.986	100.245	8.1	6.5	6.9	9.4×10^{18}	113	68	89	294	22	91	Gonghe, Qinghai	[28]
2	1997-11-08	18:02:55	35.260	87.33	40	7.5	7.4	3.4×10^{20}	250	88	19	159	71	178	Mani, Tibet	[29]
3	2001-11-14	17:26:12	35.880	90.580	15	7.8	8.1	3.2×10^{20}	113	68	89	294	22	−175	Kunlun Mt. Pass	[32]
4	2008-03-21	06:32:58	35.490	81.467	10	7.2	7.3	8.3×10^{19}	353	29	−131	219	69	−68	Yutian, Xinjiang	USGS
5	2008-05-12	14:28:01	31.002	103.322	19	7.9	8.0	2.0×10^{21}	220	32	118	8	63	74	Wenchuan, Sichuan	[33]
6	2010-04-14	07:49:37	33.271	96.625	14	6.9	7.1	3.2×10^{19}	119	83	−2	209	88	−173	Yushu, Qinghai	[30]
7	2013-04-20	08:02:48	30.314	102.934	13	6.7	7.0	1.6×10^{19}	34	55	87	220	35	95	Lushan, Shichuan	[34]
8	2014-02-12	17:19:48	35.922	82.558	12.5	6.9	7.3	1.5×10^{19}	160	80	167	252	77	11	Yutian, Xinjiang	[35]

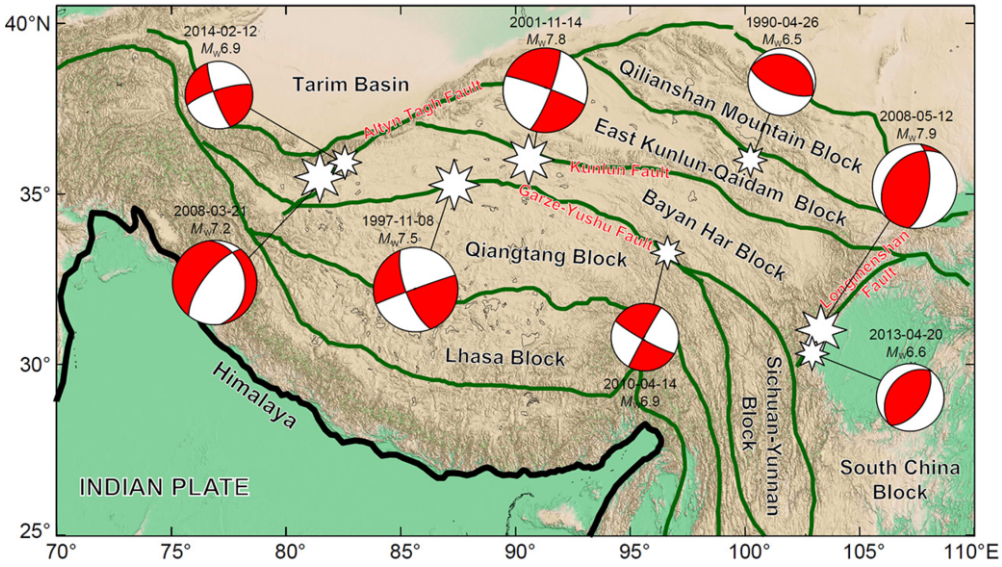

Fig. 14. – Significant earthquakes around the boundaries of the Bayan Har block in the past three decades.

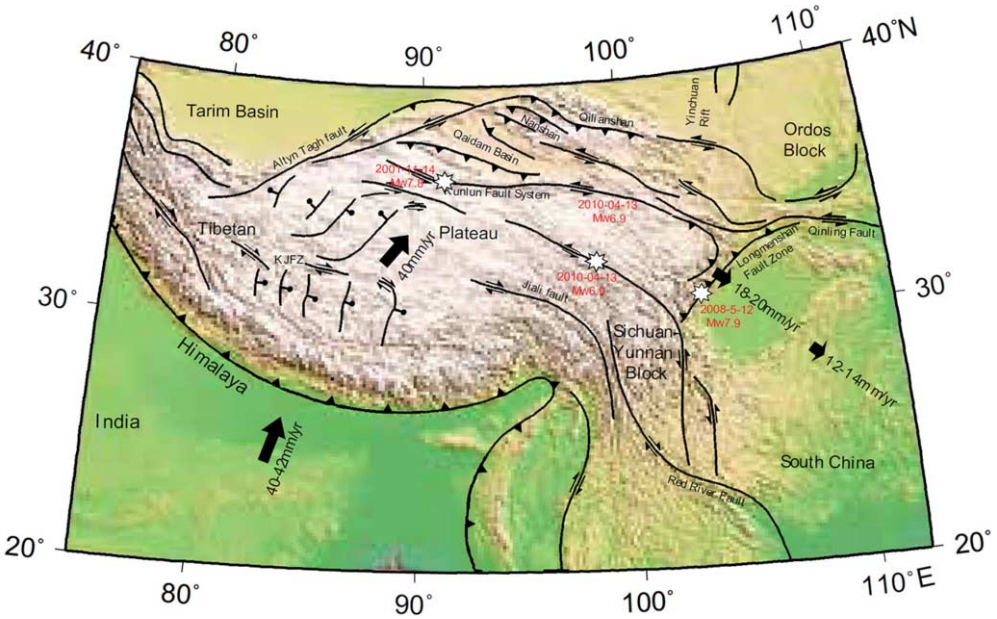

Fig. 15. – Tectonics of the Tibetan plateau and its surrounding regions.

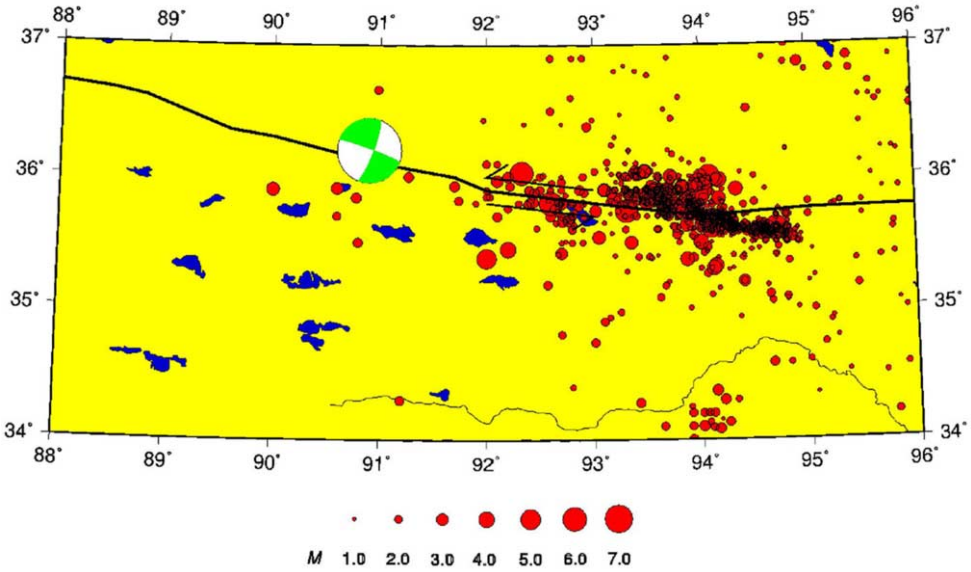

Fig. 16. – Focal mechanism of the M_w7.8 Kunlun Mountain Pass earthquake of 14 November 2001, and the distribution of more than 2000 aftershocks till 27 November 2001 recorded and located by the local seismograph network of Qinghai Province Earthquake Administration. The black line denotes the Kunlun Mountain Fault.

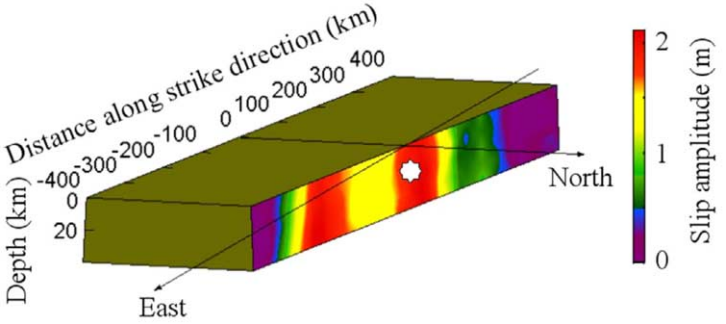

Fig. 17. – Distribution of static (final) slip on the fault plane obtained by the inversion. The white star represents the hypocenter.

3˙1.4. Distribution of static slip. The method of ASTF inversion in time domain as described in [12, 36] was used for imaging the rupture process of the KMPE. The distribution of static slip on the fault plane obtained by the inversion is shown in fig. 17. In this figure, the white star denotes the hypocenter or rupture initiation point. As shown in fig. 17, the rupture area with slip amplitude greater than 1.0 m was 420 km in length, which extended from 120 km to the west of the epicenter to 300 km to the east of the epicenter. There are two slip-concentrated patches, *i.e.*, areas with slip amplitude greater than 1.5 m. One slip-concentrated patch extended from 30 km to the east of the epicenter

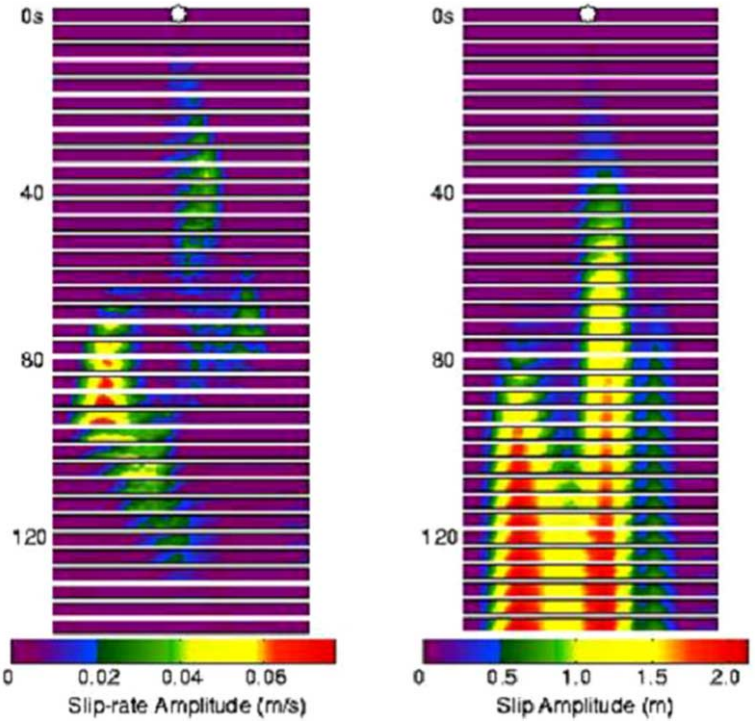

Fig. 18. – The snapshots of the slip-rate (left panel) and slip (right panel) evolution on the fault plane of the 2001 KMPE, which shows the propagation of rupture on the fault plane of 40 km in width and 800 km in length at 4 s intervals. The white star represents the hypocenter.

to 80 km to the west of the epicenter, with a length of 110 km, and another, from 150 km to 280 km to the east of the epicenter, with a length of 130 km. The slip distribution on the fault plane was spatially heterogeneous. The peak slip amplitude was about 2.2 m, and the average slip amplitude over the whole rupture area was about 1.2 m. The peak stress drop was estimated to be 7.9 MPa, and the average stress drop was 4.0 MPa.

3˙1.5. Source rupture process. Figure 18 demonstrates the spatio-temporal rupture process of the 2001 KMPE mainshock. In fig. 18, left and right panels show the spatio-temporal variations of slip-rate and slip, respectively. The white star represents the hypocenter or rupture initiation point.

The source process of the KMPE had spatio-temporal complexity but overall was characterized by unilateral rupture from west to east. The whole event can be divided into three sub-events in terms of the characteristics of spatio-temporal distribution of slip-rate and slip. The three sub-events started at different locations in the strike direction and at different time, and afterwards fused into a single event. During the rupture duration time of 140 s and on 600 km long fault, a complicated process of rupture initiation, propagation, fusion, healing and stopping occurred (fig. 18).

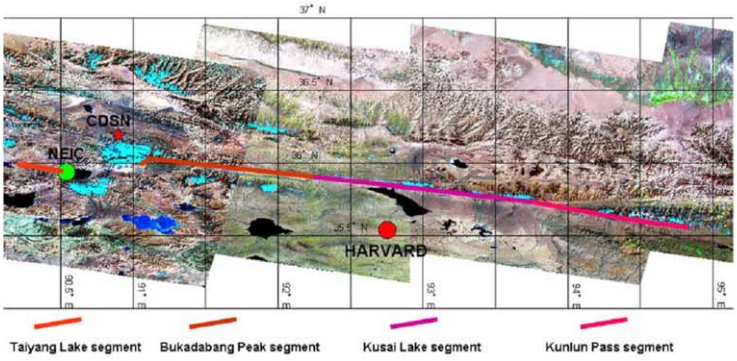

(a)

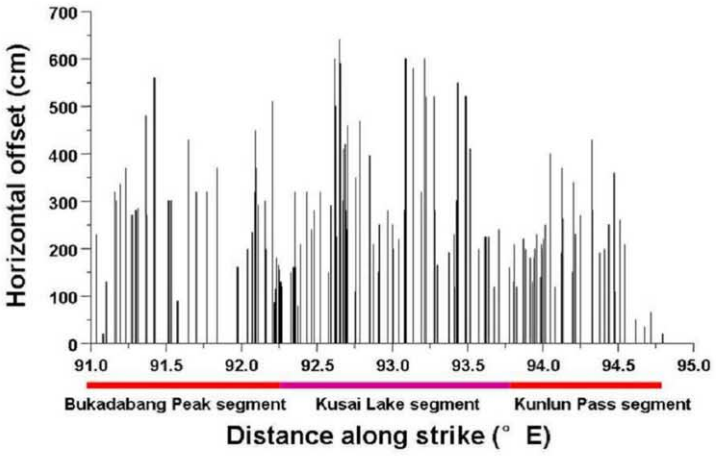

(b)

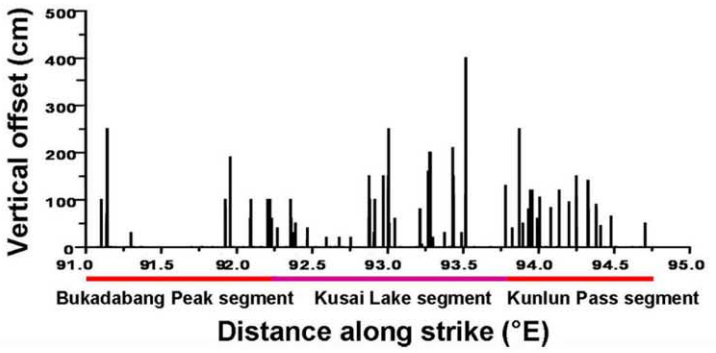

(c)

Fig. 19. – Distribution of surface ruptures of the M_w7.8 Kunlun Mountain Pass earthquake of 14 November 2001. (a) Map view of surface ruptures; (b) horizontal offset distribution along strike; (c) vertical offset distribution along strike.

3˙1.6. Surface ruptures. The surface ruptures of the KMPE were mostly distributed to the east of the epicenter of mainshock (35.97°N, 90.59°E) (fig. 19). The surface rupture length (SRL) to the east of the epicenter was estimated to be about 350 km, the fault motion was mainly left-lateral strike-slip, the offsets on the most segments of the fault were from 2 m to 4 m, and the maximum offset was about 6 m [35]. To the west of the epicenter there was an additional segment (Taiyang Lake segment) of surface rupture of about 90 km in length with the largest horizontal offset of about 5 m right near the epicenter. In total, the SRL of the M_w7.8 KMPE is about 440 km [37].

This SRL of 440 km well corresponds to the calculated length of 420 km of the rupture area with slip amplitude greater than 1.0 m. The later just corresponds to the segment to the east of the Kusai Lake Peak (Kusai Lake segment in fig. 19) where severe ground surface ruptures were found.

Based on the focal mechanism solution, the distribution of the aftershocks as well as the inverted results of the source rupture process, the KMF has been inferred to be the seismogenic fault and to have left-lateral strike-slip faulting on a nearly vertical fault. The large left-lateral strike-slip produced by the KMPE implies that the differential motion of 12–14 mm/a between the north Tibetan Plateau and the south-central Tibetan Plateau is accommodated by the KLF as seismic slip in one event. Our studies confirm that large-scale strike-slip motion along the east-west-trending KLF can accommodate the continuing penetration of the Indian Plate into the Eurasian Plate by the eastward extrusion of the Tibetan Plateau.

The source process had spatio-temporal complexity but was characterized by unilateral rupture from west to east. The slip-concentrated patches which breach through the ground surface are well correspondent to the surface rupture segment or meizoseismal area found in the field investigations after the earthquake.

It is recognized that the M_w7.8 KMPE which occurred on the northern margin of the Bayan Har Block of the eastern Tibetan Plateau was caused by a left-lateral strike-slip faulting on a nearly vertical fault, being consistent with the southeastward movement of the Bayan Har Block relative to the South China Block, and that the rupture process of the KMPE is much more complicated than we had assumed, during the rupture process of the KMPE, three fault segments or three sub-events started at different locations in the strike direction and at different time, and afterwards fused into a single event of magnitude M_w7.8. The lesson we learned from the KMPE is that in the assessment of the earthquake disaster, not only the possibility of one segment of the fault, but also more than two segments rupturing at one big event should be taken into account, and that the concentrated-slip patches which breach the ground surface are well correspondent to the surface rupture segments or meizoseismal areas.

3˙2. *The M_w 7.9 Wenchuan, Sichuan, earthquake of 12 May 2008.*

3˙2.1. Tectonic setting. The M_w7.9 Wenchuan earthquake occurred on the eastern margin of the Bayan Har Block of the eastern Tibetan Plateau. The SW-striking Longmenshan Fault (LF) lies to the northeast of the SSE-moving Sichuan-Yunnan Block of

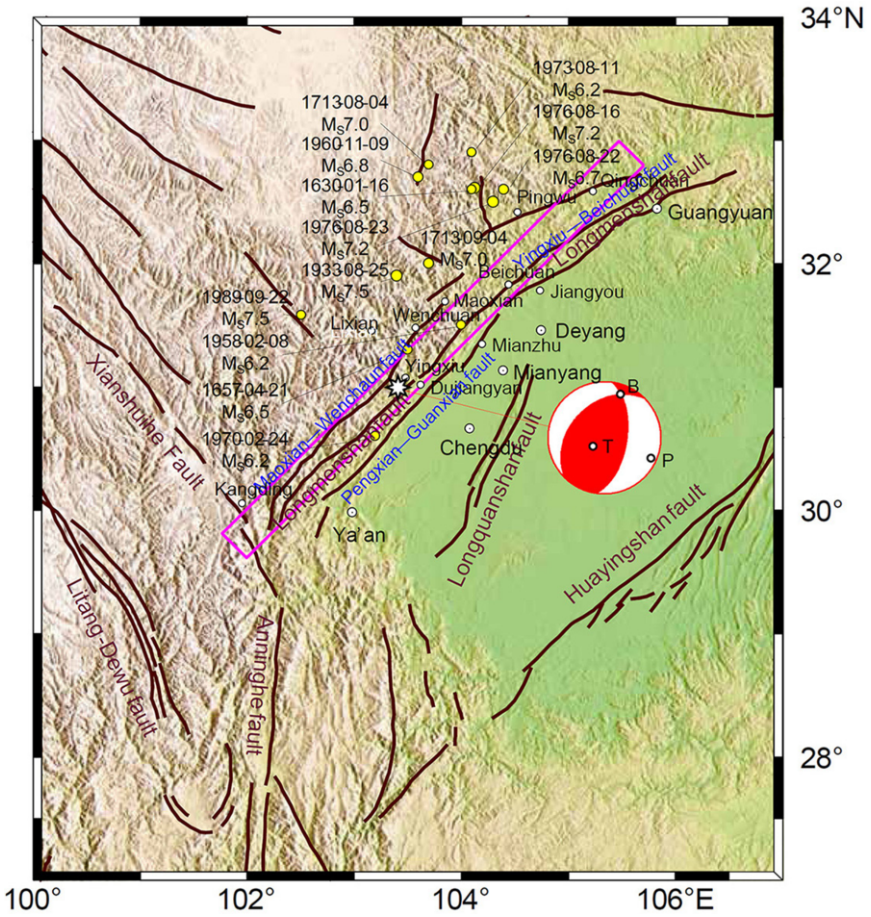

Fig. 20. – Epicenter (white star) location of the 2008 M_w7.9 Wenchuan earthquake, main faults (purple lines) in the epicentral area, historical earthquakes (yellow circles), and main cities (white circles) along Longmenshan Fault. "Beach-ball" represents the lower hemisphere projection of focal mechanism (strike 225°/dip 39°/rake 120°) of the Wenchuan earthquake.

southwest China (fig. 15). As a result of the continental collision between the Indian and Eurasian Plates at about 40–42 mm/a at N20°E, and an eastward extrusion transfer of crustal material from underneath the Tibetan Plateau to the South China Block; a predominantly thrust motion with a minor component of right-lateral motion at a rate of about 18–20 mm/a has been associated with NW-SE-thrusting of southwest China with respect to South China Block along the NE-SW striking LF. The southeastward motion of south China at a rate of 12–14 mm/a incompletely accommodates the accumulation of stress due to the NW-SE thrusting of Bayan Har Block with respect to South China Block along the LF. Thus the LF is an active tectonic structure with the highest degree of vulnerability for earthquake ruptures.

Despite its active tectonic setting, historically the LF experienced only moderate seismic activity [38-40]. Frequent earthquakes of small to moderate size occur on the fault zone, but no earthquakes larger than magnitude 7 have been documented along this fault. Some earthquakes with magnitudes around 6 have been recorded (fig. 20), which include the 21 April 1657 Wenchuan earthquake (M6.5) (epicentral location: 31.3° N, 103.5° E), the 8 February 1958 Maowen-Beichuan earthquake (M_S6.2) (epicentral location: 31.7° N, 104.3° E) occurred to the northeast of the epicenter of the 2008 Wenchuan earthquake, and the 24 February 1970 Dayi earthquake (M_S6.2) (epicentral location: 30.65° N, 103.28° E, focal depth: 15 km) occurred to the SSW of the epicenter of the 2008 Wenchuan earthquake. Based on the relocation of 10 057 earthquakes that occurred in central-western China from 1992 to 1999, Yang *et al.* [41] noted that the LF is 470 km in length and about 2 400 earthquakes with magnitudes between 1.0 and 5.0 occurred on or near the fault zone during this period. Several magnitude-7 earthquakes have occurred nearby but outside the fault zone (fig. 20), including the 25 August 1933 M_S7.5 Maowen-Diexi and the two M_S7.2 Sonpan earthquakes of 16 and 23 July 1976.

Unlike the KMPE, about 89 000 people were confirmed killed or missing in the Wenchuan earthquake. Soon after the occurrence of the earthquake, we started to analyze available seismic recordings to retrieve information describing the earthquake source mechanism, and released the preliminary results of the focal mechanism and the source rupture process to the authorities and public within 12 hours for earthquake disaster emergency response.

3˙2.2. Focal mechanism and aftershocks. Time-domain moment-tensor inversion was used to obtain the focal mechanism of the Wenchuan earthquake. The results are that one of the nodal planes has a strike of 225° with dip 39° and rake 120°, and the other has a strike of 8° with dip 57° and rake 68° (fig. 20). The epicenters of aftershocks relocated by the double-difference earthquake location algorithm are located in a NE-SW-trending zone about 320 km in length and 50 km in width which clearly coincides with the strike of the first nodal plane (fig. 21, main panel).

Vertical cross-sections along the strike direction NE-SW (fig. 21, leftmost panel) and the direction perpendicular to the strike NW-SE (fig. 21, lower panel), of the projections of the relocated hypocenters also show that the aftershocks are clustered around this nodal plane. We identify the plane striking 225° as the causative fault due to its agreement with the NE-SW-trending aftershock distribution and the NE-SW strike of the LF. Overall, the 2008 Wenchuan mainshock rupture was a predominantly thrust event with a minor right-lateral strike-slip component on a plane dipping 39° with a strike of 225° and rake 117°. Our solution (strike 225°/dip 39°/rake 120°) for the Wenchuan earthquake is very close to the moment tensor solution (strike 238°/dip 59°/rake 128°) obtained by USGS/NEIC and the Global Centroid Moment Tensor (GCMT) solution (strike 229°/dip 33°/rake 141°) obtained by the GCMT Project. The scalar seismic moment M_0 we obtained is 9.4×10^{20} Nm, corresponding to a moment magnitude of M_w7.9, and is in good agreement with that obtained by the USGS/NEIC ($M_0 = 7.5 \times 10^{20}$ Nm, $M_w = 7.8$) and GCMT Project ($M_0 = 9.4 \times 10^{20}$ Nm, $M_w = 7.9$).

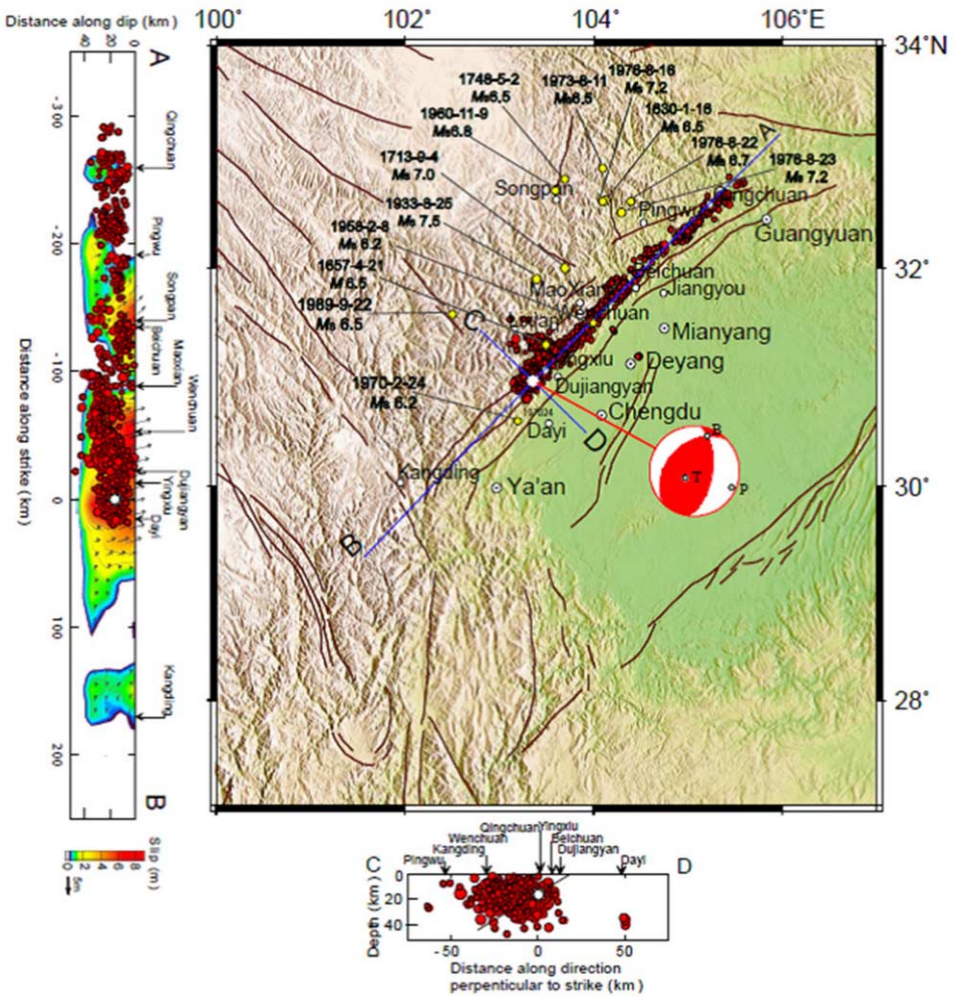

Fig. 21. – Main panel: Map showing topography and major faults (solid purple lines) in northeast Sichuan, the 2008 Wenchuan M_w7.9 earthquake epicenter (white octagonal star), the locations of relocated aftershocks (red dots), and locations of historical earthquakes (yellow dots) in and near the Longmenshan Fault (LF) which consists of three nearly parallel NE-SW-striking faults: from NW to SE, Maoxian-Wenchuan Fault (MWF), Yingxiu-Beichuan Fault (YBF) and Pengxian-Guanxian Fault (PGF). Leftmost panel: Vertical cross-section A-B along the strike direction NE-SW. Lower panel: Vertical cross-section C-D along the direction perpendicular to the strike direction NW-SE shows that the aftershocks are clustered around the fault plane striking 225°, dipping 39° with a rake 117°.

3˙2.3. Distribution of static slip. Figure 22 shows the static-slip distribution on the fault plane [17, 42]. The slip vector represents the direction and amount of displacement of the hanging wall with respect to the foot wall at each sub-fault. The Wenchuan

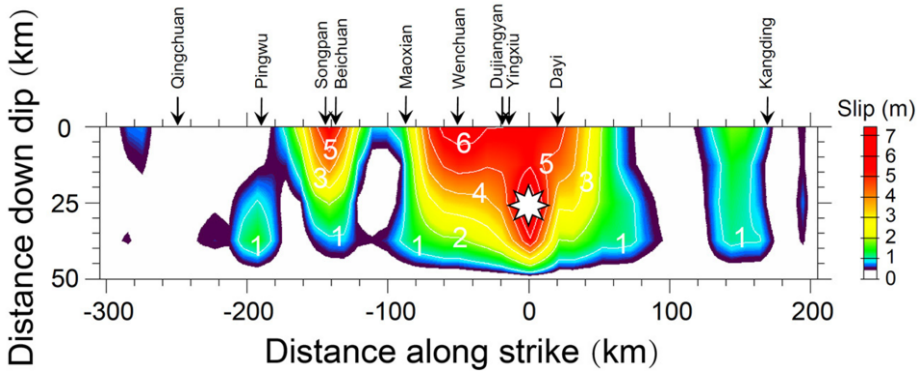

Fig. 22. – The static-slip distribution on the fault plane.

earthquake has a slip distribution with predominantly thrust faulting and a small right-lateral strike-slip component. There are four major concentrated-slip patches on the fault plane (fig. 22). From the southwest to the northeast (fig. 23), the focal mechanisms that varied from oblique thrust and right-lateral strike-slip faulting just underneath the southwestern most segment near Kangding, to predominant thrust with small right-lateral strike-slip faulting just underneath the elongated Yingxiu-Dujiangyan-Wenchuan area, to oblique thrust and right-lateral strike-slip faulting underneath the Beichuan area, and to a predominantly right-lateral strike-slip faulting with minor normal faulting just underneath the Qingchuan area. The overall focal mechanism of the Wenchuan earthquake is similar to that of the second or largest concentrated-slip patch which is one of the predominant thrust faulting with a minor right-lateral strike-slip component and in good agreement with the general NE-SW strike of the LF. The overall focal mechanism of the Wenchuan earthquake is well consistent with the tectonic setting of the generally NE-SW-striking LF and is due to the NW-SE thrusting of Bayan Har Block with respect to South China Block.

The inversion shows that the Wenchuan earthquake ruptured an area 350 km in length by 50 km in width, of the 470 km-long NE-SW-striking LF. A seismic moment of about 9.4×10^{20} Nm was released in the Wenchuan earthquake, corresponding to a moment magnitude of $M_{\mathrm{w}}7.9$. The average stress drop and the maximum stress drop in this earthquake are about 18 MPa and 65 MPa, respectively, and are comparable with an intraplate earthquake with magnitude 8.0.

As the static-slip distribution on the fault plane of fig. 22 and the beach-balls of fig. 23 show, the $M_{\mathrm{w}}7.9$ Wenchuan earthquake is a complex event consisting of four concentrated-slip patches in which there are two substantial slip-concentrated patches on the fault plane with slips of up to 8.9 m and 6.7 m, just underneath the elongated area extending from Yingxiu-Dujiangyan-Wenchuan and the area near Beichuan, respectively. These patches breached the ground surface and account for the tremendous destructive damage in these two meizoseismal areas (fig. 24). In addition to the two substantial slip-

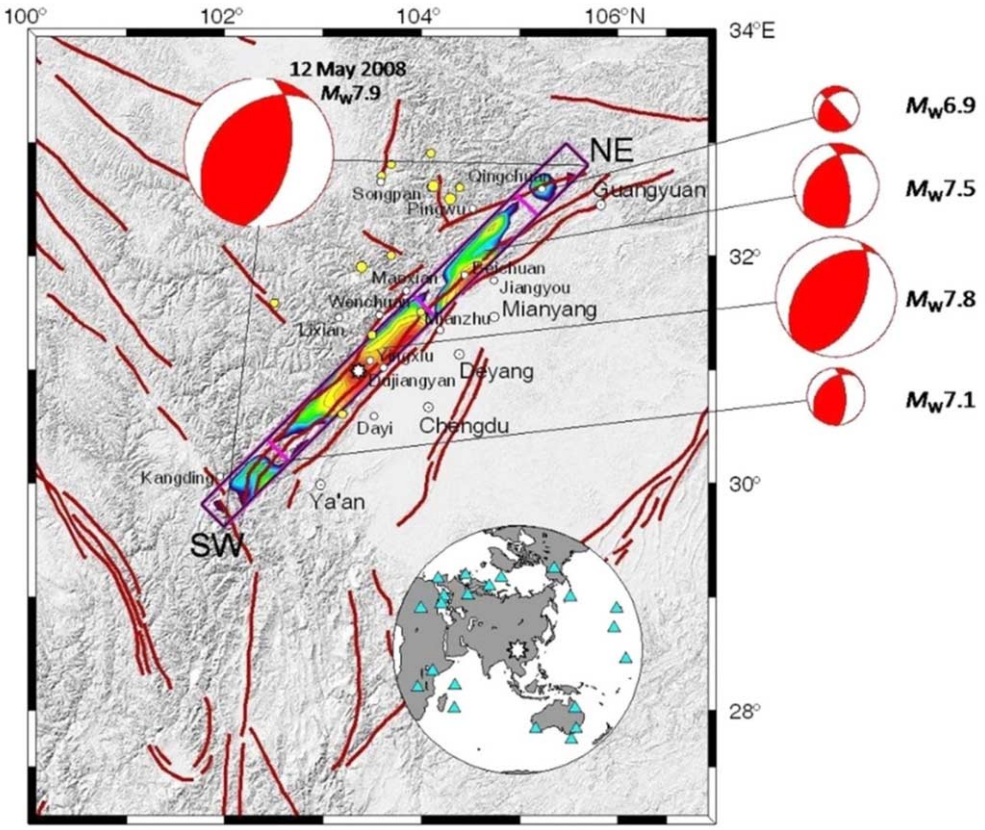

Fig. 23. – Focal mechanism of the Wenchuan earthquake (white octagonal star) and horizontal projection of the static-slip distribution on the fault plane. The background shows the topography of northeast Sichuan and the major faults (purple thick lines). The inset map shows the location of the epicenter of the Wenchuan earthquake (white octagonal star) and the IRIS seismic stations (blue triangles). Differing focal mechanisms of the four concentrated-slip patches are shown by the four beach-balls to the right of the figure with corresponding moment magnitudes.

concentrated patches, another two major concentrated-slip patches on the fault plane are of moderate slips of up to 2.3 m and 1.6 m, respectively. They are just underneath the Qingchuan and the Kangding areas, respectively, and corresponding to the areas with intensities lower than the two meizoseismal areas.

During the process of rupture growth, irregular high rupture velocities (3.6 km/s, 4.0 km/s, 4.4 km/s, 3.5 km/s in the four stages) and high rupture acceleration in the northeast direction also play an important role in enhancing the devastating damage in the northeastern part of the fracture.

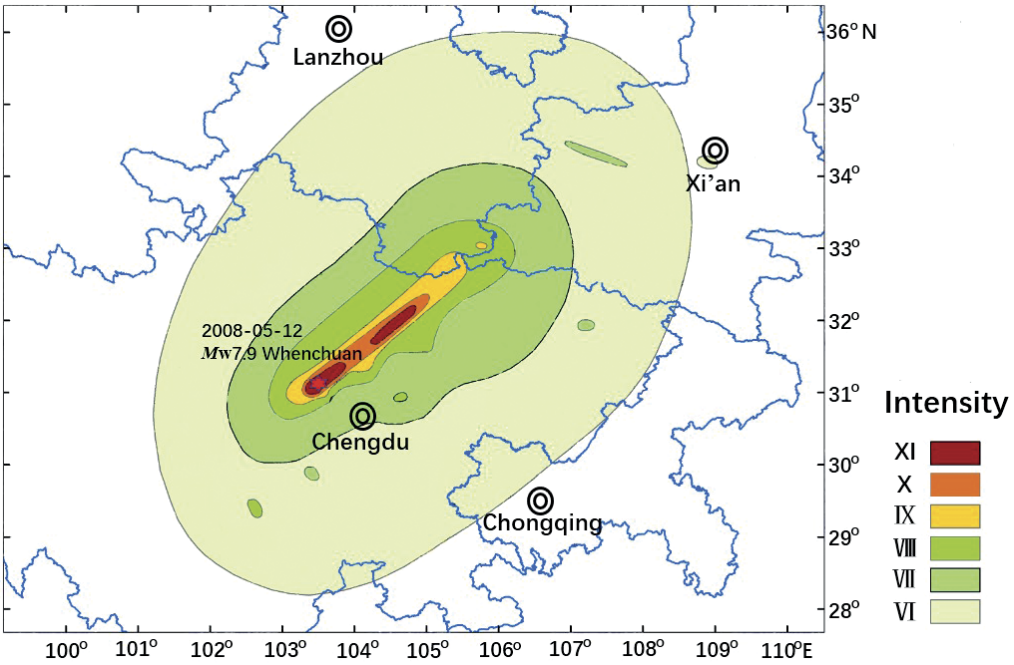

Fig. 24. – Isoseismals of the 2008 M_w7.9 Wenchuan earthquake. Two substantial concentrated-slip patches of M_w7.8 and M_w7.5 on the fault plane in fig. 23 are correspondent to the two meizoseismal areas of the intensity XI.

3˙2.4. Source rupture process. The inverted spatio-temporal rupture process of the Wenchuan earthquake shows that the earthquake is a complex asymmetric bilateral rupture with overall strong northeast directivity, with high irregular rupture velocities and long rupture duration of about 90 s (fig. 25). These characteristics account for the northeasternward elongated meizoseismal areas and the asymmetric distribution of aftershocks that are significantly more numerous to the northeast of the epicenter of the Wenchuan earthquake, and much less so to its southeast. As theoretical studies have indicated, and the field observations have confirmed, in thrust earthquakes the hanging wall moves more than the foot wall with strongly peaked velocity at the fault trace. The significant difference in damage between the meizoseismal areas (Yingxiu-Dujiangyan-Wenchuan and Beichuan-Qingchuan areas) which are located in the hanging wall of the causative thrust fault, and minor damage areas such as Chengdu-Deyang-Guang'an areas which are located in the foot wall of the causative thrust fault can be attributed to the effect of the asymmetric dipping fault geometry, *i.e.*, the hanging wall/foot wall effect.

The inverted STF suggests that the fault rupture development of the Wenchuan earthquake was divided into 4 stages (fig. 26). The first stage extends from the time of the earthquake initiation to 16 s afterward; the second stage, from 16 s to 40 s; the third stage, from 40 s to 58 s, and the last stage, from 58 s to 90 s. The rupture propagates bilaterally in the first stage. In the second stage the rupture appears to be more complicated,

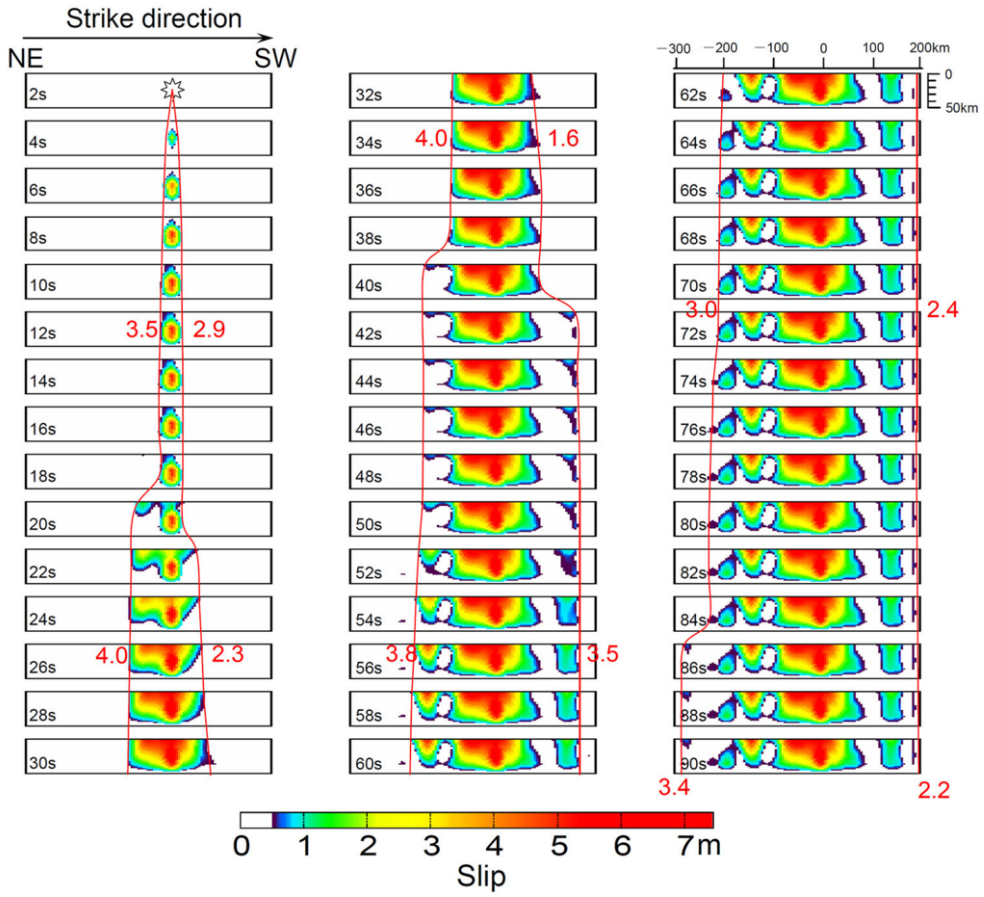

Fig. 25. – Snapshot of the inverted spatio-temporal rupture process of the Wenchuan earthquake.

starting 50 km to the northeast of the epicenter, and then propagates northeastward at first and subsequently bilaterally to the southwest; the rupture is temporally discrete and spatially fragmentary. In the third stage, the rupture took place at two patches, one, 120 km to the northeast of the hypocenter, and the other 160 km to the southwest of the hypocenter. The rupture in the last stage appears to be unilateral to the northeast only and is temporally discrete and spatially fragmentary. The solid brown line and the dotted brown line represent leading edge and trailing edge of fracture, respectively.

It is recognized that the predominantly thrust motion with a minor component of right-lateral motion of the M_w7.9 Wenchuan earthquake was consistent with the tectonic setting of the generally NE-SW-striking LF and was due to the NW-SE thrusting of Bayan Har Block with respect to South China Block along the NE-SW striking LF [43]. It is also recognized that the rupture process of the Wenchuan earthquake was extremely complicated [44]. During the rupture process of the Wenchuan earthquake, two substantial concentrated-slip patches on the fault plane breached the surface and were responsible

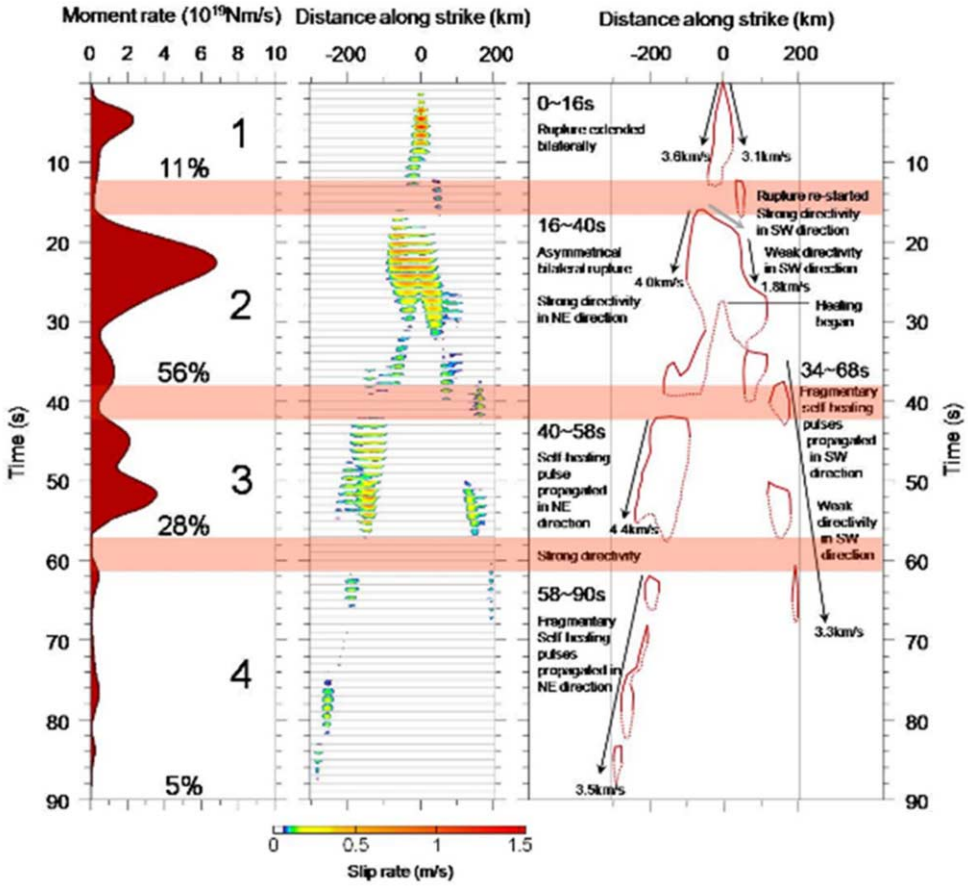

Fig. 26. – (a) Source time function (STF). (b)The spatio-temporal variation of slip-rate on the fault plane. (c)Summary of the rupture process of the 2008 Wenchuan earthquake.

for the tremendous destruction in the two meizoseismal areas. In addition, during the process of rupture growth, irregular high rupture velocities and high rupture acceleration also played an important role in enhancing the devastating damage in the meizoseismal areas. It is worth noticing that the Wenchuan earthquake is a complicated rupture event which involved rupturing of several fault segments and that in the assessment of the earthquake disaster risk, not only the possibility of one segment of the fault, but also more than two segments rupturing at one big event should be taken into account.

3˙3. *The M_w 6.9 Yushu, Qinghai, earthquake of 14 April 2010.*

3˙3.1. Tectonic setting. The M_w 6.9 (M_S7.1) Yushu earthquake occurred on 14 April, 2010, at 07:49 am (Beijing Time) (13 April 2010, 23:49 UTC). The epicenter of the Yushu earthquake was at (33.2° N, 96.6° E), 44 km northwestern of Yushu city, and the focal depth was 14 km (table II; figs. 14 and 27). By May 30th, 2010, the Yushu earthquake

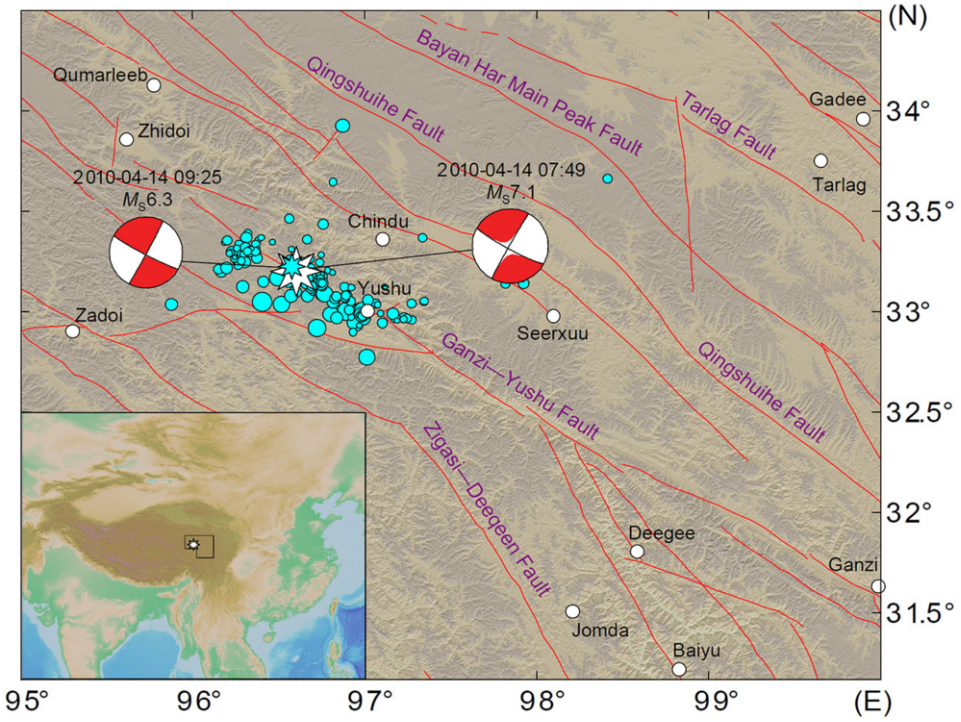

Fig. 27. – Tectonic setting of the Yushu earthquake. White and cyan stars are epicenters of the M_w6.9 (M_S7.1) mainshock and the largest aftershock of M_S6.3, respectively. Red lines denote the major faults. Beach-balls represent the focal mechanisms of the mainshock and the largest aftershock of M_S6.3 (equal-area projection of the lower hemisphere of the focal sphere). Cyan circles are locations of the aftershocks in the first 5 days after the occurrence of the mainshock (from Qinghai Province Earthquake Administration). The black frame in the left-bottom inset outlines the area of the main plot.

caused about 3 000 people to be killed or missing, over 10 000 people injured, and a large number of houses and buildings collapsed. The Yushu earthquake occurred on the Ganzi-Yushu Fault, a southeast-striking, left-lateral strike-slipping fault, which lies on the southern boundary of the Bayan Har Block [45-47]. Historically there has been high seismicity on the fault. The Yushu earthquake was the largest event on the northwestern segment of the Ganzi-Yushu fault during the last 100 years.

For fast emergency response to the earthquake disaster, we obtained the source rupture process by inverting the seismic recordings and had it released about 2.5 hours after its occurrence. About 5 hours and 2 days after the earthquake occurrence, as more data become available, we updated twice the results, respectively (`http://www.csi.ac.cn`). In order to better understand the source rupture process of the Yushu earthquake, after the fast emergency response activity, once again we inverted the carefully selected waveform data to improve the results of the source rupture process (fig. 27).

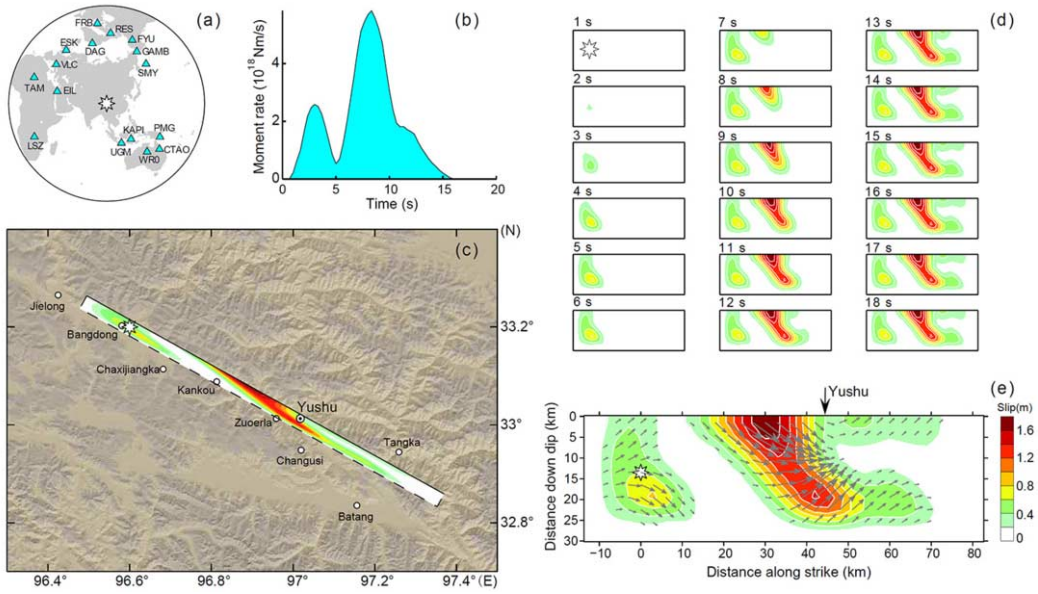

Fig. 28. – Inverted spatio-temporal rupture process of the 2010 Yushu earthquake. (a) Locations of the epicenter and seismic stations; (b)source time function; (c) projection of the static (final) slip distribution on ground surface; (d) spatio-temporal distribution of slip on the fault plane; (e) static slip distribution on the fault plane. White octagonal star represents the epicenter in (a) and (c), but the rupture initiation point in (d) and (e). Gray arrows in (e) denote the slip vectors.

3˙3.2. Focal mechanism. The inverted result (fig. 27) shows that the focal mechanism of Yushu earthquake was strike 119°/dip 83°/rake 2°, and that the scalar seismic moment was about 2.7×10^{19}Nm, yielding a moment magnitude of $M_{\mathrm{w}}6.9$ [30].

3˙3.3. Distribution of static slip. Figure 28 summarizes the inverted spatio-temporal rupture process of the 2010 Yushu earthquake [48]. As fig. 28 shows, there are two concentrated-slip patches located near the hypocenter and to the southeast of the epicenter, respectively. The first concentrated-slip patch was between 10 km northwestern and 10 km southeastern from the epicenter, with a maximum slip of 0.8 m. The second one was in the range 17–54 km southeastern from the epicenter in the strike direction (red-orange-yellow area in fig. 28c and e), with a maximum slip of 1.8 m and breached the ground surface. The average slip on the whole fault plane was about 0.6 m, and the average stress drop was 15 MPa, which was in a good agreement with the typical stress-drop ($\sim$ 10 MPa) for intraplate earthquakes.

3˙3.4. Source rupture process. The inverted results clearly show that the Yushu $M_{\mathrm{w}}6.9$ ($M_{\mathrm{S}}7.1$) earthquake consists of two distinct sub-events (fig. 28b, c, e). The first one occurred in the first 5 s releasing less seismic moment, and the second occurred in the later 11 s releasing more seismic moment. The rupturing of the concentrated-slip patch to

the southeast of the epicenter breached the ground surface. The peak-slip and peak slip-rate are about 2.1 m and 1.1 m/s, respectively. They indicate that the Yushu earthquake is an event with large slip velocity on the fault plane. Overall the Yushu earthquake is a unilateral rupture event with the rupture mainly propagating southeastward. It was inferred that the Yushu city, located 44 km to the southeast of the epicenter, would be heavily destroyed due to the facts that the concentrated-slip patch to the southeast of the epicenter breached the ground surface, and that the strong focusing of the seismic energy to the southeast of the epicenter caused by the seismic Doppler effect. These results have been reported to the authorities and released to public about 2.5 hours after the occurrence, and confirmed later by the tremendous damage in the Yushu city and proved to be very informative in the Yushu earthquake relief work.

3˙4. *Applications to the earthquake emergency response*. – On the basis of the comparison and discussion between the ASTF inversion and seismogram inversion for rupture process (table I), we design two inversion steps to perform the fast rupture process inversion. Firstly, we retrieve the ASTFs, and get a rough estimation on the overall rupture direction by analyzing ASTFs with seismic Doppler effects. Secondly, based on the rough estimation on the source characteristics, we directly invert the seismograms for rupture model. The final determined results of seismogram inversion should satisfy two conditions: 1) They suggest similar rupture directivity. 2) The obtained source time function (STF) should be similar with the average ASTF (approximately the superposition of all ASTFs).

We construct a semiautomatic operation process to fast and stably carry out the rupture process inversion, which contains several useful program modules, such as the teleseismic data processing, fast calculation of Green's function, ASTFs analysis, inversion parameters' setting, and quick display of the inverted results. In the data processing module, the P-waves were picked automatically. The teleseismic stations were re-selected by an azimuthal filter with an interval of about 5 degrees to ensure a uniform coverage of the stations over the epicenter. The teleseismic P-waves with the epicentral distance of 30° to 90° on their vertical components are downloaded from the Incorporated Research Institutions for Seismology (IRIS) website.

The fast and robust inversion method of the earthquake source rupture process we developed in the past two and more decades proved to be effective in providing information on the source characteristics. It is found that in addition to the usual earthquake source parameters, such as the epicentral location, focal depth, focal mechanism, the fast inverted results of the spatio-temporal rupture process of the earthquake sources provided additional important information such as the possible disastrous areas and the timely release of these results were very useful to earthquake emergency response and seismic disaster relief efforts. We applied this method to some of the recent significant earthquakes worldwide. Since May 2008, the source rupture processes of more than 71 significant earthquakes worldwide were inverted by using this newly developed method and the inverted results were timely released on the website within 3 to 5 and more hours in 2009 to 1–3 hours at present after the occurrence of the earthquakes (table III; figs. 29 and 30). These earthquakes include the M_{w}7.9 Wenchuan, Sichuan, earthquake

TABLE III. – *Source parameters of the significant earthquakes for which the earthquake rupture processes were inverted and released immediately after the earthquake occurrence in the time period 2009–2018* (*Part of these models can be found at* `http://www.cenc.ac.cn/cenc/_300651/index.html`).

No.	Epicentral Region	Origin Time (UTC)	Epicentral Location (Lat., Long.)	Focal Depth (km)	M_w	Time Consumed (hr)
1	North of Papua	2009-01-04 04:43	$(-0.5°, 132.8°)$	33	7.7	6.4
2	North of Papua	2009-01-04 06:33	$(-0.7°, 133.2°)$	33	7.5	5.7
3	Tonga	2009-03-19 18:17	$(-23.0°, -174.7°)$	10	7.8	8.3
4	Offshore Honduras	2009-05-28 08:24	$(16.8°, -86.2°)$	15	7.2	8.6
5	Hualian, Taiwan	2009-07-13 18:05	$(24.1°, 122.2°)$	6	6.4	3.0
6	South Island, N.Z.	2009-07-15 09:22	$(-45.7°, 166.6°)$	33	7.8	3.7
7	Andaman Islands	2009-08-10 19:55	$(14.1°, 92.9°)$	33	7.8	4.2
8	Samoa Islands	2009-09-29 17:48	$(-15.5°, -172.2°)$	33	8.0	3.3
9	Southern Sumatra	2009-09-30 10:16	$(-0.8°, 99.8°)$	60	7.6	4.5
10	Vanuatu	2009-10-07 22:03	$(-13.0°, 166.3°)$	33	7.8	2.7
11	Hualian, Taiwan	2009-12-19 13:02	$(23.8°, 121.7°)$	30	6.6	3.5
12	Haiti	2010-01-12 21:53	$(18.5°, -72.4°)$	10	7.1	5.2
13	Central Chile	2010-02-27 06:34	$(-35.8°, -72.7°)$	33	8.6	3.2
14	Central Taiwan	2010-03-04 00:18	$(23.0°, 120.7°)$	5	6.5	3.5
15	Northern Mexico	2010-04-04 22:40	$(32.1°, -115.5°)$	10	7.2	4.8
16	Southern Sumatra	2010-04-06 22:15	$(2.4°, 97.1°)$	31	7.8	3.1
17	Yushu, Qinghai	2010-04-13 23:49	$(33.1°, 96.7°)$	10	6.9	2.5
18	Nicobar Islands	2010-06-12 19:26	$(7.7°, 91.9°)$	30	7.6	4.6
18	Vanuatu	2010-12-25 13:16	$(-19.7°, 168.9°)$	20	7.4	2.4
20	Southwestern Pakistan	2011-01-18 20:23	$(28.8°, 63.9°)$	10	7.1	4.1
21	Tohoku, Japan	2011-03-11 05:46	$(38.3°, 142.4°)$	24	9.0	2.5
22	Kermadec Islands	2011-07-06 19:03	$(-29.3°, -176.2°)$	10	7.7	2.9
23	Kermadec Islands	2011-10-21 17:57	$(-29.0°, -176.2°)$	33	7.5	2.9
24	Eastern Turkey	2011-10-23 10:41	$(38.6°, 43.5°)$	20	7.3	3.0
25	Mexico	2012-03-20 18:02	$(16.7°, -98.2°)$	20	7.5	2.7
26	Northern Sumatra	2012-04-11 08:38	$(2.3°, 93.1°)$	23	8.6	3.6
27	Xinyuan, Xinjiang	2012-06-29 21:07	$(43.4°, 84.8°)$	7	6.3	3.3
28	Costa Rica	2012-09-05 14:42	$(10.1°, 85.3°)$	41	7.6	2.6
29	Haida Gwaii	2012-10-28 03:04	$(52.8°, -131.9°)$	18	7.8	3.2
30	Southeastern Alaska	2013-01-05 08:58	$(55.2°, -134.8°)$	10	7.5	2.2
31	Solomon Islands	2013-02-06 01:12	$(-10.8°, 165.1°)$	6	7.8	2.7
32	Nantou, Taiwan	2013-03-27 02:03	$(23.8°, 121.1°)$	21	6.0	2.8
33	Khash, Iran	2013-04-16 10:44	$(28.1°, 62.1°)$	82	7.7	4.3
34	Lushan, Sichuan	2013-04-20 00:02	$(30.3°, 103.0°)$	12	6.8	3.0
35	Sea of Okhotsk	2013-05-24 05:44	$(54.9°, 153.3°)$	610	8.3	2.8
36	Nantou, Taiwan	2013-06-02 05:43	$(23.8°, 121, 1°)$	20	6.2	2.6

TABLE III. – *Continued.*

No.	Epicentral Region	Origin Time (UTC)	Epicentral Location (Lat., Long.)	Focal Depth (km)	M_w	Time Consumed (hr)
37	Mingxian-Zhangxian, Gansu	2013-07-21 23:45	(34.5°, 104.2°)	10	6.0	2.4
38	Hualian, Taiwan	2013-10-31 12:02	(23.6°, 121.4°)	12	6.3	1.7
39	Scotia Sea	2013-11-17 09:04	(−60.3°, −46.4°)	10	7.8	1.6
40	Yutian, Xinjiang	2014-02-12 09:19	(35.9°, 82.6°)	13	6.9	3.2
41	Northern Chile	2014-04-01 23:46	(−19.6°, −70.8°)	20	8.2	2.8
42	Northern Chile	2014-04-03 02:43	(−20.4°, −70.1°)	20	7.7	1.3
43	Solomon Islands	2014-04-12 20:14	(−11.3°, 162.2°)	29	7.6	5.0
44	Solomon Islands	2014-04-13 12:36	(−11.5°, 162.1°)	35	7.5	2.4
45	Papua New Guinea	2014-04-19 13:27	(−6.7°, 154.9°)	31	7.5	1.3
46	Alaska	2014-06-23 20:53	(51.8°, 178.8°)	114	7.9	2.7
47	Ludian, Yunnan	2014-08-03 08:30	(27.1°, 103.3°)	12	6.1	2.4
48	Jinggu, Yunnan	2014-10-07 13:49	(23.4°, 100.5°)	5	6.0	1.6
49	Papua New Guinea	2015-03-29 23:48	(−4.8°, 152.6°)	18	7.5	2.6
50	Nepal	2015-04-25 06:11	(28.1°, 84.6°)	40	7.9	2.2
51	Nepal	2015-05-12 07:05	(27.8°, 86.1°)	15	7.2	2.9
52	Pishan, Xinjiang	2015-07-03 01:07	(37.5°, 78.1°)	15	6.3	1.7
53	Central Chile	2015-09-16 22:54	(−31.6°, −71.7°)	13	8.2	2.3
54	Farkhar, Afghanistan	2015-10-26 09:09	(36.4°, 70.7°)	213	7.5	2.0
55	Tarauaca, Brazil	2015-11-24 22:45	(−10.5°, −70.9°)	600	7.4	2.6
56	Sumatra	2016-03-02 12:49	(−4.9°, 94.2°)	10	7.7	1.0
57	South Georgia Island	2016-08-19 07:32	(−55.3°, −31.9°)	10	7.4	2.0
58	Zaduo, Qinghai	2016-10-17 07:14	(32.8°, 94.9°)	9	5.8	1.9
59	Norcia, Italy	2016-10-30 06:40	(42.9°, 13.1°)	10	6.3	1.7
60	South Island, N.Z.	2016-11-13 11:02	(−42.8°, 173.1°)	10	7.9	1.7
61	Aketao, Xinjiang	2016-11-25 14:24	(39.3°, 74.0°)	12	6.5	1.8
62	Hututi, Xinjiang	2016-12-08 05:15	(43.8°, 86.4°)	6	6.2	3.5
63	Chile	2016-12-25 14:22	(−43.4°, −73.8°)	40	7.5	1.6
64	Solomon Islands	2017-01-22 04:30	(−6.1°, 155.2°)	168	7.9	1.4
65	Jiuzhaigou, Sichuan	2017-08-08 13:19	(33.2°, 103.8°)	10	6.5	1.7
66	Jinghe, Xinjiang	2017-08-08 23:27	(44.3°, 82.9°)	11	6.3	1.1
67	Mexico	2017-09-08 12:49	(14.9°, −94.0°)	30	8.1	1.3
68	Milin, Tibet	2017-11-17 22:34	(29.8°, 94.9°)	10	6.4	1.2
69	Northern Honduras	2018-01-10 02:51	(17.5°, −83.5°)	10	7.7	1.9
70	Alaska	2018-01-23 09:31	(56.0°, −149.1°)	10	7.9	1.4
71	Papua New Guinea	2018-02-25 17:44	(−6.10°, 142.8°)	20	7.4	2.1

of 12 May 2008 (no fast inversion for this earthquake), the M_w6.3 L'Aquila, Italy, earthquake of 6 April 2009 (no fast inversion for this earthquake), the M_w7.0 Haiti earthquake of 12 January 2010 [47], the M_w8.8 Chile earthquake of 27 February, 2010, the M_w6.5

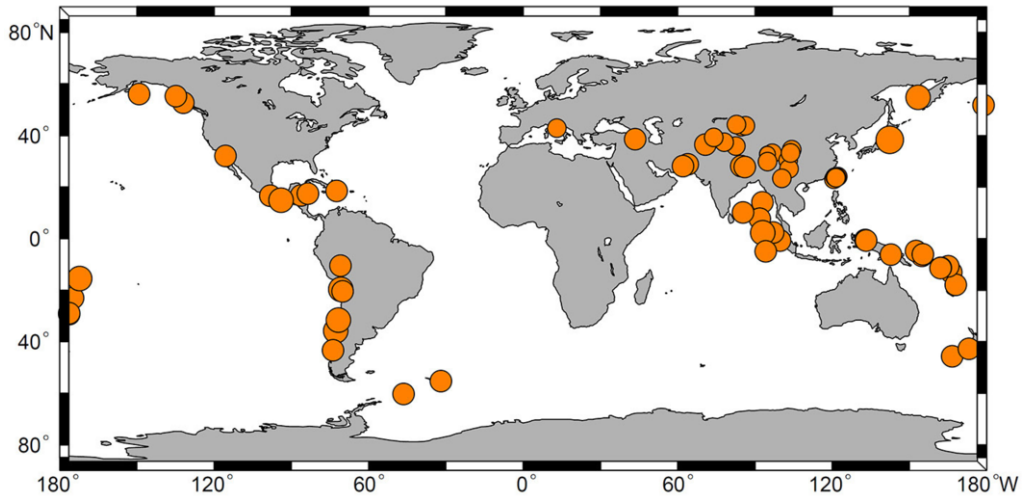

Fig. 29. – Map showing the epicentral distribution of the recent significant earthquakes whose source rupture processes were timely inverted and released after the earthquake occurrence in the time period 2009–2018.

Jiaxian, Taiwan, earthquake of 4 March 2010, the M_w7.2 Mexico earthquake of 4 April 2010 (poorly constrained model) [48], the M_w7.8 Sumatra earthquake of 6 April 2010, the M_w6.9 Yushu, Qinghai, earthquake of 13 April 2010 (14 April 2010, Beijing time), the 20 April 2013 M_w6.6 Lushan, Sichuan, earthquake [49], the 21 July 2013 M_w6.0 Mingxian-Zhangxian, Gansu, earthquake, the 3 August 2014 M_w6.1 Ludian, Yunnan,

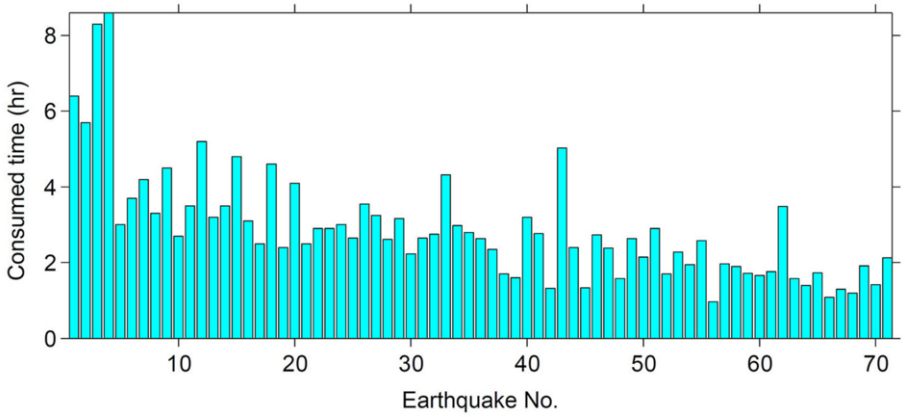

Fig. 30. – The time consumed on each of the significant earthquakes in table III for which the source rupture processes were inverted and released immediately after the earthquake occurrence in the time period 2009–2018. The abscissa represents serial number (No.) of the significant earthquake. The ordinate represents the time consumed for data processing in hour.

earthquake [50], the 25 April 2015 M_w7.8 Gorkha, Nepal, earthquake, and the 8 August 2017 M_w6.5 Jiuzhaigou, Sichuan, earthquake.

4. – Summary

The earthquake rupture process inversion is not only an important part of scientific research at present, but also a necessary work in the emergency response of earthquake disasters. We have presented the theory and the methods of earthquake rupture process inversion and have shown in this paper that the earthquake rupture model can be well determined about 1–3 hours after the earthquake occurrence, which is valuable to estimate the meizoseismic areas of disastrous earthquakes. However, for early warning of near-shore earthquake-generated tsunamis, this is far from enough because the tsunami usually reaches the coast in 10–30 minutes. To further reduce the time consumed, a feasible way is to use the local or regional data, rather than the teleseismic data. As the continuous improvement of earthquake monitoring particularly in earthquake-prone area, inversion with the near-source data would be the future direction to speed up the fast and routine source inversion.

REFERENCES

[1] BUTLER R., LAY T., CREAGER K., EARL P., FISCHER K., GAHERTY J. and TROMP J., The Global Seismographic Network surpasses its design goal, *Eos, Trans. Amer. Geophys. Union*, **85** (2004) 225.

[2] HEIDEMANN J., YE W., WILLS J., SYED A. and LI Y., *Research challenges and applications for underwater sensor networking*, in *Wireless Communications and Networking Conference, 2006*, *IEEE*, **1** (2006) 228.

[3] ZHENG X. F., YAO Z. X., LIANG J. H. and ZHENG J., The role played and opportunities provided by IGP DMC of China National Seismic Network in Wenchuan earthquake disaster relief and researches, *Bull. Seismol. Soc. Am.*, **100** (2010) 2866.

[4] ZHANG Y., CHEN Y. T. and XU L. S., Fast and robust inversion of earthquake source rupture process and its application to earthquake emergency response, *Earthquake Sci.*, **25** (2012) 121.

[5] ALLEN R. M., GASPARINI P., KAMIGAICHI O. and BOSE M., The status of earthquake early warning around the world: An introductory overview, *Seismol. Res. Lett.*, **80** (2009) 682.

[6] KIKUCHI M. and KANAMORI H., Inversion of complex body waves, *Bull. Seismol. Soc. Am.*, **72** (1982) 491.

[7] HARTZELL S. H. and HEATON T. H., Inversion of strong ground motion and teleseismic waveform data for the fault rupture history of the 1979 Imperial Valley, California, earthquake, *Bull. Seismol. Soc. Am.*, **73** (1983) 1553.

[8] DAS S. and KOSTROV B. V., Inversion for seismic slip rate history and distribution with stabilizing constraints: Application to the 1986 Andreanof Islands earthquake, *J. Geophys. Res. Solid Earth*, **95** (1990) 6899.

[9] JI C., WALD D. J. and HELMBERGER D. V., Source description of the 1999 Hector Mine, California, earthquake, part I: wavelet domain inversion theory and resolution analysis, *Bull. Seismol. Soc. Am.*, **92** (2002) 1192.

[10] Mori J. and Hartzell H. S., Source inversion of the 1988 Upland, California, earthquake: determination of a fault plane for a small event, *Bull. Seismol. Soc. Am.*, **80** (1990) 507.
[11] Xu L. S. and Chen Y. T., Tempo-spatial rupture process of the 1997 Mani, Xizang (Tibet), China earthquake of $M_S = 7.9$, *Acta Seismol. Sinica*, **12** (1999) 495.
[12] Chen Y. T. and Xu L. S., A time domain inversion technique for the tempo-spatial distribution of slip on a finite fault plane with applications to recent large earthquakes in Tibetan Plateau, *Geophys. J. Int.*, **143** (2000) 407.
[13] Zhang Y., Xu L. S. and Chen Y. T., PLD method for apparent source time function (ASTF) retrieving and its application to the 2005 Kashmir M_w7.6 earthquake, *Chin. J. Geophys.*, **52** (2009) 672 (in Chinese).
[14] Zhang Y., Chen Y. T. and Xu L. S., Rupture process of the 2005 Southern Asian (Pakistan) M_w 7.6 earthquake from long-period waveform data, in *Advances in Geosciences*, Vol. **9** *Solid Earth (SE), Ocean Science (OS) and Atmospheric Science (AS)*, edited by Chen Y. T. (World Scientific Publishing Co., Singapore) 2007, pp. 13–21.
[15] Zhang Y., Xu L. S. and Chen Y. T., Rupture process of April 6 2009 L'Aquila Italy M_w6.3 earthquake: a comparison between apparent source time function method and direct wave inversion method, *Chin. J. Geophys.*, **53** (2010) 1428.
[16] Zhang Y., Chen Y. T., Xu L. S., Wei X., Jin M. P. and Zhang S., The 2014 M_w6.1 Ludian, Yunnan, earthquake: A complex conjugated ruptured earthquake, *Chin. J. Geophys.*, **58** (2015) 153 (in Chinese with English abstract).
[17] Zhang Y.,2008 *Study on the Method of Earthquake Rupture Process Inversion*, Dissertation for Doctor Degree, Beijing, School of Earth and Space Sciences, Peking University (2008) 1–158 (in Chinese).
[18] Delouis B., Giardini D., Lundgren P. and Salichon J., Joint inversion of InSAR, GPS, teleseismic, and strong-motion data for the spatial and temporal distribution of earthquake slip: application to the 1999 Izmit mainshock, *Bull. Seismol. Soc. Am.*, **92** (2002) 278.
[19] Zhang Y., Feng W. P., Chen Y. T., Xu L. S., Li Z. H. and Forrest D., The 2009 L'Aquila M_w6.3 earthquake: a new technique to locate the hypocentre in the joint inversion of earthquake rupture process, *Geophys. J. Int.*, **191** (2012) 1417.
[20] Zhang Y., Feng W. P., Xu L. S., Zhou C. H. and Chen Y. T., Spatio-temporal rupture process of the 2008 great Wenchuan earthquake, *Sci. China, Ser. D: Earth Sci.*, **52** (2009) 145.
[21] Chen Y. T., Yang Z. X., Zhang Y. and Liu C., From the 2008 Wenchuan earthquake to the 2013 Lushan earthquake, *Sci. China, Ser. D: Earth Sci.*, **43** (2013) 1064 (in Chinese).
[22] Monastersky R., The next wave, *Nature*, **483** (2012) 144.
[23] Yagi Y., Mikumo T., Pacheco J. and Reyes G., Source rupture process of the Tecomán, Colima, Mexico earthquake of 22 January 2003, determined by joint inversion of teleseismic body-wave and near-source data, *Bull. Seismol. Soc. Am.*, **94** (2004) 1795.
[24] Hartzell S. and Iida M., Source complexity of the 1987 Whittier Narrows, California, earthquake from the inversion of strong motion records, *J. Geophys. Res.: Solid Earth*, **95** (1990) 12475.
[25] Bertero M., Bindi D., Boccacci P., Cattaneo M., Eva C. and Lanza V., Application of the projected Landweber method to the estimation of the source time function in seismology, *Inverse Problems*, **13** (1997) 465.
[26] Liu C., Xu L. and Chen Y. T., Quick moment tensor solution for 6 April 2009, L'Aquila, Italy, earthquake, *Earthquake Sci.*, **22** (2009) 449.
[27] Li X. and Chen Y. T., Inversion of long-period body-wave data for the source process of the Gonghe, Qinghai, China earthquake, *Acta Seismol. Sin. (English Edition)*, **9** (1996) 361.

[28] XU L. S. and CHEN Y. T., Source parameters of the Gonghe, Qinghai Province, China, earthquake from inversion of digital broadband waveform data, *Acta Seismol. Sin. (English Edition)*, **10** (1997) 143.

[29] XU X. T., CHEN Y. T. and WANG P. D., Rupture process of the $M_L = 4.1$ earthquake in Huailai basin on July 20, 195, *Acta Seismol. Sin.*, **12** (1999) 618.

[30] LIU C., XU L. S. and CHEN Y. T., Quick moment solution for 14 April 2010 Yushu, Qinghai, earthquake, *Earthquake Sci.*, **32** (2010) 366 (in Chinese).

[31] CHEN Y. T. and XU L. S., Source processes of recent large earthquakes in Qinghai-Xizang (Tibetan) Plateau, *J. Geol.*, **B** (1999) 216.

[32] XU L. S. and CHEN Y. T., *Observed evidence for crack fusion from the 14 November 2000 Kunlun Mountain earthquake*, in *Advances in Geosciences*, Vol. **1**, *Solid Earth (SE)*, edited by CHEN Y. T. (World Scientific Publishing Co., Singapore) 2006, pp. 51–59.

[33] LIU C., ZHANG Y., XU L. S. and CHEN Y. T., A new technique for moment tensor inversion with applications to the 2008 Wenchuan M_s8.0 earthquake sequence, *Acta Seismol. Sin.*, **21** (2008) 333 (in Chinese).

[34] LIU R. F., CHEN Y. T., ZOU L. Y., CHEN H. F., LIANG J. H., ZHANG L. W., HAN X. J., REN X. and SUN L., Determination of parameters for the 20 April 2013 Lushan M_w6.7(M_S7.0) earthquake in Sichuan Province, *Acta Seismol. Sin.*, **35** (2013) 652.

[35] ZHANG Y., XU L. S., CHEN Y. T. and WANG R.-J., Fast inversion on the rupture process of the 12 February 2014 Yutian M_w6.9 earthquake: Discussion on the impacts of focal mechanisms on rupture process inversion, *Acta Seismol. Sin.*, **36** (2014) 159.

[36] XU L. S., CHEN Y. T., TENG T. L. and PATAU G., Temporal and spatial rupture process of the 1999 Chi-Chi earthquake from IRIS and GEOSCOPE long-period waveform data using aftershocks as empirical Green's functions, *Bull. Seismol. Soc. Am.*, **92** (2002) 3210.

[37] XIE Y. S. and CAI M. B., *Compilation of Historical Materials of Chinese Earthquakes*, Vol. **3** (Science Press, Beijing) 1987, pp. 235–236 (in Chinese).

[38] MIN Z. Q., *Historical Strong Earthquake Catalog in China* (the 23th Century BC-1911 AD) (Seismological Press, Beijing) 1995, pp. 1–514 (in Chinese).

[39] MIN Z. Q., *Historical Strong Earthquake Catalog in China* (1912 AD—1990 AD) (Seismological Press, Beijing) 1995, pp. 1–636 (in Chinese).

[40] YANG Z. X., WALDHAUSER F., CHEN Y. T. and RICHARDS P., Double-difference relocation of earthquakes in central-western China 1992–1999, *J. Seismol.*, **9** (2005) 241.

[41] ZHANG Y., FENG W. P., XU L. S., ZHOU C. H. and CHEN Y. T., Spatio-temporal rupture process of the 2008 great Wenchuan earthquake, *Sci. China, Ser. D: Earth Sci.*, **52** (2009) 145.

[42] DENG Q. D., ZHANG P. Z., RAN Y. K., YANG X. P. and ZU Q. X., Basic characteristics of active tectonics of China, *Sci. China, Ser. D: Earth Sci.*, **46** (2003) 356.

[43] DU H. L., XU L. S. and CHEN Y. T., Rupture process of the 2008 Wenchuan earthquake from the analysis of the Alaska-array data, *Chin. J. Geophys.*, **52** (2009) 372 (in Chinese).

[44] LI M. F., XING C. Q., CAI C. X., GUO W. X, WU S. X. YUAN Z. Z., MENG Y. Q., TU D. L., ZHANG R. B. and ZHOU R. J., Research on activity of Yushu fault, *Seismol. Geol.*, **17** (1995) 218 (in Chinese).

[45] ZHOU R. J., WEN X. Z., CAI C. X. and MA S. H., Recent earthquakes and assessment of seismic tendency on the Ganzi-Yushu fault zone, *Seismol. Geol.*, **19** (1997) 115 (in Chinese).

[46] WEN X. Z., XU X. W., ZHENG R. Z., XIE Y. Q. and WAN C., Average slip-rate and recent large earthquake ruptures along the Garzê-Yushu fault, *Sci. China Ser. D Earth Sci.*, **46** (2003) 276.

[47] Zhang Y., Xu L. S. and Chen Y. T., Fast inversion of the rupture process of 2010 January 12 Haiti earthquake, *Acta Seismol. Sin.*, **32** (2010) 124 (in Chinese with English abstract).
[48] Zhang Y., Xu L. S. and Chen Y. T., Source process of the 2010 Yushu, Qinghai, earthquake, *Sci. China Ser. D: Earth Sci.*, **53** (2010) 1249.
[49] Zhang Y., Wang R., Chen Y. T., Xu L., Du F., Jin M., Tu H. and Dahm T., Kinematic rupture model and hypocenter relocation of the 2013 M_w6.6 Lushan earthquake constrained by strong-motion and teleseismic data, *Seismol. Res. Lett.*, **85** (2014) 15.
[50] Zhang Y., Chen Y. T., Xu L. S., Wei X., Jin M. P. and Zhang S., The 2014 M_w6.1 Ludian, Yunnan, earthquake: A complex conjugated ruptured earthquake, *Chin. J. Geophys.*, **58** (2015) 153 (in Chinese with English abstract).

This page intentionally left blank

Proceedings of the International School of Physics "Enrico Fermi"
Course 202 "Mechanics of Earthquake Faulting", edited by A. Bizzarri, S. Das and A. Petri
(IOS, Amsterdam; SIF, Bologna) 2019
DOI 10.3254/978-1-61499-979-9-177

Do plates begin to slip before some large earthquakes?

Michel Bouchon and David Marsan

Université Grenoble Alpes and Centre National de la Recherche Scientifique, ISTerre 38000 Grenoble, France

Hayrullah Karabulut and Mustafa Aktar

Kandilly Observatory and Earthquake Research Institute, Bogazici University Istanbul, Turkey

Virginie Durand

Institut de Physique du Globe de Paris rue Jussieu, 75005 Paris, France

Jean Schmittbuhl

Université de Strasbourg - 67000 Strasbourg, France

Summary. — Many earthquakes are preceded by foreshocks. However, the mechanisms that generate foreshocks and the reason why they occur before some earthquakes and not others are still poorly understood. We investigate here the evolution of seismic activity before 65 large earthquakes which have occurred in well instrumented areas. We show that most of the earthquakes occurring along the plate interfaces are preceded by foreshocks. Intraplate earthquakes which result from the internal deformation of the plates are less prone to foreshocks. This difference supports that slow slip of the plate interface precedes many large interplate earthquakes. Within this group a large difference exists in the spatial distribution of foreshocks: While foreshocks to transform fault earthquakes tend to localize close to the future hypocenter, those preceding subduction earthquakes are often spread over a broad area of the plate interface, suggesting that these earthquakes are preceded by the slow slip of a large patch of the subduction interface.

1. – Introduction

The reason why foreshocks occur before some earthquakes and not others is still poorly understood. Two mechanisms are proposed to explain their presence [1-8]:

– A cascade model where a first shock randomly triggers other shocks and one of them triggers the earthquake. The fact that this leads to a large earthquake is the result of a random throw.

– An aseismic slip model where a patch of the fault begins to slip slowly and the foreshocks are the breaking of the fault asperities resisting the slow slip.

If the first model is correct, there is no hope to ever predict earthquakes. If slow slip is what generates foreshocks, one may hope that in the future this slow slip will be directly measurable and that the preparation phase of some earthquakes will be recognizable before rupture occurs.

To further explore this problem and try to shed light on the mechanism involved, we investigate the characteristics of seismic activity before 65 large earthquakes which have occurred in some of the best instrumented regions of the world. Most of this activity will be studied statistically but particular attention will be devoted to three major events: the 1999 Izmit (Turkey), 2010 Tohoku-Oki (Japan) and 2014 Iquique (Chile) earthquakes.

2. – Izmit earthquake

The Izmit earthquake is the best recorded large strike-slip earthquake to date. It ruptured the North Anatolian Fault, a plate boundary between two horizontally moving plates, the Eurasian plate to the north and the Anatolian plate to the south. Its rupture length extended for about 150 km with an average slip of ~ 2.5 m.

On the day of the earthquake, the closest station to the epicenter, UCG located only 13 km away (fig. 1), was triggered into recording 45 minutes before the earthquake [9]. During this period it recorded 18 seismic events (fig. 2). The similarity of their waveforms shows that they were originating from the same zone while the similarity of their spectra (fig. 3) support that they were produced by the repeating stick-slip of the same asperity. A comparison of their S minus P times with the S minus P time of the mainshock shows that, within the time resolution of the data (0.01 s), all the signals were coming from the location of the future hypocenter.

Cross-correlating the recorded signals provides a precise measurement of the relative locations of their source. Figure 4 presents the cross-correlation of the first 2 foreshocks. The figure shows a difference in S minus P times between the two events of about 6×10^{-4} s, which implies a difference in location (seen from station UCG) of ~ 5 m. This value is considerably smaller than the radius of the source inferred from the spectra which is of the order of 100 m. This shows that, seen from this station, the sources of the two foreshocks overlap.

The next closest station to the epicenter, KOS, is located ~ 38 km away from the epicenter. This station recorded only the largest foreshocks. While UCG is in a direction

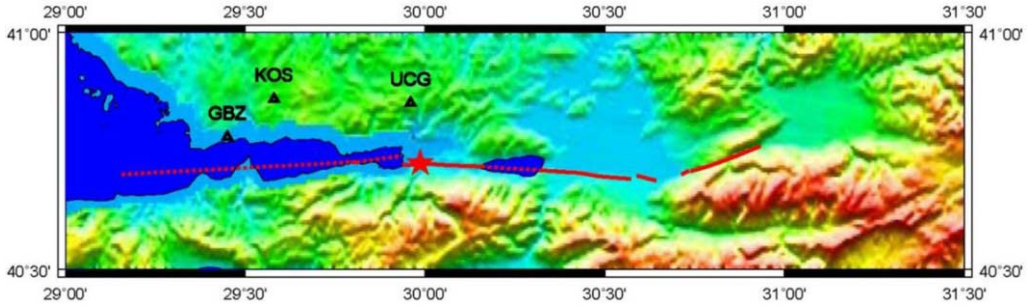

Fig. 1. – The 150 km long Izmit rupture and the closest stations to the epicenter.

almost perpendicular to the fault, KOS lies almost along fault strike (fig. 1). It is thus interesting to compare cross-correlations of the same events at the two stations. This is presented in fig. 5 for two $M > 2$ foreshocks. Because of the noise level at KOS, the records are low pass filtered at 12 Hz, which is approximatively the corner frequency of their spectra. At the two stations the difference in S minus P times between the two foreshocks is no more than ~ 0.002 s. This time difference, translated into distance, implies that the 2 stations see the center of radiation of the 2 foreshocks within ~ 17 m

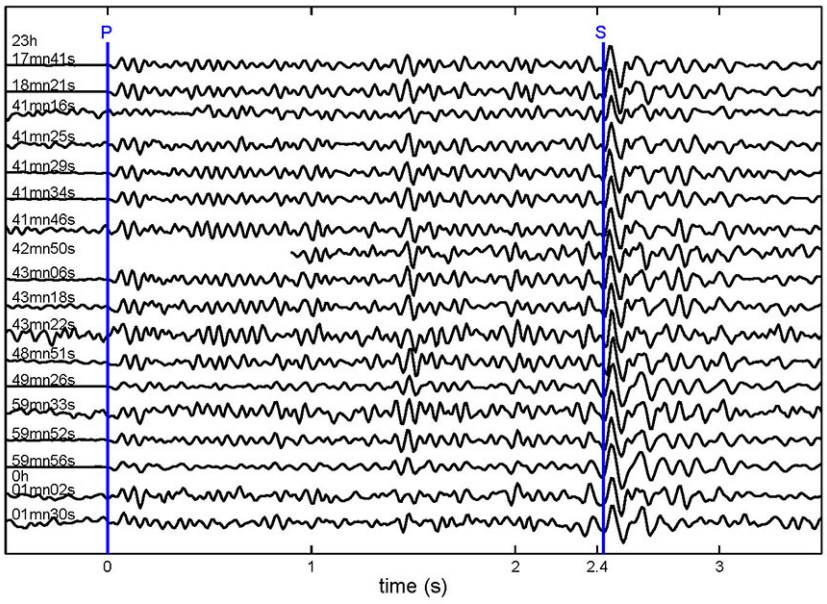

Fig. 2. – Records of the 18 shocks which preceded the Izmit earthquake. The location of the recording station (UCG) is shown in fig. 1. The P and S wave arrivals are indicated. Amplitude is normalized. Fluctuations before P arrivals show the relative noise level.

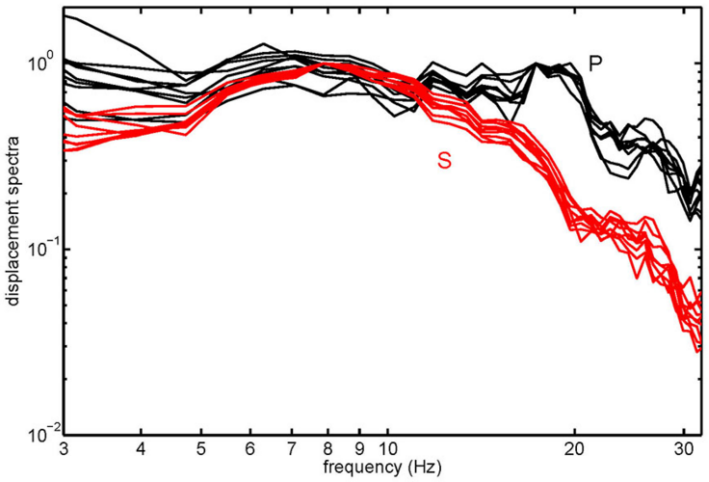

Fig. 3. – Normalized spectra of the 9 largest foreshocks of the Izmit earthquake.

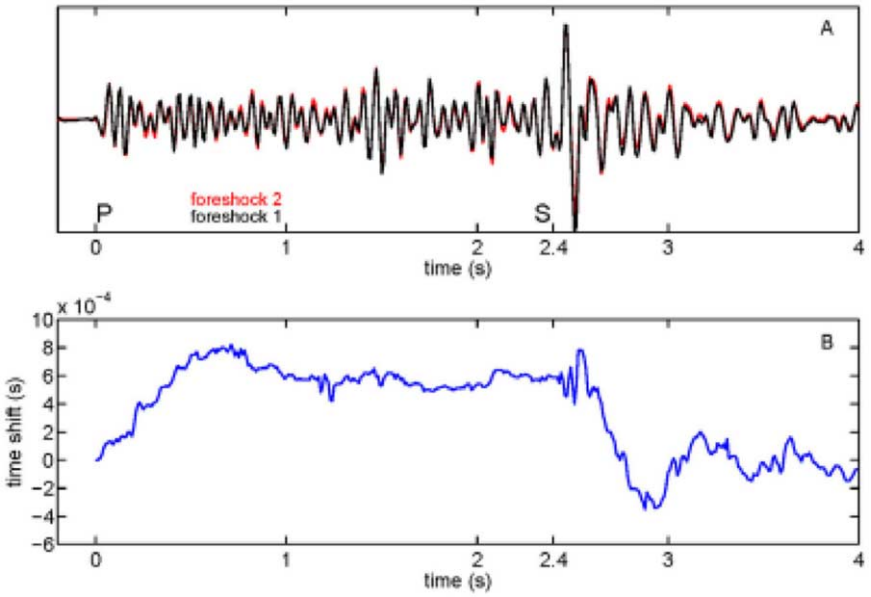

Fig. 4. – Superposition of the records of the first two foreshocks (normalized independently) and their cross-correlation.

from each other. This is considerably smaller than the source size of $M > 2$ events ($> 100\,\mathrm{m}$), and shows that for the two stations their sources overlap, indicating that the same asperity is involved. The repeating slip of the same asperity at a few minutes interval supports that the fault is locally slipping and reloading the asperity.

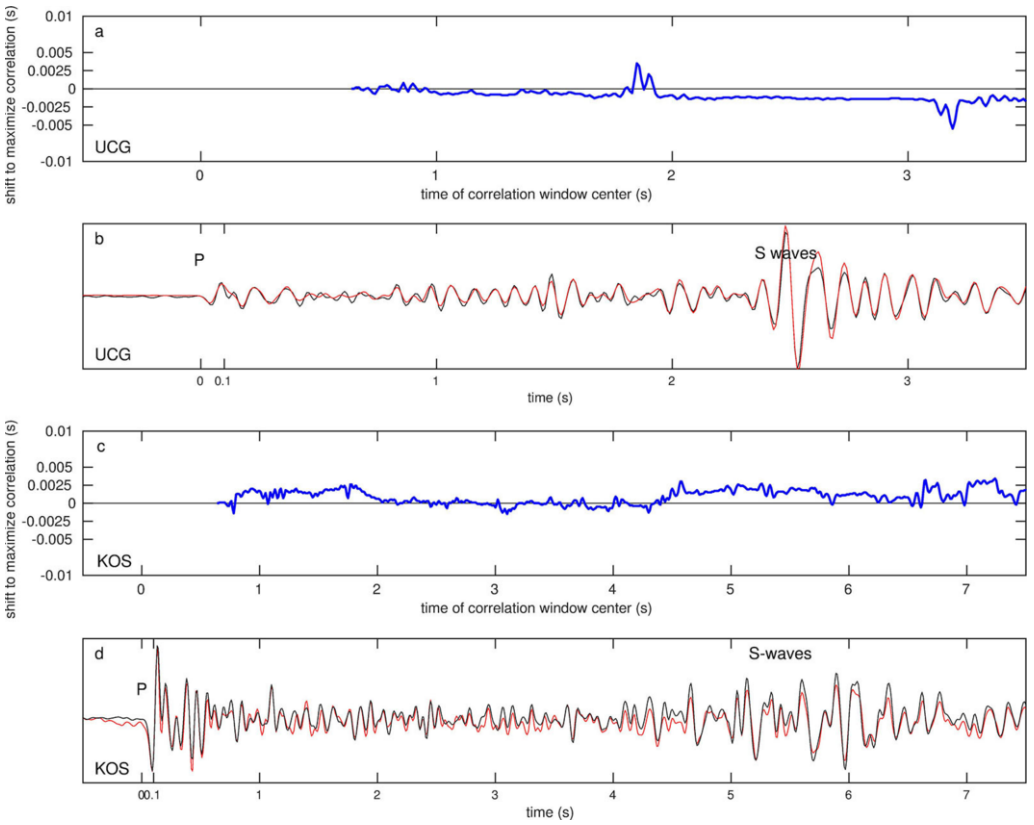

Fig. 5. – Cross-correlation between the records of two $M > 2$ foreshocks at the two closest stations from the epicenter UCG (top) and KOS (bottom). a), c) Evolution of the time shift which maximizes the correlation between the waveforms of the two foreshocks. The correlation is done over a moving window 128 points long (1.28 s). The first window begins at the P-wave arrival and corresponds to the origin of the time axis. Subsequent time shifts are measured relatively to this first window. The time shift is obtained by interpolating the correlation peak at each time step. b), d) Superposition of the records of the two foreshocks at each station. One of the records has been shifted in time (in the Fourier domain) by the time increment which maximizes the cross-correlation of the two signals. The P arrivals correpond to the origin of the time axis. The non-zero amplitude before the P arrivals shows the noise level of the records.

The similarity of the waveforms allows us to use waveform as a template to eventually detect other events present in the noise. This is done in fig. 6 where this template is cross-correlated with two 40 s long segments of the records. The first segment correlation (in black) is just before the first foreshock, the second one (in blue) immediately precedes the main shock. A correlation peak is indicative of a detected event. While no peak is present before the beginning of the foreshock crisis, 6 peaks are present in the 40 s leading to the earthquake. In all 44 foreshocks can be retrieved from the records. The long duration of the foreshock sequence and the striking acceleration of foreshock occurrences as the time

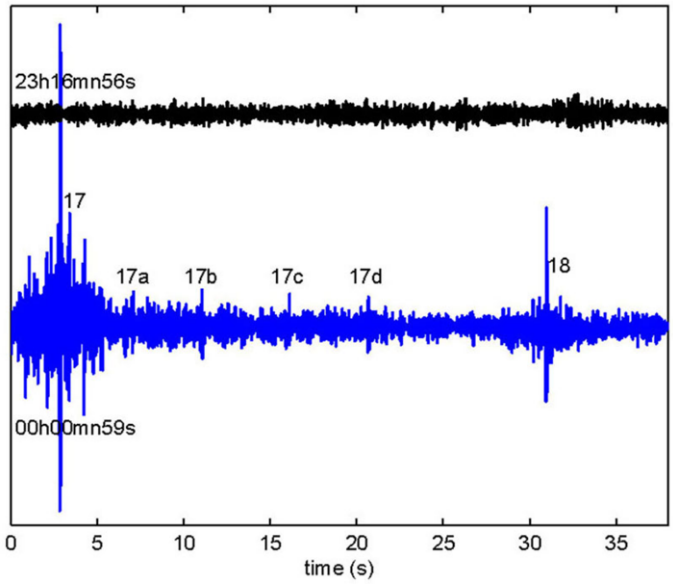

Fig. 6. – Cross-correlating the record with the template. Top: before the first foreshock. Bottom: 40 s prior to the earthquake.

of the earthquake approaches shows that a slow but accelerating process is involved. It argues for a much slower nucleation process than an elastic cascade where stress transfer would be largely controlled by elastic wave propagation.

Another piece of information we have on the nucleation of the Izmit earthquake is its location. Its hypocentral depth (17 km) places it at the very bottom of the seismogenic zone, no seismicity occurring below this depth. Based on these observations, our interpretation is that a patch of the fault located at the bottom of the brittle crust began to slip slowly 45 minutes before the earthquake. An asperity which would become the hypocenter of the earthquake was resisting this slow slip and was continuously reloaded by the slow slip around it. This phase of slow slip accelerated in time and led to the earthquake.

3. – Interplate and intraplate earthquakes

Our observation of the Izmit earthquake nucleation brings us to ask the question: Is Izmit just a special case or could it be a common case? Or phrased in another way: Are many large earthquakes preceded by a phase of slow slip accelerating (irregularly) in time?

To investigate this question, we now analyze 12 years of large earthquakes in the best instrumented areas in the world: The North Pacific from Taiwan to Japan and around North America. We consider all the $M \geq 6.5$ earthquakes which occurred in

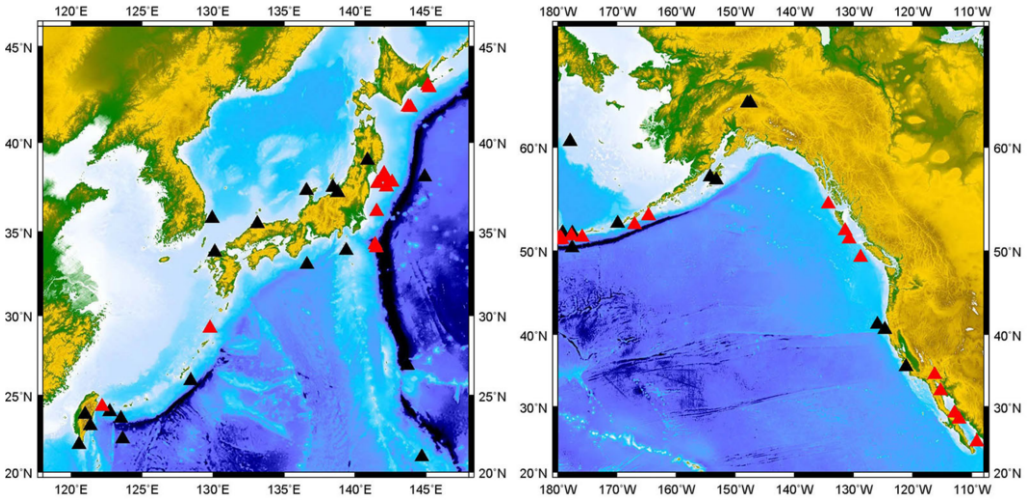

Fig. 7. – All the $M \geq 6.5$ interplate (red) and intraplate (black) earthquakes which occurred in these two densely instrumented zones between 01/01/1999 and 01/01/2011.

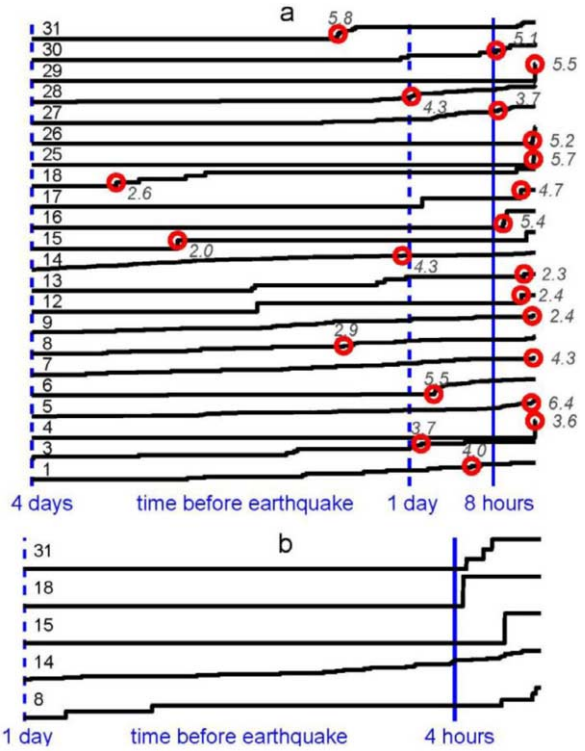

Fig. 8. – a) Cumulative number of events in the 4 days prior to 70% of the interplate earthquakes. The largest event is circled in red. b) Zoom on the final day for the 4 cases where the largest event does not fall on the last day.

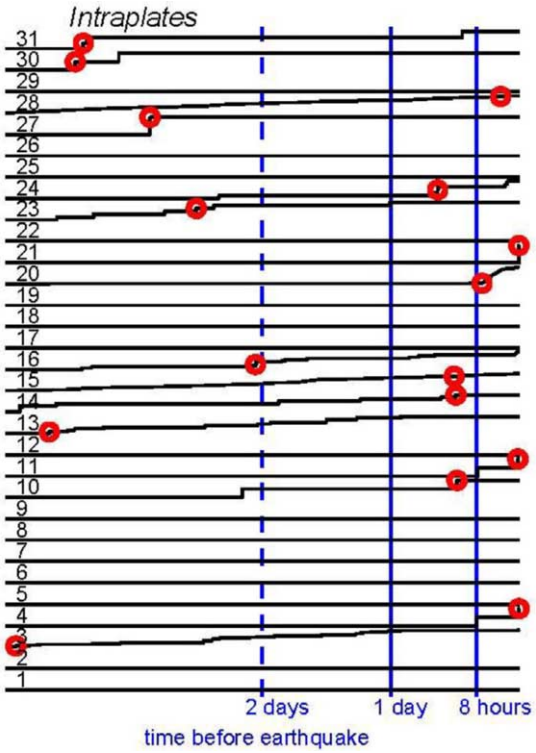

Fig. 9. – Cumulative number of events in the 4 days prior to all the intraplate earthquakes. The largest event is circled in red.

these two densely instrumented zones between 01/01/1999 and 01/01/2011 (fig. 7). We separate these events into two groups: interplate and intraplate earthquakes. We class as interplate earthquake an event which occurs on a plate interface. Large interplate earthquakes are of two types: subduction and transform fault earthquakes. We exclude earthquakes which occur less than one year after another large earthquake in the same area. For the zone studied, the two groups contain the same number of events: 31.

We first investigate how seismic activity evolves in a zone of 50 km radius around the epicenter in the few days (4) preceding the earthquakes. We observe that while 70% of the interplate earthquakes are preceded by an increase of activity in the day before (fig. 8), only 29% of intraplate earthquakes show an increase (fig. 9).

A statistical quantification of the difference between the two groups [10] confirms that: 1) most interplate earthquakes are preceded by foreshocks and 2) there is a significant difference between interplate and intraplate earthquakes, the latter group being less prone to have them.

The stack of all the seismicity evolutions preceding the 31 interplate earthquakes is presented in fig. 10. It shows a strong acceleration of the seismic activity as the time of

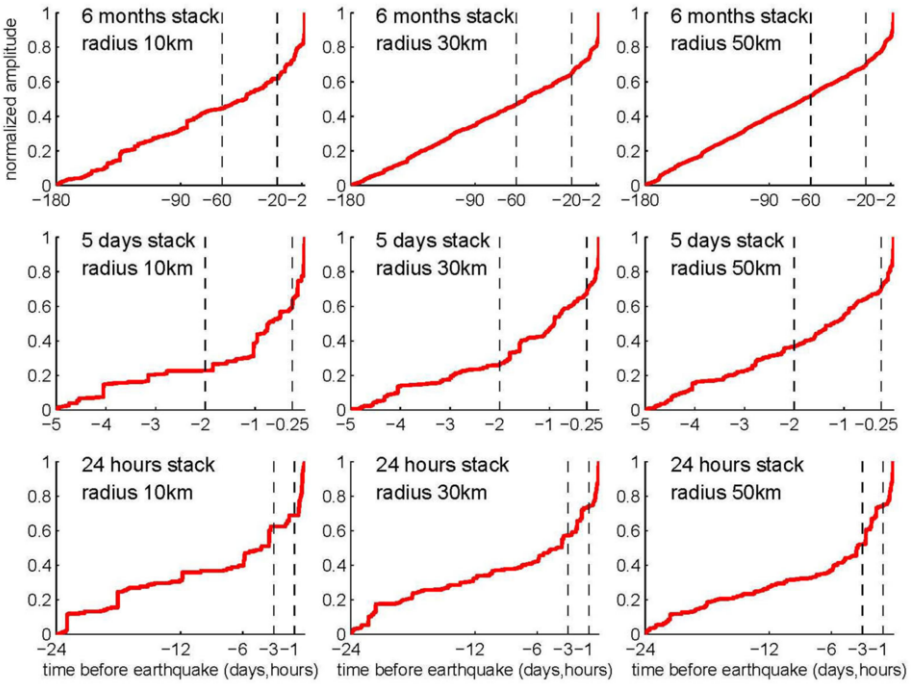

Fig. 10. – Normalized stacks of the cumulative numbers of events of all the interplate sequences. Each sequence is given the same weight. Different periods and different values of the radius of the zone around the future epicenter in which the events are counted are considered. The figure shows that the acceleration observed is independent of the time and space parametrization used.

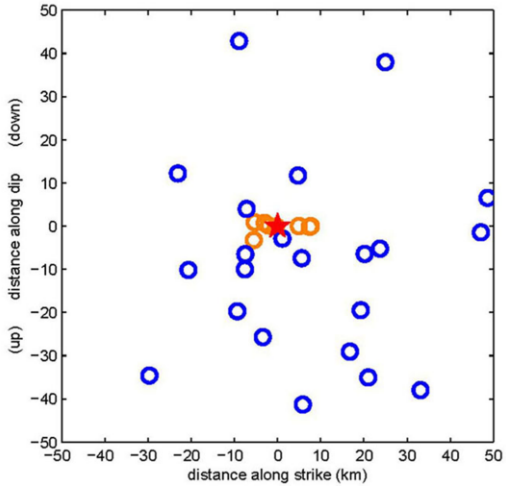

Fig. 11. – Relative locations of the last event of each pre-earthquake seismic sequence (circle) relative to the mainshock hypocenter (star) for transform fault (orange) and subduction (blue) earthquakes.

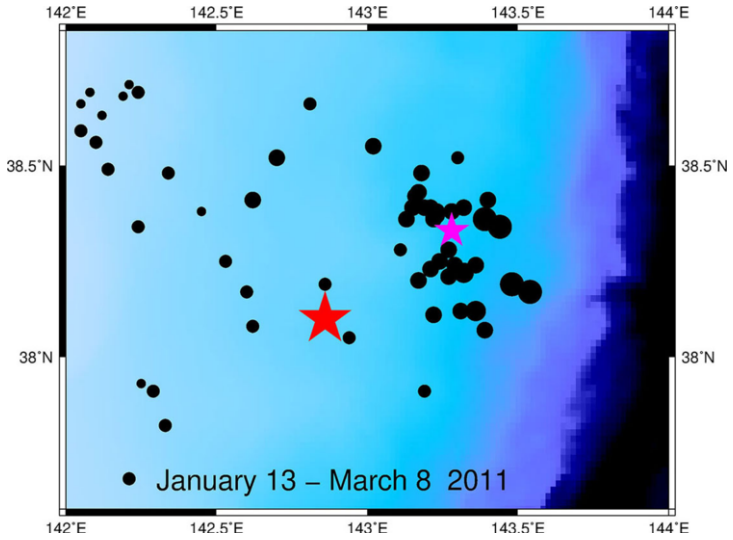

Fig. 12. – Seismic activity during the foreshock crisis before the occurrence of the large $M7.3$ foreshock (pink star) two days before the Tohoku earthquake. The red star is the Tohoku epicenter. All catalog events shallower than 25 km are shown. During this period the largest foreshock is $M5.3$ while the foreshock zone illuminates a patch of the plate interface of about 40 km by 40 km.

the mainshock approaches. This acceleration is robust and its presence is independent of the space and time parametrization used. A simulation of the sequences with the ETAS model [11] which takes into account the natural tendency of seismic events to cluster in time, shows that the observed acceleration is not due to this clustering tendency [10]. This implies the underlying presence of an accelerating process for which slow slip of the plate interface is the natural candidate.

We now investigate the spatial characteristics of this preparation phase. We show in fig. 11 the locations relatively to the mainshock hypocenter of the last event of all the pre-earthquake interplate sequences. As previously shown, most of these last events are foreshocks. A surprising feature of this figure is that while transform fault pre-earthquake shocks locate close to the hypocenter, subduction events are spread over a broad area of the plate interface. The distance involved and the small size of most events [10] generally prevents a stress transfer between subduction pre-shocks and mainshock, and indicates that a broad process unrelated to seismic waves is involved. This again points to the slow slip of a patch of the plate interface. The difference in foreshock localization must reflect inherent mechanical differences between a transform fault and a subducting slab.

The surprisingly large extent of many subduction foreshock zones is confirmed by what is observed before two of the best recorded subduction earthquakes to date, the $M9.0$ March 2011 Japan Tohoku earthquake (fig. 12), and the $M8.2$ Chile Iquique earthquake (fig. 13). The spread of foreshocks over such large zones has been interpreted as migrating

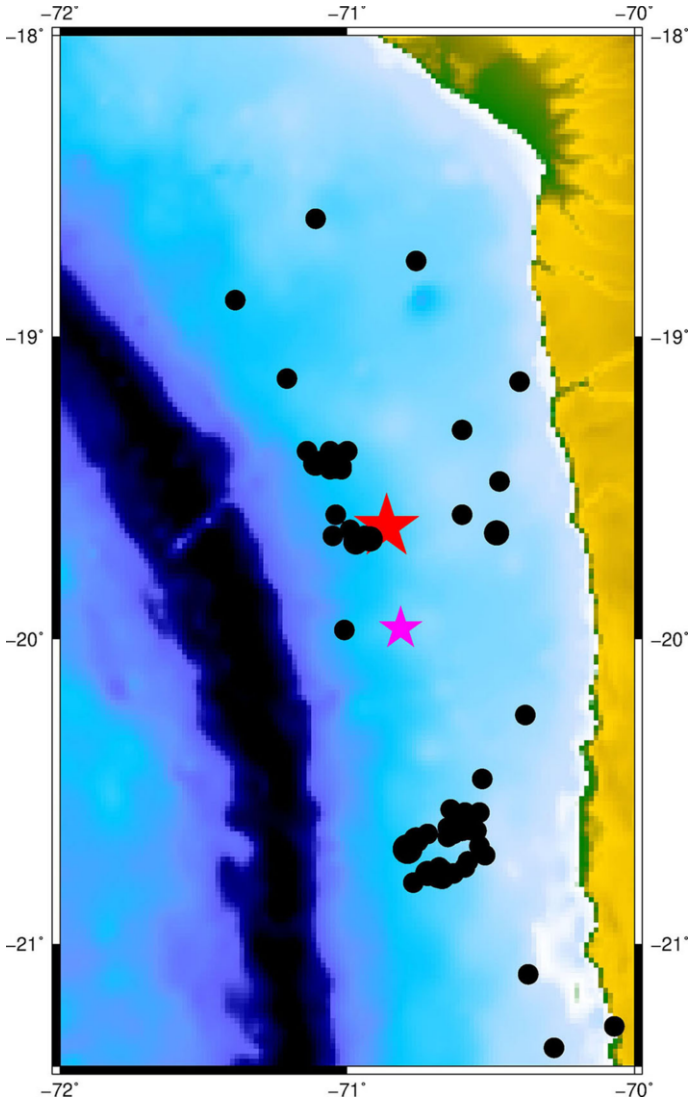

Fig. 13. – Seismic activity during the foreshock crisis before the large $M6.7$ foreshock of March 16 (pink star). All catalog events shallower than 40 km are shown. The red star is the $M8.2$ Iquique epicenter. The 3 clusters show that the foreshock zone extends over ~ 150 km.

slow slip [12, 13]. The rapidity of this spread (a few weeks) through a wide zone which is thought to be largely locked during the interseismic period however raises the question of what is the motor of this slow slip. Recent seismic and gravity observations [14, 15] provide some clues which support that this motor lies deep in the slab. The nature of this motor is still unknown.

REFERENCES

[1] JONES L. M. and MOLNAR P., Frequency of foreshocks, *Nature*, **262** (1976) 677.
[2] JONES L. M. and MOLNAR P., Some characteristics of foreshocks and their possible relationship to earthquake prediction and premonitory slip on faults, *J. Geophys. Res.*, **84** (1979) 3596.
[3] OHNAKA M., Earthquake source nucleation: A physical model for short term precursors, *Tectonophysics*, **211** (1992) 149.
[4] ABERCROMBIE R. E. and MORI J., Occurrence patterns of foreshocks to large earthquakes in the western United States, *Nature*, **381** (1996) 303.
[5] DODGE D. A., BEROZA G. C. and ELLSWORTH W. L., Detailed observations of California foreshock sequences: Implications for the earthquake initiation process, *J. Geophys. Res.*, **101** (1996) 22371.
[6] REASENBERG P. A., Foreshock occurrence before large earthquakes, *J. Geophys. Res.*, **104** (1999) 4755.
[7] HELMSTETTER A., SORNETTE D. and GRASSO J. R., Mainshocks are aftershocks of conditional foreshocks: How do foreshock statistical properties emerge from aftershock laws, *J. Geophys. Res.*, **108** (2003) 2046.
[8] MCGUIRE J. J., BOETTCHER M. S. and JORDAN T. H., Foreshock sequences and short-term earthquake predictability on East Pacific rise transform faults, *Nature*, **434** (2005) 457.
[9] BOUCHON M., KARABULUT H., AKTAR M., OZALAYBEY S. and SCHMITTBUHL J., Extended nucleation of the 1999 M_w 7.6 Izmit earthquake, *Science*, **331** (2011) 877.
[10] BOUCHON M., DURAND V., MARSAN D., KARABULUT H. and SCHMITTBUHL J., The long precursory phase of most large subduction earthquakes, *Nat. Geosci.*, **6** (2013) 299.
[11] OGATA Y., Statistical models for earthquake occurrence and residual analysis for point processes, *J. Am. Stat. Assoc.*, **83** (1988) 9.
[12] KATO A., OBARA K., IGARASHI T., TSURUOKA H., NAKAGAWA S. and HIRATA N., Propagation of slow slip leading up to the 2011 M_w 9.0 Tohoku-Oki earthquake, *Science*, **335** (2012) 705.
[13] RUIZ S. *et al.*, Intense foreshocks and a slow slip event preceded the 2014 Iquique M_w 8.1 earthquake, *Science*, **345** (2014) 1165.
[14] BOUCHON M. *et al.*, Potential slab deformation and plunge prior to the Tohoku, Iquique and Maule earthquakes, *Nat. Geosci.*, **9** (2016) 380.
[15] PANET I., BONVALOT S., NARTEAU C., REMY D. and LEMOINE J. M., Migrating pattern of deformation prior to the Tohoku-Oki earthquake revealed by GRACE data, *Nat. Geosci.*, **11** (2018) 367.

Proceedings of the International School of Physics "Enrico Fermi"
Course 202 "Mechanics of Earthquake Faulting", edited by A. Bizzarri, S. Das and A. Petri
(IOS, Amsterdam; SIF, Bologna) 2019
DOI 10.3254/978-1-61499-979-9-189

Dynamics and spectral properties of subduction earthquakes

R. Madariaga

Laboratoire de Geologie, CNRS-ENS, PSL University - Paris, France
Departamento de Geofisica, Universidad de Chile - Santiago, Chile

Summary. — We have studied the spectra of several large earthquakes in the Chilean subduction zone using both accelerograms and CNSS instruments. For the two events studied here, the Iquique $M_{\rm w}$ 8.1 earthquake of 24 April 2014 and the $M_{\rm w}$ 6.9 Valparaiso earthquake of 24 April 2017 we observe similar features. For these earthquakes the velocity records at low frequencies obtained by integrating accelerograms agree quite well with the ground velocity derived from GNSS records at the same sites. These observations show that at low frequencies the ground spectra differ quite significantly from the usual Aki-Brune spectrum used in studies of the far-field spectral properties of earthquakes. The most important difference is that at short distances the near-field term of the source dominates the spectra at low frequencies. The near-field term in seismic radiation is proportional to the moment time function of the source which is very different from the moment rate function that controls farfield. The ground velocity spectrum is flat at low frequencies and proportional to the static displacement produced by the earthquke at the observation site. The displacement spectrum on the other hand has a low-frequency asympote proportional to omega −1 instead of the usual flat spectrum predicted by the Aki-Brune model. More theoretical work is needed to identify the region where the near-field spectrum dominates.

1. – Introduction

Most studies of seismic radiation assume that the Fourier spectrum of displacement follows the omega-squared spectrum proposed by Aki and Brune [1, 11]. This is often true in the far field although many deviations from the simple omega-squared model are frequently reported (see, *e.g.* [3, 4]). In the near field it is expected that the spectrum deviates from the simple Aki-Brune model. Among other properties of seismic radiation the near-field spectrum must be compatible with the finite near-field displacement observed by dynamic GPS and the strong motion recordings observed at short distances from the source. Here we review a number of observations made in Chile where several large earthquakes have been recorded by both accelerometers and GNSS (Global Navigation Satellite System) instruments. We show that in the near field the seismic spectra are often very different from the Aki-Brune model.

In the last 15 years a number of large subduction earthquakes in North and Central Chile have been very well observed thanks to new observational data obtained by a number of new instruments deployed in the country. The series of events started with the 2005 Tarapaca [31] earthquake of 2005, it was followed by the $M_{\rm w}$ 7.7 Tocopilla earthquake [32] most important event was the $M_{\rm w}$ 8.8 Maule earthquake of 27 February 2010, followed in 2014 by the $M_{\rm w}$ 8.2 Iquique (sometimes called Pisagua) earthquake, the 15 September 2015 Illapel earthquake of $M_{\rm w}$ 8.4 and a series of events of magnitudes between 6 and 8 that provide additional insight into the radiation produced by earthquakes generated by the subduction process in Chile.

In a recent publication by [28] the spectra of the Iquique earthquake was discussed in some detail from the simultaneous observation of ground motion recorded by both accelerometers and GNSS data (see also [5]). They showed that the ground velocity spectrum is flat at low frequencies and that its amplitude is proportional to ground displacement observed by co-located GPS stations. This is in contrast with predictions by Aki-Brune that in the far field the velocity spectrum should increase at low frequencies as ω used in most studies of earthquake spectra [30, 3, 33, 4, 14]. The first observations made in Chile of deviations of the ground motion spectrum from the classical Brune model were made by [21] following the Tocopilla earthquake of November 2017. Although the data was sparse they showed that ground displacement spectra was very different from that of small aftershocks and that it had an omega -1 asymptote at low frequencies. This observation together with others made in for the $M_{\rm w}$ 8.8 Maule earthquake of 27 February 2010, showed that the near-field terms in seismic radiation significantly affects the ground motion spectrum and that the usual assumption that Brune spectrum properly describes the ground motion properties needs to be carefully revised. Of course the effects of the near-field terms are limited to the lower frequency range, but under many circumstances the effect may be much broader than what is usually assumed.

In this notes I will first review the recent observations of ground motion made simultaneously by accelerographs and GNSS instruments in Northern Chile during the Iquique earthquake of 2014 so as to set some broad properties of ground motion, specially ground velocity. Then we will look at a smaller event of magnitude $M_{\rm w}$ 7.9 that occurred near

Valparaiso on 24 April 2017. This event was very well recorded by the new National Seismological Service of the University of Chile (CSN) although only a couple of GPS stations could be used to determine the very low-fequency properties of ground displacement. We will provide a short introduction to ground motion properties derived from the usual Green function in an infinite medium and then provide some discussion about the consequences of these new observations.

2. – Observations

Northern Chile is an active seismic zone that is sometimes considered to be an active seismic gap by many authors [26, 28]. Since 2005 a large set of multi-parameter stations were deployed by the Integrated Plate Boundary Observatory Chile (IPOC), a multi-component network deployed by German, French and Chilean researchers starting from 2006. After 2013 a new network of multi-parameter instruments was deployed by CSN (Centro Sismologico Nacional of the University of Chile). Since then, northern Chile earthquakes have been well recorded by GNSS, broad band and strong motion stations mostly located on hard rock sites [24, 25, 5]. The first mayor earthquake that occurred after the installation of IPOC was the M_{w} 7.7 Tocopilla earthquake of 2007 [13, 32, 16]. [21] studied the spectral characteristics of this event and its aftershocks. They found that aftershocks had a typical omega-squared Fourier displacement spectrum [1, 11, 27]. The main-shock, on the other hand, was very different since its displacement spectrum diverged at low frequencies, increasing like omega to the power -1. They proposed that this behavior could be due to the presence of near-field waves, but that it could also be due to the complexity of this double event. The lack of near-field GNSS instruments did not permit us to resolve the low-frequency properties of the displacement spectrum in order to distinguish between these two hypotheses.

The large 2010 M_{w} 8.8, Maule mega-thrust earthquake produced excellent continuous GNSS records that were used by [41] as seismograms to model the rupture process of the event. Unfortunately no digital good-quality accelerometers were located close to the epicenter of the Maule 2010 earthquake [34]. After this event the Centro Sismologico National (CSN) of the University of Chile was created and deployed a large network of broad-band, accelerometers and GNSS stations [6, 24, 25, 5]. These stations have recorded several large earthquakes including the M_{w} 8.2 Iquique event of 1 April 2014, the M_{w} 8.3 Illapel earthquake of 15 September 2015 and the M_{w} 7.6 Chiloé earthquake of 25 December 2016. These events provide excellent recordings that have been largely used to model the events and to study their principal characteristics (*e.g.* [35, 38, 17, 20, 29, 43, 36, 30, 22]). These studies have been centered on the slip distribution, tsunami effects, nucleation process and their relation with slow-slip events, but did not mention the spectral properties of strong-motion records in the near field. Here we examine the general properties of these accelerograms. We use the records written by the Iquique earthquake of 1 April 2014 and the Valparaiso earthquake of 24 April 2017 because these events have a large number of co-located GNNS and strong-motion records on hard-rock sites [25, 24, 5]. Our goal is to understand the basic features of seismic spectra,

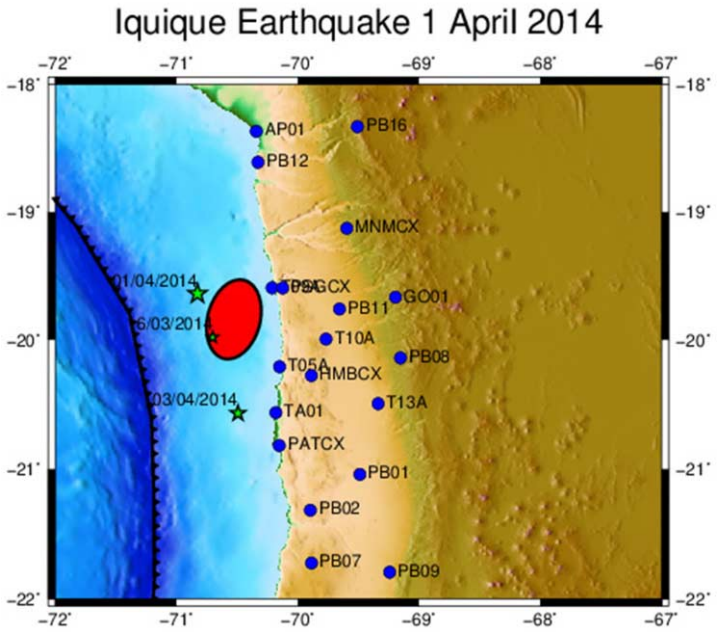

Fig. 1. – Northern Chile area hit by the $M_w = 8.1$ Iquique earthquake of 1 April 2014. The rupture area of the main event is outlined by the red ellipse (from [35]). White stars show the epicenters of the main shock as well as its main aftershock of 3 April 2014 and the 16 March 2014 foreshock. The events are situated between the trench and the Chilean coast line along the plate interface. The main stations used in the present study are shown with blue circles.

the relative role of low and high frequencies of the spectrum and their relation with the seismic moment and seismic moment rate histories.

In the following we use the ground motion records obtained during the Iquique earthquake of 1 April 2014 in Northern Chile. This event was very well recorded by stations from the IPOC network and by several accelerometers of the new network deployed by the CSN. The 2014 event was a complex event that had a small immediate precursor and a massive slip located between the foreshock and the mainland (see, *e.g.* [35, 15]). As shown in fig. 1, more than 50 records are available for this event, of which many co-located GNSS and accelerograms could be used. We will illustrate data processing using these recordings.

Accelerograms are difficult to integrate to displacement as discussed by [8] who proposed a method to integrate them taking into account changes in the average ground velocity before and after the event. Variations of this technique have been proposed by other authors [8, 18, 42, 9, 12]. Using time domain integration of accelerograms we verified that we could fit the low-frequency features observed in the GNSS records. Several examples of the fit between GNSS recordings and integrated accelerograms in Chile were recently published by [5]. The accelerograms studied here are relatively weak since none of them has a peak ground acceleration (PGA) greater than the 20% of g.

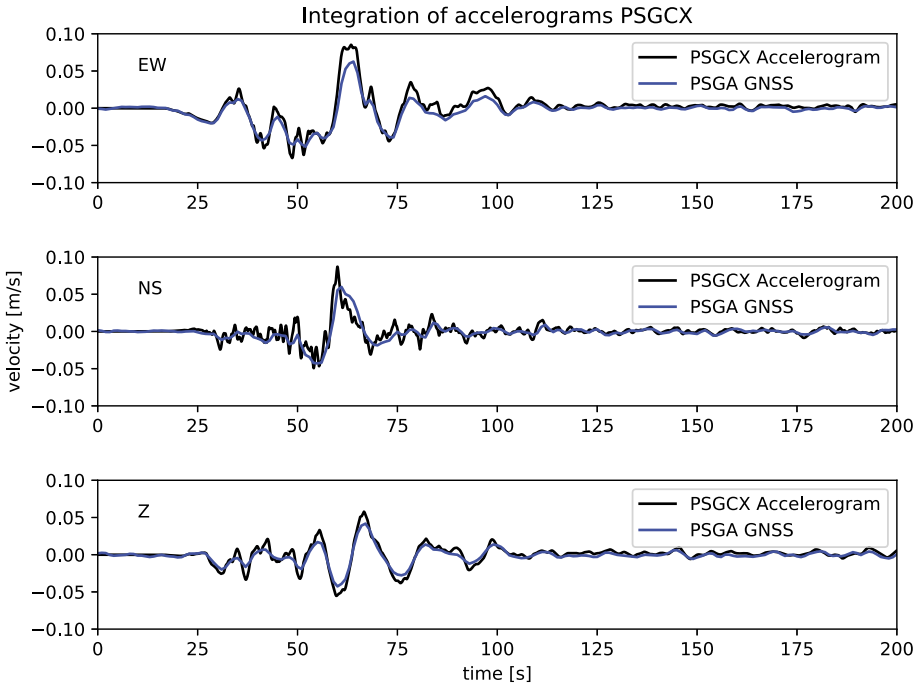

Fig. 2. – Ground velocity at the Pisagua stations computed from GNSS records (PSGA) and co-located integrated accelerogram (PSGCX). The velocity records computed from accelerograms have been low-pass filtered at 0.5 Hz in order to enhance the similarity between GNSS and ground velocity records in their common band pass.

Digital displacement records whether obtained from GNSS records or by integration of accelerograms cannot be used directly to compute displacement spectra because the finite displacement jumps at the end of the record. The reason is that the finite discrete Fourier transform used to compute the spectra records assumes that the time series is periodic with a period equal to the duration of the record. Thus the Fourier transform sees a jump in displacement at the end of the record that contaminates the computed spectrum at all frequencies. The Fourier transform of such a jump is simply the static displacement divided by frequency. All the other spectral information contained in the accelerogram is hidden by this jump. Many techniques have been proposed in the literature to remove this effect of the finite time window. Some of them consist in using a window to multiply the time signal, but these windows contaminate the low-frequency contents.

We propose a simple method to compute the displacement spectrum that uses a property of the velocity time series. The accelerograms integrated once to determine the ground velocity have been shown to be very well fit at low frequencies by the ground velocity derived from GNSS signals (*e.g.* [7, 42, 5]). Figure 2 shows the three components of the ground velocity integrated from accelerograms at the PSGCX station, and the velocities derived from the nearby PSGA GNSS recordings. The instrument response

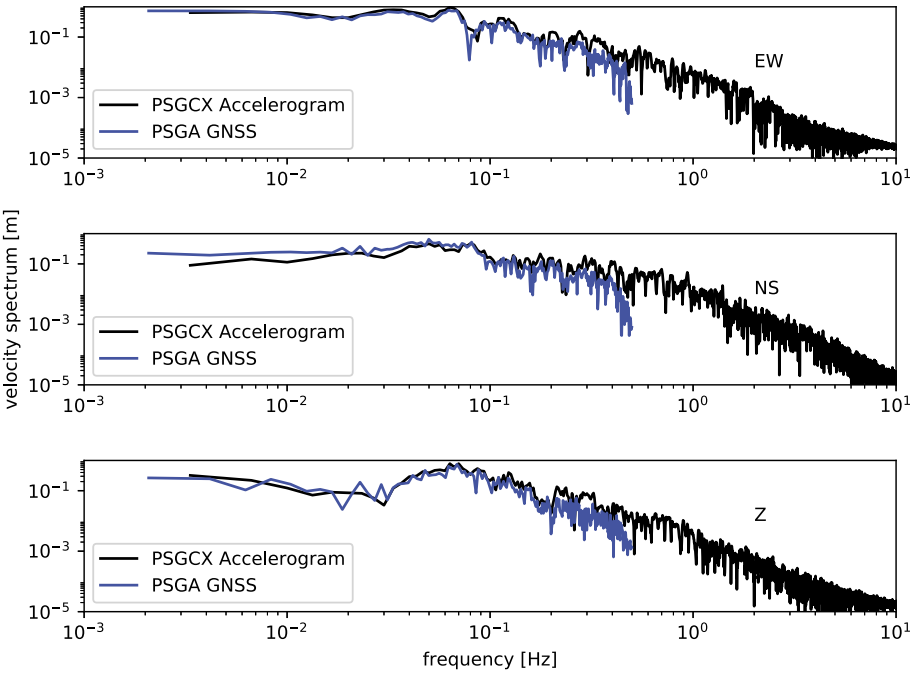

Fig. 3. – Spectra of the ground velocity computed from PSGA GNSS station and the PSGCX accelerogram. The corresponding time domain signals are shown in fig. 2. We observe that at low frequencies the accelerogram and GNSS instrument share an almost identical spectrum in spite of the different noise levels in these two types of instrument. All three components have almost flat spectra at low frequencies whose level is the co-seismic displacement at this site.

of the accelerograms was removed, and the records were low-pass filtered with a causal Butterworth filter of order 2 and corner frequency 0.5 Hz. The coincidence between the records is excellent. This representation is better than comparisons between displacement records to show that the frequency content of the two records is the same in the frequency range where they both coincide (conservatively estimated as above 0.15 Hz).

In fig. 3 we show the Fourier spectra of the velocity traces at stations PGA and PSGCX plotted in fig. 2. Since velocity returns to zero at the end of traces, except for seismic noise, we can compute the velocity spectrum without the problems of the finite displacement at the end of the time window discussed earlier. The spectra computed using regular FFT routines display a common property of ground velocity for large subduction earthquakes in Chile. The spectral trend is flat at low frequencies in contrast to predictions of far-field velocity radiation for finite sources [11,27] that it should linearly increase with fequency at low frequencies. A more detailed explanation will be provided in next section, but it is relatively easy to understand. At close distances from the source the near-field terms of the Green function dominate the radiated spectrum. The near field is dominated by the moment time function, not the moment rate, so that at close

distances the velocity spectrum at low frequencies resembles that of the integral of the far field source-time function.

3. – Theory

Computing the full field radiated by a finite seismic source embedded in a heterogeneous earth model is difficult and can only be done numerically for certain models of structure. For example, for layered media it is possible to compute the full field using spectral integration methods like Axitra [10]. Because we want to gain intuition on the properties of the field we will study here the simplest situation of a point double couple source embedded in a homogeneous elastic space.

3˙1. *Near field from a point source in an infinite medium.* – The Green's function for a point moment tensor source inside an infinite elastic medium can be written [2] as

$$
\begin{aligned}
u(r,t) = {} & \frac{1}{4\pi\rho}\frac{1}{r^4}A^N \int_{r/\alpha}^{r/\beta} \tau M_0(t-\tau)\mathrm{d}\tau \\
& + \frac{1}{4\pi\rho\alpha^2}\frac{1}{r^2}A^{IP} M_0(t-r/\alpha) + \frac{1}{4\pi\rho\beta^2}\frac{1}{r^2}A^{IS} M_0(t-r/\beta) \\
& + \frac{1}{4\pi\rho\alpha^3}\frac{1}{r}A^{FP} \dot{M}_0(t-r/\alpha) + \frac{1}{4\pi\rho\beta^3}\frac{1}{r}A^{FS} \dot{M}_0(t-r/\beta).
\end{aligned} \tag{1}
$$

This expression is usually interpreted as if the near field contained two terms: one called the near field inversely proportional to r^{-4}, and the other called intermediate field that decays like r^{-2}. Actually the first term decays in fact as r^{-2} because the integral on the first line of (1) grows with distance as r^2. In this expression the coefficients $A^N, A^{IP}, A^{IS}, A^{FP,}$ and A^{FS} are the radiation patterns. $M_0(t)$ is the moment tensor time history and $\dot{M}_0(t)$ is the moment rate time function. Thus the near field is proportional to moment, while the far field is proportional to moment rate. The time domain expression (1) is difficult to separate into P and S waves because the near-field term (the integral) can be only be split into two diverging integrals that cancel each other for times greater than the arrival time of the S-wave.

For this reason we prefer to use the frequency domain expression. We use the following definition of the Fourier transform:

$$
\tilde{f}(\omega) = \int_{-\infty}^{\infty} f(t) e^{-i\omega t}, \tag{2}
$$

which has different sign in the exponential from that adopted by [2].

The time domain Green function (1) can be transformed into

$$(3)\quad u(\tilde{r},\omega) = \frac{M_0(\omega)}{r^2}\left[\frac{1}{4\pi\rho\alpha^2}F^{INP}(\omega r/\alpha)e^{-i\omega r/\alpha} + \frac{1}{4\pi\rho\beta^2}F^{INS}(\omega r/\beta)e^{-i\omega r/\beta}\right] + \frac{\dot{M}_0(\omega)}{r}\left[\frac{1}{4\pi\rho\alpha^3}A^{FP}(\omega r/\alpha)e^{-i\omega r/\alpha} + \frac{1}{4\pi\rho\beta^3}A^{FS}(\omega r/\beta)e^{-i\omega r/\beta}\right],$$

where the coefficients F^{INP}, and F^{INS} are

$$F^{NP}(\omega r/\alpha) = A^N\frac{\alpha^2}{\omega^2 r^2}\left(\frac{i\omega r}{\alpha}+1\right) + A^{IP}$$

and

$$F^{NS}(\omega r/\beta) = -A^N\frac{\beta^2}{\omega^2 r^2}\left(\frac{i\omega r}{\beta}+1\right) + A^{IS},$$

these are self-similar functions of the non-dimensional frequency times distance divided by elastic wave speed. The near and intermediate field radiation patterns A^N, A^{IP}, A^{IS} are defined in [2].

The frequency domain Green function clearly states that there are two types of terms in the radiated elastic field: Near-field terms that are proportional to the moment time function $M_0(\omega)$ and decay like r^{-2}; and far-field terms that are proportional to the moment rate $\dot{M}_0(\omega)$ and decay like r^{-1}. What is not clear from these expressions is at which distance range the near and far field dominate. There is a clear transition for each type of wave depending on the non-dimensional term $\omega r/\alpha$ for P-waves and $\omega r/\beta$ for S-waves. The near-field terms in (3) interfere strongly so that at large distances the time difference between the arrival time of P and S waves plays an important role.

For the moment we study separately the P and S waves in order to gain some understanding of the relative role of the near and far field terms.

3˙2. *A simplified model.* – Dealing with the whole expression in (1) or (3) is not very practical to understand the relative roles of the near- and far-field terms in the Green function. We adopt an approximation in which we neglect the frequency-dependent term in the coefficients F. This approximation was used by [40] in the study of the near field of the deep Peruvian earthquake of 1994 observed by stations located above the source. Here we approximate the S-wave by the following expression in the frequency domain:

$$(4)\qquad u^S(r,\omega) = \frac{C^{NF}}{r^2}M_0(\omega) + \frac{C^{FF}}{r}\dot{M}_0(\omega),$$

where C^{NF} represents the near-field radiation pattern and normalization; and C^{FF} is the normalized far-field radiation pattern. This expression shows that the spectrum contains terms proportional to the moment and moment rate spectra. In the far field only the

last terms are usually considered. The limit at low frequencies of this expression tends to

$$\lim_{\omega \dashrightarrow 0} u^S(r,\omega) = C^{NF} M_0(\omega) = C^{NF} \frac{M_0}{i\omega}\,. \tag{5}$$

Thus the near-field spectrum is dominated by the seismic moment divided by $i\omega$. so that the low frequency displacement spectrum is dominated by the omega -1 asymptote.

An even more interesting relationship is that the Fourier spectrum of the ground velocity can be derived as

$$\lim_{\omega \dashrightarrow 0} \dot{u}^S(r,\omega) = C^{NF} M_o = u(r,0). \tag{6}$$

Thus the Fourier velocity spectrum of the ground velocity tends to be flat at low frequencies and its amplitude is a measure of the static ground displacement. Expression (6) was derived here for the approximation (4), but it is a compltely general property of ground velocity spectra, whether the source is in an infinite or a heterogeneous medium. This expression should facilitate the computation of the static ground displacement once ground velocity has been computed without the need of the inaccurate double integration of the accelerograms.

Let us now compute the spectrum expected at stations where the near field is important. For that purpose we adopt Brune's far-field radiation model. The source time function for this model is

$$\dot{M}_0(t) = M_0 \omega_0^2 t\, e^{-\omega_0 t} H(t), \tag{7}$$

where ω_0 is the corner frequency of the signal. Its spectrum is well known:

$$\dot{M}_0(\omega) = M_0 \frac{\omega_0^2}{(\omega_0 + i\omega)^2}\,. \tag{8}$$

At low frequencies the moment rate spectrum tends to M_0 the static moment of the source. Any other source time function may be used but in most applications Brune's model (8) is most often used.

The moment time history for this signal is rather complicated to write but very simple:

$$M_0(t) = M_0 \left[1 - (1 + \omega_0 t)\, e^{-\omega_0 t}\right] H(t). \tag{9}$$

The spectrum of the moment time function is just (8) divided by $i\omega$.

In fig. 4 we show the expected near-field record of diplacement that contains both near and far-field terms. The corner frequency has been chosen as $f_0 = 0.637$ and the corresponding circular frequency is $\omega_0 = 2\pi f_0 \sim 4$ and a ratio $C = C^{NF}/(rC^{FF}) = 1$. This produces a near-field signal that is very similar to those observed by dynamic GPS records, or doubly integrated from accelerograms. In fig. 5 we plot the near-field spectrum

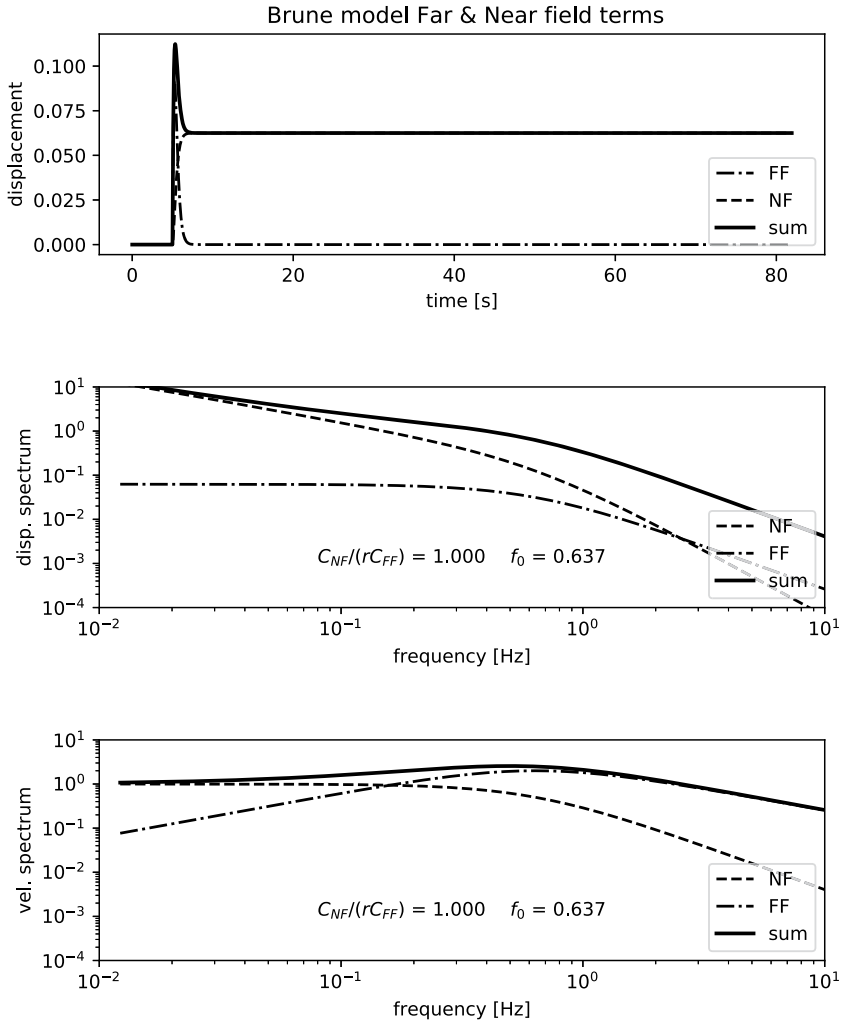

Fig. 4. – Near-field record and spectrum when the near-field term is large compared to the far field source time function. Here the coefficient in (4) is $C^{NF}/(r * C^{FF}) = 1$.

and displacement time signal for the same corner frequency and a ratio $C = 0.25$. We observe that the near field is now small so that the peak of the far-field velocity spectrum starts to emerge. The displacement spectrum, on the other hand, starts to be similar to the far-field spectrum of the Brune model.

4. – The 1 April 2014 Iquique earthquake

On 1 April 2014 a magnitude M_{w} 8.2 hit the Northern Chile region of Tarapacá near the cities of Iquique and Pisagua. Two days later the largest aftershock with magnitude

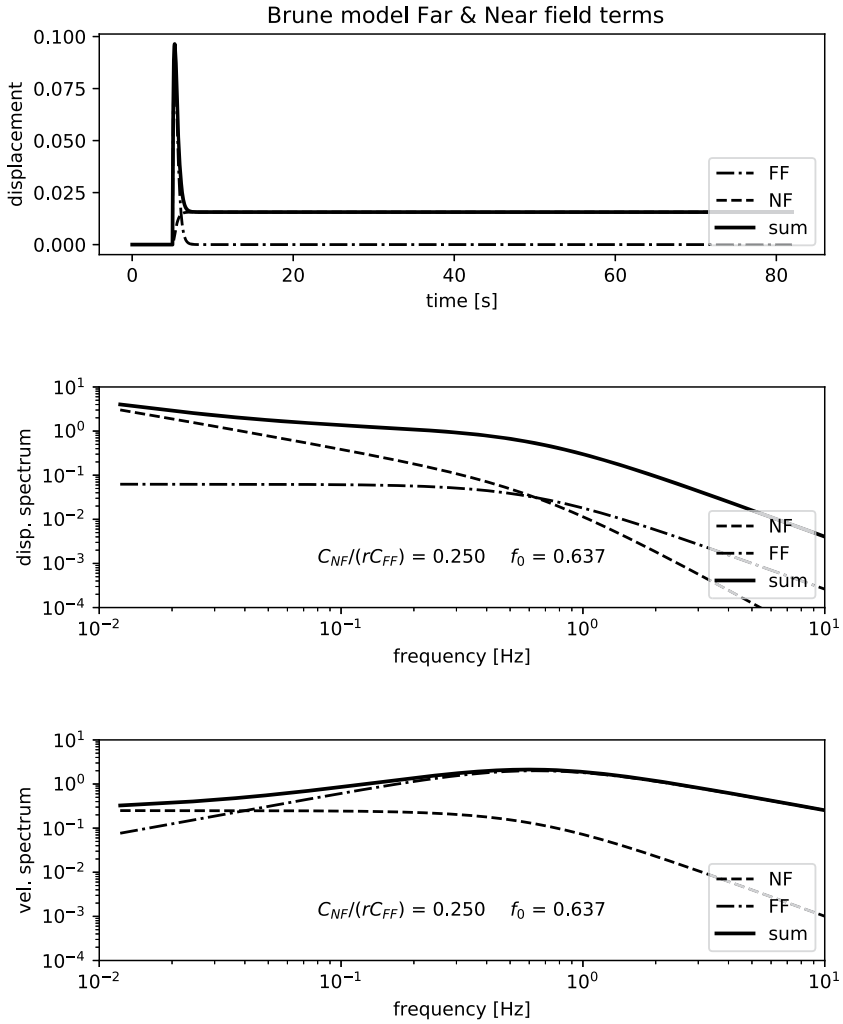

Fig. 5. – Near-field record and spectrum when the near-field term is large compared to the far-field source time function. Here the coefficient in (4) is $C/r * C^{FF} = 0.25$.

M_w 7.7 occurred (see fig. 1) [35,38,20,15]. This event has been studied by many authors, specially because it was preceded by a long series of precursory shocks that began several years before 2014 and culminated in an intense, but intermittent series of fore-shocks that started in July 2013 [23]. A slow-slip event was observed before the main shock that has been carefully documented [35, 19, 39]. The main event was studied by a number of researchers using a combination of far- and near-field data that were reviewed by [15].

In the previous section we studied the recordings at the PSGCX co-located with the PSGA GNSS instrument in Northern Chile near the town of Pisagua. This is the closest station to the earthquake epicenter as shown in fig. 1. The velocity records derived from

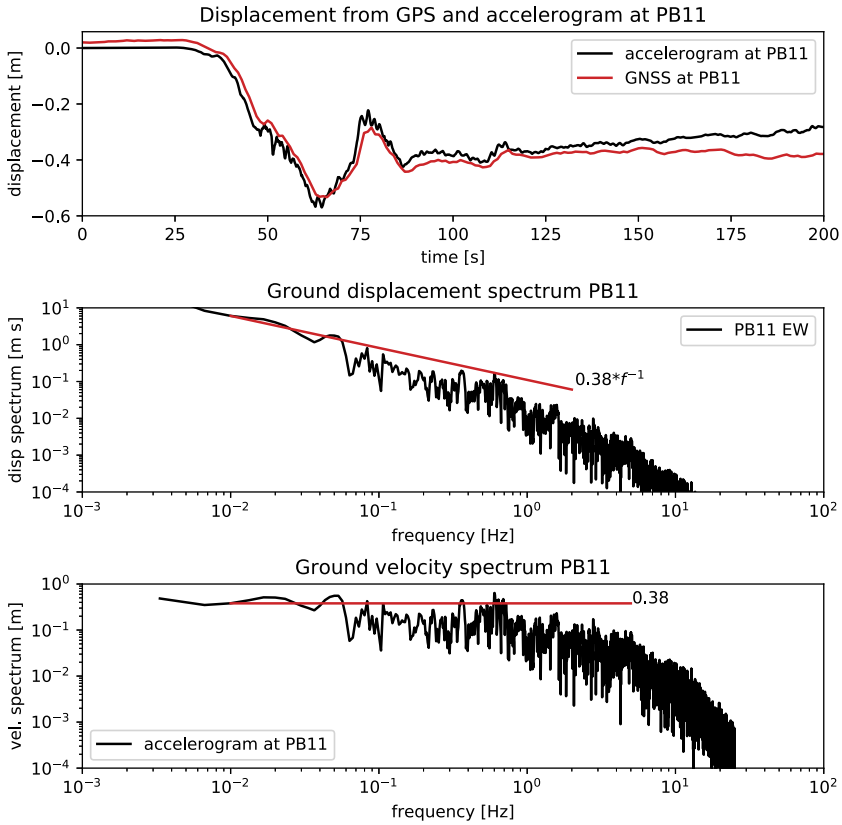

Fig. 6. – EW component of displacement integrated from the accelerogram of the PB11 station located 119 km from the epicenter of the 1 April 2014 Iquique earthquake of M_w 8.1. At the top the displacement waveform computed by integrating the accelerogram is compared with the displacement recorded by the co-located GNSS station. At the bottom, the displacement and velocity spectra computed from the accelerogram. Thei amplitude of the flat portion of the velocity spectrum agrees very well with the displacement jump of 0.38 m observed in the GNSS record.

GNSS instruments and accelerometers are essentially identical in the common frequency band of the two records (figs. 2 and 3). At this short distance the seismic moment-dependent terms in the Green function, first term in (3), dominate the spectrum. As shown in fig. 1 more than 20 stations recorded this event in the near field. Of these, we chose the records furnished by the PB11 station which is situated some 60 km inland from Pisagua and 119 km from the immediate fore-shock of the earthquake. Figure 6 shows the EW component of displacement at this station using the Boore [8] procedure discussed earlier. Superimposed on the seismic displacement trace we plot the ground displacement recorded by GNSS instrument at the PB11 IPOC multi-parametric station. The traces for both the integrated accelerogram and the geodetic data are very similar

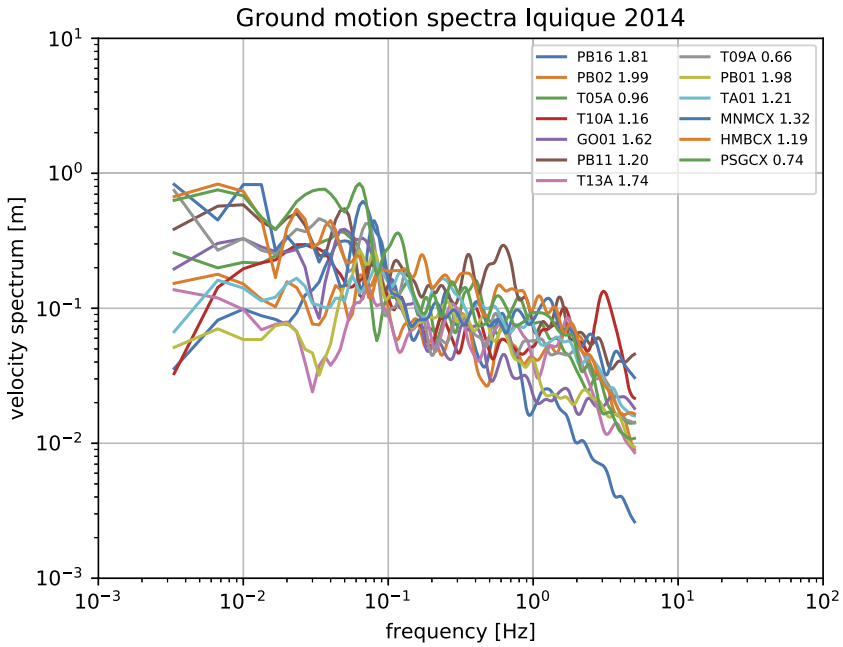

Fig. 7. – Stack of velocity spectra for 14 accelerograms that recorded the 1 April 2014 Iquique earthquake. These spectra were computed by standard Fourier transform of the ground velcoity records obtained by direct integration of accelerograms. Accelerograms were corrected by the instrument response and a removal of the mean acceleration.

and have a large static component. It is obvious that in this station the field is dominated by the moment time-function. In the two bottom panels of fig. 6 we show the ground displacement and velocity spectra computed from the accelerogram spectrum by double Fourier integration (division by omega squared). The displacement spectrum shows the characteristic omega −1 decay expected at low frequency. The velocity spectrum at the bottom has the typical flat spectrum observed for many large subduction earthquakes in Chile. The level of the flat part of the velocity spectrum is very close to the static displacement observed in the GNSS instrument trace (GPS) at the top of fig. 6, confirming relation (6) derived earlier.

In fig. 7 we show a stack of the ground velocity spectra computed for the EW component of 14 accelerograms that recorded the Iquique main shock at distances varying from 80 to 250 km. Although amplitudes are quite variable the shape of the spectra are very similar with a flat low frequency asymptote, a peak near 0.08 Hz (12.5 s) and an omega −1 decay in the frequency range from 1 to 10 Hz.

5. – The 24 April 2017 Valparaiso earthquake

An important subduction earthquake occurred near Valparaiso in the center of Chile on 24 April 2017. This event of M_w 6.9 was preceded by a strong fore-shock activity

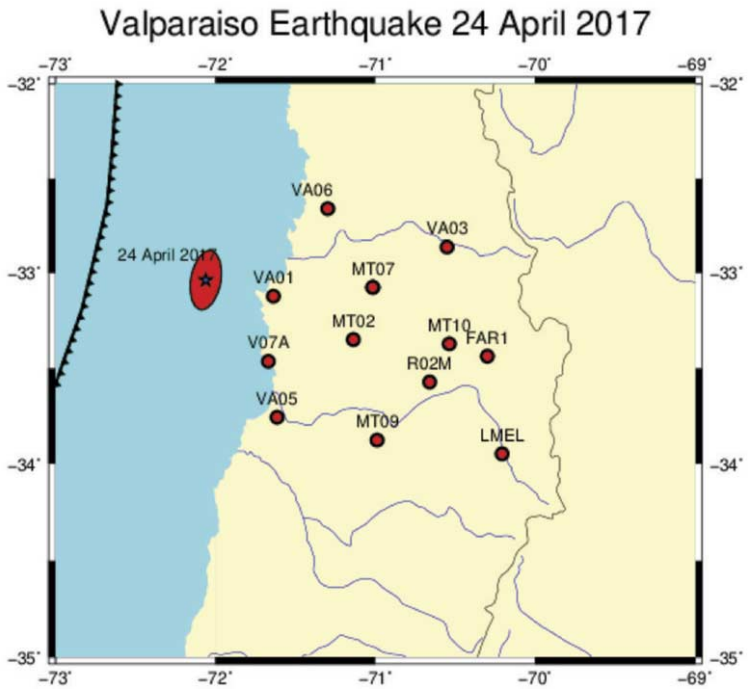

Fig. 8. – Valparaiso earthquake of 24 April 2017. The epicenter of this $M_w = 6.9$ earthquake is indicated by the blue star. The red circles denote the accelerometers used in the present work. The red ellipse over the hypocenter is the main rupture area as determined by dynamic inversion by [36].

that included large events on 22 April 2004 and was preceded by an immediate slow-slip event. The earthquake itself occurred very close to the site of the large M_w 8.0 earthquake in Valparaiso of 3 March 1995. The Valparaiso event was very well recorded by a number of seismic stations from the CSN network. Due to its relatively moderate size it was only recorded by the GNSS sites located very close to the coast. This event was the object of several studies [36, 37, 17]. The area where the Valparaiso earthquake occurred is particularly interesting because it was the site of one of the largest subduction earthquakes in the history of Chile, the 8 July 1730 earthquake. More recently Valparaiso was hit by several earthquakes of magnitude close to 8: 1821, 1906, 21 July 1971, 3 March 1985 and several others.

In fig. 8 we show the location of the earthquake and the set of accelerograms that recorded the event. There are many more than these of course but we did not used them in our study.

5˙1. *Observations of the Valparaiso earthquake.* – The closest stations to the Valparaiso earthquake were two neighboring stations in Valparaiso city. These were the VALN high-rate GNSS site and the VA01 accelerometer of the CSN National network shown in fig. 9.

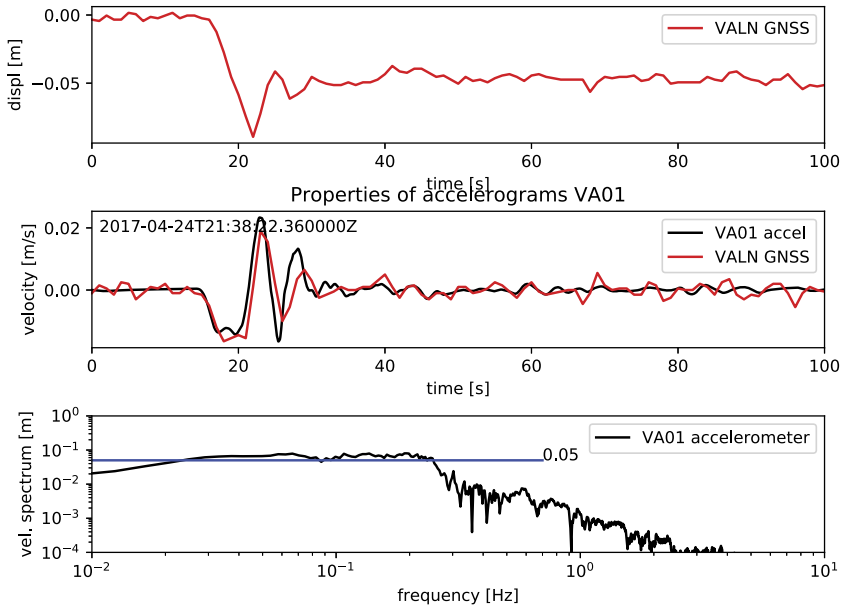

Fig. 9. – Observation of the Valparaiso earthquake of 24 April 2017 at the VALN GNSS station and the neighboring accelerogram at the VA01 CSN site. At the top we show the EW displacement observed by the VALN GPS. The static jump is 0.05 m westwards. The central panel shows the EW ground velocity signal computed from the VA01 acceleorgram and the GNSS record shown in the first panel. The last panel shows the spectrum of ground velocity computed from the accelerogram at VA01. The long plateau of the ground velocity spectrum has an amplitude that is just the static jump observed at the VALN GNSS record.

The records show all the usual properties discussed in the present work. We observe for instance that the VALN site moved about 5 cm to the West during the earthquake. The second panel in fig. 9 shows the comparison between the ground velocity obtained from the GNSS record by differentiation and from the VA01 accelerogram integrated once to velocity. No special processing was applied to the accelerogram except the removal of the instrument response that ony affects high frequencies, and the removal of the mean. Detrending the record would perturb the ground velocity computed by integration at this station. In the bottom panel of fig. 9, we present the ground velocity spectrum at station VA01 computed by classical FFT from the velocity trace integrated from the accelerogram. We observe clearly the flat low-frequency spectrum predicted by the theory discussed in previous sections. We also observe that the level of the velocity spectrum is 0.05 m (5 cm) as observed by the static displacement recorded by the VALN.

As we move away from the coast the GNSS records cannot be used to determine static ground displacement because noise dominates the records. Thus we have to use the accelerometers to try to understand the properties of the near earthquake spectrum. In fig. 10 we show a profile of 5 representative velocity records observed at a subset of the sites shown in fig. 8. Although the profiles are located inland they were not recorded

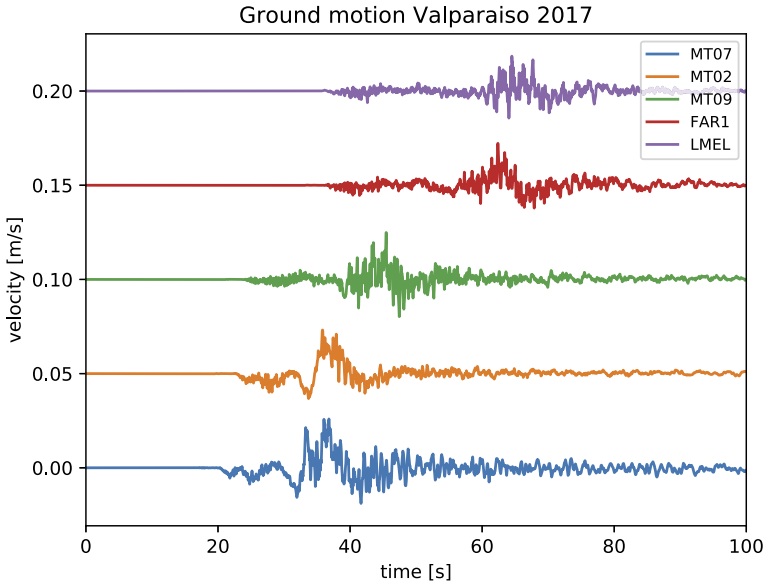

Fig. 10. – Stack of ground velocity records. These velocity signal were integarted from the accelerograms recorded five stations of the central Chile accelerometric network. The traces have been displaced by 0.05 m/s in order to appreciate the propagation of the velocity wave functions across the network.

along a line so that we cannot observe relative propagation of certain P- or S-wave phases. We have many more records but we reduced the number of records to avoid clutter. The figure shows that it is possible to study this event thanks to the velocity records that clearly show the P- and S-wave arrivals as well as a double P- and S-wave waveform. This is related to a small precursor of the 14 April 2017 earthquake that can be identified in some of the accelerograms close to the coast. The precursor occurred roughly by 5 s before the main onset. The double waveform is also observed in the VA01 GNSS record shown in fig. 9, central panel. We have not fully explored the records but there is a clear crustal phase between the P- and S-wave in the FAR1 and LMEL records at about 50 s.

Finally in fig. 11 we show a stack of the spectra of the ground velocity section shown in fig. 10. The records have not been corrected by any distance move-out, these are the raw spectra. The spectra have been smoothed at high frequencies so as to show the main features of the spectra. The similarity between the records is striking. All of them contain a peak near 0.05 to 0.1 Hz (20 to 10 s period) that is clearly related to the duration of the S-wave in the velocity records of fig. 10. For frequencies higher than this characteristic (corner) frequency we observe a decay as omega -1 predicted by the Aki Brune ground velocity spectrum (this is equivalent to the omega -2 decay in displacement). For frequencies lower than the peak in fig. 11 (frequencies below 0.05 Hz) we observe the development of the velocity plateau. This plateau is clearly related to the distance of the stations from the source.

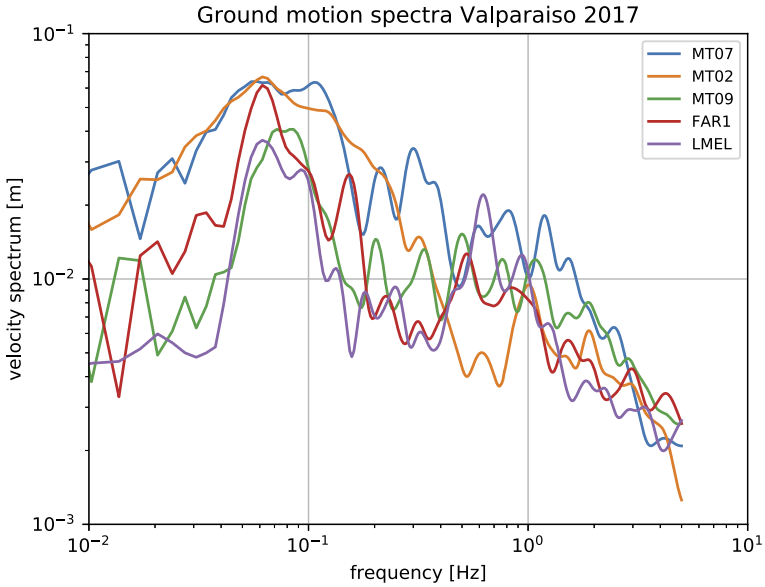

Fig. 11. – Stack of ground velocity spectra observed at the EW components of five accelerometric stations of the Central Chile network of the National seismological Center (CSN).

Finally let us consider the transition to a Brune (far field) like behavior. Station LMEL situated nearly 194 km from the source is sufficiently far although some effect of the near-field terms are still observed in the spectral stack of fig. 11. In fig. 12 we show at the top the EW velocity record at station LMEL obtained by the standard integration of the accelerogram records. The station is sufficiently far from the source of the earthquake because the S-P time (about 20 s) is longer than the duration of the source (about 10 s). The black line is the original EW velocity trace at LMEL, while the red trace is the S-wave windowed by a simple Kaiser window with Beta=6. The two traces coincide well around the S-wave and they have the maximum velocities in the record. In the central panel of fig. 12 we plot the displacement record integrated directly from the first trace, both for the entire record (black) and the windowed S-wave (red). We observe that as expected at far distances from the source the seismic record contains essentially the far field terms, because the near field has become much weaker in this distant stations. In fig. 12 we show exactly that. It is interesting to note however that the velocity spectrum for the window is nearly flat for frequencies higher than 10 Hz, while the full record (black line) increases up to 0.1 Hz. The origin of this difference is the persistence of near-field terms arriving between the P and S wave even at 194 km from the source.

6. – Discussion

It is curious that the observation of near-field terms in the radiation from large earthquakes seems not to have been previously reported. The main reason seems to be that

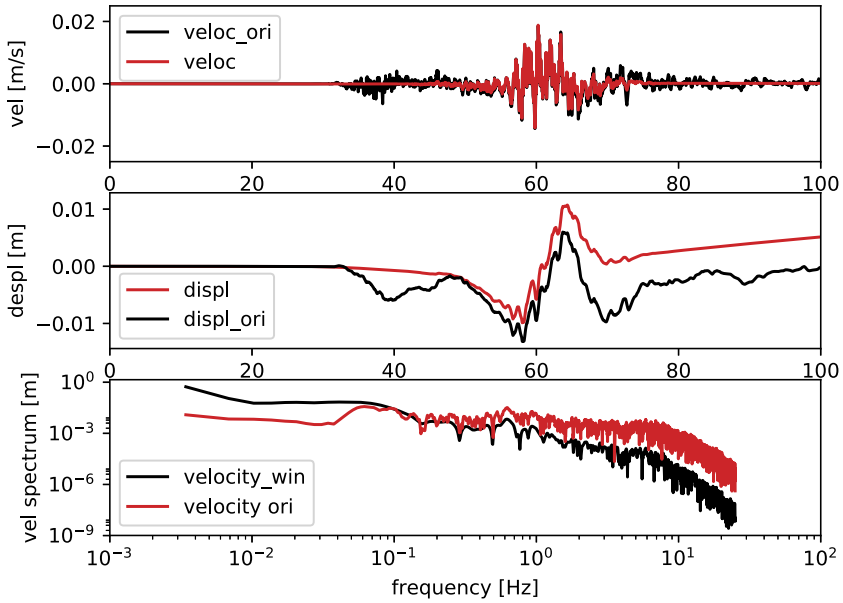

Fig. 12. – Transition to a Brune-like spectral behavior. Station LMEL is the furthest accelerogram available for this event. The top panel shows the ground velocity at MEL integrated from the original accelerogram in black and the windowed record in red. The next panel shows the integrated dispalcement at the same station. Finally, the lower panel shows the velocity spectrum computed by Fourier transform of the top panel.

low frequencies were systematically removed because they are considered inaccurate due to the problem with recovering the static component from near-field accelerograms. This is of course a serious problem that has to be resolved if possible. For the last 20 years, however, low frequency information about seismic source is available from continuous GNSS recordings (see [5] and references therein). The simultaneously recording of GNSS and accelerograms can produce a very broad-range version of the ground motion spectrum that can be used for modeling large seismic events without separating the static (GPS) from the dynamic (usually band limited ground displacements). In the present lecture we examine ground velocity spectra. For most earthquakes in Chile, and probably elsewhere, ground velocity integrated from accelerograms can be compared with GNSS records filtered in a common band. These records agree very well, giving confidence that the velocity field has been recorded over a very broad band. We have shown that here for the great 2014 earthquake in Iquique in Northern Chile and for the Valparaiso $M_{\rm w}$ 6.9 earthquake of 24 April 2017. The most important observation made here is that the near-field term contributes significantly to ground motion in a very large region where even if P and S waves are separated, the spectrum computed by classical methods contain large contributions of the so-called omega -1 in displacement, or a large flat plateau in ground velocity spectrum. This plateau has an spectral level roughly equal to the

static displacement produced at the observation site by the earthquake. This property has to be verified and tested for many other earthquakes. The main application is determining approximate ground displacements from the Fourier transform of ground velocity. More important perhaps, is that this observation provides a simple way to scale ground velocity spectra that in turn controls the more usual measurements made by engineers and seismologists (PGV and PGA, for instance).

We have purposefully kept the theoretical modeling at its simplest, making an attempt to show the most salient features of seismic radiation in the near field. This feature is that near-field terms are proportional to the moment time function, that is a unipolar function that grows continuously from zero to the static displacement level. This property is largely used in many studies of seismic moment, for instance in the determination of centroid and amplitude of the source time function. The full consequences of this relationship between ground velocity spectrum and static displacement will need further studies because it is independent of the elastic medium in which the waves propagate, but it depends heavily on the distance traveled by the seismic waves and, in particular on the P-S travel time. A careful study of this problem is required.

One of the features that we have observed for the 24 April 2017 Valparaiso earthquake is the detachment of P and S waves at high frequencies at stations located far from the source (more than 150 km). The spectrum of the windowed shear wave and that of the full record are very similar. This indicates that S waves dominate the spectrum and carry all information about the source in the transition region from near field to far field. It would be nice to have a simple expression that defines the boundary between near and far field dominated regions. Unfortunately this is not simple because propagation in the structure between the source and the accelerometers must be properly modelled and taken into account. That will require much further work.

7. – Conclusions

Using co-located GNSS and accelerograms we have found that ground velocity time and spectral signals from these two kinds of instruments coincide largely in their common frequency band, roughly from 0.01 to 0.5 Hz. We observe that the spectrum of ground motion in the vicinity of large subduction earthquakes is quite different from the classical Aki-Brune far-field spectrum, The reason is that over a large area surrounding the source the near-field terms in the Green's function are large and dominate the spectrum. The most important feature is that the ground velocity spectrum has a long flat spectral plateau with amplitude proportional to the static displacement at the recording site. The properties of this plateau are independent of the medium in which the elastic waves propagate and, we believe, should be further studied for other events.

* * *

This study was supported by FONDECYT contract N° 1170430 and by PRS (Programa Riesgo Sísmico of Universidad de Chile).

REFERENCES

[1] AKI K., *J. Geophys. Res.*, **73** (1967) 5359.
[2] AKI K. and RICHARDS P. G., *Quantitative seismology* (University Science Books, Sausalito) 2002, ISBN 0-935702-96-2.
[3] ALLMANN B. P. and SHEARER P. M., *J. Geophys. Res.*, **114** (2009) B01310.
[4] ARCHULETA R. J. and JI C., *Geophys. Res. Lett.*, **43** (2016) 12004.
[5] BAEZ J. C., LEYTON F., TRONCOSO C., DEL CAMPO F., BEVIS M., VIGNY C., MORENO M., SIMONS M., KENDRICK E., PARRA H. and BLUME F., *Seismol. Res. Lett.*, **89** (2018) 1546.
[6] BARRIENTOS S. and NATIONAL SEISMOLOGICAL CENTER TEAM, *Seismol. Res. Lett.*, **89** (2018) 467.
[7] BOCK Y., MELGAR D. and CROWELL B. W., *Bull. Seismol. Soc. Am.*, **101** (2011) 2904.
[8] BOORE D. M., *Bull. Seismol. Soc. Am.*, **91** (2001) 1199.
[9] BOORE D. M. and BOMMER J. J., *Soil Dyn. Eq. Eng.*, **25** (2005) 93.
[10] BOUCHON M., *Bull. Seismol. Soc. Am.*, **71** (1981) 959.
[11] BRUNE J., *J. Geophys. Res.*, **75** (1970) 4997.
[12] CHAO W., WU Y. and ZHAO L., *J. Seismol.*, **14** (2009) 495.
[13] DELOUIS B., PARDO M., LEGRAND D. and MONFRET T., *Bull. Seismol. Soc. Am.*, **99** (2009) 87.
[14] DENOLLE M. A. and SHEARER P. M., *J. Geophys. Res.*, **121** (2016) 6533.
[15] DUPUTEL Z., JIANG J., JOLIVET R., SIMONS M., RIVERA L., AMPUERO J. P., RIEL B., OWEN S. E., MOORE A. W., SAMSONOV S. V. and ORTEGA CULACIATI F., *Geophys. Res. Lett.*, **42** (2015) 7949.
[16] FUENZALIDA A., SCHURR B., LANCIERI M. and MADARIAGA R., *Geophys. J. Int.*, **194** (2013) 1216.
[17] HAYES G. P., HERMAN M. W., BARNHART W. D., FURLONG K. P., RIQUELME S., BENZ H. M., BERGMAN E., BARRIENTOS S., EARLE P. S. and SAMSONOV S., *Nature*, **512** (2014) 295.
[18] IWAN W., MOSER M. and PENG C., *Bull. Seismol. Soc. Am.*, **75** (1985) 1225.
[19] KATO A. and NAKAGAWA S., *Geophys. Res. Lett.*, **41** (2014) 5420.
[20] LAY T., YUE H., BRODSKY E. E. and AN C., *Geophys. Res. Lett.*, **41** (2014) 3818.
[21] LANCIERI M., MADARIAGA R. and BONILLA F., *Geophys. J. Int.*, **188** (2012) 469.
[22] LANGE D., RUIZ J., CARRASCO S. and MANRÍQUEZ P., *Geophys. J. Int.*, **213** (2017) 210.
[23] LEON-RIOS S., RUIZ S., MAKSYMOWICZ A., LEYTON F., FUENZALIZADA A. and MADARIAGA R., *J. Seismol.*, **20** (2016) 1059.
[24] LEYTON F., LEOPOLD A., HURTADO G., PASTEN C., RUIZ S., MONTALVA G. and SAEZ E., *Seismol. Res. Lett.*, **89** (2018) 519.
[25] LEYTON F., PASTEN C., RUIZ S., IDINI B. and ROJAS F., *Seismol. Res. Lett.*, **89** (2018) 512.
[26] LOMNITZ C., *Seismol. Res. Lett.*, **75** (2014) 368.
[27] MADARIAGA R., *Bull. Seism. Soc. Am.*, **65** (1976) 163.
[28] MADARIAGA R., RUIZ S., RIVERA E., LEYTON F. and BAEZ J. C., *Pure Appl. Geophys.*, (NN) 2018.
[29] MELGAR D., FAN W., RIQUELME S., GENG J., LIANG C., FUENTES M., VARGAS G., ALLEN R. M., SHEARER P. M. and FIELDING E. J., *Geophys. Res. Lett.*, **43** (2016) 961.
[30] OTH A., BINDI D., PAROLAI S. and DI GIACOMO D., *Geophys. Res. Lett.*, **37** (2010) L19304.

[31] Peyrat S., Campos J., De Chabalier J. B., Perez A., Bonvalot S., Bouin M. P., Legrand D., Nercessian A., Charade O., Patau G. and Clevede E., *Geophys. Res. lett.*, **33** (2006) 10.1029/2006GL027710.
[32] Peyrat S., Madariaga R., Buforn E., Campos J., Asch G. and Vilotte J. P., *Geophys. J. Int.*, **182** (2010) 1411.
[33] Prieto G. A., Shearer P. M., Vernon F. L. and Kilb D., *J. Geophys. Res. B*, **109** (2004) NN.
[34] Ruiz S., Madariaga R., Astroza M., Saragoni G. R., Lancieri M., Vigny C. and Campos J., *Earthquake Spectra*, **28** (2012) S1.
[35] Ruiz S., Metois M., Fuenzalida A., Ruiz J., Leyton F., Grandin R., Vigny C., Madariaga R. and Campos. J., *Science*, **345** (2014) 1165.
[36] Ruiz S., Aden-Antoniow F., Baez J. C., Otarola C., Potin B., del Campo F., Poli P., Flores C., Satriano C., Leyton F., Madariaga R. and Bernard P., *Geophys. Res. Lett.*, **44** (2017) 10,290.
[37] Ruiz J. A., Contreras-Reyes E., Ortega-Culaciati F. and Manríquez P., *Phys. Earth Plan. Int.*, **279** (2018) 1.
[38] Schurr B., Asch G., Hainzl S., Bedford J., Hoechner A., Palo M., Wang R., Moreno M., Bartsch M., Zhang Y. and Oncken O., *Nature*, **512** (2014) 299.
[39] Socquet A., Valdes J. P., Jara J., Cotton F., Walpersdorf A., Cotte N., Specht S., Ortega F., Carrizo D. and Norabuena E., *Geophys. Res. Lett.*, **44** (2017) 4046.
[40] Vidale J., Goes S. and Richards P. G., *Geophys. Res. Lett.*, **22** (1995) 1.
[41] Vigny Ch., Socquet A., Peyrat S., Ruegg J.-C., Metois M., Madariaga R. *et al.*, *Science*, **331** (2011) 1417.
[42] Wang G., Boore D. M., Igel H. and Zhou C., *Bull. Seismol. Soc. Am.*, **93** (2003) 674.
[43] Ye L., Lay T., Kanamori H. and Koper K. D., *Pure App. Geophys.*, **173** (2016) 321.

This page intentionally left blank

Proceedings of the International School of Physics "Enrico Fermi"
Course 202 "Mechanics of Earthquake Faulting", edited by A. Bizzarri, S. Das and A. Petri
(IOS, Amsterdam; SIF, Bologna) 2019
DOI 10.3254/978-1-61499-979-9-211

Earthquake occurrence, recurrence, and hazard

F. Mulargia

Dipartimento di Fisica e Astronomia, Università di Bologna - Bologna, Italy

Summary. — Probabilistic Seismic Hazard Assessment (PSHA) plays a fundamental role in the defence strategy from earthquake destruction of most countries. In light of this paramount importance, PSHA should be rooted on solid ground but it is not, since it ignores earthquake Physics starting from its most important phenomenological features. These are *scale invariance*, which allows to infer the behaviour of large earthquakes from smaller seismicity for which copious data are available, and *clustering in time and space*, which states that the more earthquakes one sees the more he should expect. The latter is just the opposite of the Characteristic Earthquake, ubiquitously used in Seismology and Geology under the paradigm of *elastic rebound*. As a consequence, PSHA estimates are essentially speculative and void of scientific significance. In practical terms, while PSHA has the merit of raising attention on an important problem, its faulty physical and statistical premises lead it to untrustworthy results. A substantial improvement comes from appropriately basing estimates on earthquake physical phenomenology, and realistically evaluating and reporting all uncertainties.

1. – Introduction

Earthquakes are among the most destructive natural phenomena and, if it were possible, prediction would apparently be the easiest option to defend from their catastrophic power for one simple reason: rushing away from weak buildings before they collapse is much cheaper than constructing seismic resistant ones. However, a timely escape could reduce earthquake casualties, which are in any case minor compared to other catastrophic

natural phenomena, but would not counter the adverse economic impact, which is the greatest. At any rate, such an option is beyond question since we are persistently unable to predict earthquakes, and this happens because earthquake precursors have never been observed and most likely do not exist [1]. Acknowledging this long ago, the goalpost was lowered from *prediction* to *forecast*, which means essentially the same but with a much lower accuracy.

Forecast is pursued in a way that goes back to the most classical treatment of uncertainty, *i.e.*, Gauss error theory, which advocates randomness to cure ignorance. Ideal examples of this approach are the games of chance. Take for example a coin toss: its Physics is well known since it just concerns the motion of a rigid body. Hence, supposing to know with accuracy the shape of the coin, its mass distribution, the momentum transfer of the flip, the initial position, the air density and flow in the flight path, and assuming also that the catch occurs at an accurately known location, there is no reason why the outcome could not be predicted. The difficulty is just that the problem has many nonlinearities and it is practically impossible to know all the relevant variables with sufficient accuracy. Therefore, ignorance is transformed into a supposedly equivalent description which depends on some random variable, thus allowing to derive the average properties of the process. According to this, one can say that an ideal model of a fair coin is the one that in a large number of tosses shows tails in approximately half of the tosses. Obviously, this leads to a completely different type of prediction, regarding not the next *single* outcome, but an *average* over a sizeable number of outcomes.

The above basic assumption can be rephrased in a variety of ways [2], with language playing a substantial role: the lack of knowledge is elegantly termed *epistemic uncertainty*, which is then translated into *aleatory uncertainty* by the introduction of randomness. The crucial fault of this argument is that it makes sense if, and only if, the Physics is known, which is hardly the case of earthquakes, for which a valid model is still lacking [3]. Beyond allowing to use sexy words, the introduction of Statistics is a smart way to produce numbers which *seem* credible, but in fact are *not*.

In principle, we could take a purely empirical perspective, since statistical modelling proves invaluable in all cases in which the observer is confronted with large amounts of data produced by repeatable and appropriately designed experiments. The validity of the physical models could then be exhaustively tested, but this perspective appears difficult to apply to earthquakes, since:

1) there is little hope to design a realistic earthquake experiment;

2) the source is deep in the Earth and the parameters of the system are difficult to measure;

3) the time scale of observation is 2–3 orders of magnitude *smaller* than the time scale of evolution of the process, while to provide a sufficient sample it should be 2–3 orders magnitude *larger*;

4) last, but absolutely not least, interest is mostly not on forecasting average properties —as Statistics can only do— but on forecasting the next *single* destructive events.

In addition to this there is an utilitarian view: behind any forecast attempt lies the tacit hope that the process has some decipherable regularity which can be of practical utility towards reducing destructive power. In the case of earthquakes, there is one particular type of forecast popular to the point that it became the standard for defining seismic design codes. This goes under the name of *Probabilistic Seismic Hazard Assessment*, from now on PSHA.

PSHA can be cast in a variety of specific forms, but the time-independent Poisson-process–based Cornell formulation [4, 5] and the Characteristic Earthquake model (from now on CE) play a central role in the seismic codes of most countries. In spite of its ubiquitous use, doubts about PSHA were repeatedly raised, with PSHA facing violent attacks [6-11] and strenuous defences [12-26]. However, discussion devoted much effort to the minute details but hardly ever to the physical and statistical bases at the roots of PSHA, which were comprehensively analysed only recently [27]. Making reference to the latter work, let us first of all recall the state-of-the-art of earthquake phenomenology, starting from the phenomenological picture and then passing on to compare it with the assumptions at the basis of PSHA.

2. – Earthquake phenomenology: the state of the art

No valid physical model still exists for earthquakes. In Seismology, research has been traditionally focused on the mechanism of wave generation alone, essentially disregarding the thermal aspects of the process, which were very rarely considered explicitly [28-31]. What is more important for hazard estimates, equally disregarded has been the Physics of earthquake occurrence, which was more or less ignored in geophysical literature since the very beginning [3]. Fortunately, the latter recently received proper attention in the physical literature, under the rationale that earthquake generation is a problem that can be effectively formulated in terms of the Statistical Mechanics of Critical Phenomena [32-36]. It is in this domain of Physics, which enjoyed important theoretical progress in the last decades, that the phenomenological features of earthquake occurrence can be firmly established, while seismological literature appears reluctant to abandon the traditional perspective merely focused on the mechanical aspects.

We will review this approach to earthquake Physics by referring to the original work and, at the same time, illustrate its features through the use of the Italian seismic catalog of Gasperini and Lolli [37]. The latter catalog is the result of a careful equalisation of bulletin records without any forced complying to the Gutenberg-Richter or Omori laws, correcting instead for the individual response of each sub-net, for the specific instruments, periods of activity, methods of analysis, etc. [38].

The catalog starts on January 1, 1981, is complete from magnitude $M \geq 2.5$ and consists of 20547 events, including 19 M5.5 + catastrophic earthquakes. It has a non-constrained b value of 0.9866 and a close fit to Gutenberg-Richter law (see fig. 1). A comprehensive view of this catalog is apparent in fig. 2, which on the horizontal axis illustrates *clustering in time* at different magnitudes. Each cluster shows sharp increases in the event rate of occurrence and smooth decreases, the latter well represented by

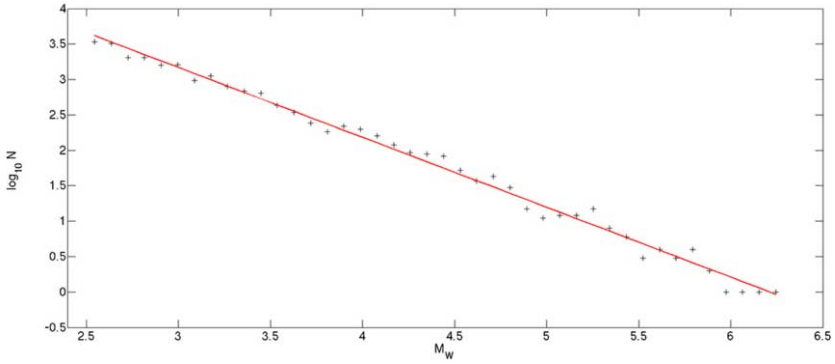

Fig. 1. – The event density *versus* magnitude for the New Italian Seismic Catalog, with the related Gutenberg-Richter fitting curve [37].

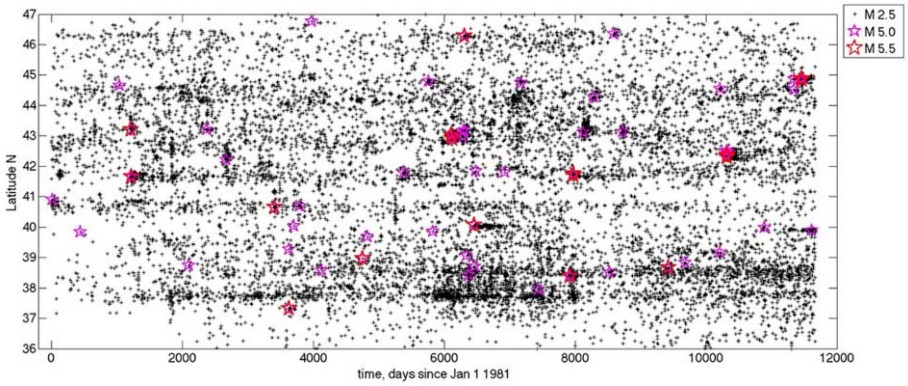

Fig. 2. – The time and space clustering in the New Italian Seismic Catalog [37].

Omori power law

$$N(t) = \frac{K}{c + t^p}\,, \tag{1}$$

with $p \sim 1$ and c a constant dependent primarily on magnitude. The same figure illustrates also the other main phenomenological feature of earthquakes, *i.e.*, that clustering in time is accompanied by clustering in space [39], as is apparent on the vertical axis. Note how a clear simultaneous picture is apparent thanks to geographic shape of Italy, which is essentially North-South and with earthquakes distributed along its structural backbone, the Apennines.

Another major phenomenological feature accompanying clustering is scale invariance. A fundamental result of Bak *et al.* [34] and Corral [36] is that an identical picture exists for the rescaled occurrence times of *all* the events independent of magnitude. In other words, the same scale-invariant picture is found to occur in a large variety of regions

of the world, irrespective of spatial extension, magnitude threshold and seismic catalog from which the data were taken. Namely, Corral [36, 40] tested this on spatial windows of L degrees in longitude and L degrees in latitude, with L spanning from 20 kilometers to the entire globe, and with magnitude threshold ranging from 1.5 to 7.5, obtaining an identical picture independent of magnitude. The mathematical environment in which this can be framed is the Renormalization Group. In quantitative terms, the phenomenology yields that the same scaling law

$$D(\tau) = Rf(R\tau) \tag{2}$$

holds, standing for a self-similarity in space and size of earthquake time occurrence. The functional form of f is close to a generalised gamma distribution

$$f(\theta) = \frac{|\delta|}{a^{\gamma}\Gamma(\gamma/\delta)} \frac{1}{\theta^{1-\gamma}} e^{-(\theta/a)^{\delta}}, \tag{3}$$

where the variable $\theta = R\tau$ is a dimensionless recurrence time, while the parameter values are $\gamma \sim 0.7$, $\delta \sim 1$, a —the dimensionless scale parameter— ~ 1.4, and Γ is the gamma function. This stands for f decaying as a power law for $\theta < 1$ and exponentially faster for $\theta > 1$. It is important to note how this concerns *experimental rates* and does *not* stand for any specific model: the scaling law only concerns the empirical event rate and is independent of any physical model of seismic occurrence.

In practical terms, this stands for a peculiar behaviour:

1) a positive clustering at short time scales, with events tending to be closer to each other in a mutual "attraction" and

2) a negative clustering at long time scales, with sparse events tending to be sparser, in a mutual "repulsion".

This leads to the apparently paradoxical consequence that the time one has to wait for the next earthquake is longer the longer one has been waiting for it. Note how the paradox is only apparent: event rate never becomes 0, and one event sooner or later will occur, immediately raising the chance of experiencing another one, so starting a new cluster. Note how this is at odds with both elastic rebound, which would imply shorter waiting for longer elapsed times and with Poisson, which would imply an independence of the waiting time on the elapsed time [36, 41].

While this may appear paradoxical to the seismologist, it is not to the physicist working in Fracture Mechanics, nor to the layman: assume one is walking over a frozen lake and the surface around him experiences some sudden and loud breaking: would he —as a CE model believer— stand still since according to the historical record that lake experiences major breaks every eight months and it is just two months since last one? Or would he —as a PSHA hazard map believer— leave himself to the mercy of fate, since in the same community there is consensus on the fact that failures cannot be predicted

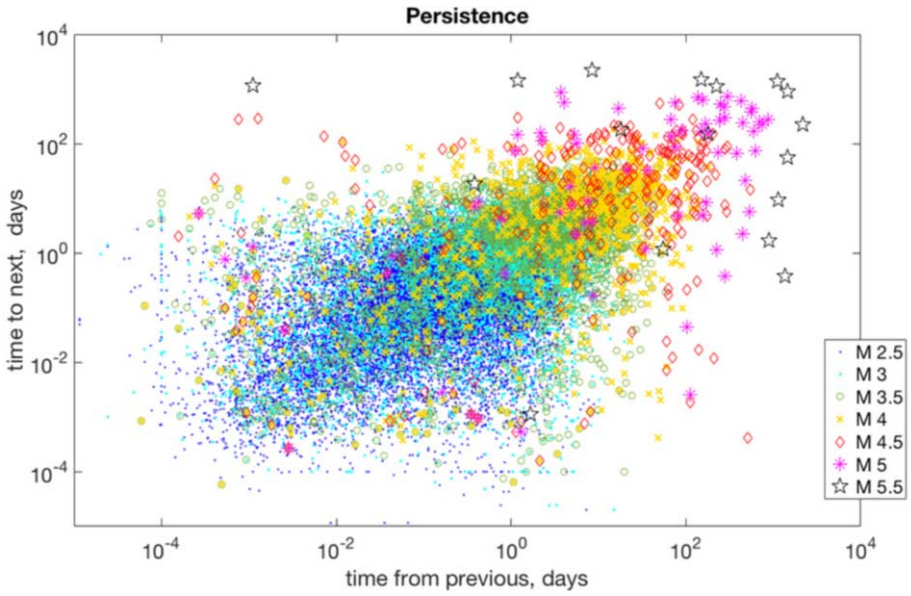

Fig. 3. – The time to next event in days *versus* the time from previous event: the persistence realised by event clustering.

and can occur identically at any time? Or would he rather rush away since he knows that fractures tend to cluster and the chance of a freezing plunge is highly increased?

In addition to this, earthquakes do exhibit "memory" in several respects and there exist a number of correlations in seismicity [40,42]. First of all, events do not occur independently at any time as prescribed by a Poisson process, but remember the occurrence of the last event(s). The effect of memory is obvious in Omori's law and in the time evolution of any cluster, as is illustrated by fig. 3. The same occurs identically also outside major clusters (in the time intervals called "stationary" by Corral [36,40]), standing for the fact that clustering occurs at any scale. The existence of memory is apparently surprising when considering large areas, since one could think that the superposition of the seismicity of different areas can be traced to the sum of many independent processes, so that the seismicity of a broader region should converge to a Poisson process [43], but this is never realised in practice [40], and earthquake memory effects can be summarized as:

1) Pre-earthquake conditions are identical due to the lack of correlation of the magnitude on previous seismicity, confirmed also by palaeoseismic data for single faults [44,45].

2) The larger an earthquake, the shortest the time till next, due to the negative correlation between magnitudes and forward recurrence times.

3) The shortest the time since last earthquake, the shortest the time till next, due to the positive correlation between consecutive recurrence times.

4) The longer the time since the last earthquake, the longer the expected time till next, due to long time positive correlations [46].

Note how the first point can be condensed into *no earthquake knows how big it will be*, while the subsequent three points can be summarised into *seismicity follows persistence* (fig. 3). No comprehensive physical model incorporating these features has been so far developed at neither the deterministic nor the statistical level. In the last fifteen years the ETAS model [47, 48], which somehow combines the Gutenberg-Richter law, the Omori law and an aftershock production rule enjoyed much popularity for its simplicity and qualitative resemblance to some features of real life. However, while this model brings in some clustering, it is not scale invariant —at odds with the main feature of real earthquakes— and it is therefore physically unacceptable. It can be seen —at best— as a rough proxy to real seismicity, perhaps usable as a null-hypothesis test model.

We will now proceed to compare this phenomenology with what earthquakes are assumed to be in the oversimplified engineering-seismological approach, *i.e.*, PSHA.

3. – Earthquakes according to PSHA

PSHA relies on several assumptions, which we will review.

Assumption 0. A probabilistic model of earthquake occurrence can be derived. – PSHA, from the first word of its acronym —Probabilistic— takes for granted that a statistical model for earthquakes exists, *i.e.*, that for earthquakes

1) the sample space

2) the probability distribution

are definable.

Unfortunately, from the statistical point of view the concept of probability itself is very difficult to define for earthquakes [13]. In fact, it is not possible to use a frequentist approach, *i.e.*, repeat identically the same configuration of stress, deformation, fluid circulation, creep, temperature, etc. a large number of times and observe —defining it as probability— the *fraction favourable to the occurrence of a given earthquake*. The difficulty lies in the fact that one would need to repeat the time history over and over again identically, an experiment which is definitely hard to conceive. Nor it appears more feasible a Bayesian approach, which defines probability as the *subjective degree of belief of the observer*, relating it to a subjective state of mind rather than tying it to the physical system. Why should one observer care about the state of mind of other observers, and —more importantly— why should a physical system care about the state of mind of its observers?

Experimentally, what is available is occurrence *rates*, but rates do not equate to probabilities. If rates are used into models producing numbers comprised between 0 to 1 that, even if commonly called probabilities, are not probabilities in any meaningful sense. They are just labels: adding "Sport" to the name of a car does not make it go any faster

unless some real mechanical modifications are included. The only interpretation which appears to make sense is to depict probability as a mere property of a mathematical model which hopefully describes the process. In such a view, the justification for using a model is its validity in either 1) empirical terms or 2) according to Physics. Hence, the whole credibility of PSHA hinges on how empirically, or theoretically, the models it uses are good. These models are essentially two: the CE model and the Poisson process model, which are based on a set of assumptions, and are fit to the data according to a set of other operational assumptions, that we will now review.

Assumption 1. Seismicity is known. – PSHA estimates the seismicity rates of a given region from past earthquake occurrences. This hypothesizes in turn that a complete earthquake catalog is available up to the largest possible magnitudes, correctly reporting recurrences of all events relevant to hazard in a number large enough to allow significant statistics. This is totally unrealistic: instrumental seismic catalogues forcedly span about a century —instruments were introduced around 1900— while non-instrumental ones are tied to the fuzzy quality of historical reports. Even the Italian macroseismic catalogues, which for historical and geographic reasons —the Italian territory is small and was site of civilisation since over two millennia— are likely to be the most extended and accurate in the world, fail to report 9 earthquakes out of the largest 10 in each seismic region [41].

In principle, palaeoseismology may extend the time span of seismic catalogues to thousands of years, allowing to include several recurrences of the larger earthquakes on the same tectonic structure [49]. However, exposed faults are rare and it is safe to state that a direct measure of earthquake recurrence times is generally unavailable [35] and that only very approximate estimates of maximum magnitude are possible on the basis of geologic evidence.

Indirect estimates of larger seismicity can in principle be achieved by extrapolating Gutenberg-Richter law from lower magnitudes, using the main phenomenological feature of earthquakes, *i.e.*, scale invariance. Thanks to it, the behaviour of large earthquakes, for which data are insufficient or absent altogether, can perhaps be inferred combining geology and smaller seismicity —for which data are available. However, this has all the risks and inaccuracies of any extrapolation, in this case aggravated by the logarithmic scale and by the fact that in general the data for the largest magnitudes are insufficient for a direct estimate of maximum magnitude. In addition, the data often (but not in the case of Italy, see fig. 1) indicate a tapering of the Gutenberg-Richter above some corner level [50], which involves further uncertainty. In practice, the lack of sizeable learning set leads to crucial mistakes when "the largest historic magnitude" is taken as an upper limit [41]: the Tohoku 2011 earthquake is a good example of a 9.3 earthquake occurring where the wrongly estimated maximum magnitude was 8.0 [25].

In conclusion, assumption 1 appears generally unjustified and is likely to lead to wrong estimates if catalog occurrences alone are used.

Assumption 2. Seismicity is time independent. – If seismic catalogues 10^5 years long were available, seismicity would perhaps appear asymptotically time independent. The

reason is that the time scale of geological processes, of the order of $\sim 10^6$ years, is much longer than that of earthquake recurrence on the same fault patch, *i.e.*, 10^2–10^3 years. Unfortunately, available seismic catalogs cover reliably time intervals even shorter than the latter.

In conclusion, also assumption 2 appears generally unjustified.

Assumption 3. Tectonic strain is released by large earthquakes. – The classical view identifies earthquakes as the main way to release crustal stresses [51,52], so that all experimental discrepancies —like the one concerning the geodetically observed rates and the maximum magnitude expected in the Tohoku trench [53, 25]— are ascribed to aseismic slip. However, our knowledge of the problem is insufficient and ascribing to earthquakes the leading mechanism for releasing tectonic strain appears no less reductive than conversely ascribing the leading contribution to aseismic slip. The picture is often hazy because of a lack of data, but even when these are available matters are all but clear. This is apparent in fig. 4, which shows the GPS measurements on North-Central Italy for the last 10 years. Several earthquakes above magnitude 6 occurred in this period: the Apr. 6, 2009 L'Aquila M6.2 event, famous for the ensuing trial in court [54] and the Central Italy 2016-2017 large seismic cluster, which included a few events above 6 and one M6.6. None of these clusters, nor the one slightly below M6 of the Emilia, May 2012, appears to bear relation with the GPS measurements, which seem totally independent of seismicity, with large strains concentrated where no particular activity is present and, conversely. no strain concentration where earthquakes did occur.

In conclusion, assumption 3 appears insufficiently constrained by available experimental evidence, which does not allow any firm conclusion.

Assumption 4. Strain energy is released by Characteristic Earthquakes. – PSHA views earthquakes according to the Elastic Rebound paradigm, and maintains Continuum Mechanics and Linear Elasticity as the basic playground. This perspective has its earthquake prototype in the CE model, where an earthquake is the eventual result of a cycle in which elastic strain slowly accumulates to be suddenly released by identical system-size earthquakes.

The never ending success of the CE model derives that it is intuitively appealing to the point of being *the* model in most textbooks in Geology and Seismology. At its roots, earthquakes are stick-slip frictional instabilities on pre-existing plane faults, so that they must be ruled by rock friction on plane surfaces [51, 55-57], with the implicit assumption that the behaviour at laboratory pressures, velocities and geometries can be extrapolated to real Earth conditions. Laboratory results have been condensed into *rate and state* laws [30], which are nevertheless just a set of empirical equations lacking the immediate appeal of a conceptual model, which is instead provided by the CE.

The CE model coincides with the original Reid's idea and is the oldest and the most simple earthquake model. It prescribes that the crust operates into independent domains, at the core of which resides a slip plane, the seismic fault. Each seismic fault, which geologists identify with its observed counterpart, is seismically ruled by the largest

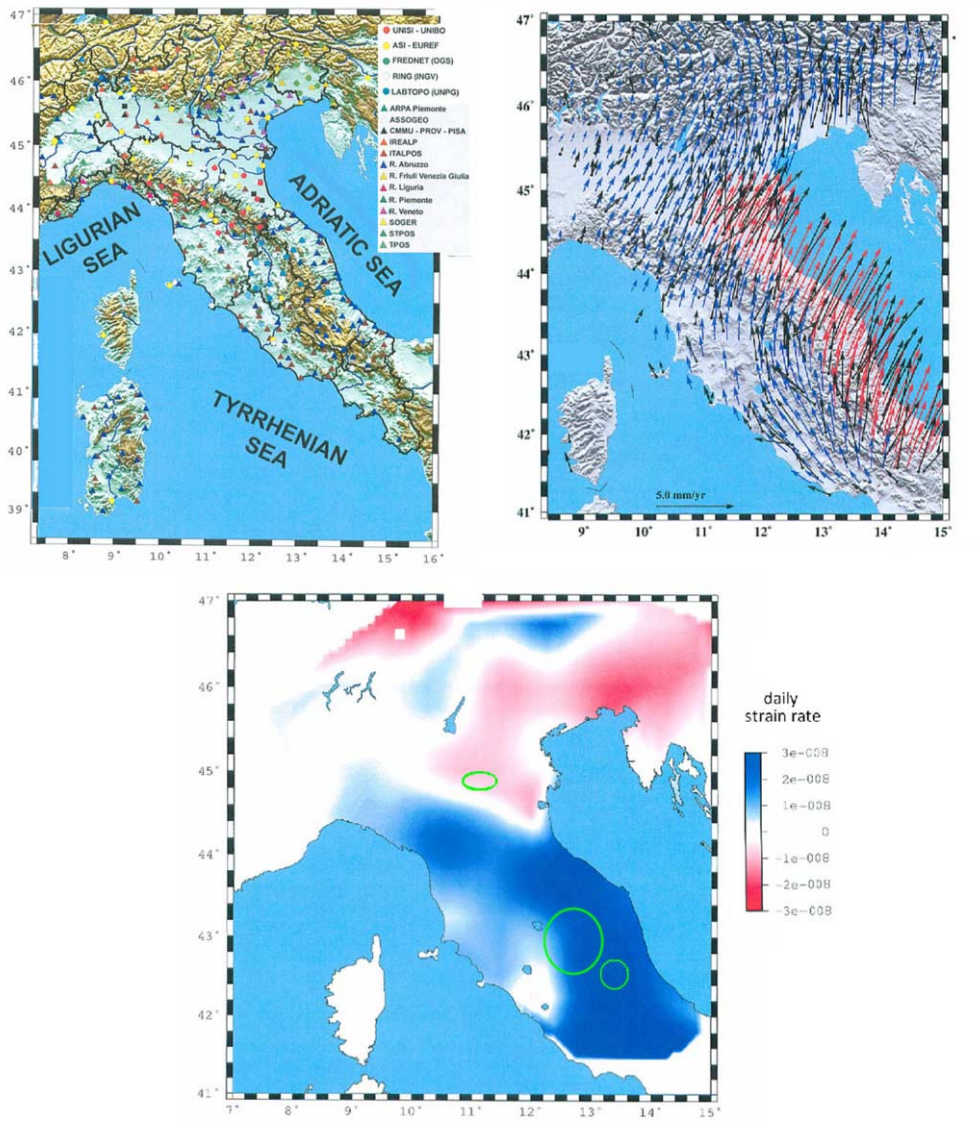

Fig. 4. – The crustal strain measured by the $N > 10^3$ GPS stations (Istituto Nazionale di Geofisica + public administration + private collaborating survey companies) operating over the Italian territory averaged over the last 10 years. Extension is indicated in blue, compression in red. The green ellipses indicate —starting from the North— the epicentral areas of the Emilia May 2012, Central Italy Big Cluster 2016-2017 and L'Aquila April 2009 earthquakes.

possible earthquake it can host. This is a system-size event that abruptly releases all the accumulated strain and resets the strain energy to its ground level. Tectonics then slowly rebuilds strain and starts a new "cycle". Given that tectonic strain rate is likely to

be constant and that the maximum and minimum strain levels are material parameters that are likely to be fixed, this model should produce regular recurrences at fixed time intervals —the *return time* τ. Repeatedly and exhaustively tested for statistical significance, it was shown to be statistically untenable [11, 58, 59], a result that could have been easily anticipated, since if the CE model were applicable, it would allow routine predictions like it happens for solar eclipses. The generalization of the CE model in the Time Predictable and Slip Predictable models [60], which are equivalent to assuming respectively a fixed maximum or a fixed minimum strain threshold in the region, have been equally demonstrated to be inapplicable [61].

A clear example of how the CE paradigm may lead to wrong paths is the Parkfield prediction experiment [62], the inconsistence of which with experimental evidence was unquestionable [11, 59]. Nevertheless, the elementary appeal of CE is strong enough to warrant it a central role in the PSHA hazard estimates for [63]:

1) specific fault subsections, which supposedly follow a characteristic behaviour
2) critical facilities, like nuclear power plants, through alternative statistical approaches
3) all attempts to estimate hazard by modeling *ab initio* the whole seismic wave field.

In conclusion, assumption 4 appears at odds with experimental evidence.

Assumption 5. The impossible assumption: Characteristic Earthquakes occurring at random. – Even if assuming that a "random" occurrence of earthquakes were to make sense, which it does not (see discussion above), PSHA focuses its main interest on the maximum possible size of events according to the CE model, but relaxes its assumption of regularity in time of occurrence. This is logically inconsistent: how can a process be simultaneously fully regular *and* irregular?

In conclusion, assumption 5 appears logically inconsistent.

Assumption 6. Exceedance probability and Return Time. – In the Cornell formulation, by far the most common worldwide, and at the basis of both US NHERP and of the European EC8 building codes, PSHA estimates are generally built upon two quantities, the *return time* τ and the *exceedance probability* p, both borrowed from hydrology [64]. By exceedance probability $p(t)$ is meant the probability that at least one event past some given threshold occurs (*i.e.*, exceeds the threshold) in the time interval t. The (adimensional) return time τ is simply defined as the inverse of the exceedance probability [15, 22] as

$$\tau = 1/p \tag{4}$$

and gives a measure of "how rare" an event larger than the threshold should be. Note how p requires a *valid model* to be calculated from experimental occurrence rates, and this is mostly ignored, simply equating rates and probabilities (cf. above). Note also how the "return" term evokes a regularity in recurrence, which is indeed present in the CE model, but intrinsically absent in the other model generally adopted by PSHA

i.e., the Poisson process. The Poisson process is the most simple model of earthquake occurrence: it assumes no memory whatsoever and total independence among events. As such, it is at odds with the phenomenology, a conflict which is traditionally resolved in a peculiar way: in spite of the fact that clustering is *the* main feature of earthquake phenomenology, it is discarded altogether. The discarding procedure —tacitly justified by the fact that aftershocks are practically non-interesting in terms of hazard— throws away a large fraction of events through *declustering algorithms*, guillotine computer codes designed to sort out the supposedly independent events.

Declustering algorithms may be divided into two main classes [65]: *mainshock window* methods and *linked-window* methods. Mainshock window methods remove all earthquakes in a space-time window around every "mainshock", which may seem an objective and scientifically sound definition, but it is *not* since it depends on a subjectively chosen algorithm. A prototype of this approach is the Gardner and Knopoff algorithm [66].

Linked-window methods [67] calculate a space-time window —with subjectively chosen window parameters— for each event in the catalog rather than just for mainshocks. Following the identification of clusters, a declustered catalog is created by a) removing all events in the cluster except the first one, or b) by removing all events except the largest, or c) by replacing the whole cluster with a single "equivalent event" with magnitude representing the summed moment of all events in the cluster. This allows to *a posteriori* identify mainshocks, aftershocks, independent events and, for some specific algorithms, also foreshocks. However, the parameter choice is subjective, just as the choice among the a), b) or c) options.

In conclusion, declustering discards the main phenomenological feature of earthquake occurrence —clustering— in favour of a subjective entity —mainshocks. As such, it is against physical evidence, and therefore unacceptable. Incidentally, the current declustering approaches are faulty even from a strictly statistical viewpoint, since they are unable to produce truly Poisson residual catalogs [65].

Assumption 7. The sum of ignorance leads to knowledge: the cognitive democracy of logic trees. – PSHA acknowledges that ignorance on earthquake occurrence is large and attempts to treat it with the main tool of democracy: consensus. At the time of the Cold War it was of primary interest to estimate the outcome of a full-scale nuclear conflict, but the available knowledge did not allow any reliable guess. The Rand corporation was contracted to devise something as close as possible to a firm result: *credible scenarios*. They achieved this through the *Delphi Method* [68]. The Delphi Technique is based on the Hegelian Principle of achieving oneness of mind through a three step process of *thesis, antithesis, and synthesis*. In thesis and antithesis, a group of "experts" present their opinion or views on the given subject, establishing views and opposing views. In synthesis, opposites are brought together to form the new thesis upon which consensus is reached. In practice, a large —but not too large— group of experts (typically 7 to 12 in number) is convened in isolation and brainstorming is promoted as long as consensus emerges. At the heart of this is Bayesian approach, but rather than using the Scientific Method to derive experimental models and study their validity on real data,

all the experts' opinions are considered and a weight to each is attributed. Consensus is then reached on final scenarios, which are elaborated by assigning subjective weights to the various branches of a *logic tree* or, alternatively, by calculating averages through a subjective weighting scheme on which consensus has been reached, to obtain *ensemble models*. In both cases uncertainties are apparently under tight control, so that the consensus or ensemble models can both sport an apparently high accuracy. Unfortunately, this is just an illusion: it relies on subjective judgement rather than on solid evidence.

In conclusion, the scenario approach can provide *apparently realistic* pictures, but such videogame-like results can in no way be taken as scientific, since the relativity principle upon which the Scientific Method is based is violated: the *opinion* of experts is by definition not objective.

4. – Discussion

PSHA, when compared with the state-of-the-art of earthquake Physics, appears to rely on a number of assumptions which are either undemonstrated or at odds with phenomenology. This being against the Scientific Method is apparently no cause of concern in the geophysical literature: for example, the "universal" scaling paradigm has been contended by Molchan [69], who maintained universality to be apparent because it was simply traceable to the fraction of mainshocks *versus* aftershocks. But this is an argument against logics: how can an objective piece of evidence like scale-invariant clustering be invalidated by "mainshocks", an entity which can only be defined subjectively? This is just the first of several paradoxes: the Characteristic Earthquake and the Poisson process models are the standard for most PSHA estimates in critical facilities and sites, but have diametrically opposite implications, respectively regular, and highly irregular occurrences. Even more paradoxically, since neither the Characteristic Earthquake nor the Poisson earthquake models account for scale invariance and clustering, the most fundamental phenomenological feature of earthquakes —clustering— is discarded because, otherwise, none of these models could be fitted to the data.

An old proverb of Bologna, in North-Central Italy, says "Piutòst che gninta l'è méi piutòst", literally "rather than nothing, rather is better". This seems the best argument one can get in favour of PSHA. There is no scientific motivation for PSHA hazard estimates to be trusted, but it had the undeniable merit to point at an important problem —seismic hazard— and to pull out numbers which, even if scientifically unrooted and practically wrong, have attracted attention from engineers towards designing seismic resistant construction. It does not matter that the chance of a destructive earthquake is wrongly called "probability", that the earthquake models are at odds with experimental evidence, that the whole picture is flawed, and that the estimated accelerations are given with a three-digit accuracy while uncertainty would not even allow one. What matters is that some beneficial effect has been undoubtedly achieved in reducing earthquake destruction by merely raising attention on the problem. In this respect, PSHA could be taken as a typical example of how some good results may stem from bad premises. Yet, we are now in a position to do much better, by simply accounting for earthquake

Physics and avoiding to cheat on uncertainties through fancy logic trees and friendly expert opinions.

5. – Conclusions

Comparing the state-of-the-art in earthquake Physics to the assumptions at the basis of PSHA shows the many weaknesses and inconsistencies of the latter. PSHA estimates must therefore be regarded as speculative, attaching to its apparently accurate predictions uncertainties of at least several tens of percent. Available earthquake catalogs are too short to allow a reliable forecast of the chance of experiencing a destructive event in any given region. Future earthquakes are likely to occur on active tectonic structures, mostly at sites different than those of the historical and instrumental past [41]. This can be condensed in completing Hiroo Kanamori's [70] post-Fukushima words: *"expect the unexpected"*, with *"which unexpected shouldn't be"*.

Occam's razor may be advocated in favour of the simplest possible model in agreement with the data, but Hanlon's razor suggests an even wiser alternative: do not use any model as long as you do not have a good one. The goal of an effective earthquake defence can be achieved on the basis of preparedness and common sense relying on our knowledge of earthquake Physics, which is so far limited to phenomenology, but has firmly established that earthquakes occur in clusters in both time and space. Hence, we can monitor the territory for any increase in activity and merely use persistence as a forecast tool: organize preparedness for a destructive earthquake in all seismically active regions, and increase the level of alert whenever an increase in seismicity is observed. This simple precautionary strategy [71] has been profitably adopted by the post L'Aquila Italian Major Risk Committee since January 2012, and was successful in minimising the death toll, actually preventing not only casualties, but also injuries in the largest and most destructive Italian earthquake of the last 37 years, the October 30 M6.6 Central Italy event.

REFERENCES

[1] GELLER R. J., JACKSON D. D., KAGAN Y. Y and MULARGIA F., *Science*, **275** (1997) 1616.
[2] WYNNE B., *Global Env. Change*, **2** (1992) 111.
[3] BEN-MENAHEM A., *Bull. Seismol. Soc. Am.*, **85** (1995) 1202.
[4] CORNELL C. A., *Bull. Seismol. Soc. Am.*, **58** (1968) 1583.
[5] BENDER B. and PERKINS D. M., *Seisrisk III: a computer program for seismic hazard estimation* (U.S. Geological Survey, Denver) 1987.
[6] NAS/NRC, *Probabilistic seismic hazard analysis: Report of the Panel on Seismic Hazard Analysis* (National Academy Press, Washington, D.C.) 1988.
[7] FRANKEL A., MUELLER C., BARNHARD T., PERKINS D., LEYENDECKER E., DICKMAN N., HANSON S. and HOPPER M., USGS Open File Rep., 96-532 (1996).
[8] NAS/NRC, *Review of Recommendations for Probabilistic Seismic Hazard Analysis: Guidance on Uncertainty and Use of Experts* (National Academy Press, Washington, D.C.) 1997.

[9] SSHAC - Senior Seismic Hazard Analysis Committee, *Recommendations for Probabilistic Seismic Hazard Analysis: Guidance on Uncertainty and Use of Experts*, NUREG/CR-6372, (1997).
[10] STEIN S., GELLER R. J. and LIU M., *Seismol. Res. Lett.*, **82** (2011) 623.
[11] KAGAN Y. Y., JACKSON D. D. and GELLER R. J., *Seismol. Res. Lett.*, **83** (2012) 951.
[12] CASTANOS H. and LOMNITZ C., *Engin. Geol.*, **66** (2002) 315.
[13] FREEDMAN D. A. and STARK P. B., "What is the chance of an earthquake", in *Earthquake Science and seismic risk reduction*, edited by MULARGIA F. and GELLER R. J. (Kluwer, Dordrecht) 2003, pp. 201–213.
[14] STEIN S., TOMASELLO J. and NEWMAN A., *Eos Trans.*, **84** (2003) 184.
[15] WANG Z., WOOLERY E., SHI B. and KIEFER J., *Eos Trans. AGU*, **84** (2003) 501.
[16] FRANKEL A., *Seismol. Res. Lett.*, **75** (2004) 575.
[17] MUSSON R. M. W., *Eos Trans.*, **85** (2004) 235.
[18] REITER L., *Seismol. Res. Lett.*, **74** (2004) 282.
[19] KLÜGEL J. U., *Engin. Geol.*, **78** (2005) 285.
[20] LOMNITZ C., *Engin. Geol.*, **82** (2005) 71.
[21] MUSSON R. M. W., TORO G. R., COPPERSMITH K. J., BOMMER J. J., DEICHMANN N., BUNGUM H., COTTON F., SCHERBAUM F., SLEJKO D. and ABRAHAMSON N. A., *Engin. Geol.*, **82** (2005) 43.
[22] WANG Z., *Eos Trans.*, **86** (2005) 51.
[23] KLÜGEL J. U., *Engin. Geol.*, **90** (2007) 186.
[24] GELLER R. J., *Nature*, **472** (2011) 407.
[25] STEIN S., GELLER R. J. and LIU M., *Tectonophysics*, **562-563** (2012) 1.
[26] MUSSON R. M. W., *Seismol. Res. Lett.*, **83** (2012) 130.
[27] MULARGIA F., STARK P. B. and GELLER R. J., *Phys. Earth Plan. Inter.*, **264** (2017) 63.
[28] KANAMORI H. and HEATON T. H., "Microscopic and macroscopic physics of earthquakes", in *Geocomplexity and the Physics of Earthquakes*, edited by RUNDLE J. B., TURCOTTE D. L. and KLEIN W. (AGU Publ., Washington) 2000, pp. 147–163.
[29] MULARGIA F., CASTELLARO S. and CICCOTTI M., *Geophys. J. Int.*, **158** (2004) 98.
[30] BIZZARRI A., *Rev. Geophys.*, **49,** RG3002 (2011) 432.
[31] MULARGIA F. and BIZZARRI A., *Phys. Earth Plan. Inter.*, **261** (2016) 118.
[32] RUNDLE J. B., KLEIN W., GROSS S. and TURCOTTE D. L., *Phys. Rev. Lett.*, **75** (1995) 1658.
[33] TURCOTTE D. L., *Fractals and Chaos in Geology and Geophysics*, 2nd edition (Cambridge University Press, N.Y.) 1997.
[34] BAK P., CHRISTENSEN K., DANON L. and T. SCANLON, *Phys. Rev. Lett.*, **88** (2002) 178501.
[35] MULARGIA F. and GELLER R. J. (Editors), *Earthquake Science and seismic risk reduction* (Kluwer, Dordrecht) 2003.
[36] CORRAL A., *Phys. Rev. E*, **68** (2003) 035102(R).
[37] GASPERINI P., LOLLI B. and VANNUCCI G., *Bull. Seismol. Soc. Am.*, **103** (2013) 2227.
[38] LOLLI B., GASPERINI P. and VANNUCCI G., *Geophys. J. Int.*, **199** (2014) 805.
[39] KAGAN Y. Y. and JACKSON D. D., *Geophys. J. Int.*, **104** (1991) 117.
[40] CORRAL A., *Phys. Rev. Lett.*, **95** (2005) 028501.
[41] MULARGIA F., *Bull. Seism. Soc. Am.*, **103** (2013) 2946.
[42] CORRAL A., *Tectonophysics*, **424** (2006) 177.
[43] COX D. R. and LEWIS P. A. W., *The Statistical Analysis of Series of Events* (Methuen, London) 1966.
[44] WELDON R., SCHARER K., FUMAL T. and BIASI G., *GSA Today*, **14** (2004) 4.
[45] CISTERNAS M. *et al.*, *Nature*, **437** (2005) 404.

[46] CORRAL A., *Phys. Rev. E*, **71** (2005) 017101.
[47] OGATA Y., *J. Am. Stat. Assoc.*, **83** (1988) 9.
[48] OGATA Y., *Pure Appl. Geophys.*, **155** (1999) 471.
[49] SIEH K., STUIVER M. and BRILLINGER D., *J. Geophys. Res.*, **94** (1989) 603.
[50] KAGAN Y. Y., *Earthquakes: Models, Statistics, Testable Forecasts* (Wiley) 2013.
[51] SCHOLZ C. H., *The Mechanics of Earthquakes and Faulting*, 2nd edition (Cambridge University Press, N.Y.) 2002.
[52] JENNY S., GOES S., GIARDINI D. and KAHLE H. G., *Tectonophysics*, **415** (2006) 81.
[53] KANAMORI H., "Seismic and Aseismic Slip along Subduction Zones and their Tectonic Implications", in *Island arcs, deep sea trenches, and back-arc basins*, edited by TALWANI M. and PITMAN III W. C., Maurice Ewing Ser., 1 (AGU, Washington, D.C.) 1977, pp. 163–174.
[54] YEO M., *Earth Science Rev.*, **139** (2014) 406.
[55] MARONE C., *Annu. Rev. Earth Plan. Sci.*, **26** (1998) 643.
[56] DIETERICH J. H., in *Earthquake Seismology, Treatise on Geophysics*, edited by H. KANAMORI, Vol. **4** (Elsevier, Amsterdam) 2009, pp. 107–129.
[57] TULLIS T. E., "Friction of rock at earthquake slip rates", in *Earthquake Seismology, Treatise on Geophysics*, edited by H. KANAMORI, Vol. **4** (Elsevier, Amsterdam) 2009, pp. 168–193.
[58] KAGAN Y. Y., *Bull. Seismol. Soc. Am.*, **83** (1993) 7.
[59] GELLER R. J., MULARGIA F. and STARK P. B., "Why we need a new paradigm of earthquake occurrence", in *Subduction Dynamics: From Mantle Flow to Mega Disasters*, edited by MORRA G. *et al.* Geophys. Monograph 211 (American Geophysical Union, Washington, DC, USA) 2015, pp. 183–191.
[60] SHIMAZAKI K. and NAKATA T., *Geophys. Res. Lett.*, **7** (1980) 279.
[61] MULARGIA F. and GASPERINI P., *Geophys. J. Int.*, **120** (1995) 453.
[62] KAGAN Y. Y., *Tectonophysics*, **270** (1997) 207.
[63] USGS - WGCEP, *Earthquake Probabilities in the San Francisco Bay Region: 2000 to 2030. Summary of Findings By Working Group on California Earthquake Probabilities*, Open-File Report 99-517 (1999).
[64] GUPTA R. S., *Hydrology and Hydraulic Systems* (Prentice Hall, Upper Saddle River, N.J.) 1989.
[65] LUEN B. and STARK P. B., *Geophys. J. Int.*, **189** (2012) 691.
[66] GARDNER J. K. and KNOPOFF L., *Bull. Seismol. Soc. Am.*, **64** (1974) 1363.
[67] REASENBERG P. A., *J. Geophys. Res.*, **90** (1985) 5479.
[68] DALKEY N. and HELMER O., *Manag. Sci.*, **9** (1963) 458.
[69] MOLCHAN G., *Pure Appl. Geophys.*, **162** (2005) 1135.
[70] KANAMORI H., *Nature*, **473** (2011) 147.
[71] ALEXANDER D. E., *Nat. Hazards*, **72** (2014) 1159.

International School of Physics "Enrico Fermi"
Villa Monastero, Varenna
Course 202
2 – 7 July 2018

Mechanics of Earthquake Faulting

Directors

Andrea Bizzarri
INGV, Sezione di Bologna
Via Donato Creti 12
40128 Bologna
Italy
tel: +39 0514151432
andrea.bizzarri@ingv.it

Shamita Das
University of Oxford
Department of Earth Sciences
South Parks Road
Oxford, OX1 3AN
UK
tel: +44 1865272015
das@earth.ox.ac.uk

Alberto Petri
CNR, Istituto dei Sistemi Complessi
Dipartimento di Fisica
Università di Roma La Sapienza
Piazzale Aldo Moro 5
00185 Roma
Italy
tel: +39 0649913488
alberto.petri@isc.cnr.it

Scientific Secretary

Anna Maria Loguercio
CNR, Istituto dei Sistemi Complessi
Dipartimento di Fisica
Università di Roma La Sapienza
Piazzale Aldo Moro 5
00185 Roma
Italy
tel: +39 06 49913120
annamaria.loguercio@cnr.it

Lecturers

Ralph J. Archuleta
U.C. Santa Barbara
Department of Earth Science
1006 Webb Hall
Santa Barbara, CA 93106-963
USA
tel: +1 805 893 8441
ralph.archuleta@ucsb.edu

Michel Bouchon
Université Grenoble Alpes
Institut des Sciences de la Terre
BP 53
38041 Grenoble
France
tel: +33 4 76635213
michel.bouchon@univ-grenoble-alpes.fr

Yun-tai Chen
Institute of Geophysics
China Earthquake Administration
5 Minzudaxue Nan Road
Haidian District
Beijing 100081
China
tel: +86 10 68415370
chenyt@cea-igp.ac.cn

William L. Ellsworth
Stanford University
Department of Geophysics
397 Panama Mall
Mitchell Building 373B
Stanford, CA 94305-2215
USA
tel: +1 650 7239390
wellsworth@stanford.edu

Aitaro Kato
University of Tokyo
Earthquake Research Institute
113-0032, Yayoi 1-1-1
Bunkyo-ku, Tokyo
Japan
akato@eri.u-tokyo.ac.jp

Raul Madariaga
ENS - Ecole Normale Supérieure
Laboratoire de Géologie
24 rue Lhomond
75231 Paris CEDEX 05
France
tel: +33 1 44 32 22 16
madariag@geologie.ens.fr

Chris J. Marone
Penn State University
Department of Geosciences
536 Deike Building
University Park, PA 16802
USA
tel: +1 814 865 7964
cjm38@psu.edu

Francesco Mulargia
Università di Bologna
Dipartimento di Fisica e Astronomia
Viale Berti Pichat 6/2
40127 Bologna
Italy
tel: +39 051 20 9 5022
francesco.mulargia@unibo.it

Alexandre Schubnel
ENS - Ecole Normale Supérieure
Laboratoire de Géologie
24 Rue Lhomond
75231 Paris CEDEX 05
France
tel: +33 1 44 32 22 11
aschubnel@geologie.ens.fr

Students

Lauren Abrahams	Stanford University, USA
Sebastian Anger	Gräfelfing, Germany
Jérôme Aubry	Ecole Normale Supérieure, France
Elvira Battimelli	Università di Salerno, Italy
Piero Brondi	OGS Trieste, Italy
Paula Burgi	Cornell University, USA
Jose Nicolas Castro Perdomo	King Abdullah University of Science and Technology, Saudi Arabia
Camilla Cattania	Stanford University, USA
Xiang Chen	Chinese University, Hong Kong
Jinhui Cheng	University of Science and Technology, China
Shanna Chu	Stanford University, USA
Rishabh Dutta	King Abdullah University of Science and Technology, Saudi Arabia
Figen Eskikōy	Bogazici University, Turkey
Paola Forlenza	Università di Salerno, Italy

Barnaby Fryer	EPF Lausanne, Switzerland
Jorge Jara	Ecole Normale Supérieure, France
Sivasubramonain Jayalakshmi	King Abdullah University of Science and Technology, Saudi Arabia
Takamasa Kanaya	University of Maryland, USA
Itzhak Lior	Tel-Aviv University, Israel
Lou Marill	Université de Grenoble Alpes, France
Deepa MeleVeedu	Nanyang Technological University, Singapore
Maddalena Michele	INGV, Italy
Arefeh Moarefvand	Ecole Normale Supérieure, France
Guilhem Mollon	LaMCoS - INSA Lyon, France
Corentin Noël	EPF Lausanne, Switzerland
Kurama Okubo	Institut de Physique du Globe de Paris, France
Francesca Pelusi	Università Tor Vergata, Italy
Camilla Penney	Cambridge University, UK
Jan Premus	Charles University, Czech Republic
Camilla Rossi	Università di Bologna, Italy
Leah Salditch	Northwestern University, USA
Marty Samson	Ecole Normale Supérieure, France
Hugo Samuel Sanchez Reyes	ISY Terre, France
Luyi Shen	University of Alberta, Canada
Verena Simon	ETH Zurich, Switzerland
Anna Skorkina	Russian Academy of Sciences, Russia
Taufiqurrahman Taufiqurrahman	Ludwig-Maximilians-Universität München, Germany
Carlos Villafuerte	Universidad Nacional Autónoma de México
Clay Wood	Pennsylvania State University, USA
Houyun Yu	University of Science and Technology, China

Observers

Alina Besedina	Russian Academy of Sciences, Russia
Harsha Suresh Bhat	Ecole Normale Supérieure, France
Blandine Gardonio	Ecole Normale Supérieure, France
Toni Kraft	Swiss Federal Institute of Technology, Switzerland
Christine J. Ruhl	Berkeley University, USA
Marion Thomas	Ecole Normale Supérieure, France
Luigi Vadacca	Politecnico di Milano, Italy
Gilles Hillel Wust-Bloch	Tel Aviv University, Israel
Alon Ziv	Tel Aviv University, Israel

Finito di stampare
nel mese di luglio 2019

This page intentionally left blank